

**SYNTHESIS, CHARACTERISATION AND APPLICATIONS OF
INDIUM BASED METAL OXIDE NANOPARTICLES**

THESIS

Submitted to

GOA UNIVERSITY

For the award of the degree of

DOCTOR OF PHILOSOPHY

In

CHEMISTRY

By

Ms. MADHAVI ZILBA NAIK

Under the guidance of

PROF. A. V. SALKER

Professor in Chemistry, Department of Chemistry,

Goa University

Taleigao Plateau, Goa

SEPTEMBER 2016

CERTIFICATE

This is to certify that the thesis entitled, “**Synthesis Characterisation and Applications of Indium based Metal Oxide Nanoparticles**” submitted by Ms. **Madhavi Zilba Naik**, is a record of research work carried out by the candidate during the period of study under my supervision and that it has not previously formed the basis for the award of any degree or diploma or other similar titles.

Prof. A. V. Salker

Research Guide

Department of Chemistry

Goa University

Goa -403206, India

September 2016

DECLARATION

I hereby declare that the work embodied in the thesis entitled “**Synthesis, Characterisation and Applications of Indium based Metal Oxide Nanoparticles.**” is the result of investigations carried out by me under the guidance of **Prof. A. V. Salker** at Department of Chemistry, Goa University and that it has not previously formed the basis for the award of any degree or diploma or other similar titles.

In keeping with the general practice of reporting scientific observations, due acknowledgement has been made wherever the work described is based on the findings of other investigators.

Ms. Madhavi Zilba Naik

Research Student

Department of Chemistry

Goa University

Goa-403206,India.

September 2016

ACKNOWLEDGEMENT

For any work to be done three things are essential, vision, knowledge and dedication. In my Ph. D. course, I am highly blessed to be guided by a person with all these qualities. I express my sincere gratitude to my guide **Prof. A.V. Salker**, Dean, faculty of natural sciences, Goa University, for his valuable guidance, continuous motivation and timely suggestions. He has always encouraged and allowed me to grow as a research student.

I extend my thanks to **Prof. B. R. Srinivasan**, Head, Department of chemistry, Goa University, former Deans **Prof. J. B. Fernandes** and **Prof. J. Disa**, former Head **Prof. S. G. Tilve**, and **Dr. V. M. S. Verenker**, my subject expert, for their thoughtful suggestions and continuous evaluation.

I thank **Prof. V. Sahni**, Vice-chancellor Goa University, Registrar **Prof. Y. V. Reddy**, **Prof. S. Shetye**, former Vice-Chancellor and **Prof. V. P. Kamat** former registrar for allowing us to work in the university and for providing us with the necessary facilities.

I also thank **Prof. V. S. Nadkarni**, **Dr. R. N. Shirsat** and **Dr. S. N. Dhuri** for their kind help as and when needed. I am indebted to **Dr. S. C. Ghadi** and **Mr. S. N. Meena**, Department of Biotechnology, **Dr. M. M. Naik**, Department of Microbiology, **Dr. S. K. Shyama** and **Mr. Praveen Kumar**, Department of zoology, Goa University for their cooperation in carrying out biological studies. I extend my thanks to **Dr. Prachi Torney** and **Ms. Lima Rodrigues** for their help in some organic catalytic reactions.

I express my earnest gratitude to **Mr. Girish Prabhu** and **Mr. Arif**, NIO-Goa, **Dr. T. Shripathi**, **Dr. V. Reddy** and **Dr. N. P. Lalla**, UGC-DAE Consortium for scientific research, Indore and **Ms. Sahina Gazi** NCAOR – Goa, SAIF-IIT Bombay and IIT Kharagpur for providing instrumental facilities for characterisation of my compounds.

My sincere thanks to **Dr. Pranay Morajkar** and **Dr. Kiran Naik** for their help in my literature studies. I am grateful to **Dr. Satish, Dr. Rohan, Dr. Shrikant, Dr. Amit, Dr. Meghnath, Mr. Pranav and Mr. Jaykantam** for rendering their help in my analysis and motivating me in this journey.

Words will fall short for me to thank the following people, who have been with me through every thick and thin in this journey. Special thanks to **Mr. Shambhu, Satu, Prajesh, Sagar, Mira, Mithil, Dattaprasad** and **Daniel** for their help and support in every single step.

A healthy environment always creates a positive energy in work, I am grateful to my lab mates, **Mrs. Celia, Ms. Sudarshana, Mr. Chandan** and **Mr. Rahul** for being kind and helpful. I also thank my seniors **Dr. Lactina, Ms. Kiran, Dr. Sandesh, Dr. Chinmay** and **Dr. Hari**, my friends **Diptesh, Abhijeet, Durga, Savita, Rita, Mayuri, Pooja, Sudesh, Prajyoti, Pratik, Pratibha** and all my lovely juniors for their support. I will always cherish the time spent with all.

I take this opportunity to thank the teaching and non teaching staff of department of chemistry-Goa University, the librarian and other staff in library of Goa University for being kind and helpful. I also thank the faculty of chemistry department St. Xavier's college, Mapusa-Goa for their kind support.

Above all I thank God for keeping me calm and determined and showering his blessings on me. Last but not the least I thank my parents **Shri. Zilba, Mrs. Bharati**, my brothers **Keshav, Mahesh**, my sister-in-laws **Anjali, Priya** and my niece **Anshika** for their motivation, constant support, never ending love and patience they have shown with me, without their blessings this wouldn't have been possible.

ABBREVIATIONS

AC	Alternating current
BE	Binding Energy
BET	Brunauer Emmett Teller
BMP	Bound magnetic polaron
CVD	Chemical vapour deposition
DC	Direct current
DMO	Dilute magnetic oxide
DMS	Dilute magnetic semiconductor
DNSA	Dinitro salicylic acid
DRS	Diffused reflectance spectroscopy
DSC	Differential scanning calorimetry
DTA	Differential thermal analysis
ED	Electron diffraction
EDTA	Ethylenediaminetetraacetic acid
FCE	F-Centre exchange
FC	Field cooled
ITO	Indium tin oxide
IR	Infra red
MBE	Molecular beam epitaxy
NMR	Nuclear Magnetic Resonance
NPG	Nitrophenol α -glucopyranoside
PVA	Polyvinyl alcohol
RE	Rare earth
RT	Room Temperature
RKKY	Ruderman-Kittle-Kasuya-Yoshida

SCS	Solution combustion synthesis
SEM	Scanning electron microscopy
TCO	Transparent conducting oxide
TEM	Transmission electron microscopy
TG	Thermo gravimetry
TM	Transition metal
UV	Ultra violet
VSM	Vibrating sample magnetometer
XRD	X-ray Diffraction
XPS	X-ray Photoelectron Spectroscopy
ZFC	Zero field cooled

CONTENTS

CHAPTER 1

1.	INTRODUCTION	1
-----------	---------------------	----------

CHAPTER 2

2.	LITERATURE REVIEW	8
2.1	Introduction	8
2.2	Dilute Magnetic Semiconductors	8
2.3	Pristine and doped In₂O₃	13
2.3.1	Structure and properties	14
2.3.2	Methods of preparation	15
2.3.3	Solid state properties	18
2.3.3.1	Electrical properties	18
2.3.3.2	Magnetic properties	19
2.3.4	Catalysis	21
2.3.5	Biomedical applications	21
2.4	Pristine and doped CeO₂	22
2.4.1	Structure and properties	22
2.4.2	Methods of preparation	23
2.4.3	Solid state properties	25
2.4.3.1	Magnetic properties	25
2.4.4	Catalysis	26
2.5	Pristine and doped MgFe₂O₄	28
2.5.1	Structure and properties	28
2.5.2	Methods of preparation	30
2.5.3	Solid state properties	32

2.5.3.1 Magnetic properties	32
2.5.4 Catalysis	33

CHAPTER 3

3.	EXPERIMENTAL	35
-----------	---------------------	-----------

3.1 Preparation of nanoparticles	35
3.1.1 Combustion method	35
3.1.1.1 $\text{In}_{2-x}\text{M}_x\text{O}_3$ (M= Co, Cr and Ag)	35
3.1.2 Sol-gel method	36
3.1.2.1 $\text{Ce}_{1-x}\text{In}_x\text{O}_2$	36
3.1.2.2 $\text{MgFe}_{2-x}\text{In}_x\text{O}_4$	36
3.2 Physico-Chemical characterisations: Theory and practice	37
3.2.1 Thermal analysis (TG-DTA/DSC)	37
3.2.2 X- ray powder diffraction (XRD)	37
3.2.3 Infra red spectroscopy (IR)	38
3.2.4 Scanning electron microscopy (SEM)	39
3.2.5 Transmission electron microscopy (TEM)	40
3.2.6 Surface area analysis	40
3.2.7 X-ray photoelectron spectroscopy (XPS)	41
3.2.8 UV-visible absorbance/diffused reflectance spectroscopy (UV-DRS)	42
3.2.9 Mossbauer spectroscopy	43
3.2.10 Nuclear magnetic resonance spectroscopy (NMR)	43
3.2.11 DC-Electrical resistivity	44
3.2.12 AC-Magnetic susceptibility	45
3.2.13 Vibrating sample magnetometer (VSM)	45

CHAPTER 4

4.	SPECTROSCOPIC AND SOLID STATE STUDIES	47
-----------	--	-----------

4.1 Thermal analysis (TG-DTA/DSC)	47
4.2 X- ray powder diffraction (XRD)	52
4.3 Infra red spectroscopy (IR)	58
4.4 UV-visible absorbance/diffused reflectance spectroscopy	65
4.5 Scanning electron microscopy (SEM)	72
4.6 Transmission electron microscopy (TEM)	75
4.7 X-ray photoelectron spectroscopy (XPS)	81
4.8 Mossbauer spectroscopy ($\text{MgFe}_{2-x}\text{In}_x\text{O}_4$)	90
4.9 Electrical resistivity	91
4.10 Magnetic studies	96

CHAPTER 5

5.	CATALYTIC AND BIOMEDICAL APPLICATIONS	112
5.1	Surface area analysis	112
5.2	CO oxidation	113
5.3	Organic transformations	117
5.4	Biomedical application: Enzyme inhibition	133
5.5	Toxicity studies	138

CHAPTER 6

6.	SUMMAARY AND CONCLUSION	145
6. 1	Summary	145
6.2	Conclusions	153
	REFERENCES	155
	APPENDIX I	182

INTRODUCTION

Material science is an area of science which is instrumental in up-gradation of human life and lifestyle. The innovation in materials with enthralling applications has played a dynamic part in technological developments. The arrival of nanotechnology has brought a new revolution in the field of material science.

Nanotechnology and nanomaterials have emerged as a core of scientific inventions and discoveries from last couple of decades. May it be in the field of electronics, catalysis or biomedical applications, nanomaterials have left their footprints at all places. From miniaturisation of equipments, to developing new gadgets, nanomaterials have made a huge contribution in adding ease and smartness to human life.

The concept of nanotechnology was first introduced by physicist Richard P. Feynman in his talk titled “**There’s Plenty of Room at the Bottom**” at an American Physical Society meeting at Caltech in 1959 [1]. The technological significance of nanoscale phenomena and its devices was promoted by Dr. K. Eric Drexler in 1980 and the term nanotechnology acquired its current sense [2, 3]. However, in heterogeneous catalysis field obtaining high surface was always a challenge for better catalytic activity, but high surface area would achieve if the particles are in nano size. Even Physicist showed the concept of nanotechnology; which was widely used in heterogeneous catalysis.

It first instigated with manipulating size in the scale of nanometre. The unit of nanometre is drawn from its prefix ‘nano’ a Greek word meaning dwarf or extremely small. This followed the research on various possible shapes that could be obtained preserving the nanometre size. From spherical particles to cubes, rods to wires, crystals to

thin films [5-9] nanotechnology has excelled in its entire facet. It has not just paved path to the interdisciplinary research but at the same time has strengthen it. Ability to control and manipulate materials at atomic and molecular levels thereby understanding their fundamental processes has led to the future advancement and innovations.

Nano-materials can be pure metals, ceramics, polymeric materials or composite materials. The size constraints often produce qualitatively new behaviour which can be even contradictory to the same material in micro-scale. It is not just reducing size but all together formation of a new material with unique functionalities. Oxide nano-materials are imperative part of this ever growing field of nanotechnology. It has emerged as an important class of materials with a rich collection of properties and great potential for device applications. These include; transparent electrodes, high-mobility transistors, gas sensors, photovoltaic's, photonic devices, energy harvesting, storage devices and non-volatile memories [10].

Pristine and doped metal oxides such as ZnO, TiO₂, Cr₂O₃, Mn₂O₃, Co₃O₄, NiO, CuO, SnO₂, In₂O₃, Fe₂O₃, Y₂O₃, Bi₂O₃, spinels, perovskites etc. with different size and shapes have been explored for their properties and applications, this research has been growing exponentially over the years. It has pioneered the new areas in field of chemical science.

Dilute Magnetic Semiconductors (DMS) is one of the phenomena recently associated with metal oxides and nanostructures. In semiconductor devices, charge of electrons play a major role, on the other hand magnetic materials are more focussed on the orientation of electron spin. For the development of new electronics both, charge and spin of electrons are focussed where the spin of electrons that carries the information can be used as an added degree of freedom in novel electronic devices. Such devices are

known as Spintronics (or spin-based electronics) [11]. Discovery of ferromagnetism in the Mn-doped III–V semiconductors (In, Mn)As and (Ga, Mn)As stimulated the DMS phenomena [12–14]. Diluted Magnetic Oxides (DMO) is a type of DMS materials where a magnetic impurity is added to a diamagnetic host. Transition metal doped ZnO, CeO₂, TiO₂, Ga₂O₃, SnO₂ and In₂O₃ [15, 16] have been the materials of interest in this field. Many reports are available on existence of room temperature ferromagnetism in these metal oxides. Presently the existence and origin of ferromagnetism in DMS has caught the eyeballs of researchers all over the world. In the present study pristine and doped (Co, Cr and Ag) indium oxide and indium doped CeO₂ nanoparticles have been explored for their dilute magnetic properties.

Magnetic nano-ferrites is yet another class of magnetic materials which finds its application in computer memory chips, high density recording media, high frequency transformers, heterogeneous catalysis etc. [17-20]. Super-paramagnetism is one such exceptional property of magnetic nanoparticles that is significant in modern technology including magnetic resonance imaging, ferro-fluids, magneto-caloric refrigeration, drug delivery and so on [21-25]. Investigation of the basics of magnetism in nano-size which would stimulate some unique properties that can be tailored for the future application is a challenging field. In the present work we have focussed on the magnesium ferrite preparation and characterisation, where variations in its magnetic properties are studied on doping with indium.

Catalysis is one of the fundamental fields of research in chemistry. A catalyst has the ability to increase the rate of a reaction by lowering the activation energy. Heterogeneous catalysis is a type of catalysis in which a catalyst is insoluble in solvent or reaction mixture. Advent of nano-materials has served as a boon to catalytic field. Nano-

materials render a high surface area owing to reduction in size. This property can be very well exploited in the field of catalysis. Metal oxide nanomaterials have been extensively utilized as heterogeneous catalyst in various reactions including detoxification of exhaust gases [27], degradation of dyes by photo-catalysis [28] and several organic transformations [26]. The important property of the heterogeneous catalyst is that it can be recycled and used over and over again. The high surface area makes it feasible to use lower concentrations of catalyst, thus making the process faster as well as economical.

Use of magnetically separable catalyst adds yet another simplicity and ease to the process and has been a topic of interest among the researchers in recent past. Magnetically separable catalyst can be easily separated from the reaction mixture thus can be easily recycled. We have shown the application of the prepared nanoparticles in the field of heterogeneous catalysis for CO oxidation and few organic transformations.

Use of nanotechnology in biomedical field has fascinated the scientific community over several years and their potential applications have increased in the last decade owing to their exceptional optical properties, oxidation resistance and high penetration. Nano-materials have displayed their key role in antimicrobial activity, diagnostics and recently in enzyme inhibition. Owing to the small size of nanoparticles they are highly used as drug delivery agents, thereby targeting the specific cells. Further improvements are brought about in the activity of nanoparticles by functionalising. The nanoparticles are functionalised by organic components and then used for desired application such as target specific reactions [29]. In the present work we have explored the enzyme inhibition activity of Ag doped In_2O_3 nanoparticles against alpha-amylase and alpha- glucosidase enzyme.

Nanoparticles, despite showing the captivating applications in biomedical fields are accompanied with a toxicity risk. The small size which serves as a boon for several applications may also prove to be a limitation in certain situations if found toxic by retaining in the body. This motivated us to carry out the toxicity studies of few of our samples employed for biomedical and catalytic applications.

Synthesis plays a key role in governing the applications of nano-materials. Designing a profound preparative method that would yield the nanoparticles with desired shape and size is all together an amazing science. Optimising a preparative method for such a shape or size directional synthesis can be simple as well as complex. The two well known approaches for the synthesis of nano-materials include top down where a bulk material is cut down to get nano-sized particle while another is bottom up where starting from atomic level the material is grown into nanoparticle. Both the approaches are widely used and both encompass their own pros and cons. Chemical synthesis is a widely used bottom up approach for synthesizing nanoparticles. Various methods have been reported in literature of chemical synthesis viz co-precipitation [30], precursor [31], sol-gel [32], hydrothermal [33], chemical vapour deposition [34], micro-emulsion [35] combustion [36, 37] etc.

Considering the case of metal oxide nanoparticles, incorporating the metal ions as dopants and thereby manipulating its properties directing towards a particular application has led to several new inventions. In the present work, combustion and sol-gel are the two techniques employed for the nanoparticle preparation. The prepared nanoparticles are thoroughly characterised by employing several spectroscopic and microscopic techniques and their application in the magnetic, catalytic and biomedical field has been explored.

The emergence of nanotechnology and adaptation of its fundamental processes for the betterment of society has developed as the prime function of scientists and researchers worldwide. The growth in this field has been exponential and the output has been enormous. This period might be recognised as nanotechnology era in the coming years. In view of curiosity generated for learning the facts and processes that nano-materials and its applications brings, the work presented in the thesis has been carried out. It is the aura of this field that has motivated us for this work.

Highlights of the Thesis

- Pristine, and Co, Cr and Ag doped indium oxide nanoparticles have been prepared by glycine combustion method while pristine, and In doped CeO₂ and MgFe₂O₄ nanoparticles have been prepared by sol-gel method using citric acid.
- The prepared compounds have been characterised by X-ray diffraction (XRD), Thermal analysis (TG-DTA/DSC), Infrared spectroscopy (IR), UV-Visible Diffuse reflectance spectroscopy and X-ray photoelectron spectroscopy. Scanning and Transmission electron microscopy has been used to study morphology and size of the metal oxides.
- DC- electrical resistivity studies has been carried out on two probe electrical resistivity set up and magnetic properties of the compounds are studied using Vibrating Sample Magnetometer (VSM). AC susceptibility and Mössbauer analysis has been carried out for In doped MgFe₂O₄ compounds.
- The prepared compounds have been investigated for their catalytic activity in CO oxidation and few organic transformations.
- Pristine and Ag doped In₂O₃ nanoparticels have been explored for *In vitro* enzyme inhibition activity. The toxicity studies are also reported for Co and Ag doped indium oxide compound.

Organisation of thesis

The present thesis is divided into following chapters:

Chapter 1.Introduction: Brief introduction about the metal oxide nano-materials, and their importance is highlighted.

Chapter 2.Literature Review: Literature studies highlighting the work carried out on the systems presented in the thesis

Chapter 3.Experimental and characterisation techniques: Details of synthetic procedures and characterisation techniques employed.

Chapter4. Spectroscopic and solid state studies: Different spectroscopic analysis and magnetic studies carried out on the compounds are highlighted.

Chapter 5.Catalytic and biomedical applications: This chapter discusses the application of prepared nanomaterials in catalytic CO oxidation, organic transformations and enzyme inhibition; also toxicity studies of few compounds are reported.

Chapter 6. Summary and Conclusion: In this chapterthe results are summarised and based on them the conclusions are derived.

LITERATURE REVIEW

2.1 Introduction

Nanomaterials with their unique properties have created an important place for themselves in the scientific field. Mixed metal oxides in nano size have captured a lot of attention owing to their easy preparation, stability and striking applications. Several methods have been reported for the preparation of nanoparticles which further govern their structural and physical properties. Substitution/doping of ions in metal oxides also alter their physical properties and influence their applications. In this chapter we have discussed some of the noteworthy findings that have been reported on the metal oxides presented in the thesis, and their properties.

2.2 Dilute Magnetic Semiconductors

Dilute Magnetic Semiconductor (DMS) has been ruling the semiconductor field ever since the discovery of magnetism in transition metal doped II-VI semiconductors (a combination of elements from group 2 or 12 and group 16 of periodic table) like CdTe, CdSe, ZnSe and CdS [38]. The advancement in the field led to the observation of ferromagnetism in III-V material (a combination of elements from group 13 and group 15 of periodic table), *p*-type (In, Mn)As prepared using molecular beam epitaxy (MBE) by H. Munekata et al. [12,13]. Further improving the Curie temperature (T_c) of the material was the basic interest of researchers [14]. The first report of wide band gap Dilute Magnetic Oxide (DMO) material was on Mn doped ZnO by T. Fukumura et al. in 1999 [39]. This was followed by the *ab initio* calculations based on the local density approximation that investigated ferromagnetism in ZnO-based semiconductors and the work in this field started accelerating [40].

Meanwhile in 2000 Dietl et al. using Zener model explained magnetic properties in $\text{Ga}_{1-x}\text{Mn}_x\text{As}$ and $\text{Zn}_{1-x}\text{Mn}_x\text{Te}$ and predicted T_c for various Mn doped p -type semiconductors [41]. The theory is based on charge carriers and requires high hole concentration ($>\sim 10^{20} \text{ cm}^{-3}$) to achieve higher T_c . He further predicted the existence of room temperature T_c for GaN and ZnO based DMS [42, 43]. Possibility of high T_c ferromagnetism in n -type ZnO as well as Transition metal (TM) doping was reported by K. Sato et al. [44]. The work of Y. Matsumoto et al. which reported room temperature ferromagnetism in cobalt doped TiO_2 , activated the research field towards DMO and experimental work in this field was triggered [45]. This began a new era of DMS's based on oxides. Diamagnetic oxides doped with transition metals including ZnO [46-49], TiO_2 [50-53], SnO_2 [54-57], In_2O_3 [58-63] and CeO_2 [64-67] caught the attention of researchers all over the world. As a bulk material, nano-sized or thin film, extensive experimental work was directed towards studying their synthesis and magnetic properties. Many new materials are still under investigation and in near future might prove to be candidate for DMS. The advance state of this work proceeded and eventually rare earth (f block) and alkaline (p-block) elements were also doped in diamagnetic oxides and their magnetic properties were studied. Controversial reports on presence / absence of magnetism in TM, rare earth (RE) or alkaline doped metal oxides started publishing. Over the period the origin of magnetism became a hot topic of discussion. Then the reports displaying the unconventional RT ferromagnetism in un-doped diamagnetic oxides such as HfO_2 , SnO_2 , Al_2O_3 , In_2O_3 , ZnO, CeO_2 , and TiO_2 [68-71] be it in bulk form, nanoparticle or films, made the matter even more complex. The room temperature magnetism here is thought to be originated from intrinsic defects which are stable at room temperature.

Various explanations for the origin of RT ferromagnetism have been given as per observed results including, coupling between the 3d and 2p electrons, segregation of

magnetic impurity forming a secondary phase, defects formed during synthesis, cation/anion vacancy, cation/anion interstitials, the surface defects due to nano-size etc. They are discussed further in the individual literature for In_2O_3 and CeO_2 . Some reports show the presence of ferromagnetism in nano-form and absence in bulk whereas others show its consistency in both forms. The presence of ferromagnetism is also attributed to the synthetic process used for preparation. Various explanations are given to the different observed results.

Although the origin of dilute magnetism is not fully understood, there have been various theoretical models put forward to explain ferromagnetism in DMS. They are basically dependent on exchange mechanisms direct or indirect. Some of these are discussed below.

2.2.1. The Zener model

Zener model [72-73] states that there are two types of super-exchange interactions direct and indirect. The direct interaction is between the half-filled d-shell electrons of transition element and filled p-orbital of anion, where both the adjacent atoms of transition element occupy the same p-level. According to Pauli Exclusion Principle their spins should be opposite. This results in an anti-ferromagnetic coupling of closest neighbour cation through a shared anion [74].

The indirect super exchange occurs when the d shell electrons of transition metal mediated by the delocalised band carriers align the spins of partially filled d shells in ferromagnetic manner [75]. According to Zener model ferromagnetism is produced only when the direct super exchange interaction is dominated by indirect super exchange interaction.

2.2.2. Ruderman-Kittel-Kasuya-Yoshida (RKKY) model

The RKKY model explains the indirect magnetic interaction between a single localized magnetic ion and the delocalized conduction band electrons. Such interaction was first proposed by M. A. Ruderman and C. Kittel [76]. It was further studied by T. Kasuya and K. Yosida and then the present model came into existence called RKKY model [77]. In this interaction the conduction electrons near to the magnetic ion gets magnetized and serve as an effective field to influence the polarization of close by magnetic ions where polarisation decays in an oscillatory manner. The interaction can be ferromagnetic or anti-ferromagnetic exchange depending on the separation between the pair of magnetic ions [78].

2.2.3. The mean field approach /mean field-Zener model

In the mean field approach ferromagnetism arises through interactions between the local moments of the dopant atoms mediated by free holes in the material. The mean field approximation is used assuming spin-spin coupling to be a long-range interaction. T. Dietl et al. used the mean field-Zener model in 2001 [75] to explain the hole mediated interaction between localised magnetic spins in semiconductor. It is based on Zener and the RKKY interaction which depends on the spin-orbit coupling in the valence band. It is used to explain the T_c of different DMS material such as Mn doped GaAs and ZnTe [79].

2.2.4. The double exchange method

The double exchange method was used for the first time by Zener [80] to explain the observed ferromagnetism in manganite with perovskite structures. It is a type of magnetic exchange that occurs between the ions with different valence states, like in Mn^{3+}/Mn^{4+} doped compounds. The model involves the virtual hopping of the extra

electron from one ion to another which leads to the coupling of magnetic ions in different charge states. This electron exchange between the two species determine whether the compound is ferromagnetic or anti-ferromagnetic and the exchange is facile if the exchanged electrons do not change the spin direction as per the Hund's rule and is only feasible when one atom has an extra electron compared to the other.

2.2.5. Super-exchange

The super-exchange interaction is almost similar to the double exchange except for the fact that the ferromagnetic or anti-ferromagnetic alignment occurs between the two atoms with same oxidation state. Here the coupling is between the two neighbouring cations via an anion. The bridging is by a non magnetic anion which mediates the magnetic interaction between the localised spins. Considering Pauli Exclusion principle when two magnetic ions with half occupied orbitals couple through a non magnetic ion, the super-exchange will be anti-ferromagnetic, and if the coupling is between an ion with half-filled and one with filled orbital it will be ferromagnetic whereas if the coupling is between either filled or half filled orbital and an empty orbital it can be ferro or anti-ferromagnetic [81].

2.2.6. Bound magnetic polaron (BMP) model

The BMP concept was introduced by Coey et al. [49] which explained the low temperature metal-insulator transition in oxygen deficient compound. Here the donor electrons near to the conduction band play a vital role in mediating the long ranged ferromagnetism. The insulating behaviour is retained by oxygen vacancies which donate as well as trap electrons. It includes the interaction between the magnetic spins of localised TM with the much lower number of weakly bound carriers. This alignment

results in the formation of bound magnetic polaron. Long range ferromagnetism is observed when the neighbouring magnetic polarons overlap, where the ferromagnetic transition takes place when polaron and sample size is equal [43, 44]. The model is suitable for samples with low carrier density. It is applicable to study both *p*- and *n*-type materials [82].

There is another sub class to this BMP model known as F-centre exchange (FCE) mechanism which has been used to explain RT ferromagnetism in magnetic insulator [83]. It explains the mechanism for oxygen vacancies mediated ferromagnetism. The phenomena is explained on the basis of three charge states of oxygen vacancies as follows: (a) F^{2+} centre with zero trapped electrons, (b) F^+ centre where one electron is trapped and (c) F^0 centre with two electrons trapped. For F^0 the charge states are singlet ($S=0$) and constitute a shallow donor level or lie above the conduction band edge. Here only weak ferromagnetic interactions between magnetic dopants can be mediated. Sometimes impurity band formed due to the F^0 centre states may overlap with the conduction band of host oxide (4s band) thereby favouring the weak FM whereas singly occupied vacancies (F^+ centre) lie deep in the gap and can favour a strong FM [83,84].

Introduction of the systems on which the present thesis work is based on is presented in the following sections.

2.3 Pristine and doped In_2O_3

Indium oxide (In_2O_3) is an important *n*-type semiconductor with wide band gap that ranges from 3.55-3.75 eV. It displays interesting properties such as high transparency to visible light, high electrical conductance, and strong interaction between certain poisonous gas molecules and its surfaces [85].

2.3.1 Structure and properties

Indium oxide exists in three different phases categorised by space group symmetries $I2_13$ (S. g. 199), Ia_3 (s. g. 206) and R_3c (s. g. 167). Among the three space groups listed above In_2O_3 with Ia_3 (s. g. 206) is the most widely studied form theoretically as well as experimentally, and is similar to many trivalent rare-earth oxides, such as Yb_2O_3 and Dy_2O_3 . It is a stable phase at low to normal temperature. It crystallizes in a cubic bixbyite-type structure which has 80-atoms in its unit cell. The unit cell is body centered (bcc) as shown in Fig. 2.1 and contains eight formula units. It has two types of indium atoms and one type of oxygen atom at Wyckoff positions 8b, 24d and 48e, respectively [86]. The 'b' and 'd', are the preferred cation sites. The 'b' site cations have six equidistant oxygen anion neighbours, which lie approximately at the corners of a cube with two anion structural vacancies along one body diagonal.

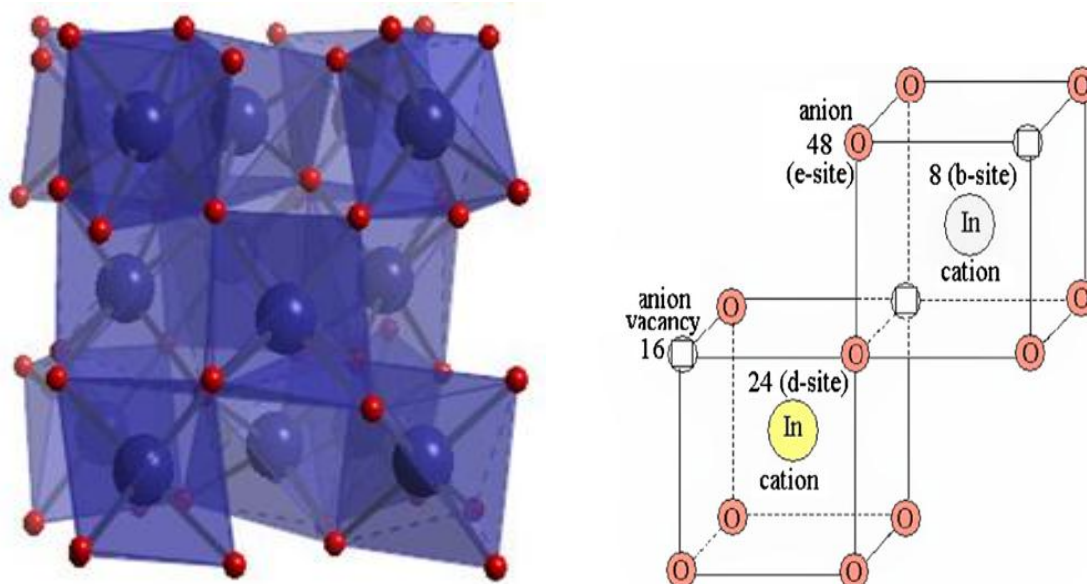


Fig. 2.1 (a) The bixbyite crystal structure and (b) unit cell representation of In_2O_3 .

The sites of the cations are coordinated with six oxygen anions at three different distances, which lie near the corners of a distorted cube with two empty ions along one face diagonal. The two types of indium atoms are surrounded by oxygen in octahedral and trigonal coordination respectively [86-88].

As seen from the above description it is understood that the indium oxide exists with anion vacancies. This defect structure displays amazing new properties which can be further used in designing its several applications. The defect concentration can be tuned and varied by doping with other ions. The method of preparation also plays a vital role in formulating structure, properties and size of the metal oxides. There are several wet chemical methods reported in the literature for the preparation of pristine and doped indium oxide, in nanosize as well as thin films. In this section we shall discuss some of the reported methods in literature.

2.3.2 Methods of preparation

2.3.2.1 Co-precipitation

One of the simplest and widely studied preparative methods is co-precipitation. In this method, metal salts such as nitrates or chlorides are dissolved in water (or other solvent), these are then precipitated as hydroxides using a base such as NaOH, NH₄OH etc. The precipitate is then filtered and dried followed by calcinations. Sintering in the required cases is carried out at a temperature that would not destroy the nano-size. In case of mixed metal oxides this method sometimes fails to produce homogeneity. Several modifications such as use of surfactants, capping agents, heating in inert atmosphere are done to overcome this problem and obtain smaller size particles. These emerge as novel and feasible alternatives that modify the resulting solid thereby displaying different

morphological characteristics [89]. Many reports are available where pristine and doped In_2O_3 are obtained by simple or modified co-precipitation method [90-97].

2.3.2.2 Sol-gel

Sol -gel is the most widely explored method for the preparation of nanoparticles which is known to yield nano-size as well as good homogeneity. In a typical method metal salts and the gelling /complexing agent which is mostly an organic acid, are taken in desired ratio and dissolved in water. The colloidal solution of the reactants is continuously stirred at 80°C until it becomes a sol which leads to the formation of gel. The obtained gel is heated at desired temperature which gives the solid compound. The compound is then powdered/ground and further calcined or sintered as per the requirements [32, 98]. Many reports are available for organic acid mediated sol- gel synthesis of pristine and doped In_2O_3 nanoparticles [63,99-103]. Few modifications are also carried out in this method such as addition of glycol as polymerising agent [104], NH_3 for pH regulation as some metals precipitate forming a stable complex.

2.3.2.3 Combustion method

Solution combustion synthesis (SCS) is a versatile, simple and rapid process, which allows effective synthesis of a variety of nano-size materials. This process involves a self-sustained reaction in homogeneous solution of oxidizer (like metal nitrates) and fuel (like urea, glycine, hydrazides). Depending on the type of the precursors, as well as on conditions used for the process organization, the SCS may occur as either volume or layer-by-layer propagating combustion modes. Smaller particle size and homogeneity are the highlights of this method. [36, 37,105].

2.3.2.4 Hydrothermal /Solvothermal method

Starting with new raw materials, solvents, and reaction temperatures and altering experimental parameters, researchers have prepared various kinds of nanostructures through hydrothermal/solvothermal approaches including metal oxides, carbonaceous nanostructures etc. The metal salts are dissolved in water/solvent and added into the teflonlined autoclave with an additive, such as polyethylene glycol (PEG), cetyltrimethylammonium bromide (CTAB) and polyvinyl pyrrolidone (PVP). The autoclave is then sealed and heated at desired temperature and pressure for required amount of time, it is then cooled and the precipitate formed is centrifuged and dried. Different morphologies of nano-materials can be obtained by this method. [33,106-114]

2.3.2.5 Chemical Vapour Deposition (CVD)

In CVD, powders, nano-crystalline products and thin films are prepared from reactants in the vapour phase. Volatiles or the starting materials are heated to form vapours, then mixed at a suitable temperature and transported to the substrate by carrier gas. Typical starting materials include halides, hydrides, and organometallic compounds [115]. Indium oxide nanoparticles and thin films have been extensively prepared by this method [62,116-119].

2.3.2.6 Pulsed laser deposition (PLD)

It is a vapour deposition technique in which a high-power pulsed laser beam is focused inside a vacuum chamber to strike a target of the material that is to be deposited. Several reports are available in the literature for the preparation of In_2O_3 thin films by PLD [120-122].

2.3.2.7 Sputtering

It is also a physical vapour deposition (PVD) method for thin film deposition. This involves ejecting material from a target source onto a substrate such as a silicon wafer. Radio frequency sputtering where power used is AC, and DC Magnetron sputtering which uses a DC power are the two different methods reported for In_2O_3 thin films preparation [123-127].

2.3.2.8 Miscellaneous Methods

Few other methods with certain modifications used for In_2O_3 preparation include spray pyrolysis [128] sonochemical [129] pulsed laser ablation [130] thermal decomposition of $\text{In}(\text{acac})_3$ [131] and precursors formed from Aleovera plant extract and $\text{In}(\text{acac})_3$ [85].

2.3.3 Solid State Properties:

2.3.3.1 Electrical Properties

Indium oxide is one of the leading transparent conducting metal oxides (TCOs) owing to the amalgamation of properties like optical transparency in the visible region and electrical conductivity. The non-stoichiometric In_2O_3 are found to be more conducting due to the presence of free carrier concentration coming from the oxygen vacancies [132]. It has high electron affinity and low electron effective mass making it intrinsically n-type and highly susceptible to extrinsic electron doping, e.g. Sn-doped In_2O_3 (ITO) [133].

Hafeezullah et al. reports semiconducting behaviour of In_2O_3 nanoparticles where current increases as a function of temperature up to 250 °C, no further change was observed in the current as a function of temperature [134]. K. Palandage et al. observed

increase in conductivity with increase in temperature where they conclude that the oxygen vacancies act as shallow donor states but their contribution can be clearly enhanced by the presence of indium interstitials, where donor states give rise to high conduction electron densities observed in experiments. The reduction in particle size shows decrease in conductivity and increase in activation energy [86]. E.A. Forsh et al. confirmed that the thermal activation of electrons dominates the conduction in In_2O_3 [135]. Literature reports on resistivity measurements of Sn doped In_2O_3 thin films suggests that resistivity rapidly decreases with Sn doping till a certain dopant concentration, further increase in concentration do not have any effect on conduction. This is owing to the increases in carrier concentration but decrease in mobility of free carriers [136,137]. Few reports are available on electrical properties of TM doped In_2O_3 that includes a report by Be´rardan et al. where samples show high resistivity values when doped with Mn and Cr, exceeding that of un-doped samples [138]. Similar results are also observed in case of Cu doping [58,124,138,139].

2.3.3.2 Magnetic studies

In_2O_3 is one of the important materials studied for DMS along ZnO, TiO_2 , and SnO_2 . The transition metal (TM) doped In_2O_3 nanostructures and thin films have received a great deal of interest in this prospect. Many reports claim the existence of room temperature ferromagnetism in TM doped In_2O_3 (where TM = Cr, Co, Ni, Mn, Cu and Fe) [9, 58-63,106,120,124,138,139]. Many contradictory observations have been reported on the existence of dilute magnetism.

X. Meng et al. reports room temperature ferromagnetism in Co doped In_2O_3 where the strong d-d coupling between magnetic atoms, weak p-d coupling between the Co 3d states and O 2p states are found to be responsible for observed behaviour [63]. Whereas,

Sun et al. reports a paramagnetic nature of the Co doped In_2O_3 nano-particles [106]. Room temperature ferromagnetism is also reported in the Co doped In_2O_3 thin films [9,140]. Paramagnetism with weak anti-ferromagnetic interactions was observed by S. Khatoon and co-worker [141]. Recently N.Deng et al. reports room temperature ferromagnetic in pristine as well as Co doped In_2O_3 nanospheres prepared by nanocasting synthesis [142].

In case of Cr doped In_2O_3 Gauer et al. reports the room temperature ferromagnetism in Cr doped compounds prepared by ceramic method. The ferromagnetism is said to be originating from Cr_2O_3 or CrO_2 impurity phases [143]. Farvid et al. reveals intrinsic ferromagnetism in $\text{Cr}^{3+}:\text{In}_2\text{O}_3$ nano-crystalline structures [31]. H. Raebiger et al. in their density functional calculations found that Cr doped In_2O_3 is a ferromagnetic semiconductor and the ferromagnetism can be turned on and off by regulating the carrier concentration by means of external doping [144]. Ferromagnetism in Cr doped In_2O_3 thin films have also been reported [120, 145, 146] where F-X Jiang et al. suggests that ferromagnetism can be enhanced by co-doping with Sn. P. Kharel et al. revealed carrier mediated origin of ferromagnetism in high vacuum annealed samples. Theoretical studies by A. Gupta et al. also reports ferromagnetism in these compounds with Curie temperature well above room temperature, [147] whereas L.M. Huang's theoretical study confirms the ferromagnetism to be defect induced [148]. Also G. Z. Xing et al. shows similar observation [62]. D. J. Payne et al. reports clear in-homogeneity in Cr doped In_2O_3 films, yet no ferromagnetism was present [149]. It has also been argued that p-type intrinsic defects such as In vacancies or O interstitials mediate ferromagnetism [148]. Another important observation that was made in this field was by Sundersan et al. which state that ferromagnetism is a universal phenomenon of all diamagnetic oxides in nano-size [150]; this was followed by several other reports which display room

temperature ferromagnetism in pristine In_2O_3 in small size [151]. Silver doped In_2O_3 has not been much studied for ferromagnetism. Considering the existing uncertainties about the presence as well as origin of ferromagnetism, it becomes an interesting phenomenon for further investigation.

2.3.4 Catalysis

Over the years metal oxides have been extensively used in the field of heterogeneous catalysis where In_2O_3 has been explored for photo-catalysis earlier but recently few researchers have also explored catalytic activity of In_2O_3 nanoparticles in organic synthesis including synthesis of propargylamines via C–H and C–Cl bond activations [152], C-S cross-coupling of thiols with aryl halides [153], synthesis of 3-buten-1-ol from 1,4-butanediol [154], 1,2-disubstituted benzimidazoles [155] and tandem cyclization of amidine with nitro olefin [156]. In_2O_3 can act as a Lewis acid; this is the property which makes it one of the valuable candidates for heterogeneous catalysis. In_2O_3 supported on Si-MCM-41 has been used for Friedle-Craft reactions [157]. Catalytic detoxification of gases is an area where metal oxide catalysts are extensively used. In_2O_3 rarely is considered in this field. Few available recent reports include low-temperature CO oxidation on Au/ In_2O_3 - TiO_2 catalysts [158], Promoting effects of In_2O_3 on Co_3O_4 for CO oxidation [159] and CO oxidation activities of indium oxide nanostructures: 1D-wires, 2D-plates, and 3D-cubes and donuts [160]. We have explored the catalytic side of In_2O_3 nanoparticles for organic transformations as well as for CO oxidation.

2.3.5 Biomedical Applications

A nano-material in a biomedical field is an area of interdisciplinary research that finds its application in the drug delivery, as anticancer agent, biosensors, and

antimicrobial agents. Enzyme immobilization or inhibition by nanoparticles has also been reported by several researchers [161-162]. Carbon nano-tubes, graphene oxide, ZnO, silver and gold nanoparticles have also been evaluated for the same [163-168]. Further, silver, aluminium and magnesium coated nanoparticles have been acknowledged for treating enzymatic dermatitis due to their ability to inhibit lipases and proteases [166,168]. Biogenic silver has also been reported to inhibit the enzymes [169]. In the present study we have explored the activity of Ag doped In_2O_3 for α - amylase and α -glycosidase inhibition.

The applications of nanoparticles in biomedical and catalytic field also bring in question about their toxicity to life as well as environment. The above Co and Ag doped nanoparticles have also been studied for their toxic effects on zebra fish and blood samples.

2.4 Pristine and doped Cerium oxide

Cerium oxide is a well-known rare earth oxide used in various applications, mainly in catalysis [170-173] and Solid oxide fuel cells [174-176]. The presence of redox equilibrium ($\text{Ce}^{3+} \leftrightarrow \text{Ce}^{4+}$), electronic structure and mobility of vacancies govern most of its applications [177].

2.4.1 Structure and Properties

Cerium oxide exists in two stoichiometries, Cerium dioxide (CeO_2) also commonly known as ceria and dicerium trioxide (Ce_2O_3) also known as sesquioxide. Cerium dioxide is the most stable and widely studied form over the decades. In ambient conditions CeO_2 crystallizes as fluorite type structure. It is a face centered cubic structure with space group Fm_3m . It has a cubic close packing arrangement where cerium ions with

oxygen ions occupy the tetrahedral holes. The vertices and the faces of cubic unit cell are occupied by cerium where Ce (IV) is coordinated with eight oxygen ions while each oxygen ion is surrounded by four cerium ions in a tetrahedral arrangement. The lattice parameter reported is about 5.411Å [177,178]. Ceria has amazing capacity to store and release oxygen owing to its ability to shuffle between Ce⁴⁺ and Ce³⁺ states. This makes it the most sorted rare earth metal oxide which has been studied widely in bulk as well as in nano-form.

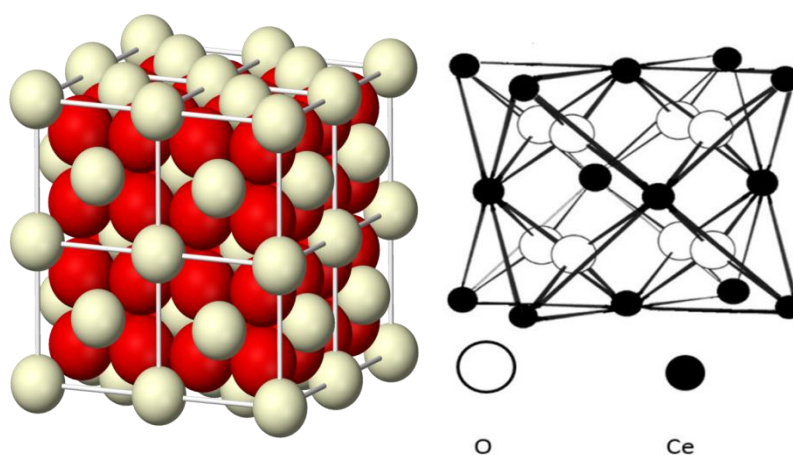


Fig. 2.2 Fluorite structure of CeO₂ and unit cell representation [179].

2.4.2 Methods of preparation

2.4.2.1 Co-precipitation

One of the simplest preparative methods used to prepare metal oxides. The metal ions are precipitated as hydroxides using alkali like NaOH, KOH and NH₄OH. In case of cerium, a gelatinous white precipitate is obtained on addition of alkali which is then filtered, washed dried and calcined at desired temperatures [180-183]. Further there are many modifications carried out for this technique such as addition of surfactants, de-agglomerating agents and capping agents.

2.4.2.2 Sol-gel processing

It is the one of the most reliable methods to prepare doped metal oxides, which ensures homogeneity in the prepared mixed metal oxide. The metal salts are mixed with the organic acids which act as a gelling agent, on heating the solvent evaporates and the gel is formed due to the complexation of metals with organic component. This gets decomposed on further heating producing the nanoparticles [184-188]. The nanoparticles are calcined at desired temperature to get final mixed metal oxides. The pH is maintained using ammonia in case of certain metals. Organic acids such as citric acid, acetylacetonate have been used CeO_2 preparation.

2.4.2.3 Combustion method

In this method metal nitrates are taken which act as oxidising agents and are reacted with a fuel which is a reducing agent, highly exothermic redox reaction occurs and the decomposition of the precursor takes place giving the desired nanoparticles. These are then heat treated as per requirements. Cerium oxide has been prepared by combustion method using fuel like glycine [189, 190].

2.4.2.4 Hydrothermal synthesis and Microwave assisted hydrothermal synthesis

These are the modern techniques for nanoparticle synthesis of different size and shapes. In hydrothermal synthesis the metal precursors are placed in an autoclave where the temperature and pressure can be regulated. It is basically a high pressure low temperature synthesis [191-193]. In case of microwave assisted hydrothermal synthesis the autoclave containing the metal precursors is placed in a microwave [194-197]. Under the microwave regulation the synthesis takes place. The obtained precipitate is then washed dried and calcined.

2.4.2.5 Miscellaneous methods

Other methods used for preparing CeO₂ in nano-forms include sonochemical using sonicator vibrations [198,199], thermal decomposition of the metal precursors[200-202] Spray pyrolysis [203-204] Thermal hydrolysis [205-206] and Micro emulsion [207-208].

2.4.3 Solid state studies

2.4.3.1 Magnetic properties

With the emergence of dilute magnetic semiconductor oxides, the various metal oxides pristine and doped have been screened for their participation in this field. Cerium oxide also follows this clan of DMS oxides. Several reports are available on pristine [209, 210] and transition metal doped cerium oxide nanoparticles revealing their magnetic properties [64-67, 83, 211-215].

Ferromagnetism origination from magnetic ions mediated by oxygen vacancies is reported for Co and Ni doped ceria [209, 216]. Similar explanation is given by R. A. Kumar et al. for the ferromagnetism observed in pristine and Fe, Gd co doped cerium oxide nanoparticles [190].

The influence of oxygen vacancies (V_o) on FM in Co doped CeO₂ was revealed Q-Y. Wen and co-workers where they concluded that the larger surface to volume ratio leads to stronger RT FM owing to higher concentration of V_o [217]. The vacancy mediated FM in Co doped ceria was further explained by Y.Q. Song and co-workers, by annealing the samples in O₂ and Ar/H₂ where former reduces the FM whereas latter enhances it by increasing V_o density [218]. S.Y. Chen et al. showed that Cr³⁺ incorporation

in CeO₂ promotes FM by reducing the distance between magnetic Ce³⁺ and increasing the defect density [219]. Ferromagnetism originating from F centre has also been shown by S.Phokha et al. in Cr doped Samples [220]. The ferromagnetism in rare earth doped cerium oxide bulk samples is investigated by M. C. Dimri et al., the Nd and Sm doped compounds showed RT FM whereas in La, Tb, Gd, Er and Dy it was found to be absent. Here the FM is attributed to oxygen vacancies and not surface defects owing to the presence of FM in bulk sintered samples also [221].

Effect of non-magnetic dopant (Ca²⁺) on the magnetic property of CeO₂ was studied by X. Chen et al., where they observed V_o plays a vital role in regulating the magnetic property [189]. While there are several reports available which attribute the observed ferromagnetism to oxygen vacancies in doped as well as pristine as mentioned above [209, 210, 222] at the same time Y. Liu et al. reveals no linkage between observed FM in pristine CeO₂ and V_o but attributes it to the smaller particle size [223]. Recent paper by S. Sonsupapa et al. displayed ferromagnetism in Fe doped CeO₂ nano-fibers originating from V_o/defects where calcinations increases the FM ordering which is attributed to the increased participation of Fe³⁺ ions in exchange mechanism [224].

These observations attracted us to work on this system. In the present study we report magnetic properties of In³⁺ doped CeO₂. No reports are available in literature on this system.

2.4.4 Catalysis

CeO₂ has been explored worldwide for their catalytic activities in various reactions such as detoxification of automotive exhaust, photo-degradation, and organic transformations. The catalytic activity has been accredited to ability of this material to

store oxygen. Its easy shift between Ce^{3+} to Ce^{4+} oxidation state enhances the oxygen mobility which is known to be exploited for several of its catalytic applications [225-229]. Further research continued in order to tune the oxygen availability in the catalyst by managing defects through doping or by applying new synthetic procedures. The emergence of nanotechnology has brought even more excitement into the catalytic field. Preparing catalysts in nanosize with variety of shapes and sizes has eventually flourished the field.

Some of the reports on catalytic activity of CeO_2 are include, organic transformations such as the, alkylation of aromatic compounds [230,231] dimerization of alcohol[232, 233],carboxylic acid [234, 235], aldehyde and ester to ketones[236], reduction of benzoic acid [237], cyclization of diols [238], and dehydration of butanediols [239-242]. One pot synthesis of esters from nitriles and alcohols [243], carbamates from amines, alcohols and CO_2 [244], and transformation of nitriles and amides have also been reported [245]. R. W. Snell et al. has given the insights into ketonization reaction catalysed by ceria giving the mechanism [246]. Nano cerium oxide has also been employed for transalkylation reactions [247], synthesis of aminophosphonate [248, 249], and benzimidazole,benzothiazole, benzoxazole synthesis [250].

Ceria has been often used as a composite material with other oxides such as TiO_2 . It has been widely used as a support material also for supporting noble metals for CO oxidation, NO decomposition and NO catalytic reduction [251-254]. Cu- CeO_2 , Pd/ CeO_2 and Au/ CeO_2 catalyst has been studied for CO oxidation [255-258].T. Alammar et al. reported CO oxidation on CeO_2 prepared by ionic liquid assisted sonochemical method where complete conversion was obtained at around $375^\circ C$ [259]. Rare earth in combination with CeO_2 have also been explored, where D. N. Durgasri et al. displayed

CO oxidation activity of $\text{CeO}_2\text{-Gd}_2\text{O}_3$ mixed oxide catalyst which shows best activity around 350°C [260]. B. M. Reddy et al. prepared Zr, Hf, Tb and Pr doped CeO_2 where Pr showed the complete oxidation of CO around 480°C , best among other dopants [261]. Mesoporous CeO_2 prepared by J. Zhang et al. showed complete CO conversion at 270°C [262].

In the present work pristine and In doped CeO_2 have been studied for CO oxidation and few organic transformations.

2.5 Pristine and doped Magnesium Ferrite

Magnetic nano-ferrites have fascinated the science community over the years, owing to their unique properties which are contrary to those of bulk materials thereby entering into a vast applicative area of magnetic, optoelectronic, catalytic, and biomedical sciences [263-265]. Ferrites in the form of thin film have been extensively used for gas sensing also. Super-paramagnetism is one such exceptional property of magnetic nanoparticles that is significant in modern technology including magnetic resonance imaging, ferro-fluids, magneto-caloric refrigeration, drug delivery etc. [22-25, 266].

2.5.1. Structure and Properties

Ferrites are cubic spinels with formula AB_2O_4 . They crystallize in a face centered cubic structure with Fd_{3m} space group. Here the FCC lattice is made up of oxygen atoms where tetrahedral and octahedral sites are occupied by cations. One unit cell of AB_2O_4 consists of eight formula units containing 32 octahedral and 64 tetrahedral sites respectively. The occupancy for octahedral sites is one fourth and that of tetrahedral is one eighth which suggests that 16d octahedral sites and 8a octahedral sites are occupied [267].

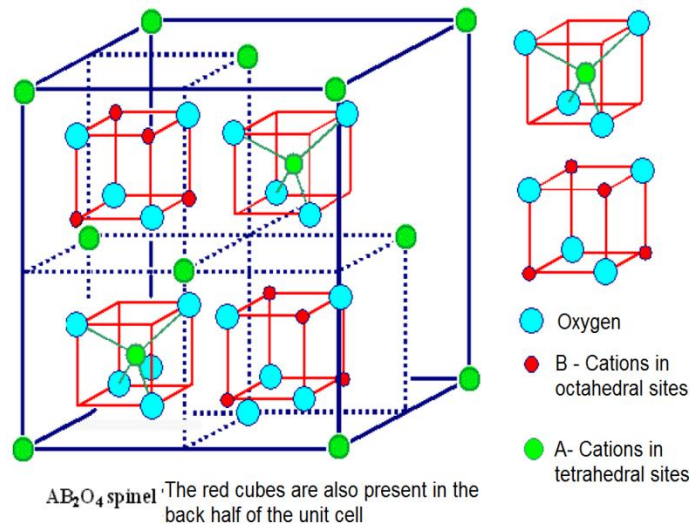


Fig.2.3 Unit cell of cubic spinel structure [268].

Depending on the distribution of cations in octahedral or tetrahedral sites cubic spinels are categorised in two types as follows:

1] Normal Spinel :When all the divalent cations occupies the tetrahedral sites and the octahedral sites are occupied by the trivalent cations the spinel network is defined as a normal one.It can be represented as $(A^{2+}) [B^{3+}]_2 O_4$, () , [] represent tetrahedral and octahedral sites respectively.

2] Inverse Spinel: In this arrangement all the divalent A^{2+} cations occupy some of the octahedral sites whereas trivalent B^{3+} cations occupy all the tetrahedral and remaining octahedral sites. It can be represented as $(B^{3+}) [A^{2+}B^{3+}] O_4$. The() and [] represents tetrahedral and octahedral sites respectively.

The occupancy of the cations plays a vital role in regulating magnetic and other physical properties of these compounds. The spins of cations in tetrahedral sites are oppositely oriented with respect to the cations in octahedral sites. Playing with cationic distribution between the two sites can lead to the discovery of new magnetic materials.

Ferrites are further classified as hard and soft ferrites. Ferrites with high coercivity (H_c) and high remanance (M_r) after magnetisation are known as hard ferrites whereas those with low coercivity (H_c) are known as soft ferrites. Among the different ferrites studied for the past couple of decades magnesium ferrite ($MgFe_2O_4$) is one of the soft ferrite and has created a niche for itself. It finds its application as humidity and gas sensors [269, 270], in catalysis and magnetic devices [271, 272]. It possesses unique properties such as high resistivity and low coercivity, when synthesized with a crystallite size below a certain value it exhibits super-paramagnetism. This property makes it an important material for application in high frequency transformers, microwave devices, satellite communication, audio-video in digital recording, computer memory chips, high density recording media, heterogeneous catalysis [17-20, 273]. Super-paramagnetism makes this material a strong candidate for the biomedical applications such as contrast agents in Magnetic Resonance Imaging (MRI) [274, 275,] in magnetic hyperthermia [276–278] and targeted drug delivery [279,280].

2.5.2 Methods of preparation:

Preparation of a ferrite material plays a very important role in governing their properties by influencing the cation distribution and crystallite size. Ceramic method is an age old technique used for the ferrite preparation. Other literature reported methods for the synthesis of $MgFe_2O_4$ include, co-precipitation [25], combustion synthesis [281], solvo/hydro-thermal method [282, 283] sol-gel [284], solid-state reaction [285] ball milling [286], mechanochemistry synthesis [287] micro emulsion [288] and microwave processing approaches [289]. As the research in the nano- ferrites progressed the wet chemical methods for the synthesis of ferrites received lot of attention. Few among the

above listed methods which were extensively used for MgFe_2O_4 synthesis are discussed below:

2.5.2.1 Combustion synthesis

It is one of the best known methods for preparing ferrite material in nanosize and with pure single phase. Nitrates of iron and other metals involved are taken as per desired stoichiometries which act as oxidisers; to this a reducing agent is added such as glycine, urea and hexamethylenediamminetetraacetic acid. The ratio of metal nitrates to the fuel is taken as per optimisation, either stoichiometric, fuel efficient or fuel deficient. On heating the redox reaction takes place, resulting in the combustion reaction. The powdered compounds obtained are then dried, ground and calcined [281, 290].

2.5.2.2 Sol-gel

Here the metal salts dissolved are water and to this organic acid such as citric acid, oxalic acid or malic acid is added as gelling agent in a requisite ratio, on heating this mixture losses water and organic part starts complexing with metal ion which further leads to the formation of gel. The gel is then decomposed to burn off the entire organic moiety leaving the metal oxide nanoparticles i.e the ferrites in the present case; they are then calcined and sintered at desired temperatures. Literature shows synthesis of MgFe_2O_4 using sol gel method with gelling agents like citric acid and [265, 291], ethylenediamminetetraacetic acid (EDTA) [292, 293].

2.5.2.3 Sol-gel combustion

It is a preparative method which combines sol-gel and combustion together. Here the gelling agent and fuel both are added to the metal salts, on heating it form a gel, the gel then undergoes combustion forming the compound in a voluminous mass. The method

has been used for ferrite preparations using combination of citric acid and ethylene glycol etc.[267, 294 , 295].

2.5.2.4 Co-precipitation

The simplest and the most common method used for the preparation of metal oxides including ferrites. The metal salts are precipitated as hydroxides using base such as NH_3 , KOH or NaOH . Though the method has lot of shortcomings like phase segregations, it is employed for preparing ferrites with several modifications such as pH regulations and adding surfactants. The MgFe_2O_4 has been reported to synthesize by precipitation [25, 296]. Synthesis using Na_2SiO_4 has also been reported [297].

Thermal decomposition of the precursors such as poly vinyl alcohol (PVA) [298] acetates [299] forming ferrites are also reported.

2.5.3 Solid state properties

2.5.3.1 Magnetic studies

Magnesium ferrite being a soft magnetic material can be easily magnetised and (de)magnetised. Distribution of the cations in tetrahedral (A) sites and octahedral (B) sites, govern the physical and chemical properties of the spinels .The distribution can be varied with size or the type of dopant impurity. In a bulk MgFe_2O_4 half of Fe^{3+} ions are known to occupy the tetrahedral sites and remaining half along with Mg^{2+} ions occupy the octahedral sites. Interestingly MgFe_2O_4 shows magnetism even though the Mg^{2+} ions are diamagnetic; which is attributed to the formation of inverse spinel structure [297].

In such a case, it will be even more interesting to study the change in properties of MgFe_2O_4 when doped with other metals. Earlier as per the literature Cr [265,300], Gd

[293], Dy [301], Sm [302], Co [303], Ni–Co [304], Cu [305], Co–Cr [306], Cd [307], Pr [308], Tb [309], Li [310], Mn [311,312], Zn [313], Al [314], and Ca [315], etc. have been used as dopants in ferrites and their properties have been explored. Room temperature super-paramagnetic (SPM) nature of pristine MgFe_2O_4 nanoparticles prepared by co-precipitation is reported by Q.C. et al. [25] and M. I. M. Omer et al. [296]. M. G. Naseri et al. also observed RT SPM in MgFe_2O_4 compounds prepared by simple thermal decomposition [298] whereas S. I. Hussein et al. observed in nano-powders prepared by EDTA assisted sol gel method [316].

In case of doped samples where Fe is substituted by other metal ions, A.S. Elkady et al. reports increase in magnetisation values of MgFe_2O_4 nanoparticles with Gd incorporation up to $x=0.1$, which is attributed to the change in cubic and tetragonal spinel ratio [293]. In Ni substituted MgFe_2O_4 R. Tadiet. al observed that the magnetisation increases when Ni^{2+} occupies octahedral sites [299]. Ca^{2+} substituted MgFe_2O_4 shows increase in magnetisation for $x \leq 0.05$ whereas for $x > 0.05$ it is found to decrease. These results are attributed to the different distribution of cations in octahedral and tetrahedral sites with increasing dopant concentration [315]. Cr doped MgFe_2O_4 shows reduction in crystalline size and a super paramagnetic behaviour, the magnetisation and coercivity (H_c) decreases with increase in Cr concentration [317, 265].

This suggests that properties of the doped ferrites largely depend on the size, charge, concentration and nature of the dopant ion. Here the stoichiometry, cation distribution, as well as the final particle size plays a key role which in turn is highly influenced by the preparative method used.

2.5.4 Catalysis

Recently nano ferrites are gaining a lot of attention in the catalytic field. The highlighting advantage here is the ease with which the catalyst is separated. Nano-size with magnetic nature makes it one of the best catalytic materials. Several ferrite materials AFe_2O_4 (where $A = Co, Cu, Ni, Fe$) have been explored for their catalytic applications [318] such as aldol condensation, Prins condensation and also in synthesis of, α - β unsaturated ketones, α - amino nitriles 1,8-dioxodecahydroacridines. Few of them are also found active for CO oxidation reaction.

The $MgFe_2O_4$ is also gaining a lot of importance in catalytic field recently. Few of the reaction studied using this catalyst include dehydrogenation of butenes [319] ozonation of Acid Orange II, [320] synthesis of α -hydroxy and α -aminophosphonates [321] 3,4-dihydropyrimidin-2(1H)-one/thione [322] carbon removal [323] etc. Gold supported on $MgFe_2O_4$ has also been used for CO oxidation [324].

In the present work In doped $MgFe_2O_4$ nanoparticles are prepared and studied for their magnetic and catalytic properties.

EXPERIMENTAL

3. 1. Preparation of nanoparticles

3.1.1 Combustion Method

3.1.1.1 $\text{In}_{2-x}\text{M}_x\text{O}_3$ (M = Co, Cr and Ag)

$\text{In}_{2-x}\text{Co}_x\text{O}_3$ and $\text{In}_{2-x}\text{Cr}_x\text{O}_3$ nano-particles were synthesised by a solution combustion method where glycine was used as a fuel. Starting materials used were pure chemicals as follows In_2O_3 (Sigma Aldrich 99.9%), $\text{Co}(\text{NO}_3)_2 \cdot 6\text{H}_2\text{O}$ (Sigma Aldrich 99%), $\text{Cr}(\text{NO}_3)_3 \cdot 9\text{H}_2\text{O}$ (Sigma Aldrich 99%), Glycine (Thomas Baker 99.7%) nitric acid (70% Sigma Aldrich) and double distilled water. In the beginning, In_2O_3 being insoluble in water was brought into solution by dissolving it in minimum amount of dilute nitric acid, to this solution calculated amount of respective metal nitrate ($\text{Co}(\text{NO}_3)_2 \cdot 6\text{H}_2\text{O}$ / $\text{Cr}(\text{NO}_3)_3 \cdot 9\text{H}_2\text{O}$) and the fuel glycine was added in a requisite amount. The ratio of oxidising to reducing valances was maintained as 1: 0.5. The metal nitrate and glycine mixture was kept for stirring for 30 minutes to ensure the complete homogenisation. It was then kept on a hot plate with continuous stirring. At first it resulted in the evaporation of water from the mixtures, which on further heat treatment lead to the formation of a thick gel. Once the ignition temperature was reached, a redox reaction takes place resulting in the combustion of the precursor into a voluminous ash. It was then ground using mortar and pestle and calcined at 500 °C for 5 h in a muffle furnace.

Similar procedure as above was followed for the synthesis of $\text{In}_{2-x}\text{Ag}_x\text{O}_3$ (x = 0.00, 0.04, 0.10) nanoparticles. Here AgNO_3 (Thomas baker 98%) was used as a source of silver. As mentioned earlier In_2O_3 was dissolved in dilute HNO_3 , to this solution calculated amount of AgNO_3 and glycine was added. The oxidising to reducing valances

ratio was maintained 1:0.25 in this particular synthesis. The mixture was homogenised by stirring for 30 minutes and then heated. On heating first the evaporation of water takes place, further heating results in the formation of a thick gel which then combusts to give the voluminous ash. This was then ground and sintered at 600 °C for 6 h.

3.1.2 Sol-gel method

3.1.2.1 Ce_{1-x}In_xO₂

Ce_{1-x}In_xO₂ (x = 0.02, 0.04, 0.06, 0.10, 0.15) nanoparticles were prepared by sol gel method. The starting materials used were Ce(NO₃)₃.6H₂O (sd fine chem. Ltd. 99%), In₂O₃ (Sigma Aldrich 99.9%) and citric acid (Thomas baker 99.7%). Stoichiometric amounts of Ce(NO₃)₃.6H₂O was dissolved in minimum amount distilled water, to this In₂O₃ (dissolved in dilute HNO₃) was added followed by citric acid and the mixture was homogenised by stirring. It was then heated on a hot plate. Evaporation of water takes place which proceeds in the formation of a gel. The gel undergoes decomposition in a highly exothermic reaction giving the fine powder which was then sintered at 600°C for 5 h.

3.1.2.2 MgFe_{2-x}In_xO₄

MgFe_{1-x}In_xO₄ nanoparticles (where x = 0.00, 0.04, 0.08, 0.12, 0.16) were prepared by sol-gel method using citric acid as a complexing agent. All the chemicals used were of analytical grade. Indium oxide (In₂O₃, Sigma Aldrich 99.9%) was first brought into solution by dissolving it in nitric acid (Sigma Aldrich). As per the calculated stoichiometries magnesium nitrate Mg(NO₃)₂.6H₂O (Thomas Baker 99.8%) and iron nitrate Fe(NO₃)₃.9H₂O (Thomas Baker 99.0%) were added to the above solution with continuous stirring which was followed by the addition of citric acid (Thomas baker

99%). The metal nitrates to citric acid (Thomas Baker 99.0%) molar ratio was 1: 3. These were further heated with constant stirring until a thick gel was obtained. The gel then undergoes decomposition giving solid powder. The obtained powder was ground and sintered at 600 °C for 10 h in a furnace wherein the desired nanoparticles were obtained.

3.2. Physico-Chemical characterisation: Theory and practice

3.2.1. Thermal analysis (TG-DTA/DSC)

Thermogravimetry (TG) is an analytical technique in which change in weight of a sample is recorded as a function of temperature or time. This technique enables one to measure the change in physical and chemical properties of a substance under study. The major variation that includes weight gain or weight loss can be accurately detected. In a graphical representation of this analysis % weight loss is plotted against the temperature. Differential thermal analysis (DTA) is a technique that measures the difference in temperature (ΔT), between the sample and inert reference material as a function of temperature whereas Differential scanning calorimetry (DSC) measures the enthalpy changes that occurs in a substance as a function of either temperature or time. Along with the weight loss these techniques determine the polymorphic transitions also and characterises each phenomenon taking place as exothermic or endothermic event [325]. In the present study Thermo gravimetric – Differential thermal analysis /Differential scanning calorimeter measurements for the gel precursors were performed on (NETZSCH TG-DSC STA 409PC) in air or in oxygen with the heating rate of 10 °C/ min in the temperature range of 30 to 700 °C.

3.2.2. Powder X-ray diffraction (XRD)

XRD is the most powerful tool in the material characterisation field. It serves a key role in the identification of a crystalline material through phase determination. In this technique the incident monochromatic X-rays (like Cu K α or Mo K α) interact with the material under study where the atoms present in the material scatter the X-rays. The scattering produces a constructive or destructive interference. The constructive interference of the scattered X-rays by atoms in an ordered lattice produces a diffraction pattern determined by the Bragg's law as follows:

$$n\lambda = 2d\sin\theta$$

Where λ is the wavelength of the beam, d is the spacing between diffracting planes, θ is the incident angle and n is an integer called order of the reflection. The diffraction pattern determines the size and shape of the unit cell and also the kind and arrangement of atoms in the crystal structure. Diffraction pattern obtained gives the intensity of the scattered radiation as a function of scattering angle 2θ . The maximum intensity peaks at specific angles helps in estimating spacing between the lattice planes (d) whereas width of the peaks helps in calculating the crystallite size using Scherrer equations [326] which can be expressed as:

$$D = n\lambda / \beta \cos\theta$$

Where D is crystallite size, n = shape factor with typical values of about 0.9, λ =X-ray wavelength, β = FWHM (full width at half maximum intensity) and θ =Bragg's angle. The X-Ray diffraction studies presented in the present work were carried out using a RIGAKU MINIFLEX Diffractometer with Cu K α radiation, filtered through Ni absorber in steps of 0.02°

3.2.3. Infrared spectroscopy (IR)

IR spectroscopy is a form of vibrational spectroscopy that determines the specific vibrational frequency of a molecule characteristic of their structure. A “change in dipole moment” is the necessary conditions for a molecule to be IR active. In a typical Fourier transform infrared analysis a beam of infrared light passes through a sample, when the frequency of incident light matches the vibrational frequency of a bond which is proportional to the difference in energy between vibrational ground and excited state, the absorption takes place. It is a valuable technique for the analysis of organic molecules where the bonds such as C-H, N-H, C=O, C-H, O-H etc. vibrate at a characteristic frequency confirming their presence in the molecule therefore aids in the identification of a molecule and its structure. Metal oxygen vibrations can also be detected by this technique which shows peaks in a lower frequency region.

In the present work the gels obtained during the combustion or sol-gel synthesis were characterised using FT-IR. Infra red spectra for the sintered metal oxide were also recorded along with the analysis of organic compounds. The measurements were performed on SHIMADZU IR-PRESTIGE-21 spectrophotometer in the range of 400–4000 cm^{-1} . For solid samples the background was run with KBr, where the samples were ground in KBr and then their spectra were recorded. For liquid samples the spectra were recorded using NaCl pellets.

3.2.4. Scanning electron microscopy (SEM)

Scanning electron microscopy is a microscopic technique that produces images which reveals the topography, size and shape of the samples. In a typical analysis an electron beam is produced which strikes the atoms in a sample and produces various signals which are then detected. Gold coating is carried out initially to avoid the charging of the particles. In the present work the SEM analysis were carried on JEOL model

5800LV Scanning Electron for $\text{In}_{2-x}\text{M}_x\text{O}_3$ (M= Co, Cr, Ag) and $\text{Ce}_{1-x}\text{In}_x\text{O}_2$ nanoparticles. For $\text{MgFe}_{2-x}\text{In}_x\text{O}_4$ nanoparticles SEM analysis were performed using JEOL JSM- 6360 LV scanning electron microscope.

3.2.5. Transmission electron microscopy (TEM)

Transmission electron microscopy is a very important technique for the direct determination of particle size, shape, grain boundaries etc. where it enables the imaging of structures at atomic levels. It offers a very high magnification ranging from 50 to 10^6 or even more in the newly fabricated instruments. In a particular analysis an electron gun produces a stream of monochromatic electrons that are focused by two condenser lenses into small, coherent beam. This electron beam interacts with the sample producing scattered or un-scattered electrons. The signals produced here are detected which contains the sample information [327]. The scattering is of two types, elastic scattering which produces the diffraction pattern and inelastic scattering which gives the information about grain boundaries, defects, density variation and so on. TEM along with selected area (electron) diffraction (SEAD) is a promising tool for the characterisation of a material, along with determination of particle size and shape also facilitates identification of the crystal structure and defects.

Particle sizes of the calcined samples in the present work were determined using PHILIPS CM 200 Transmission Electron Microscope, operating at an accelerating voltage of 200 kV providing a resolution of 2.4 Å.

3.2.6. Surface area analysis

Determination of the surface area of the nanoparticles is the crucial step of characterisation that can find its application in fields like catalysis. Brunauer-Emmett-

Teller (BET) method for surface area analysis is the most widely used method which is defined by the equation:

$$p/v(p_0-p) = 1/C v_m + (C-1)p/C v_m p_0$$

where p = adsorption equilibrium pressure, p_0 = standard vapour pressure of the adsorbent, v = volume at STP occupied by molecules adsorbed at pressure p , v_m = volume of adsorbate required for a monolayer coverage, C = constant related to heat of adsorption.

Surface area of the nanoparticles is estimated on Quntachrome autosorb (ASiQC0100-4) system by nitrogen adsorption/desorption measured as a function of relative pressure using a fully automated analyser.

3.2.7 X-ray photoelectron spectroscopy (XPS)

X-Ray photoelectron spectroscopy is the most powerful chemical analysis technique used for material characterisation. It is based on the photoelectric effect where the binding energy (E_B) of a core level electron is overcome by the energy ($h\nu$) of the impinging soft X-ray photon. In the process the core level electron is excited and eventually ejected from the analyte. The kinetic energies of the ejected photoelectrons, E_K , is measured by an electron spectrometer. Invoking the conservation of energy, the following relationship is obtained [328].

$$E_B = h\nu - E_k - \phi$$

ϕ is the work function of the spectrometer. The binding energy is the characteristic of the orbital from which the photoelectron originates. The study of the ejected photoelectrons provides important information about the element under study. Initially a full scan also called survey scan is recorded over a broad binding range, which allows the identification of elements present. Then high resolution spectra are obtained in the binding energies of interest. A peak fitting of which gives the information on the oxidation state of the

element present. The valence states and the binding energies of the elements in $\text{MgFe}_{2-x}\text{In}_x\text{O}_4$ were determined employing a VSW SCIENTIFIC INSTRUMENT with Al $K\alpha$ as the incident source and excitation energy of 1486.6 eV.

Whereas for $\text{In}_{2-x}\text{M}_x\text{O}_3$ (M = Co, Cr, Ag) and $\text{Ce}_{1-x}\text{In}_x\text{O}_2$ the samples were excited using Mg- $K\alpha$ radiations ($h\nu = 1254.6\text{eV}$) and the spectra was analyzed using a VG make CLAIM2 analyzer system in the energy range 0 –1000 eV.

3.2.8 UV-Visible diffused reflectance spectroscopy (UV-DRS)

UV-Visible diffused reflectance spectroscopy is a technique mainly used for the solid sample analysis. When a light is incident on the solid (opaque) surface, it is reflected either symmetrically known as specular reflection, or scattered in all directions known as diffused reflection. Here a relative change in the amount of reflected light off of a surface is measured. It is a non-destructive technique providing the information about the structure, composition, purity etc. It is also an important tool for estimating the band gap of semiconductor materials. Diffused reflectance spectra for all the samples were recorded on Shimadzu UV 2450 UV-Visible spectrophotometer in the wavelength range of 200-800 nm using BaSO_4 as a reference. The optical band gap of the nano-particles was determined using Tauc equation [329] as given below

$$\alpha h\nu = A (h\nu - E_g)^n$$

Where A = constant, α = absorption coefficient, h = Planck's constant, ν = frequency of vibration, $n=1/2$ for direct band gap semiconductor and E_g is the optical band gap. The graphs of $(\alpha h\nu)^2$ v/s photon energy ($h\nu$) in eV were plotted for all the samples. The point of intersection on the x-axis ($h\nu$) obtained by extrapolating the linear region of a plot where $(\alpha h\nu)^2$ is on the y-axis, gives the optical band gap value (E_g).

3.2.9 Mössbauer spectroscopy

Mössbauer spectroscopy basically deals with transitions between energy levels within the nuclei of atoms. In a typical analysis a solid sample is exposed to a beam of γ - radiation where intensity of the beam transmitted through the sample is detected. The atoms in the source emitting the γ - rays must be of the same isotope as the atoms in the sample absorbing them. It detects even small changes in the nuclear environment of the relevant atoms. The three major nuclear interactions that are observed include isomer shift also known as chemical shift, quadrupole splitting and hyperfine splitting also called as Zeeman splitting. The limited number of γ - ray sources and analysis restricted to only solid samples are the two drawbacks of Mössbauer spectroscopy.

We have employed the Mössbauer spectroscopy method for studying the $\text{MgFe}_2\text{-}_x\text{In}_x\text{O}_4$ nanoparticles. It helps to determine the presence, chemical state and environment of iron atoms thereby promoting the understanding about their magnetic properties. The room temperature ^{57}Fe Mössbauer measurements were carried out in transmission mode with a ^{57}Co radioactive source in constant acceleration mode using a standard PC based Mössbauer spectrometer, equipped with a Weissel velocity drive. Velocity calibration of the spectrometer was performed with a natural iron absorber at room temperature.

3.2.10 Nuclear magnetic resonance spectroscopy (NMR)

Nuclear magnetic resonance (NMR) spectroscopy is a technique majorly employed to identify the organic compounds. Its application in inorganic and biochemistry is also known where it helps to determine the structure of the compounds. The nuclear magnetic resonance basically deals with the nuclear spin of the atom denoted as (I). The nucleus should be magnetic in order to be studied by this method. Not all

isotopes are magnetically active. The active components studied by NMR include ^1H and ^{13}C others which can be studied are ^{14}N , ^9F , ^{17}O , ^{33}S and ^{31}P . When placed in an external magnetic field the electromagnetic radiations are absorbed by the nuclei at its characteristic frequency. It aligns in a predictable fashion with definite orientations. The nuclei can absorb the energy and go from lower to the higher energy state. The energy absorbed or released during the relaxation of nuclei is observed by Fourier Transfer Method. The magnetic field felt by the nuclei includes the applied fields as well as the field of neighbouring nuclei which results in the shifting of the absorption frequency when compared to that obtained for single atom. The frequency is therefore always measured with respect to the standard Tetramethylsilane(TMS) which is defined as zero. The spectrum obtained is of Chemical shift (δ) v/s Intensity where each nuclei with particular environment has its characteristic δ value with reference to TMS. The ^1H NMR spectra of the few organic compounds are recorded using 400MHz on Bruker machine. The TMS was used as an internal standard and CDCl_3 and DMSO as solvents depending on solubility of compounds.

3.2.11 DC (Direct current) Electrical resistivity

Electrical resistivity measures the resistance of a material towards the flow of current. It serves to be a valuable technique for the study of semiconductor metal oxides. To carry out the analysis first pellets were prepared by pressing the powdered compound in a hydraulic press at a pressure of 3-5 ton. The measurements of the pelletized samples were carried out using two probe conductivity cells from 100 to 500 °C. Change in current was measured with increasing temperature at a constant voltage of 2 Volts. The resistivity of the samples was thus calculated using the following equation:

$$R = \rho L/A$$

R = resistance

A= cross sectional area of the pellete

L = thickness of the pellete

The plots of $\log \rho$ verses $10^3/T$ are shown for all the samples.

3.2.12 AC-Magnetic Susceptibility

The temperature dependence of the magnetic susceptibility (χ) is measured in the above analysis. A sample under study is magnetised by application of an external magnetic field, the alignment of magnetic domains results increasing the χ values. The domains can stay aligned even if the external magnetic field is removed. The rise in temperature can increase the energy possessed by the ions and electrons, which can further enhance the structural disorder. This can randomize the ordered domains until the Curie temperature (T_c) is attained at which leads to the demagnetisation of the sample.

The AC-magnetic susceptibility analysis were mainly carried out to find the T_c of a $\text{MgFe}_{2-x}\text{In}_x\text{O}_4$ nanoparticles on DOSE AC susceptibility instrument by ADEC Pvt. Ltd., in a magnetic field of 5000 Oe at an operating frequency of 315Hz. The instrument was calibrated with Ni standard.

3.2.13 Vibrating sample magnetometer (VSM)

Vibrating sample magnetometer is one of the advanced instruments for exploring the magnetic properties of the samples. The major components of the instrument include motor transport (head) for vibrating the sample; a coil set puck for detection, electronics for driving the linear motor transport and detecting the response from the pickup coils. Sample is placed in a brass holder at the end of the sample rod which is then inserted in the magnetometer where a constant magnetic field is applied. The sample oscillates near

the pickup coil and the voltage induced is then detected using lock – in amplifier. The signals produced are then converted into the desired information which are analysed with the help of computer software.

The magnetic measurements that are presented in this work were performed using QUANTUM DESIGN PPMS Vibrating Sample Magnetometer (VSM). The magnetization with varying magnetic field ($M-H$) of up to 30 K Oe was measured at 50 K and 300 K. The magnetisation with varying temperature ($M-T$) was also studied at the applied constant magnetic field. The plots of magnetisation (emu/g) v/s field (Oe) and magnetisation (emu/g) v/s temperature (K) are presented in the thesis.

SPECTROSCOPIC AND SOLID STATE STUDIES

Several techniques were employed to characterise prepared material in gel/powder form such as TG/DTA, XRD, IR, SEM, TEM, Mössbauer and XPS. Solid state properties of the materials including electrical resistivity, AC susceptibility and magnetisation as a function of field and temperature on VSM have been thoroughly investigated. These results are discussed in this chapter.

4.1 Thermal analysis (TG-DTA/DSC)

The gels obtained during the combustion and sol- gel syntheses of compounds have been subjected to thermal analysis and the results obtained are discussed below.

4.1.1 $\text{In}_{1.88}\text{Co}_{0.12}\text{O}_3$

The metal nitrate –glycine melt obtained in the form of gel during combustion synthesis, for the composition $\text{In}_{1.88}\text{Co}_{0.12}\text{O}_3$ was examined for its decomposition by thermal analysis in the temperature range of 30°C to 700°C. The TG-DSC and DTG (Derivative Thermogravimetric) curves are shown in Fig. 4.1.

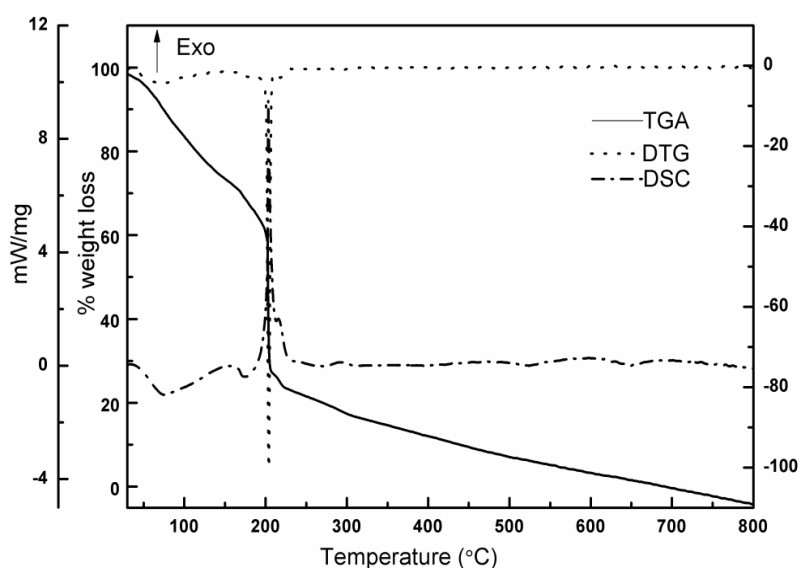


Fig. 4.1 TG-DSC and DTG curves of $\text{In}_{1.88}\text{Co}_{0.12}\text{O}_3$ gel.

The TG curve shows a gradual weight loss from 30 °C to 200 °C accompanied by two small endotherms in the DSC curve. The weight loss in this region is attributed to the dehydration process. The first region from 30 °C to 100 °C shows a marginal weight loss and an endothermic peak at around 80 °C corresponding to the loss of physisorbed water whereas the other region from 100 °C – 180 °C with endothermic peak at 170 °C is due to the loss of coordinated water accounting to the weight loss of 36%. A major weight loss of 44.07% was observed from 180 °C to 230 °C with a sharp exothermic peak at 200 °C. This is due to the oxidative decomposition of the gel which further results in the evolution of oxides of nitrogen and carbon. Oxidation of the residual carbon is evident from a small exothermic shoulder at 217 °C. No major weight loss is observed further which shows that the compound is stable. This is also supported by the DTG plot which shows no variation after 230 °C.

4.1.2 $\text{In}_{1.90}\text{Cr}_{0.10}\text{O}_3$

The TG-DTA curves for the $\text{In}_{1.90}\text{Cr}_{0.10}\text{O}_3$ gel obtained in the combustion process are presented in Fig. 4.2. The weight loss is shown in two major steps. First step shows a weight loss of around 50% in the region from 30 °C to 200 °C. A steady decrease in weight is seen, corresponding to the loss of water, initially the physisorbed water followed by the loss of coordinated water. This suggests that the gel used for analysis was highly hydrated. This is supported by a sharp endothermic peak observed at 108 °C. A slow decrease in weight is further observed until a temperature of 200 °C was reached. A steep fall in weight is observed at 200 °C attributing to the weight loss of 22%. This is the temperature at which the combustion takes place which is supported by a prominent exothermic peak around 200 °C. The oxidative decomposition reaction results in the

formation of metal oxide and evolution of the oxides of nitrogen and carbon. No further change in weight is seen from the plot which suggests the stability of the compound beyond 230 °C.

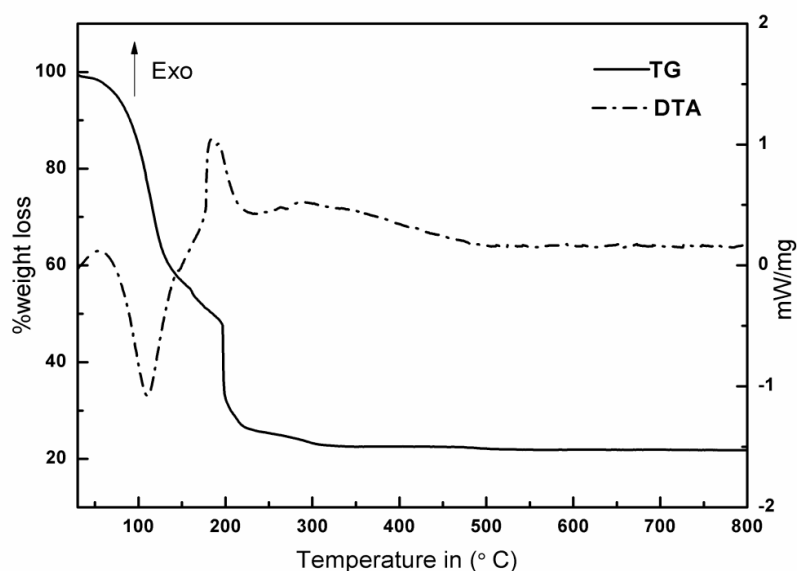


Fig.4.2 TG-DTA curves of $In_{1.90}Cr_{0.10}O_3$ gel.

4.1.3 $In_{1.96}Ag_{0.04}O_3$

Thermal analysis graph for $In_{1.96}Ag_{0.04}O_3$ gel is displayed in Fig.4.3. In initial stage the gel undergoes dehydration in the temperature range of 30 °C to 190 °C. The gradual decrease in weight is observed corresponding to loss of physisorbed water followed by the loss of coordinated water. It is well supported by an endothermic band corresponding to the above region that shows a minor hump at 94 °C and a major peak at 150 °C. The total weight loss observed in this region is around 35%. Further the combustion of the gel is initiated. A sudden fall in weight is observed around 200 °C corresponding to the oxidative decomposition of the components. This is followed by the calcination of the sample with minor reduction in weight. The total weight loss observed in this region is around 20%. The combustion process is marked by a sharp exothermic peak at 198 °C in

DTA. After a temperature of 300 °C the sample is highly stable as no weight loss is observed. This is further confirmed by the DTG curve, which shows no variation after 30 °C.

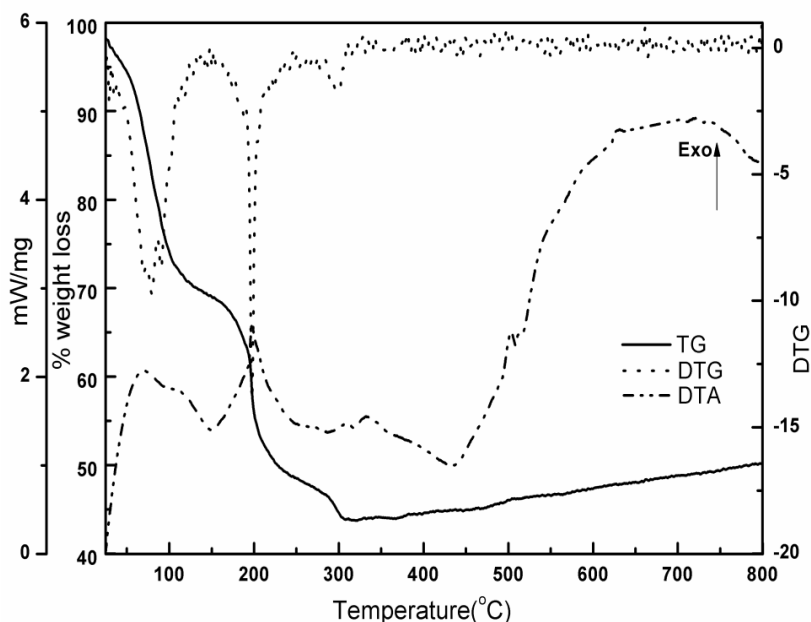


Fig.4.3 TG-DTA curves of $In_{1.96}Ag_{0.04}O_3$ gel.

4.1.4 $Ce_{0.90}In_{0.10}O_2$

The sol-gel method using citric acid was used for the synthesis of $Ce_{1-x}In_xO_2$ compounds. The TG-DTA curves of $Ce_{0.90}In_{0.10}O_2$ gel obtained during the process are presented in Fig.4.4. The initial weight loss is about 50% corresponding to loss of water molecules. TG shows a gradual weight loss in this region attributed to the loss of physisorbed and coordinated water accompanied by a sharp endothermic peak at 100 °C and slight shoulder around 135 °C. The decomposition of the gel proceeds via two steps, around 10% of weight loss is observed in the temperature region of 175 °C – 255 °C, with an exothermic peak at 207 °C. A sudden drop in weight is observed at 278 °C with a weight loss of around 23%. This is the temperature at which the gel is completely decomposed producing the desired compound, and the oxides of carbon are released. A

sharp exothermic peak is distinct at 294 °C characteristic of the decomposition process. Further only the calcination takes place by removing any carbonaceous material leftover. The compound is highly stable beyond 310 °C, no variation in weight was observed.

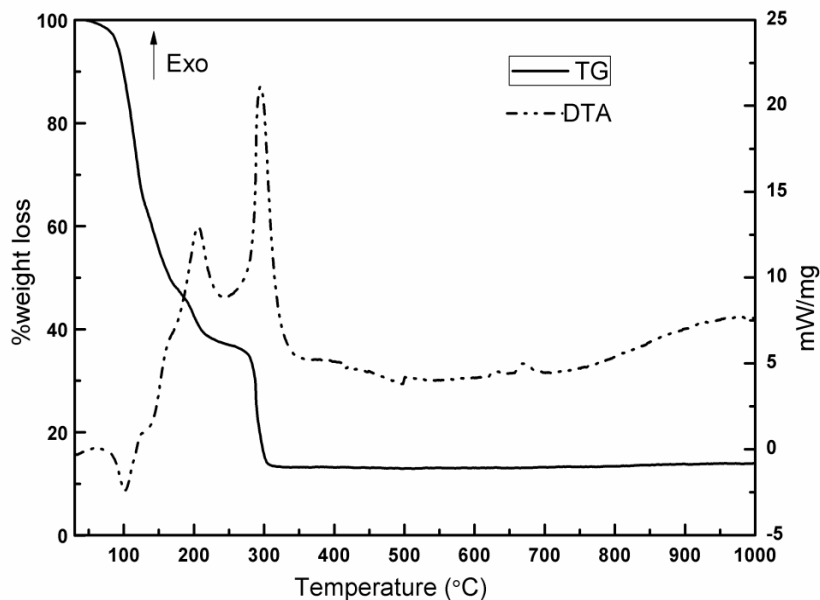


Fig. 4.4 TG-DTA curves of $Ce_{0.90}In_{0.10}O_2$ gel.

4.1.5 $MgFe_{1.96}In_{0.04}O_4$

The TG-DTA curves of the metal-citrate gel for the composition $MgFe_{1.96}In_{0.04}O_4$ are shown in Fig.4.5. The first weight loss was observed in the region 60°C to 140 °C

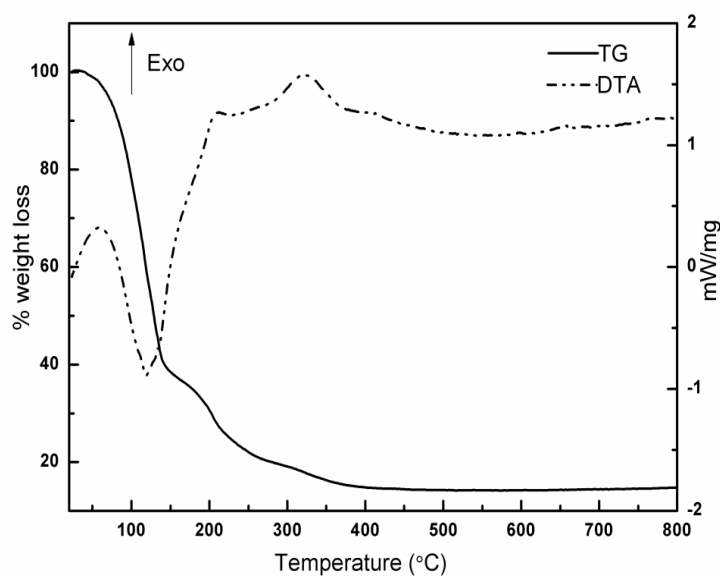


Fig. 4.5 TG-DTA curves of $MgFe_{1.96}In_{0.04}O_4$ gel.

with a prominent endothermic peak which is owing to the water loss as the gel was highly hydrated. This was followed with the decomposition of the metal citrate complex between the 140°C to 350 °C accompanied by two exothermic peaks at 206 °C and 322 °C respectively, suggesting that the complete decomposition of the gel occurred in two steps. No major weight loss was observed after 400 °C which confirmed that beyond this temperature only sintering of the sample takes place.

4.2 X-ray Diffraction Technique (XRD)

4.2.1 $\text{In}_{2-x}\text{Co}_x\text{O}_3$

Fig.4.6 shows the X-ray diffractograms of $\text{In}_{2-x}\text{Co}_x\text{O}_3$ ($x = 0.00, 0.04, 0.08, 0.12, 0.20,$ and 0.30) compounds sintered at 500 °C for 5 h. All the observed diffraction peaks could be indexed based on unit cell of cubic bixbyite In_2O_3 . The phase identification is carried out by matching the obtained diffractograms with the JCPDS data card 06-0416.

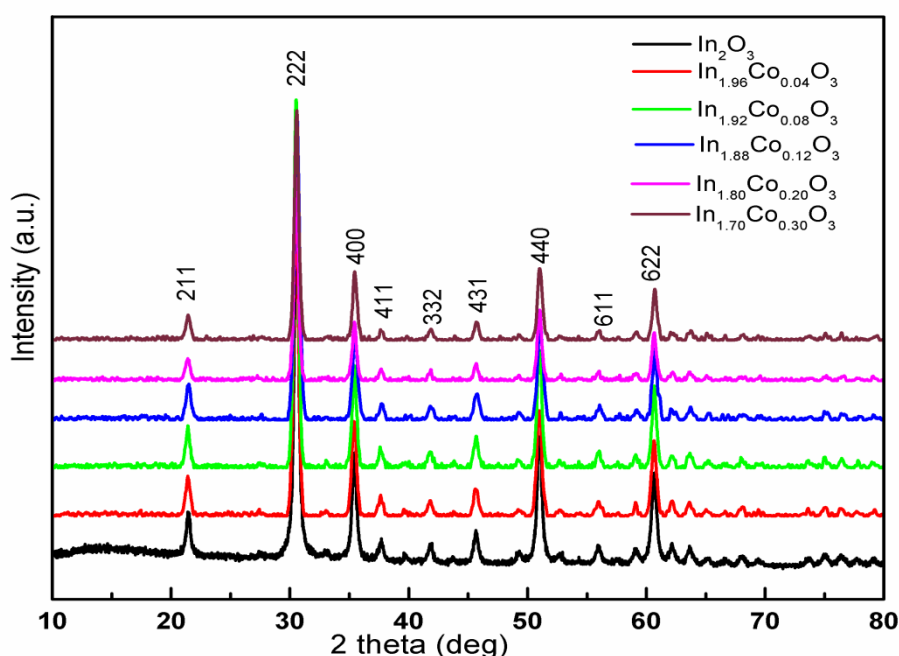


Fig. 4.6 X-ray powder diffraction pattern of $\text{In}_{2-x}\text{Co}_x\text{O}_3$ compounds sintered at 500 °C.

All the samples synthesised are found to be monophasic with no extra reflection of cobalt

oxides corresponding to the formation of any secondary phase. A systematic shift is observed towards the higher angle with Co substitution for all the samples. The peaks are indexed with the corresponding hkl values. The average crystallite size estimated from the broadening of the XRD peaks using Scherrer's formula and the lattice parameters calculated are shown in the Table 4.1. The average crystallite size ranges between 10 - 25 nm. Uniform decrease in the value of lattice constant (a) and lattice volume (v) is observed with increasing dopant concentration. Contraction of lattice on Co substitution is seen due to the smaller ionic radius of Co^{2+} (0.58 Å) as compared to that of In^{3+} (0.80 Å)[330]. This indicates the incorporation of Co ions in the In_2O_3 host lattice, thereby verifying the Vegard's law.

Table 4.1 Crystallite size and lattice parameters calculated for $\text{In}_{2-x}\text{Co}_x\text{O}_3$.

Sample	Crystallite size (nm)	Lattice Constant (a=b=c)(Å)	Lattice volume (Å) ³
In_2O_3	21.90	10.1363	1041.45
$\text{In}_{1.96}\text{Co}_{0.04}\text{O}_3$	20.15	10.1356	1041.23
$\text{In}_{1.92}\text{Co}_{0.08}\text{O}_3$	21.20	10.1320	1040.12
$\text{In}_{1.88}\text{Co}_{0.12}\text{O}_3$	19.38	10.1109	1033.64
$\text{In}_{1.80}\text{Co}_{0.20}\text{O}_3$	22.67	10.1316	1040.00
$\text{In}_{1.70}\text{Co}_{0.30}\text{O}_3$	21.99	10.1163	1035.29

4.2.2 $\text{In}_{2-x}\text{Cr}_x\text{O}_3$

The X-ray diffraction patterns for the compositions $\text{In}_{2-x}\text{Cr}_x\text{O}_3$ ($x=0.00, 0.02, 0.04, 0.08$ and 0.10) are shown in Fig. 4.7. The formation of a pure single phase is observed where all the peaks correspond to the cubic bixbyte structure of In_2O_3 (JCPDS data card 06-0416). No impurity phase corresponding to oxide of chromium is seen. On doping all

the peaks shows a shift towards the higher angle region. The crystallite size and lattice parameters are calculated using Scherrer's formula and are shown in Table 4.2.

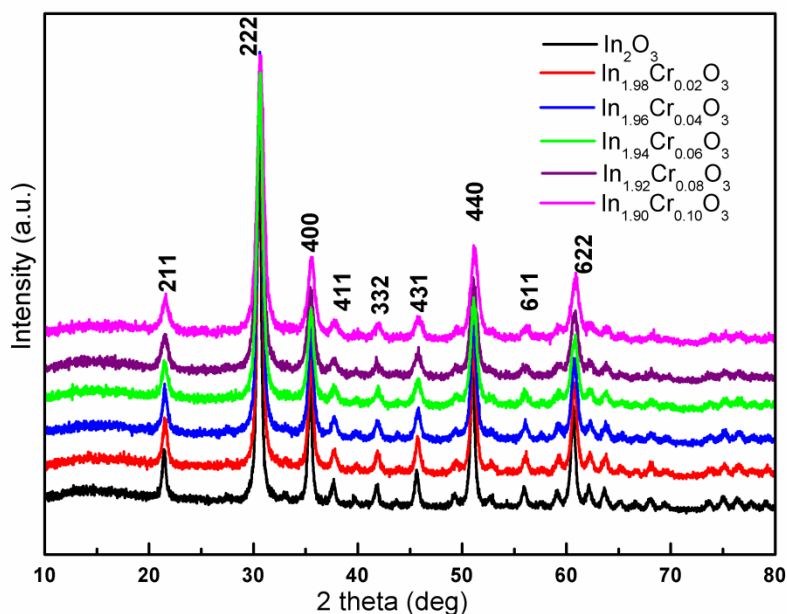


Fig. 4.7 X-ray powder diffraction pattern of $\text{In}_{2-x}\text{Cr}_x\text{O}_3$ compounds sintered at 500°C .

Table 4.2 Crystallite size and lattice parameters calculated for $\text{In}_{2-x}\text{Cr}_x\text{O}_3$.

Sample	Crystallite size (nm)	Lattice Constant (a=b=c)(Å)	Lattice volume (Å) ³
In_2O_3	21.90	10.1363	1041.44
$\text{In}_{1.98}\text{Cr}_{0.02}\text{O}_3$	18.11	10.0995	1030.14
$\text{In}_{1.96}\text{Cr}_{0.04}\text{O}_3$	16.35	10.0993	1030.08
$\text{In}_{1.94}\text{Cr}_{0.06}\text{O}_3$	14.87	10.1013	1030.69
$\text{In}_{1.92}\text{Cr}_{0.08}\text{O}_3$	13.28	10.1047	1031.74
$\text{In}_{1.90}\text{Cr}_{0.10}\text{O}_3$	12.55	10.0852	1025.77

The lattice constant values of the Cr doped compounds decreases compared to that of pristine thus revealing the incorporation of Cr into the lattice. The crystallite size is found to decrease with increase in dopant concentration. It ranges between 12 - 22 nm thus confirming the formation of nanoparticles.

4.2.3 $\text{In}_{2-x}\text{Ag}_x\text{O}_3$

The X-ray powder diffraction patterns for the compositions $\text{In}_{2-x}\text{Ag}_x\text{O}_3$ ($x=0.00$, 0.04 and 0.10) are shown in Fig. 4.8. The sample where $x = 0.04$, along with pristine showed the formation of single phase cubic bixbyte structure matched with the JCPDS data card 06-0416. Whereas the sample with higher dopant concentration i.e. $x = 0.1$, shows an additional impurity peak corresponding to the silver oxide. The hkl values corresponding to pure bixbyte phase are also shown in the XRD pattern.

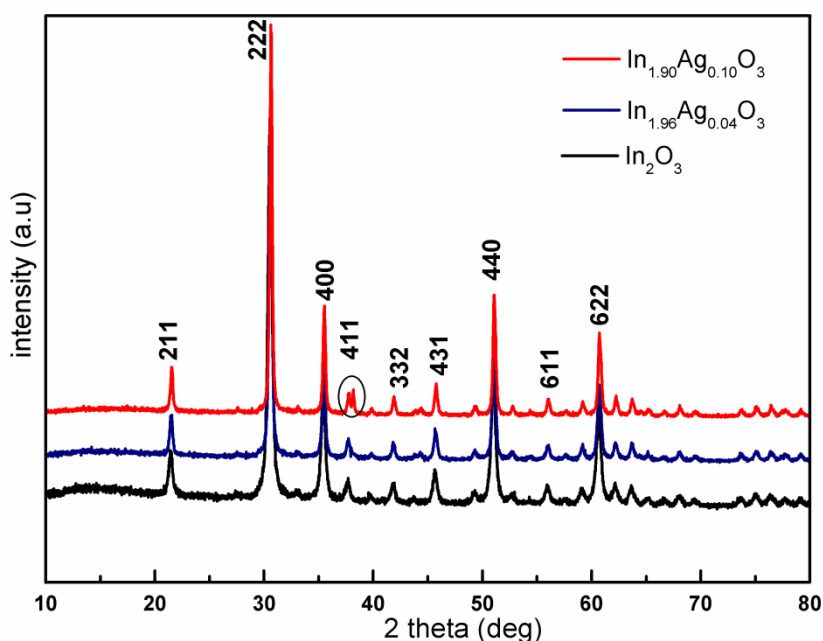


Fig. 4.8 X-ray powder diffraction pattern of $\text{In}_{2-x}\text{Ag}_x\text{O}_3$ compounds sintered at 600°C

Table 4.3 Crystallite size and lattice parameters calculated for $\text{In}_{2-x}\text{Ag}_x\text{O}_3$.

Sample	Crystallite size (nm)	Lattice Constant (a=b=c)(Å)	Lattice volume (Å) ³
In_2O_3	22.0	10.1231	1037.38
$\text{In}_{1.96}\text{Ag}_{0.04}\text{O}_3$	30.5	10.1363	1041.44
$\text{In}_{1.90}\text{Ag}_{0.10}\text{O}_3$	36.1	10.1123	1034.06

The crystallite size calculated by Scherrer's formula shows increase in size on Ag doping. The lattice constant was also seen to expand on Ag incorporation. This is owing

to the larger ionic radii of Ag^+ compared to In^{3+} . The lattice parameters and the crystallite size are shown in Table 4.3.

4.2.4 $\text{Ce}_{1-x}\text{In}_x\text{O}_2$

Fig 4.9 shows the X-ray powder diffraction patterns for $\text{Ce}_{1-x}\text{In}_x\text{O}_2$ ($x = 0.02, 0.04, 0.06, 0.10$ and 0.15). Pristine and In^{3+} doped CeO_2 crystallizes in fluorite structure (JCPDS No.34-0394). The broadening of the peaks suggests the formation of nanoparticles. No impurity phase corresponding to In_2O_3 is obtained which shows the substitution of In^{3+} ion in place of Ce^{4+} .

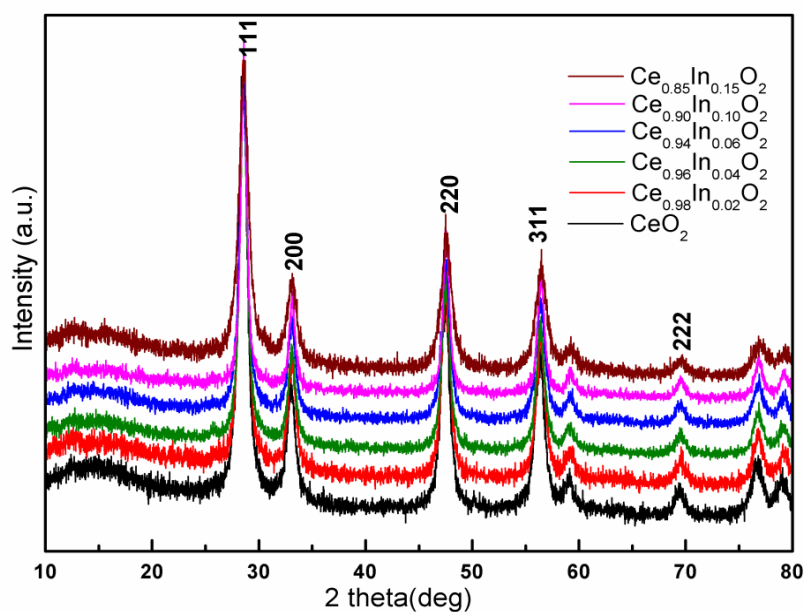


Fig. 4.9 X-ray powder diffraction pattern of $\text{Ce}_{1-x}\text{In}_x\text{O}_2$ compounds sintered at $600\text{ }^\circ\text{C}$.

The hkl values are also indexed in the XRD pattern corresponding to the respective 2θ values. The lattice parameters and crystallite size calculated by Scherrer's formula are reported in the Table 4.4. The lattice constant is found to decrease with In^{3+} doping. This is due to the substitution of Ce^{4+} (ionic radii 1.04 \AA) by In^{3+} having smaller ionic radii (0.94 \AA) which leads to the contraction of lattice. The crystallite size ranges between 10-16 nm.

Table 4.4 Crystallite size and lattice parameters calculated for $Ce_{1-x}In_xO$.

Compositions	Crystallite size (nm)	Lattice constant (a=b=c) Å	Lattice Volume (Å) ³
CeO_2	11.63	5.4121	158.52
$Ce_{1.98}In_{0.02}O_2$	12.50	5.4057	157.96
$Ce_{1.96}In_{0.04}O_2$	13.39	5.4077	158.13
$Ce_{1.94}In_{0.06}O_2$	10.81	5.4077	158.13
$Ce_{1.92}In_{0.08}O_2$	16.01	5.4022	157.65
$Ce_{1.90}In_{0.10}O_2$	10.57	5.4022	157.65

4.2.5 $MgFe_{2-x}In_xO_4$

Structural characterisation of the above samples was carried out by X-ray powder diffraction. Fig. 4.10 displays the diffraction pattern obtained for the $MgFe_{2-x}In_xO_4$ (where $x = 0.00, 0.04, 0.08, 0.12$ and 0.16). All the peaks were indexed as per the cubic spinel structure of ferrite (JCPDS File No. 01-089-3084) with their corresponding hkl values. It was observed that as the In^{3+} concentration was increased to $x = 0.16$, impurity peak

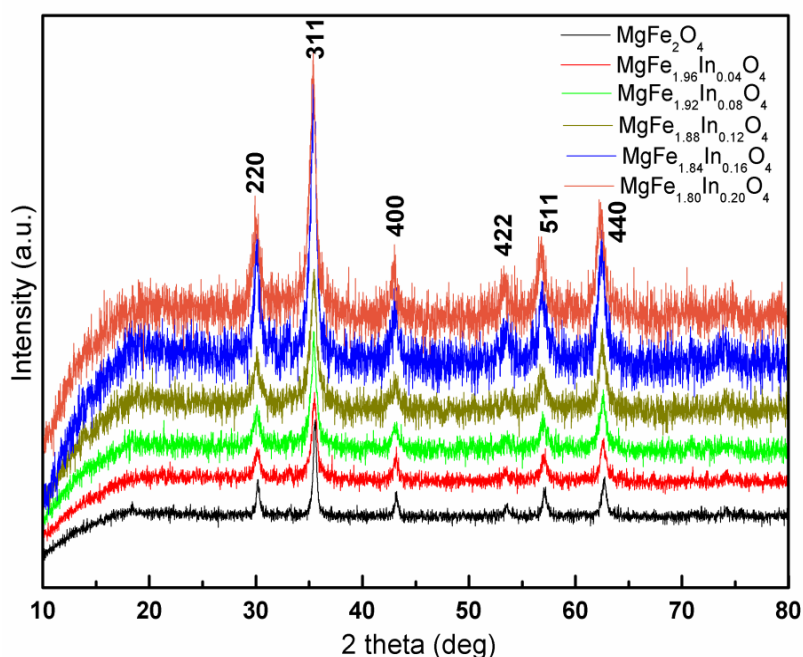


Fig. 4.10 X-ray powder diffraction pattern of $MgFe_{2-x}In_xO_4$ compounds sintered at 600 °C.

corresponding to α -Fe₂O₃ was observed. Below this concentration, no impurity phase was detected. All the peaks appeared to be broad in nature thereby suggesting the formation of ferrites in the nano-crystallite form. The average crystallite size was estimated using Scherrer's formula and it ranges between 10 - 24 nm. Table 4.5 shows the calculated crystallite size, lattice constant (a) and lattice volume (v). Considering the larger ionic radii of In³⁺ compared to Fe³⁺ its substitution should increase the lattice parameters and the same is observed in the present case [331]. As the concentration of In³⁺ increases the lattice constant increases linearly, thus following the Vegard's law. This confirms the incorporation of In³⁺ in the spinel lattice.

Table 4.5 Crystallite size and lattice parameters calculated for MgFe_{2-x}In_xO₄.

Compositions	Crystallite size (nm)	Lattice constant (a=b=c) Å	Lattice Volume (Å) ³
MgFe ₂ O ₄	24.01	8.3652	585.36
MgFe _{1.96} In _{0.04} O ₄	12.40	8.3810	588.69
MgFe _{1.92} In _{0.08} O ₄	12.10	8.3925	591.11
MgFe _{1.88} In _{0.12} O ₄	10.12	8.3956	591.77
MgFe _{1.84} In _{0.16} O ₄	12.71	8.3992	592.53
MgFe _{1.80} In _{0.20} O ₄	11.45	8.4133	595.52

4.3 Infrared Spectroscopy

4.3.1 In₂O₃

The infrared spectra of gel (a), as prepared (b) and calcined sample at 500 °C (c) for In₂O₃ are shown in Fig. 4.11. In spectrum (a) two broad bands are observed at around 3560 and 3155 cm⁻¹ corresponding to the N-H and O-H stretching respectively. Signals at 1757 and 1571 cm⁻¹ represent the asymmetric and symmetric stretching frequencies of the

metal carboxylate linkages present in the gel matrix. Prominent peaks at 1386 and 821cm^{-1} are assigned for the $(\text{NO}_3)^{-1}$ stretching frequency and in plane deformation frequency [3]. The peak observed at around 2390 cm^{-1} can be attributed to CO_2 [95]. Most of the above peaks disappear on combustion as seen from spectrum (b). Since, most of the organic components are decomposed, only the peaks corresponding to O-H and $(\text{NO}_3)^{-1}$ stretchings are present as impurities. The disappearance of all the above peaks in the spectrum (c) suggests that upon heating at $500\text{ }^\circ\text{C}$ the pure metal oxide nanoparticles are obtained without any organic impurity. The appearance of peaks at 601 , 567 , 538 and 426 cm^{-1} in the spectra which are characteristic of In-O vibrations, confirms the crystallization of nano-particles in cubic phase of In_2O_3 [95,333,334]. Thus the sintered samples are highly pure in nature suggesting that $500\text{ }^\circ\text{C}$ is an optimum temperature for complete decomposition of gel to form metal oxide.

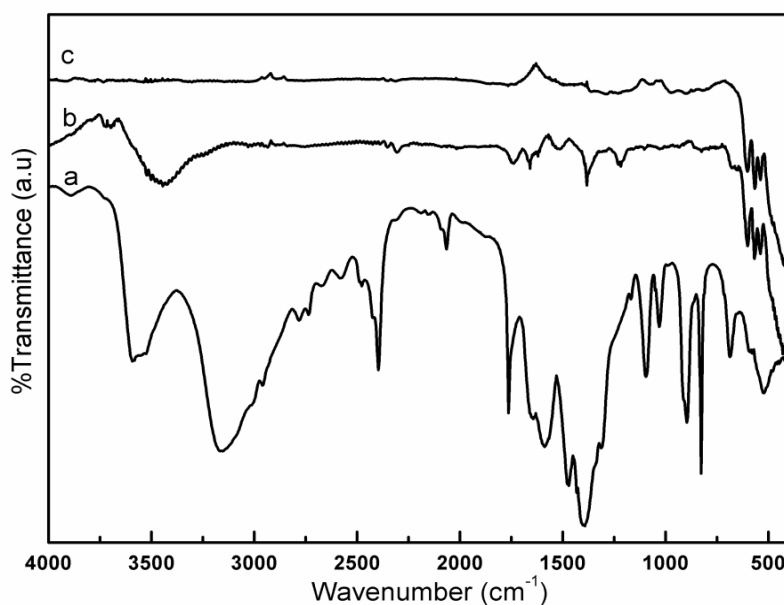


Fig.4.11 The infra red spectra of gel (a), as prepared (b) and calcined sample at $500\text{ }^\circ\text{C}$ (c) for In_2O_3 .

4.3.2 $\text{In}_{2-x}\text{Co}_x\text{O}_3$

The Infrared spectra for $\text{In}_{2-x}\text{Co}_x\text{O}_3$ ($x = 0.00, 0.04, 0.08, 0.12, 0.20$ and 0.30)

samples sintered at 500 °C are shown in Fig. 4.12 where the M-O bands corresponding to In-O vibrations are consistent with all the samples. The well resolved peaks are observed around the following frequencies 601, 567, 538 and 426 cm^{-1} [95,333,334]. This supports the formation of monophasic compounds where no other impurity vibrations are visible.

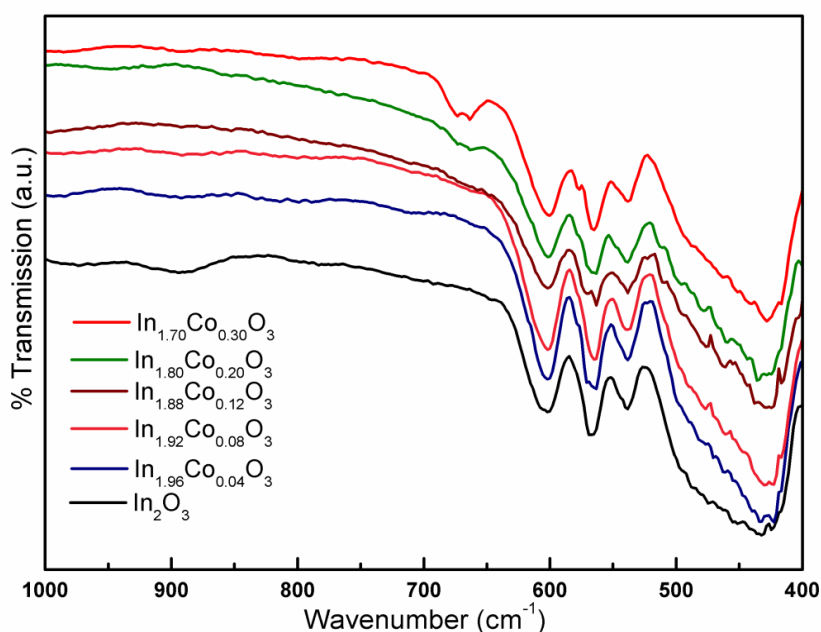


Fig. 4.12 Infrared spectra of $\text{In}_{2-x}\text{Co}_x\text{O}_3$ compounds sintered at 500 °C.

4.3.3 $\text{In}_{2-x}\text{Cr}_x\text{O}_3$

The infrared spectra of $\text{In}_{2-x}\text{Cr}_x\text{O}_3$ ($x=0.00, 0.02, 0.04, 0.08$ and 0.10) compounds sintered at 500 °C are shown in Fig. 4.13. All the samples show metal oxide vibrational peaks in the region 400 – 610 cm^{-1} . The peaks corresponding to In-O vibrations are observed typically at 601, 567, 538 and 426 cm^{-1} [95,333,334], which are consistent with all the samples. This suggests crystallisation of the samples in the bixbyte structure. No other peaks are observed above 600 cm^{-1} thus confirming the formation of pure metal oxides with no organic impurities.

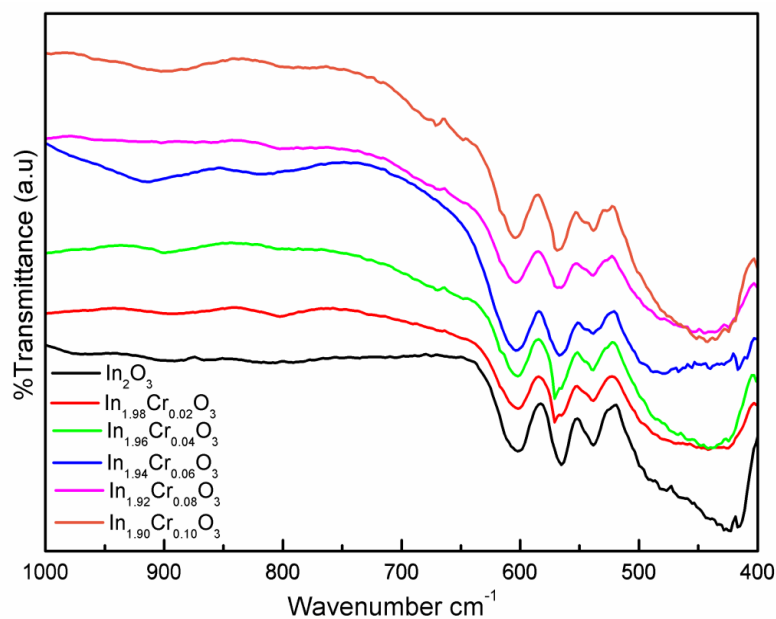


Fig. 4.13 Infrared spectra of $In_{2-x}Cr_xO_3$ compounds sintered at 500 °C.

4.3.4 $In_{2-x}Ag_xO_3$

The Infra red spectra of $In_{2-x}Ag_xO_3$ ($x=0.00, 0.04$ and 0.10) samples sintered at 600 °C are shown in Fig. 4.14. As explained in the earlier spectra, here also the characteristics M-O vibrational bands corresponding to In-O are observed at around 601, 567, 538 and 426 cm^{-1} .

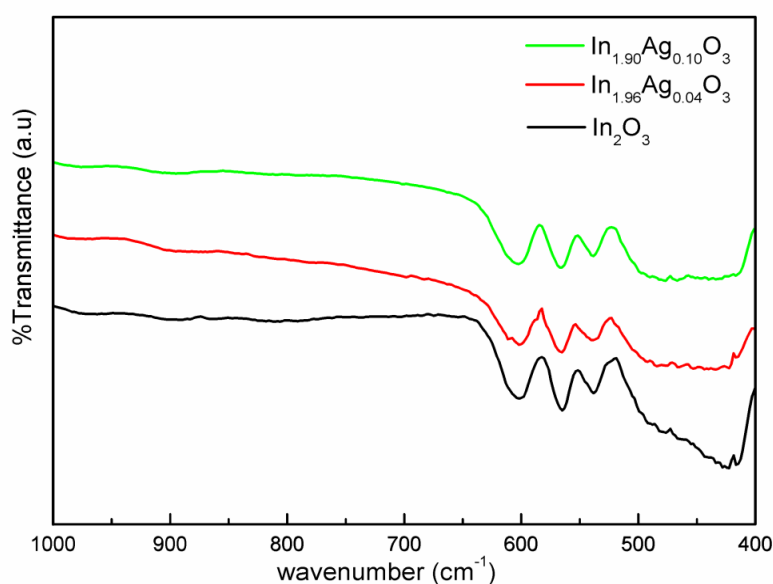


Fig.4.14 Infrared spectra of compounds sintered at 600 °C.

4.3.5 $Ce_{0.90}In_{0.10}O_2$

The representative infrared spectra of the $Ce_{0.09}In_{0.10}O_2$ gel, as prepared sample and the sintered sample are shown in Fig.4.15. The gel obtained consists of the metal nitrate –citric acid complex. A broad band in the region from 3000-3600 cm^{-1} is attributed to the O-H stretching frequency. The bands obtained at 1324, 1469 and 1600 cm^{-1} are attributed to the asymmetric and symmetric vibrations of COO^- group where metal is coordinated to the carboxy group whereas peak at 1700 cm^{-1} corresponds to the free carboxylic acid group [335]. In the as prepared sample only the O-H band and metal carboxylate peaks are seen in lower concentration whereas the sintered samples does not show any of these peaks which shows that the organic component has been completely decomposed giving the pure nanoparticles. The Ce-O vibrations are observed around 400 cm^{-1} .

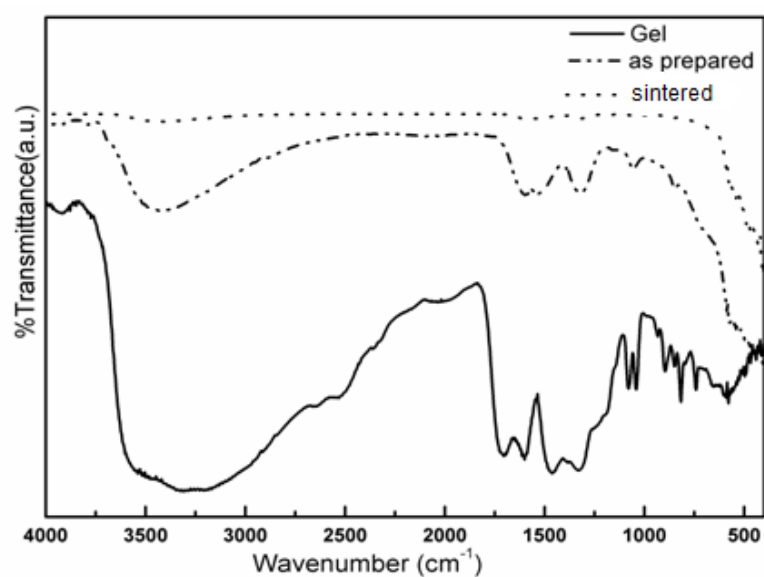


Fig. 4.15 Infrared spectra of $Ce_{0.90}In_{0.10}O_2$ gel, as prepared and sintered (600 °C) sample.

4.3.6 $Ce_{1-x}In_xO_2$

The infra red spectra for the sintered samples of $Ce_{1-x}In_xO_2$ ($x = 0.02, 0.04, 0.06, 0.10$ and 0.15) are shown in Fig. 4.16. No peak in the region from 1000 – 500 cm^{-1} is

visible. The M-O stretching vibrations are observed consistently in all the samples around 400 °C owing to Ce-O vibrations.

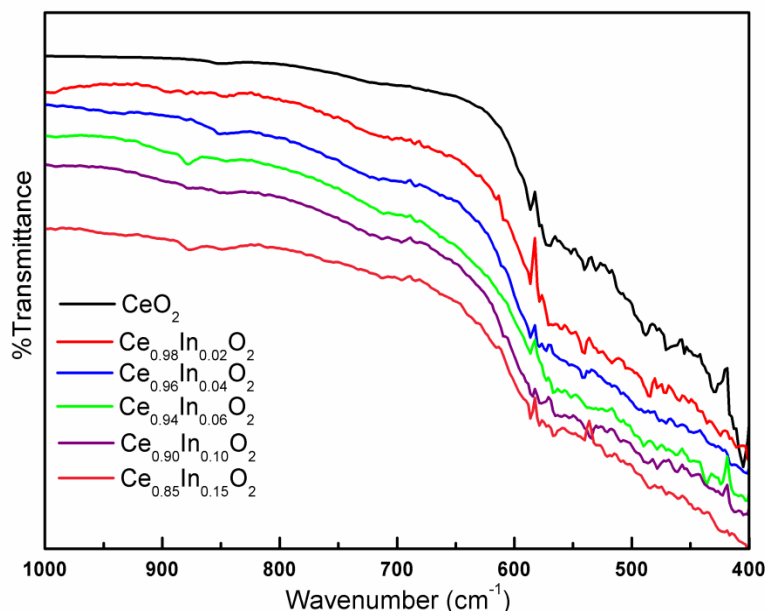


Fig. 4.16 Infrared spectra of $Ce_{1-x}In_xO_2$ sintered at 600 °C.

4.3.7 $MgFe_{1.96}In_{0.04}O_4$

A representative IR spectra of the gel, as prepared (decomposed at 400 °C) and sintered sample for the composition $MgFe_{1.96}In_{0.04}O_4$ is displayed in Fig. 4.17. The initial gel which consists of metal nitrate and citric acid complex shows the peaks corresponding to organic moieties, mainly a broad band at around 3414 cm^{-1} and 1630 cm^{-1} corresponding to O-H stretching and bending vibrations, C=O at 1740 cm^{-1} representing free carbonyl stretching and the prominent peaks at 1377 and 819 cm^{-1} can be assigned to $(NO_3)^{-1}$ stretching frequency. The gel here was highly hydrated further concentrating the mixture leads to the complexation of acid with the metal. This is also observed in the as prepared sample where the peak around 1504 cm^{-1} is visible due to the presence of metal carboxylate ion. All the above mentioned peaks are seen in the as prepared samples also, but in slightly lower intensity. The appearance of characteristic M-O bands is also

observed. The absence of the above mentioned peaks in the sintered sample shows that the organic part is completely decomposed and the Mg-Ferrite nano-particles are obtained with strong peaks at 578 and 408 cm^{-1} characteristic of tetrahedral and octahedral M-O stretching vibration modes respectively [292].

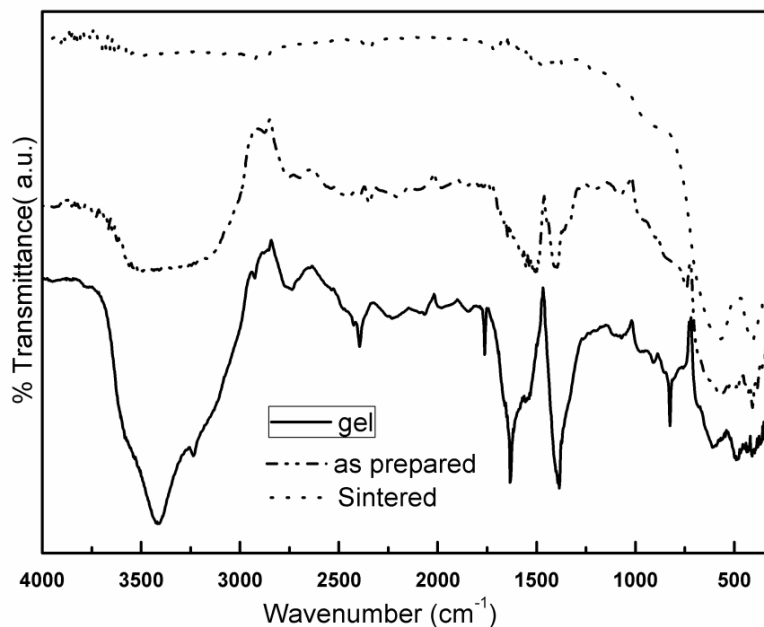


Fig. 4.17 Infra red spectra of $\text{MgFe}_{1-x}\text{In}_x\text{O}_4$ gel, as prepared and sintered ($600\text{ }^\circ\text{C}$) sample.

4.3.8 $\text{MgFe}_{2-x}\text{In}_x\text{O}_4$

Fig.4.18 represents the infrared spectra of $\text{MgFe}_{2-x}\text{In}_x\text{O}_4$ sintered samples. The

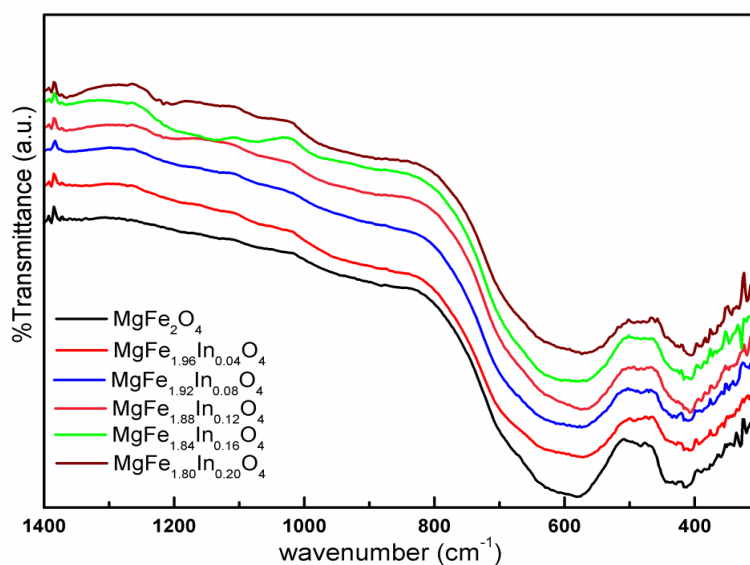


Fig. 4.18 Infrared spectra of $\text{MgFe}_{1-x}\text{In}_x\text{O}_4$ sintered at $600\text{ }^\circ\text{C}$.

characteristic M-O vibrations were observed for all the compositions at 578 and 408 cm^{-1} respectively. These can be assigned to the tetrahedral and octahedral M-O stretching respectively. This also shows the formation of ferrite nanoparticles qualitatively.

4.4 UV-Visible Absorbance / Diffused Reflectance Spectroscopy.

The diffused reflectance spectra for all the nanoparticles were converted to absorption using Kubelka Munk function. The band gap is calculated using Tauc equation by plotting $(\alpha h\nu)^2$ v/s $h\nu$ (Energy in eV).

4.4.1 $\text{In}_{1-x}\text{Co}_x\text{O}_3$

The spectra of absorption v/s wavelength for pristine In_2O_3 is shown in Fig. 4.19, the charge transfer absorption band is obtained in the region 200 - 320 nm, which on Co doping is found to grow broader in the visible region as shown in Fig. 4.20. The intensity of absorption is found to be higher for the doped samples compared to that of pristine.

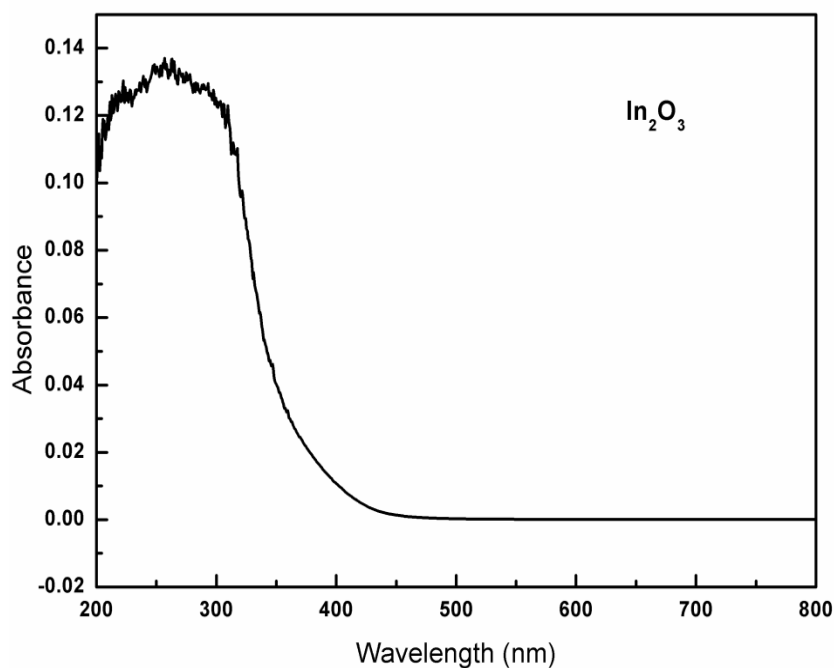


Fig. 4.19 UV absorbance spectra of In_2O_3

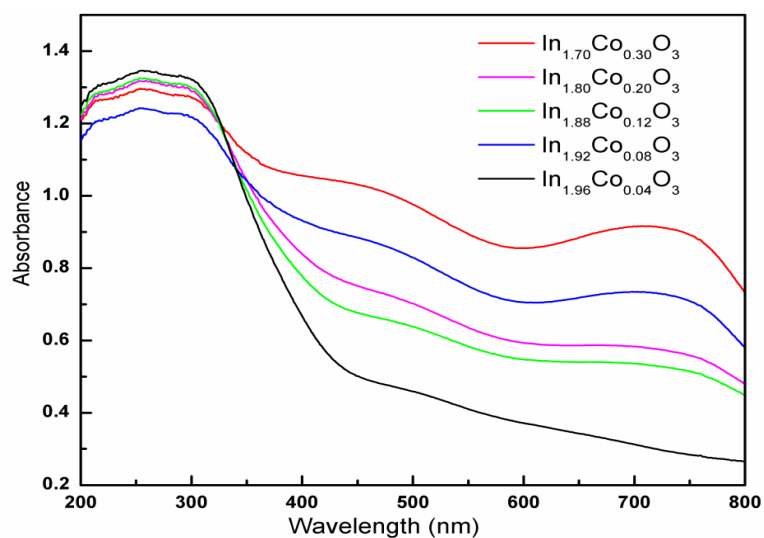


Fig. 4.20 UV absorbance spectra of $In_{2-x}Co_xO_3$ compounds sintered at $500\text{ }^\circ\text{C}$.

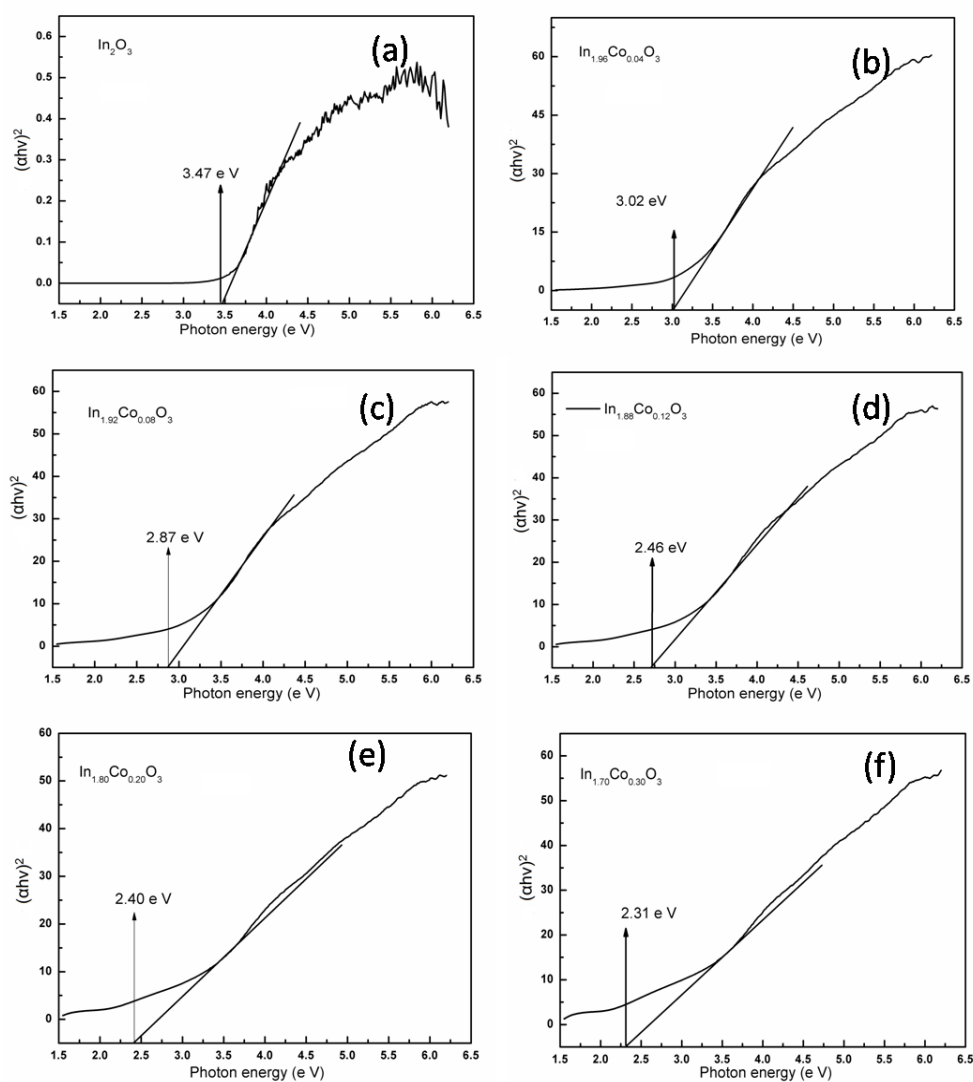


Fig.4.21 Plot of $(ahv)^2$ v/s photon energy (hv) in e.V for (a) In_2O_3 (b) $In_{1.96}Co_{0.04}O_3$ (c) $In_{1.92}Co_{0.08}O_3$ (d) $In_{1.88}Co_{0.12}O_3$ (e) $In_{1.80}Co_{0.20}O_3$ (f) $In_{1.70}Co_{0.30}O_3$.

The band gaps were calculated from Tauc plot as shown in the above Fig. 4.21. The band gap value obtained for the pristine In_2O_3 is 3.65 eV which is in agreement with the band gap (3.5 - 3.7 eV) reported in literature [336, 337]. With Co doping the band gap values of the nano-particles were subsequently found to decrease. Cobalt as a dopant results in the formation of an acceptor band above the valence band which results in the narrowing of the band gap [338,339]. Similar red shift is in band gap of In_2O_3 on Co doping is also observed by N. Deng et al. which is attributed to the sp-d exchange between band electrons and localised d electrons of dopant [142].

4.4.2 $\text{In}_{2-x}\text{Cr}_x\text{O}_3$

The absorption spectra for pristine as well as Cr doped In_2O_3 displayed in Fig. 4.22 shows a similar pattern where the charge transfer band is seen in the UV region. The intensity of doped compounds is slightly higher than that of pristine. No other absorption peak is observed. The Tauc plot are presented in Fig. 4.23 showing the band gaps of the compounds where the doped compounds shows band gaps in the similar range (3.55 - 3.58 eV) as that of pristine (3.51 eV). The slight reduction could be attributed to reduced crystallite size obtained on doping as discussed in XRD but no specific trend is seen.

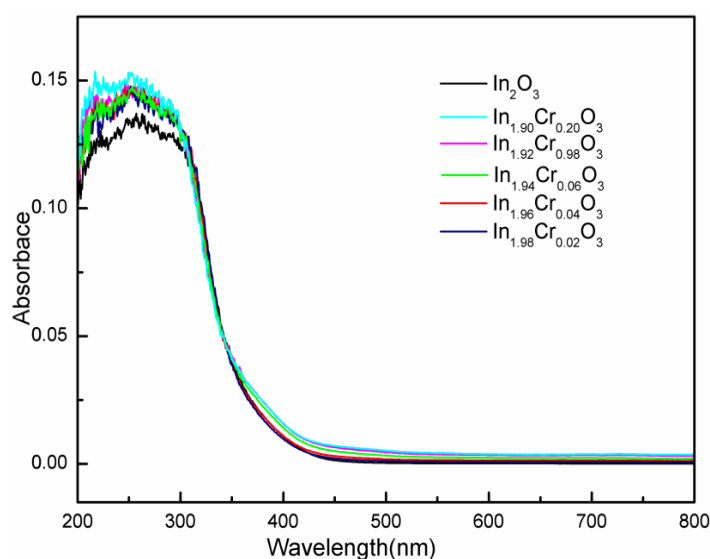


Fig. 4.22 UV absorbance spectra of $\text{In}_{2-x}\text{Cr}_x\text{O}_3$ ($x = 0.00, 0.02, 0.04, 0.06, 0.08, \text{ and } 0.10$)

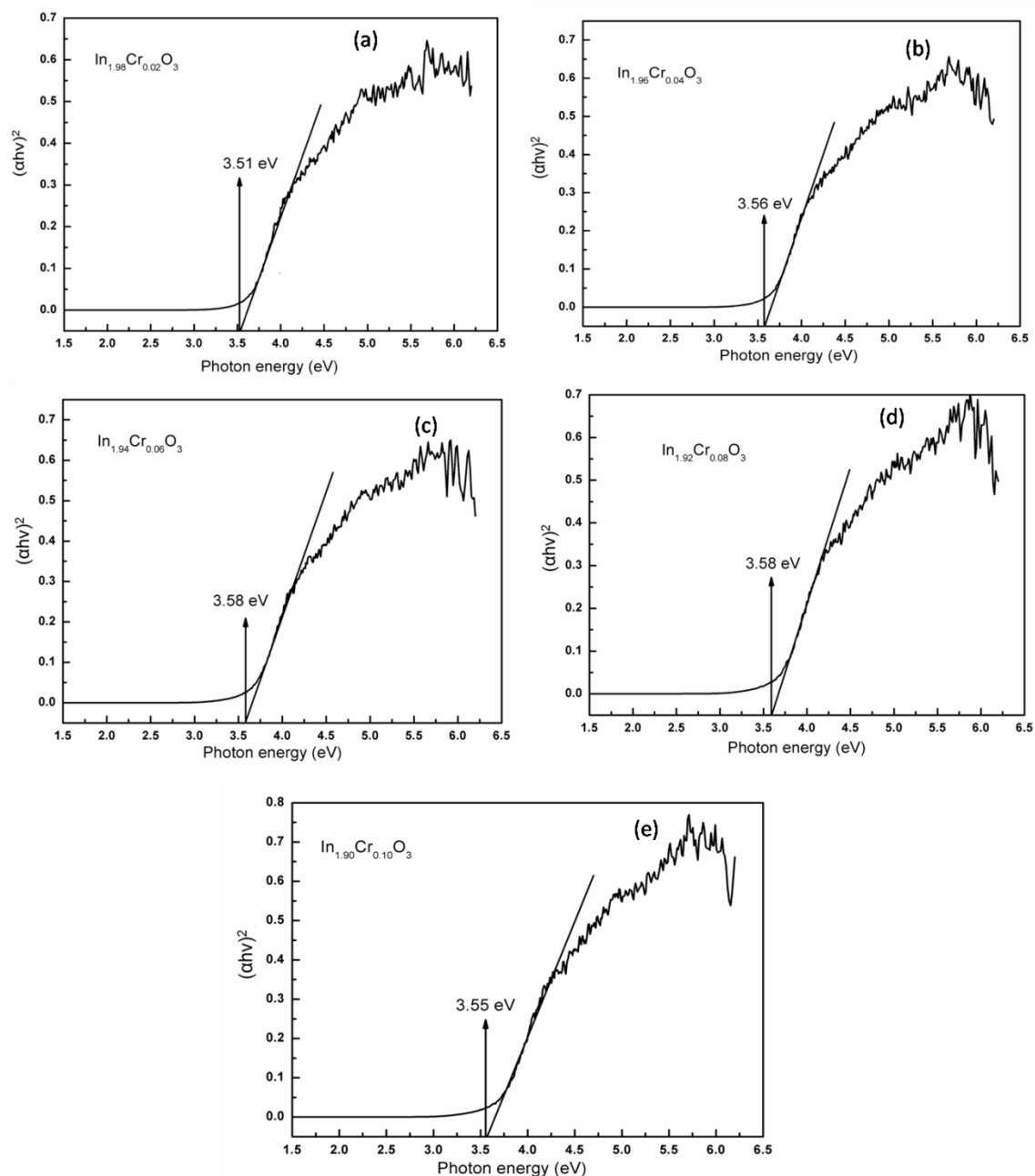


Fig. 4.23 Plot of $(\alpha h\nu)^2$ v/s photon energy $(h\nu)$ in e.V for (a) $In_{1.98}Cr_{0.02}O_3$ (b) $In_{1.96}Cr_{0.04}O_3$ (c) $In_{1.94}Cr_{0.06}O_3$ (d) $In_{1.92}Cr_{0.08}O_3$ (e) $In_{1.90}Cr_{0.10}O_3$.

4.4.3 $In_{2-x}Ag_xO_3$

The absorption spectra for pristine and Ag doped In_2O_3 compounds shown in Fig. 4.24 also displays the charge transfer band in UV region. The calculated band gap value for silver-doped In_2O_3 shows slight decrease compared to pristine which can be attributed to the expansion of crystal lattice on incorporation of larger silver ions, thereby

decreasing the band gap. This is also in accordance with the increased crystallite size obtained for the doped sample. Further decrease in band gap for the $x = 0.05$ can be attributed to its mixed phase. The Tauc plots are shown in Fig. 4.25.

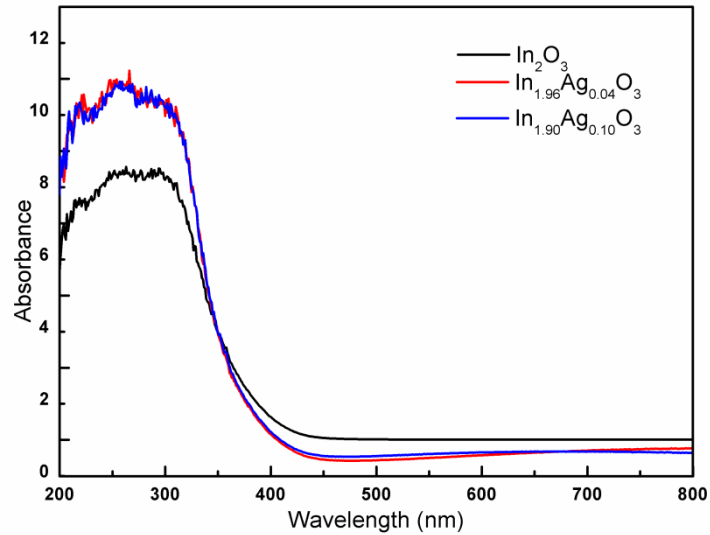


Fig. 4.24 UV absorbance spectra of $In_{2-x}Ag_xO_3$ ($x = 0.00, 0.04$ and 0.10)

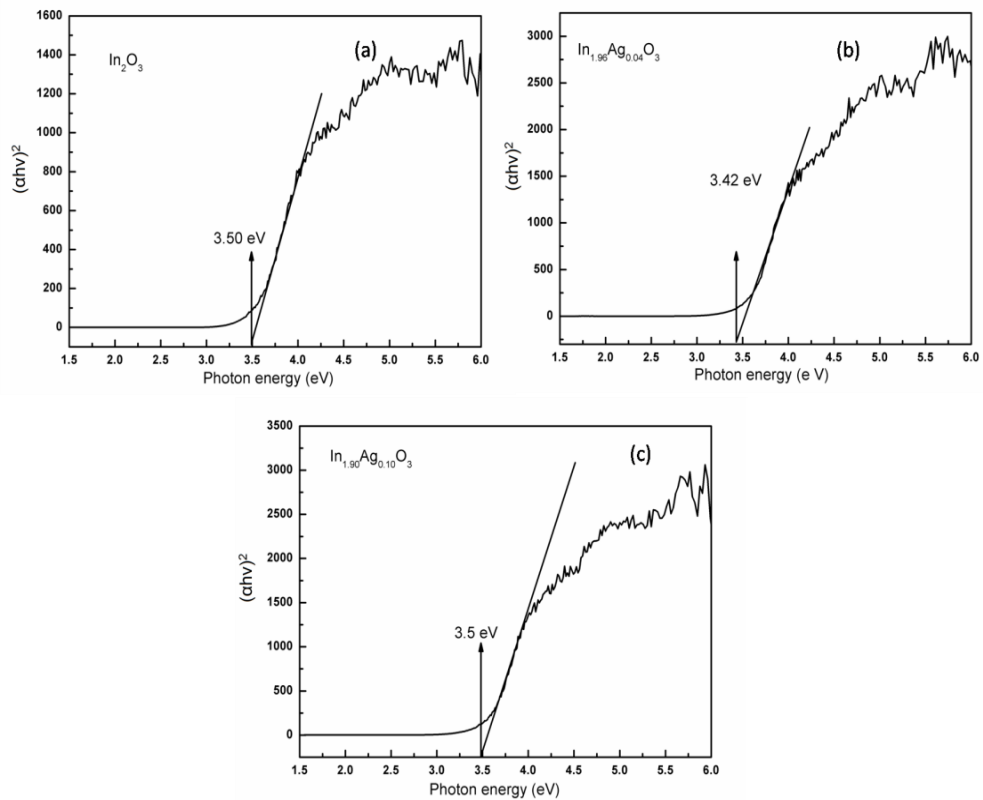


Fig. 4.25 Plot of $(\alpha h\nu)^2$ vs photon energy $(h\nu)$ in eV for (a) In_2O_3 (b) $In_{1.96}Ag_{0.04}O_3$ (c) $In_{1.90}Ag_{0.10}O_3$.

4.4.4 $Ce_{1-x}In_xO_2$

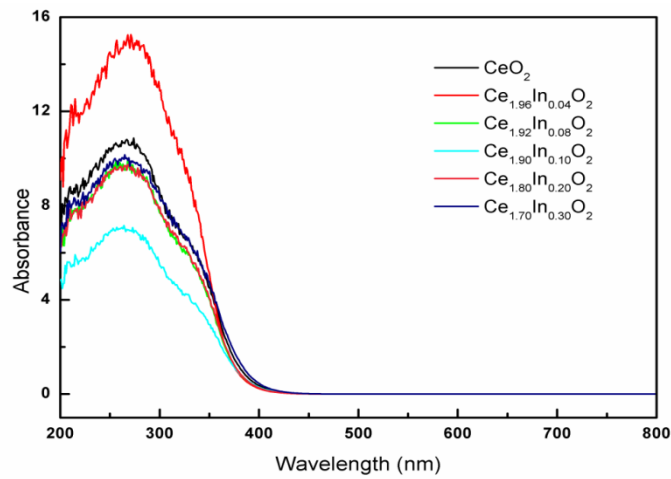


Fig. 4.26 UV absorbance spectra of $Ce_{1-x}In_xO_2$ compounds sintered at 600 °C.

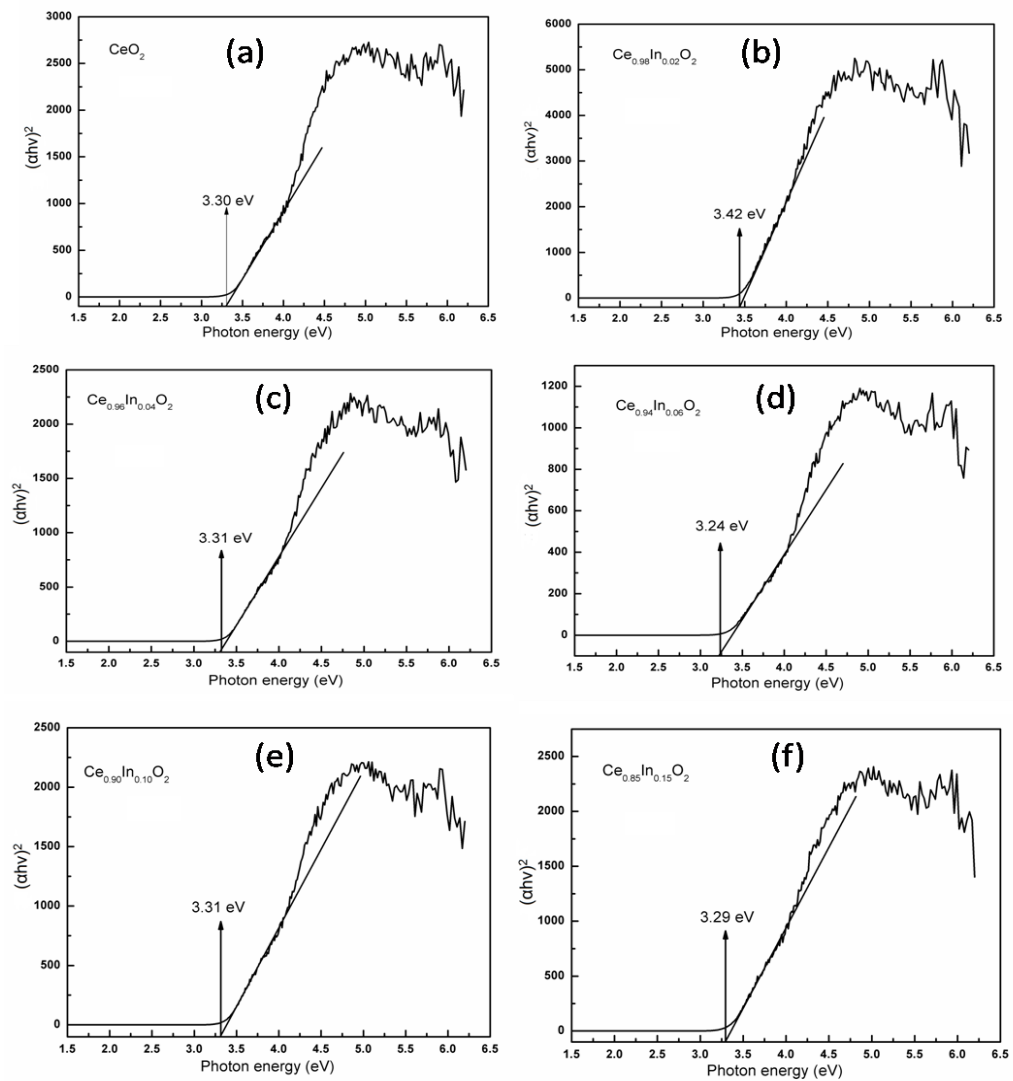


Fig. 4.27 Plot of $(ahv)^2$ v/s photon energy (hv) in eV for (a) CeO_2 (b) $Ce_{0.98}In_{0.02}O_2$ (c) $Ce_{0.96}In_{0.04}O_2$ (d) $Ce_{0.94}In_{0.06}O_2$ (e) $Ce_{0.90}In_{0.10}O_2$ (f) $Ce_{0.85}In_{0.15}O_2$.

The absorption spectra for pristine and In doped CeO₂ is presented in Fig.4.26 where the charge transfer band is observed in the region from 200-350 nm. The intensity here does not follow any trend similar to the observed band gap values which lies between 3.20-3.50 eV. The Tauc plots for the series are presented in the Fig. 4.27 representing the band gaps.

4.4.5 MgFe_{2-x}In_xO₄

Fig. 4.28 shows the absorption spectra for pristine and In doped Magnesium ferrite compounds. The UV absorption band in 200-350 nm is followed by a small hump at 475 nm in the visible region. The Tauc plots for all the compositions are shown below in Fig. 4.29. The band gap value obtained for pristine MgFe₂O₄ is 2.71 eV which is higher than the reported value for bulk which is in the range of 2.2 - 2.4 eV. This is due to the decrease in particle size i.e. the formation of particles in nano-range [17, 340]. Further the band gap values are reduced on doping with In³⁺ for the monophasic samples.

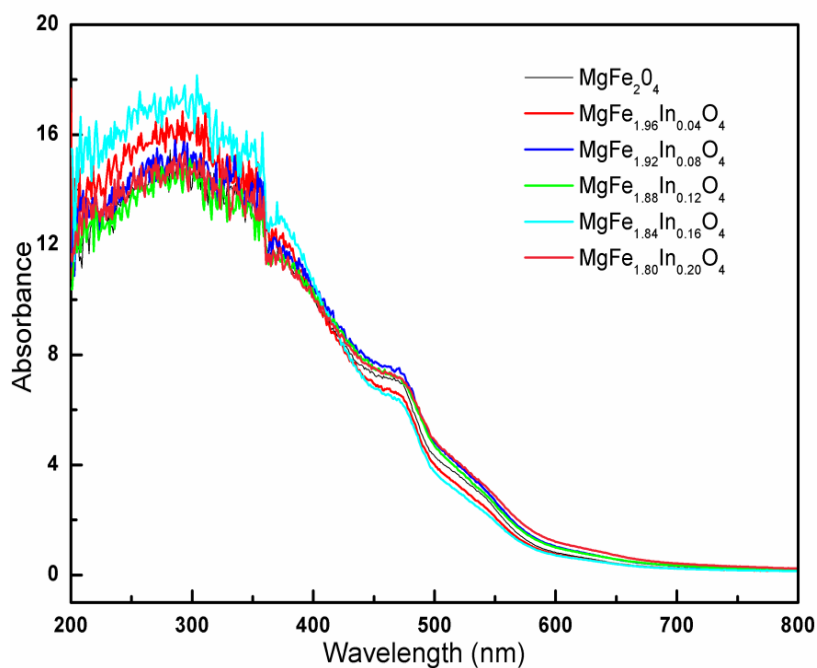


Fig. 4.28 UV absorbance spectra of MgFe_{2-x}In_xO₄ compounds sintered at 600 °C.

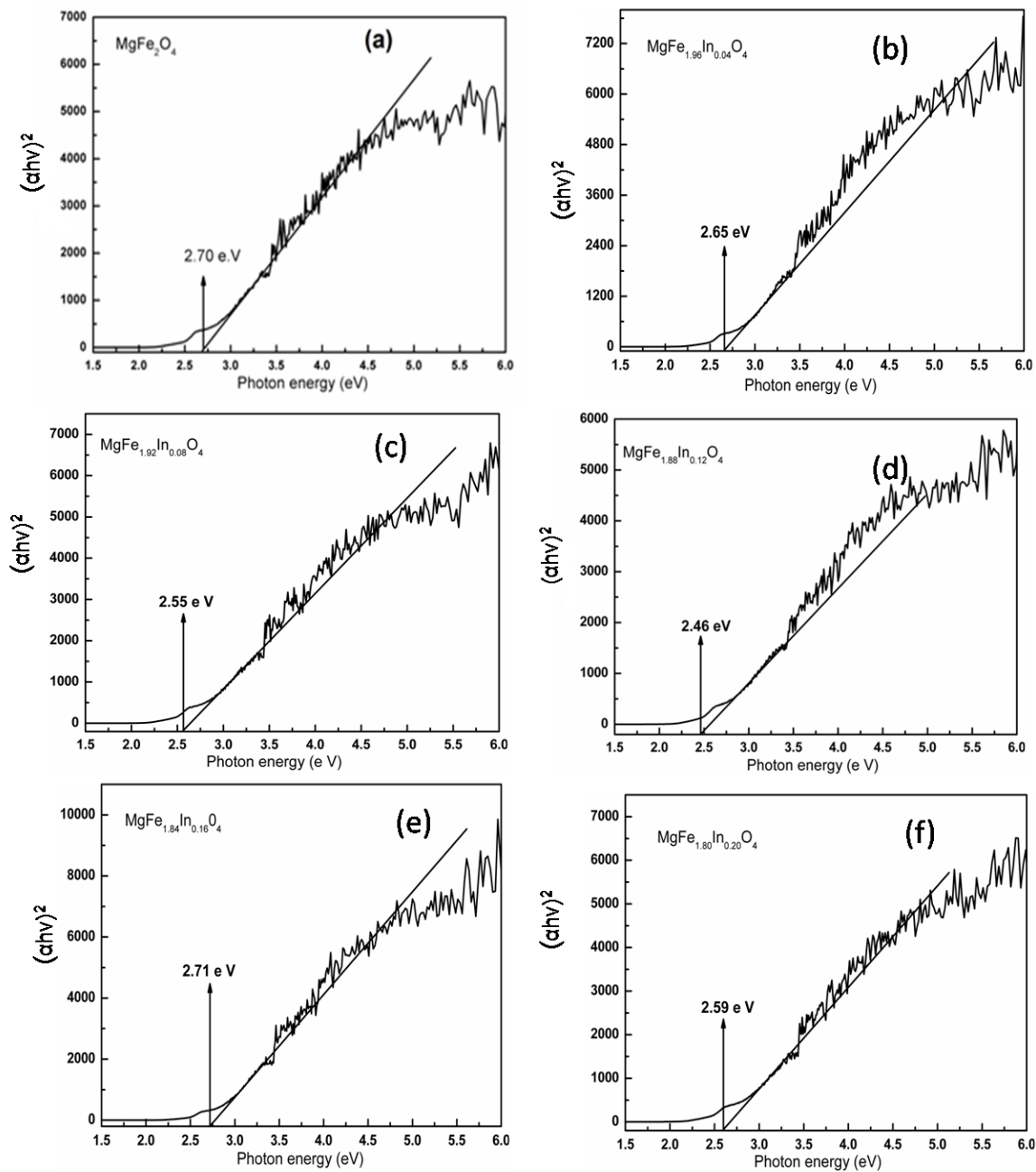


Fig. 4.29 Plot of $(\alpha h\nu)^2$ vs photon energy $(h\nu)$ in eV for (a) MgFe_2O_4 (b) $\text{MgFe}_{1.96}\text{In}_{0.04}\text{O}_4$ (c) $\text{MgFe}_{1.92}\text{In}_{0.08}\text{O}_4$ (d) $\text{MgFe}_{1.88}\text{In}_{0.12}\text{O}_4$ (e) $\text{MgFe}_{1.84}\text{In}_{0.16}\text{O}_4$ (f) $\text{MgFe}_{1.80}\text{In}_{0.20}\text{O}_4$

4.5 Scanning Electron Microscopy

4.5.1 $\text{In}_{2-x}\text{Co}_x\text{O}_3$

The SEM images for $\text{In}_{2-x}\text{Co}_x\text{O}_3$ compounds are presented in Fig. 4.30. All the samples exhibit a porous nature as seen from images. The spherical morphology and

nano-particulate size is also very much clear. Smaller particles aggregate resulting in the formation of few agglomerates.

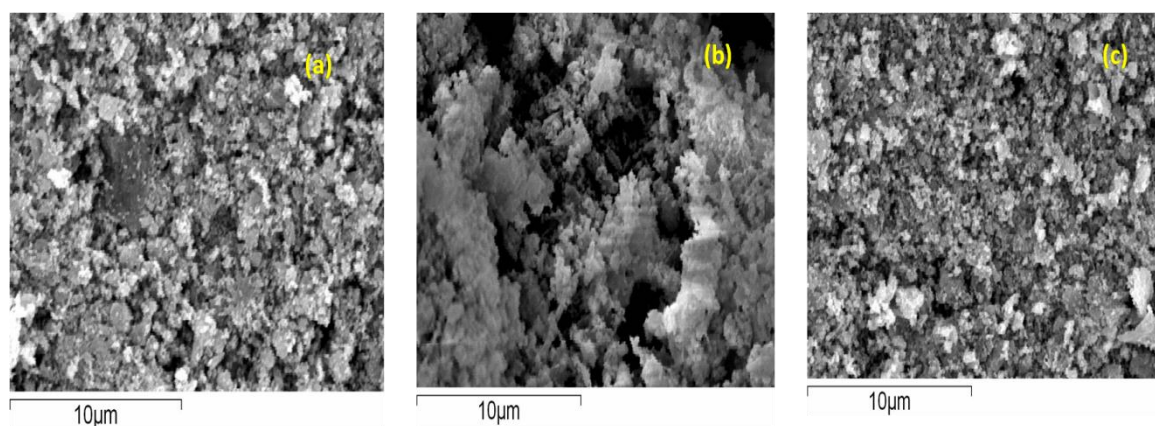


Fig.4.30 SEM images of (a) In_2O_3 (b) $In_{1.96}Co_{0.04}O_3$ (c) $In_{1.80}Co_{0.20}O_4$ compounds sintered at $500^\circ C$.

4.5.2 $In_{2-x}Cr_xO_3$

Fig.4.31 represents the SEM images of $In_{2-x}Cr_xO_3$ compounds. Here also the particles appear to be spherical in morphology and porous in nature. The average particle size falls in the nano-range. A huge agglomerate consist of small tiny individual particles is seen in a micrograph representing $In_{1.90}Cr_{0.10}O_4$ composition.

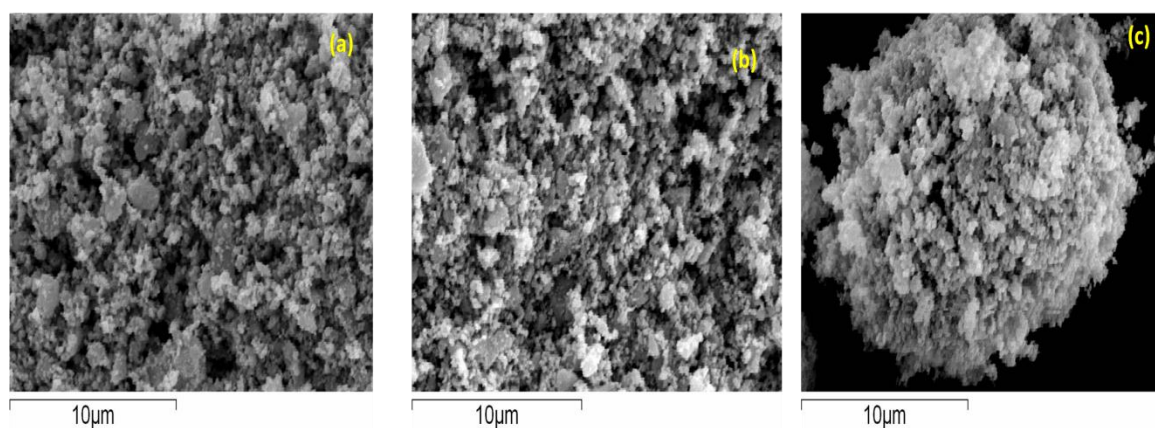


Fig.4.31 SEM images of (a) $In_{1.98}Cr_{0.02}O_3$ (b) $In_{1.94}Cr_{0.06}O_4$ (c) $In_{1.90}Cr_{0.10}O_4$ compounds sintered at $500^\circ C$.

4.5.3 $In_{2-x}Ag_xO_3$

The SEM image for $In_{1.96}Ag_{0.04}O_3$ sample is displayed in Fig.4.32. The spherical nature is consistent with this compound. The porosity is found to decrease on

silver incorporation compared to the pristine and Co and Cr doped samples. The exact particle size would be clear from TEM images. The particles appear to be agglomerated.

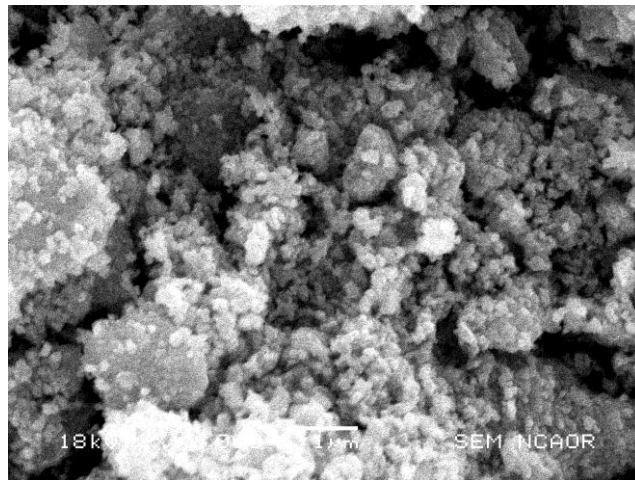


Fig.4.32 SEM image of (a) $In_{1.96}Ag_{0.04}O_3$ compound.

4.5.4 $Ce_{1-x}In_xO_2$

The SEM images for (a) CeO_2 and (b) $Ce_{0.85}In_{0.15}O_2$ compounds are shown in Fig.4.33. Both the images display a flaky nature of the particles which is highly porous. This is owing to the highly exothermic reaction that took place during the synthesis. The exact morphology cannot be well understood from these images.

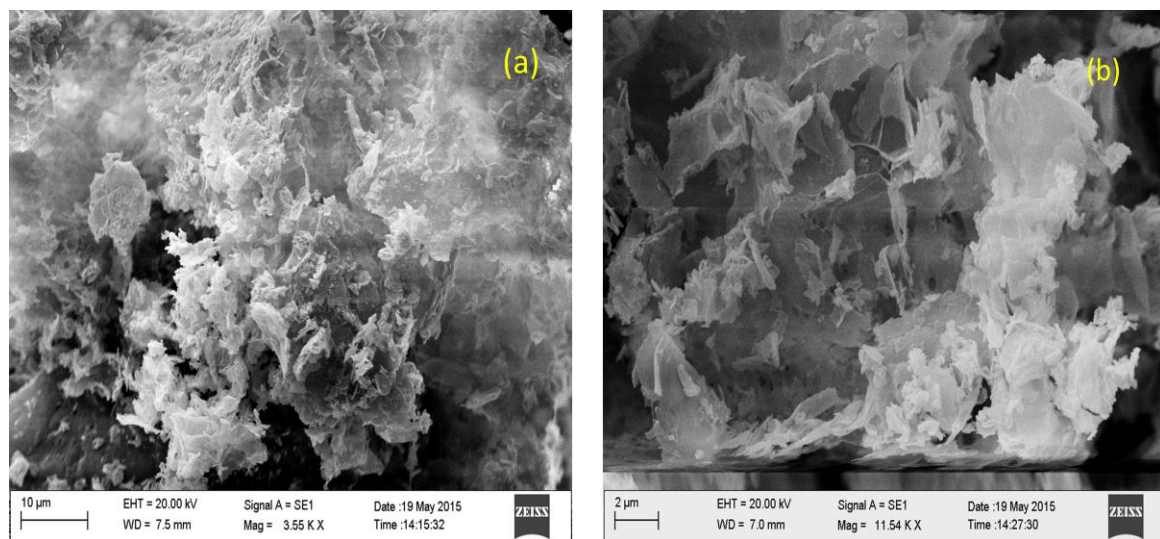


Fig.4.33 SEM images of (a) CeO_2 and (b) $Ce_{0.85}In_{0.15}O_2$ compounds sintered at 600 °C.

4.5.5 $\text{MgFe}_{2-x}\text{In}_x\text{O}_4$

Fig. 4.34 represents the SEM images for $\text{MgFe}_{2-x}\text{In}_x\text{O}_4$ compounds. The spherical nature is very much clear from the images. The particles also are formed in nano-range and are homogenously distributed. The agglomeration is seen in all the images owing to the magnetic nature of the compounds.

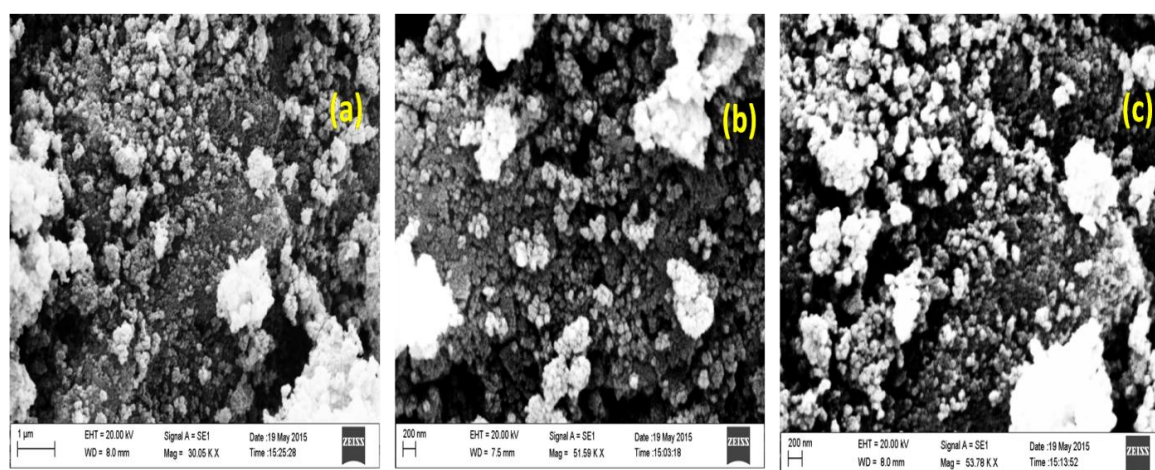


Fig.4.34 SEM images of (a) MgFe_2O_4 (b) $\text{MgFe}_{1.96}\text{In}_{0.04}\text{O}_4$ (c) $\text{MgFe}_{1.80}\text{In}_{0.20}\text{O}_4$ compounds sintered at 600 °C.

4.6 Transmission Electron Microscopy

4.6.1 $\text{In}_{2-x}\text{Co}_x\text{O}_3$

The transmission electron micrographs for pristine and $\text{In}_{2-x}\text{Co}_x\text{O}_3$ are shown in Fig. 4.35. Individual particles can be very well identified where their spherical nature is revealed. The particle size ranges in 15 - 25 nm as observed in all the micrographs thus confirming the formation of nanoparticles. TEM images are also accompanied by ED pattern which consist of concentric rings made up of continuous points. These rings correspond to the respective peaks that are observed in XRD with specific d values. The rings are indexed with respective *hkl* values.

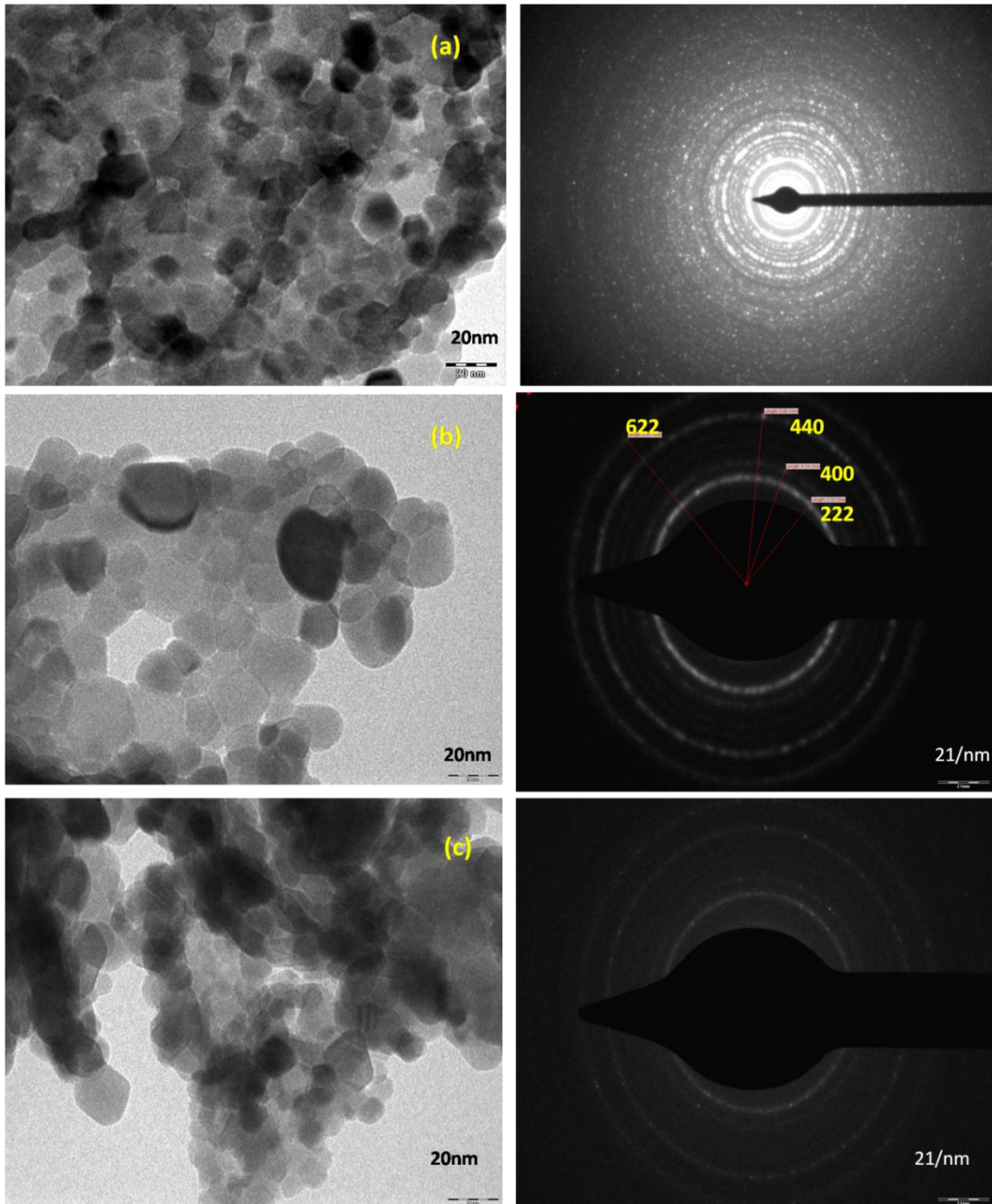


Fig.4.35 TEM images and corresponding ED patterns of (a) In_2O_3 (b) $In_{1.88}Co_{0.12}O_3$ (c) $In_{1.80}Co_{0.20}O_3$ compounds sintered at 500 °C.

4.6.2 $In_{2-x}Cr_xO_3$

Fig. 4.36 represents the TEM images of $In_{2-x}Cr_xO_3$ compounds. The average particle size obtained is found to be in the range of 10-20 nm. The particles are spherical

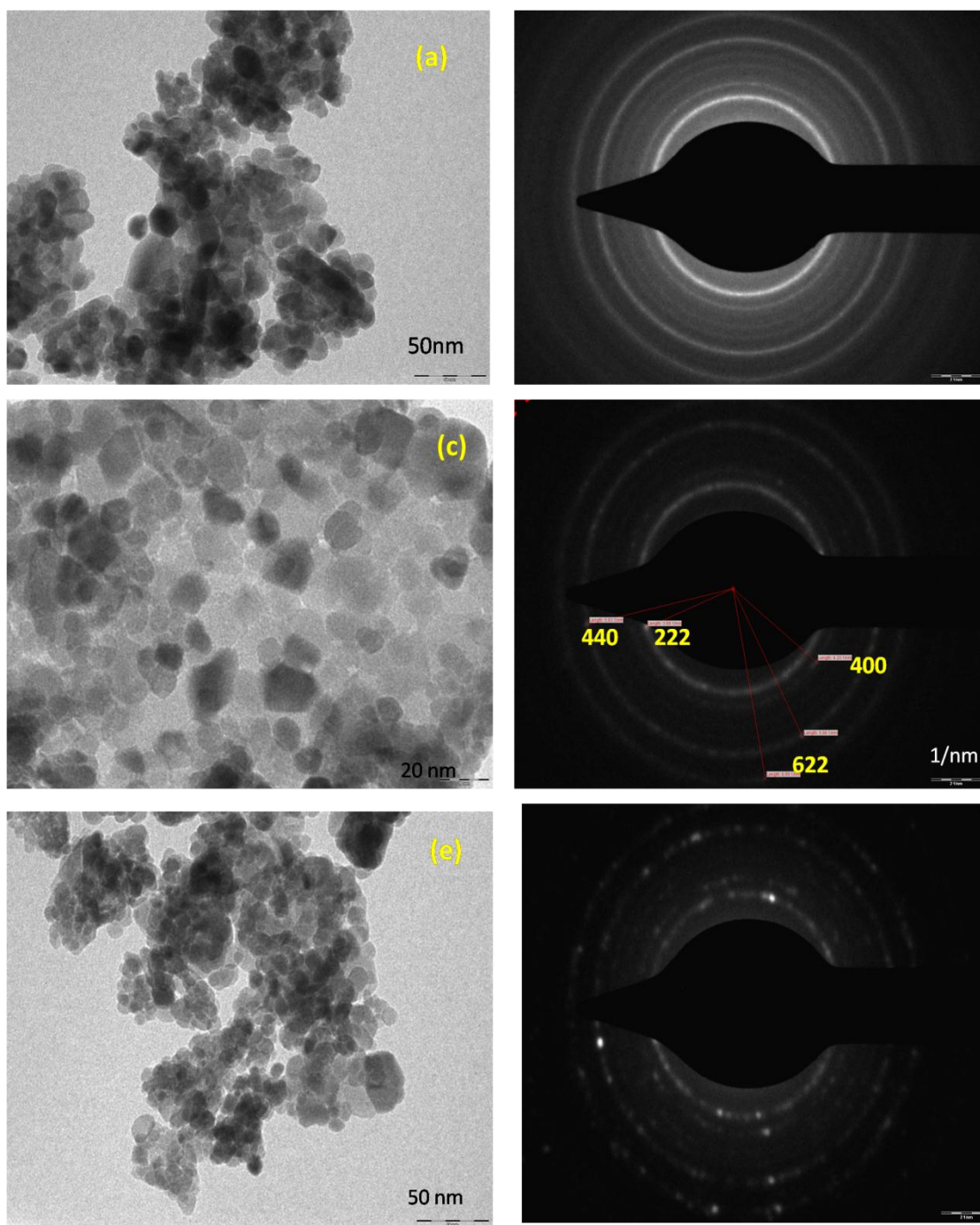


Fig.4.36 TEM images and corresponding ED patterns of (a) $In_{1.94}Cr_{0.06}O_3$ (b) $In_{1.92}Cr_{0.08}O_3$ (c) $In_{1.90}Co_{0.10}O_3$ compounds sintered at 500 °C.

andhomogenous in nature. The ED pattern shows the well distinct concentric rings representing each peak observed in XRD. It is observed that as the concentration of Cr increases the points forming the concentric rings are more scattered. This might be due the reduction in the size of the nanoparticles on doping. The ED pattern is indexed

with corresponding hkl values which perfectly match the cubic bixbyte structure of In_2O_3 , thus confirms the formation of Cr substituted compound.

4.6.3 $\text{In}_{2-x}\text{Ag}_x\text{O}_3$

The TEM image for $\text{In}_{1.96}\text{Ag}_{0.02}\text{O}_3$ compound presented in Fig. 4.37 shows spherical nature of the particles. Considering the larger ionic size of Ag compared to In, its incorporation expands the lattice parameter as explained in XRD and this effect is consistently observed for particle size as well. The particle size observed here is larger than 20 nm. Particles appear to be slightly agglomerated in nature.

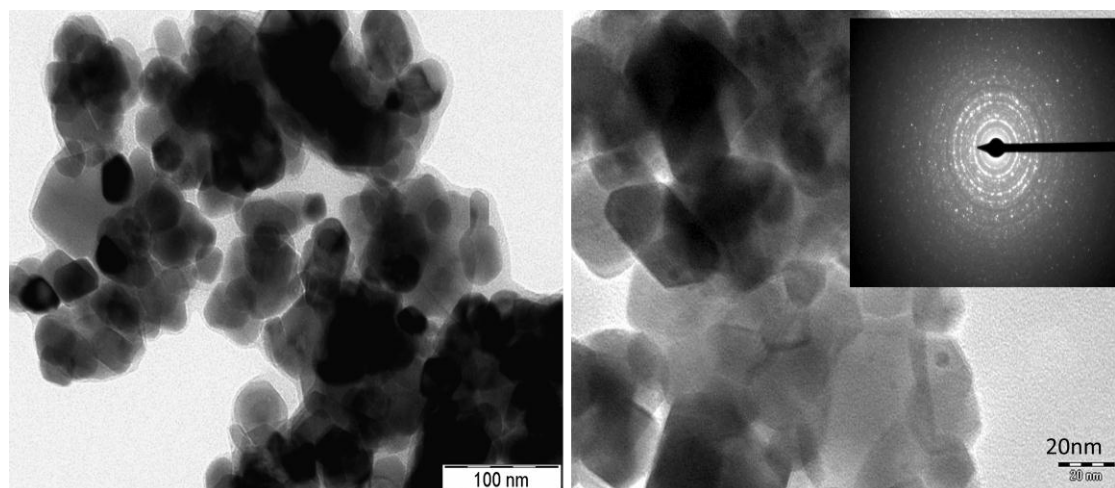


Fig.4.37 TEM images with different resolutions and corresponding ED pattern for $\text{In}_{1.96}\text{Ag}_{0.02}\text{O}_3$ compound sintered at 600 °C.

4.6.4 $\text{Ce}_{1-x}\text{In}_x\text{O}_2$

Fig. 4.38 displays the TEM images for $\text{Ce}_{1-x}\text{In}_x\text{O}_2$ compounds. Well resolved particles with spherical morphology are obtained. A systematic arrangement of particles is seen where no agglomeration could be noticed. Average particle size obtained for pristine is less than 20 nm which is even more reduced on doping with indium. The corresponding ED patterns are indexed with hkl values that perfectly match with that of XRD.

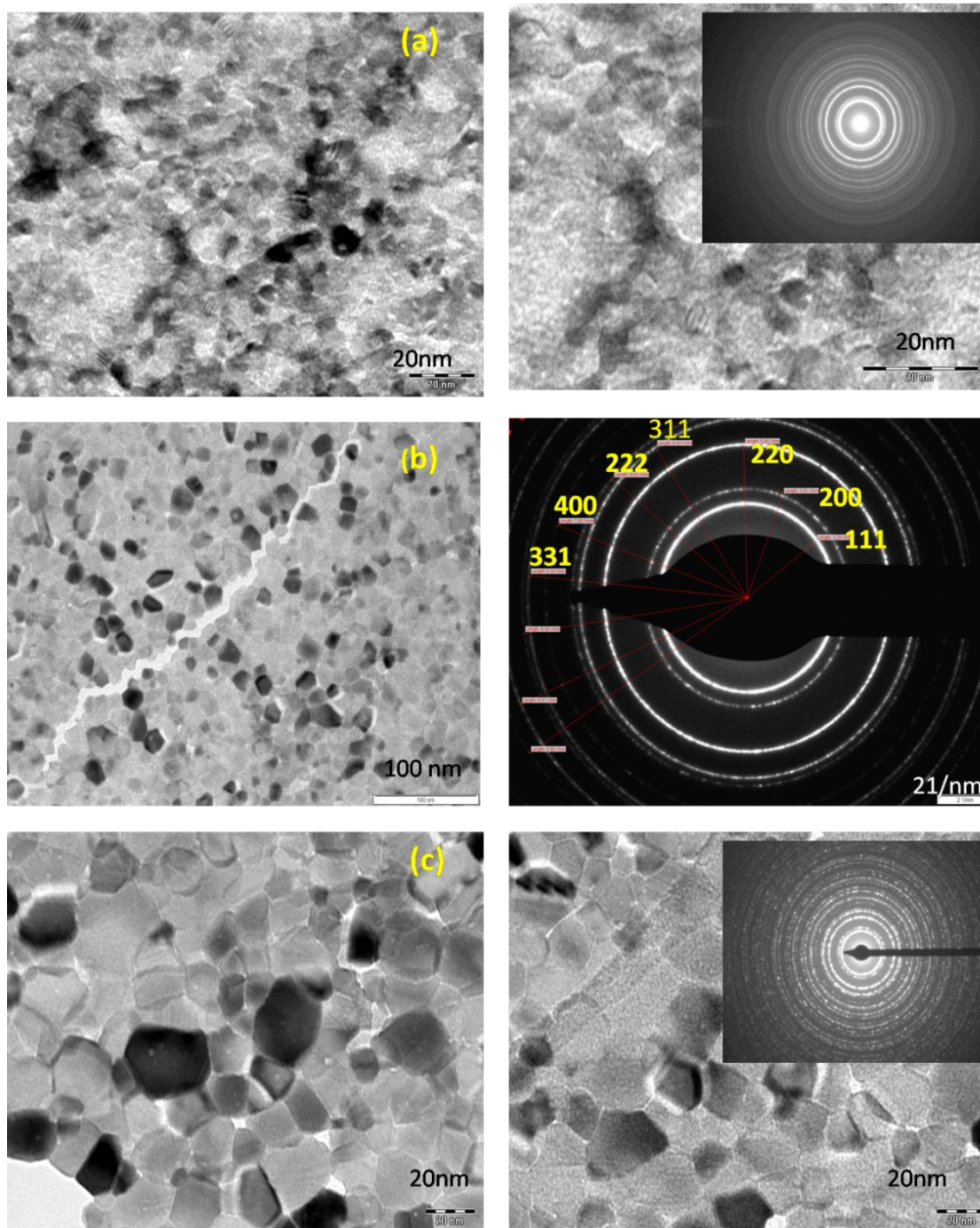


Fig.4.38 TEM images and corresponding ED patterns of (a) CeO_2 (b) $Ce_{0.94}In_{0.06}O_2$ (c) $Ce_{0.90}In_{0.15}O_2$ compounds sintered at 600 °C.

4.6.5 $MgFe_{2-x}In_xO_4$

TEM images for $MgFe_{1-x}In_xO_4$ compounds are shown in Fig. 4.39 respectively; it confirmed the nano-particulate size of the prepared samples. The particle size ranges between 15-30 nm. The agglomeration of particles is seen for all the samples owing to its

magnetic nature. ED pattern is also displayed where the concentric rings are indexed with the corresponding hkl values. The hkl values are matched with the peaks observed in XRD.

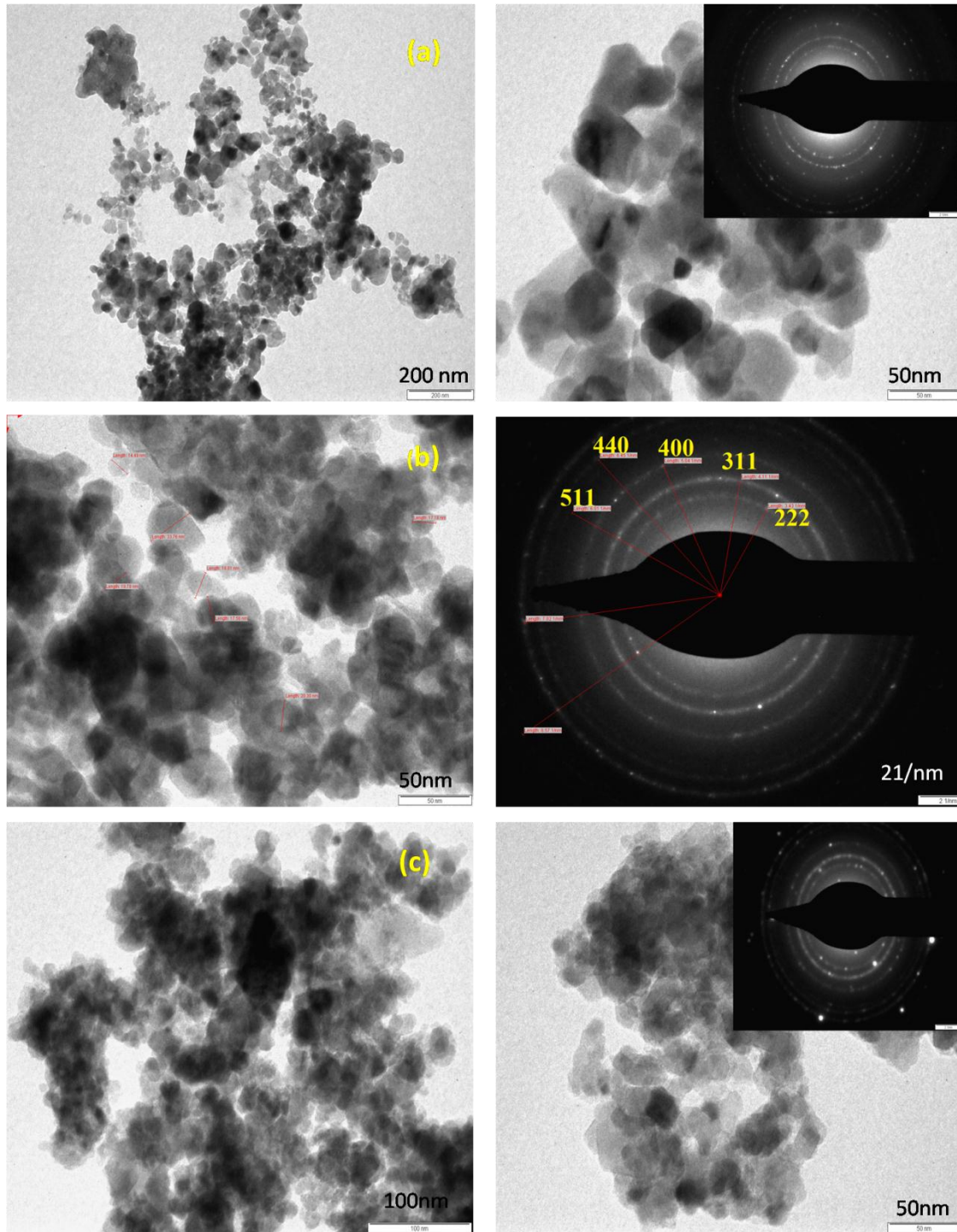


Fig.4.39 TEM images and corresponding ED patterns of (a) $MgFe_2O_4$ (b) $MgFe_{1.92}In_{0.08}O_4$ (c) $MgFe_{1.80}In_{0.20}O_4$ compounds sintered at 600 °C.

4.7 X-ray Photoelectron Spectroscopy

XPS analysis was carried out to investigate presence of the elements and to determine their exact oxidation states. Charging correction for carbon is carried out for all the spectral data. The individual elemental spectra are deconvoluted using XPS peak fitting software.

4.7.1 In_2O_3

The XPS analysis spectra for pristine In_2O_3 , calcined at $500\text{ }^\circ\text{C}$ are presented in Fig.4.40. The full scan spectrum validates the presence of indium and oxygen species. The In 3d core spectra shows two peaks at 444.1 and 451.3 eV corresponding to $\text{In}3d_{5/2}$ and $\text{In}3d_{3/2}$ states respectively confirming its existence in +3 oxidation state. These values are in accordance with those reported in the literature [341,342].

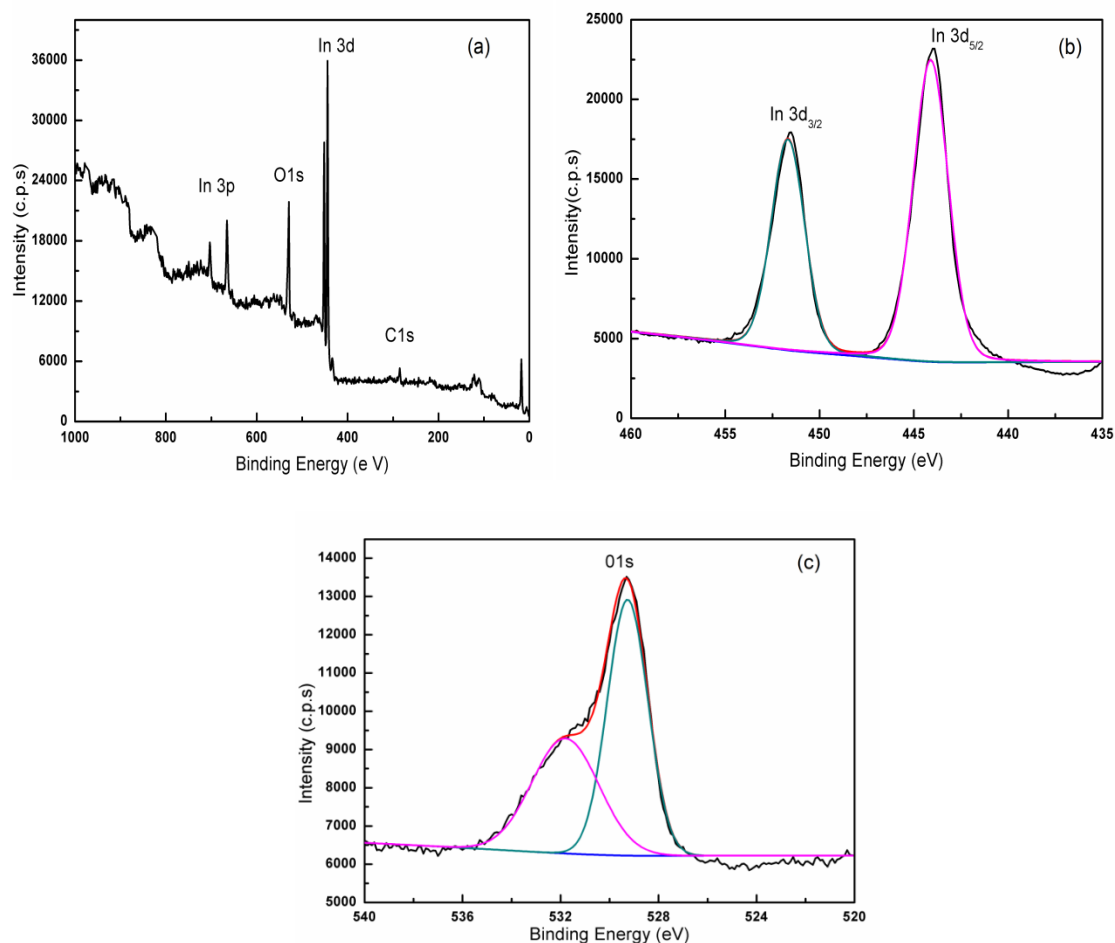


Fig.4.40 XPS plots for pristine In_2O_3 showing (a) full scan (b) In 3d (c) O 1s peaks.

The O1s fitting spectra shows two peaks at 529.3 and 531.8 eV , the former can be assigned to the In-O bonded lattice oxygen whereas latter could be originating from the vacancy induced environment of oxygen. No other major elemental peak could be indexed which confirms the purity of sample.

4.7.2 $\text{In}_{1.88}\text{Co}_{0.12}\text{O}_3$

The X-ray photoelectron spectra for $\text{In}_{1.88}\text{Co}_{0.12}\text{O}_3$ are presented in Fig.4.41. The peaks corresponding to O1s, In 3d, In 3p and Co 2p are observed in full scan confirming the existence of these elements in the system. XPS spectra shows peak for In 3d_{5/2} at 443.1eV and In 3d_{3/2} at 450.7 eV. The observed values are slightly blue shifted

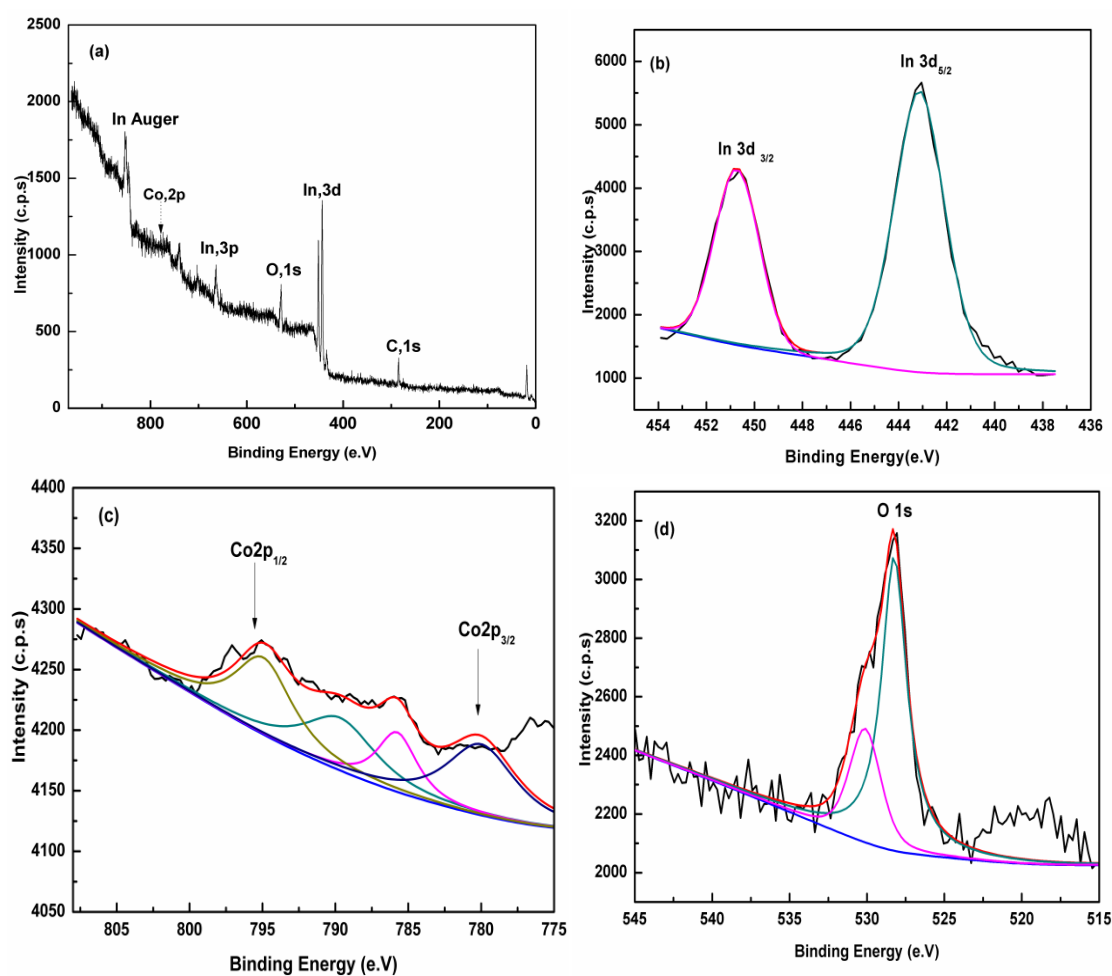


Fig. 4.41 XPS plots for $\text{In}_{1.88}\text{Co}_{0.12}\text{O}_3$ showing (a) full scan (b) In 3d (c) Co2p and (d) O1s peaks.

compared to that obtained for pristine as discussed in previous spectra and also to thereported for bulk In_2O_3 in literature. The fitted spectrum for O 1s shows two peaks. A distinct peak at 528.3 eV corresponding to the oxygen bond of In–O–In and other at 530.1 eV originating from the oxygen defects in the lattice of metal oxide are observed [343]. The observed binding energy for Co $2p_{1/2}$ is 795.6 eV and for Co $2p_{3/2}$ is 780.8 eV with the corresponding satellite peaks seen at 789.4 and 785.6 eV respectively validating the high spin divalent state of Co^{2+} [344].

4.7.3 $\text{In}_{1.70}\text{Co}_{0.20}\text{O}_3$

For the same dopant cobalt with higher concentration i.e. $\text{In}_{1.70}\text{Co}_{0.30}\text{O}_3$, XPS plots are presented in Fig. 4.42 where the full scan shows the presence of In, Co and O elements. The core spectra for In 3d shows peaks at 443.8 and 451.4 eV for $3d_{5/2}$ and

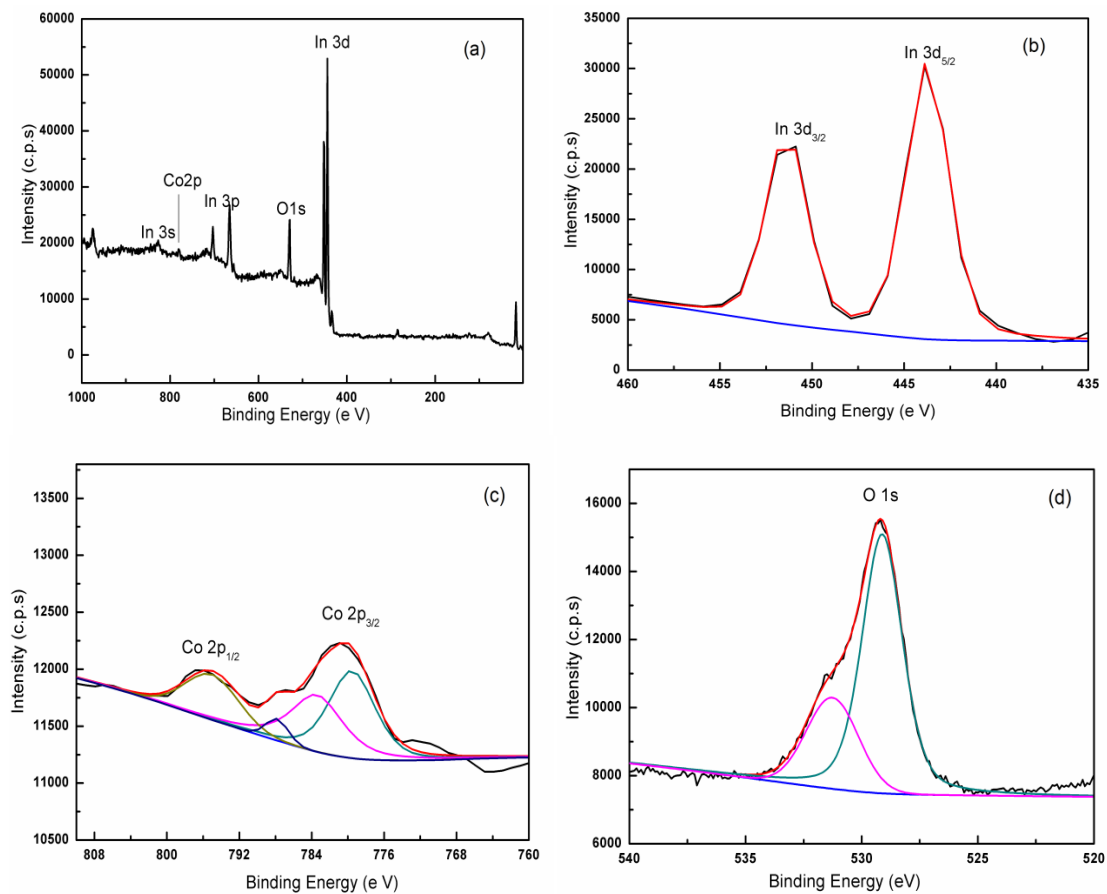


Fig.4.42 XPS plots for $\text{In}_{1.70}\text{Co}_{0.20}\text{O}_3$ showing (a) full scan (b) In 3d (c) Co2p and (d) O1s peaks

3d_{3/2} states. The Co 2p spectrum shows well resolved peaks for this sample owing to its higher concentration. The 2p_{3/2} and 2p_{1/2} peaks are observed at 780.4 and 795.6 eV along with their satellite peaks at 783.6 and 788.2 eV respectively. The O1s spectrum represents a similar splitting of the peaks as observed for earlier, here the peak originating from In – O lattice bonds is at observed 529.1 eV whereas the one present at 531.3 eV can be assigned to oxygen defects. The presence of trivalent indium (In³⁺) and divalent cobalt (Co²⁺) is confirmed from the observed spectra.

4.7.4 In_{1.90}Cr_{0.10}O₃

Fig.4.43 displays XPS plots for In_{1.90}Cr_{0.10}O₃ nanoparticles. The full scan shows the presence of In, Cr and O peaks. Spectrum for In 3d shows peak for In 3d_{5/2} at 443.5 eV and In 3d_{3/2} at 451.0 eV. The peak for Cr 2p_{1/2} and Cr 2p_{3/2} are observed at 586.5 eV

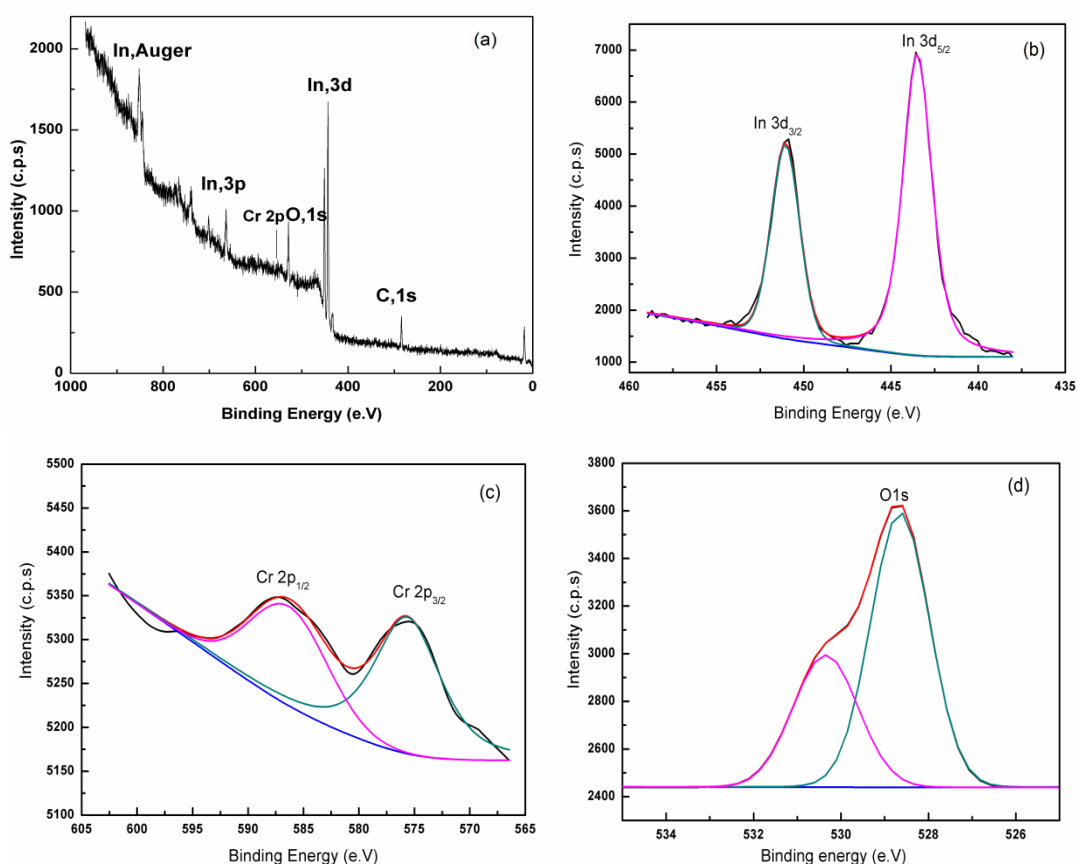


Fig.4.43 XPS plots for In_{1.90}Cr_{0.10}O₃ showing (a) full scan (b) In3d (c) Cr2p and (d) O1s peaks.

and 575.9 eV respectively. These peaks can be assigned to Cr^{3+} [345], the peak for $2p_{3/2}$ is slightly shifted in the lower energy region than expected value [346]. The presence of any other oxidation state is ruled out as only two peaks were obtained after deconvolution. The fitting of O1s spectrum shows two distinct peaks at 528.6 and 530.3 eV respectively. The former is due to the presence of oxygen bond In-O-In as shown in case of Co doped sample whereas the latter is originating from the non stoichiometric oxide.

4.7.5 $\text{In}_{1.96}\text{Ag}_{0.04}\text{O}_3$

The XPS analysis of $\text{In}_{1.96}\text{Ag}_{0.04}\text{O}_3$ nanoparticles validates the presence of In, Ag and O peaks in the full scan spectrum as shown in Fig 4.44 (a). The 3d peaks for indium are observed at 443.3 and 451.0 eV corresponding to $3d_{5/2}$ and $3d_{3/2}$ respectively

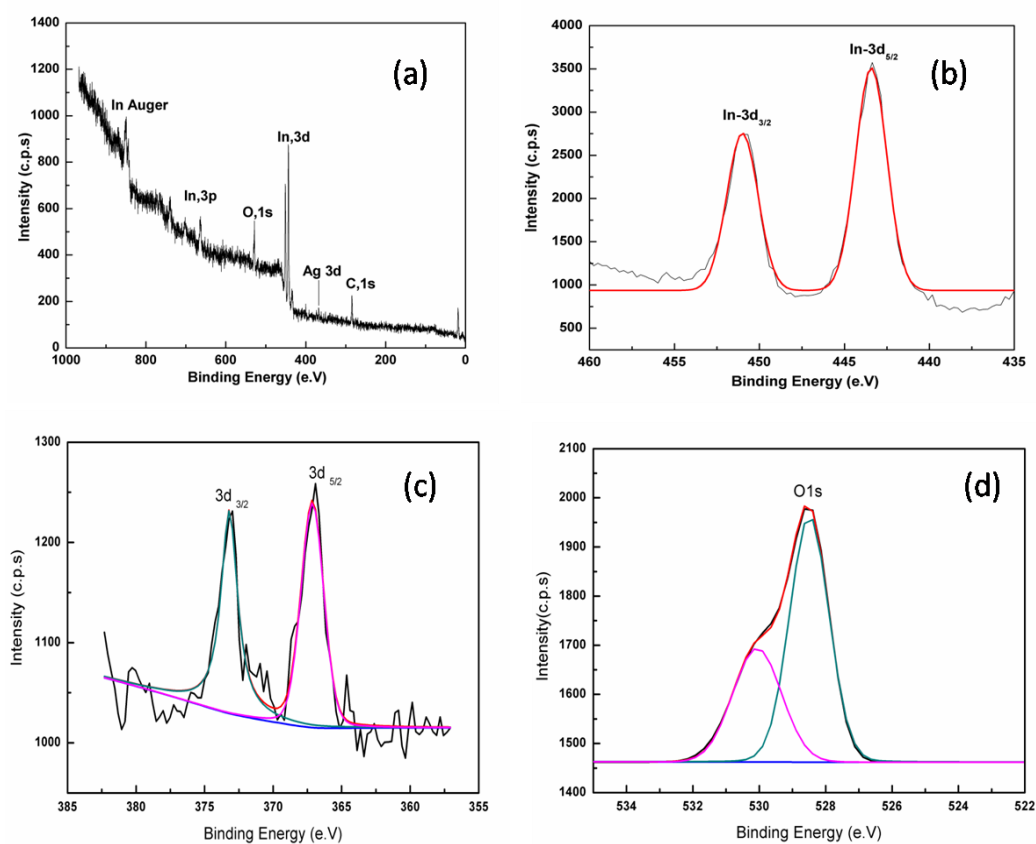


Fig. 4.44 XPS spectra of $\text{In}_{1.96}\text{Ag}_{0.04}\text{O}_3$ (a) Full Scan (b) In 3d (c) Ag 3d (d) O1s.

confirming the oxidation state as In^{3+} . The spectra for silver shows two distinct peaks at 367.11 for $3d_{5/2}$ and 373.19 for $3d_{3/2}$ which are shifted to the lower energy compared to the values obtained for bulk metallic silver at 368.3 eV for $\text{Ag } 3d_{5/2}$ and 374.3 eV for $\text{Ag } 3d_{3/2}$ [347, 348]. This suggests that silver is present in univalent oxidation state having low binding energy. The O1s peak is split into two, the lower binding energy peak at 528.4 eV corresponds O^{2-} ion present as In-O bond in crystal lattice whereas the peak at 530.3 eV could be related to oxygen defect.

4.7.6 $\text{Ce}_{0.90}\text{In}_{0.10}\text{O}_2$

The XPS for $\text{Ce}_{0.90}\text{In}_{0.10}\text{O}_2$ has been displayed in Fig. 4.45. The full scan confirms the presence of chemical species such as Ce, In and O. The fitted spectrum for Ce shows

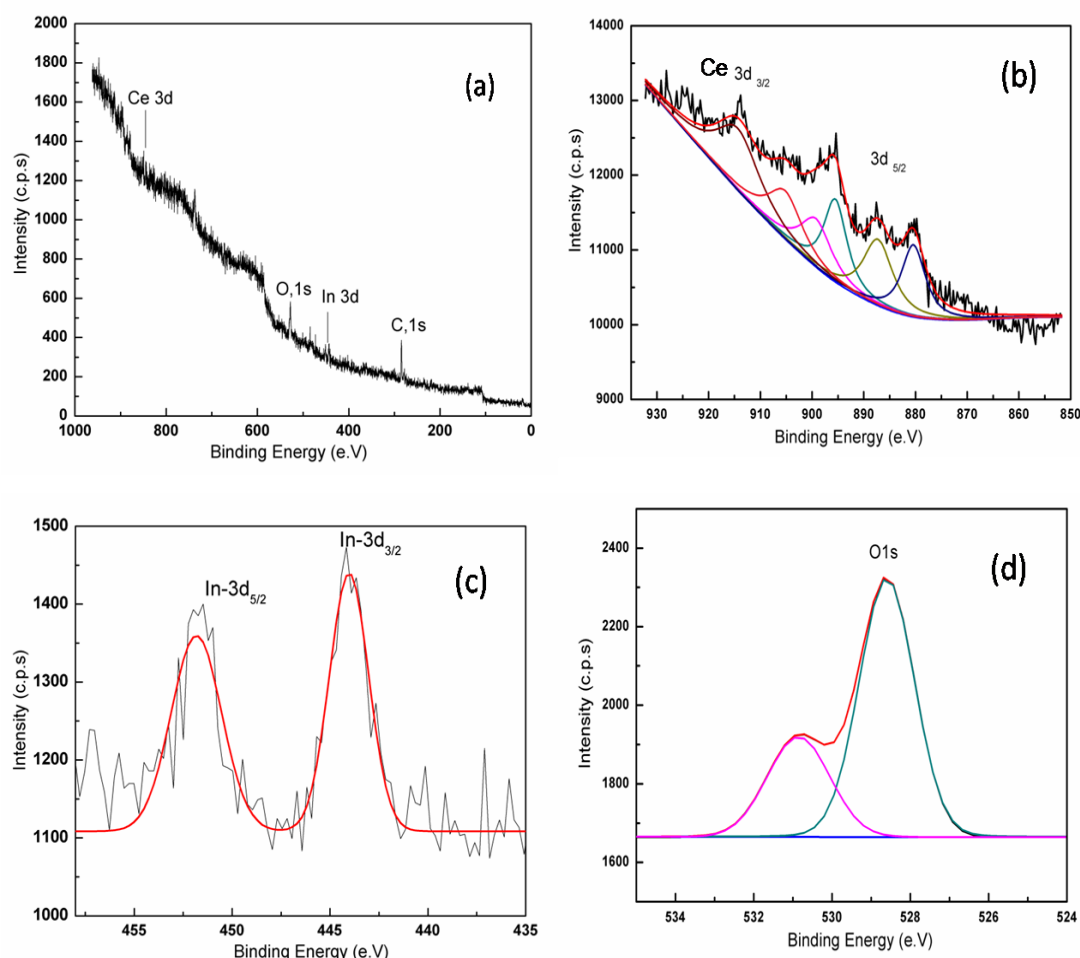


Fig.4.45 XPS plots of $\text{Ce}_{1.90}\text{In}_{0.10}\text{O}_2$ (a) Full scan (b) Ce3d (c) In3d (d) O1s.

total six peaks for $3d_{3/2}$ and $3d_{5/2}$ components. The peak values observed are as follows 881.24, 887.41, 895.70, 899.61, 905.78 and 915.2 eV [349, 350]. These peaks suggest the major oxidation state present is Ce^{4+} , whereas slight presence of Ce^{3+} is also noticed. This is basically due to the replacement of Ce^{4+} by In^{3+} ions which alter the oxygen content thereby converting some Ce^{4+} to Ce^{3+} . This defect structure plays a very important role in governing the magnetic properties of the samples [351]. The indium core spectra confirmed its +3 oxidation state where $In3d_{5/2}$ peaks observed at 443.99 and $In 3d_{3/2}$ at 451.70 eV. The O1s peak shows a prominent splitting where a peak at 528.63 eV is owing to the Ce-O bond in the lattice whereas the peak at 530.90 can be originating from oxygen deficient condition. The spectra confirmed the defect structure of $Ce_{0.90}In_{0.10}O_2$ nanoparticles.

4.7.7 $MgFe_2O_4$

The oxidation state plays a vital role in determining the number of unpaired electrons which governs the properties of these materials especially magnetic properties. The X-ray photoelectron spectra for pristine $MgFe_2O_4$ are shown in Fig. 4.46. The spectra confirm the presence of Fe, O and Mg elements in the compound. The Mg 1s spectrum shows a peak at 1303.2 eV, the Fe 2p fitted spectrum shows two major peaks at 711.2 eV and 725.3 eV corresponding to $2p_{3/2}$ and $2p_{1/2}$ states respectively with a satellite peak at 719.1 eV which is 0.8 eV above the main peak confirming the presence of Fe in +3 oxidation state. [341,352,353]. The Mg 2p peak is obtained at 48.6 eV and Fe 3p peak at 55.6 eV. The O1s peak is observed at 529.6 eV with a small hump at 531.3 eV. The former peak is known to originate from lattice oxygen bond whereas the latter one obtained at higher energy is identified to be associated with the oxygen defects in the lattice [354].

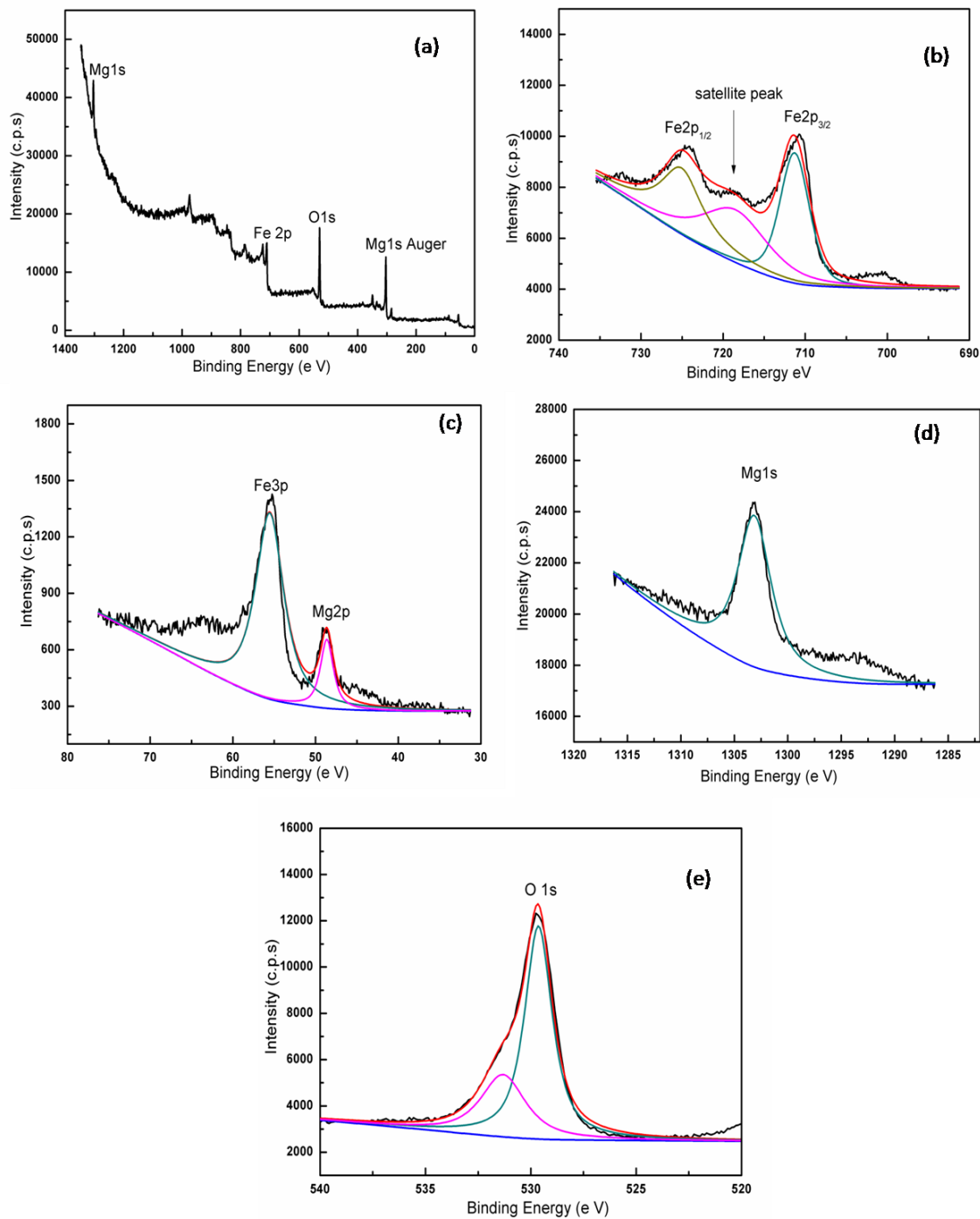


Fig. 4.46 XPS plots of MgFe_2O_4 (a) Full scan (b) $\text{Fe}2p$ (c) $\text{Fe}3p$ and $\text{Mg} 2p$ (d) $\text{Mg}1s$ and (e) $\text{O}1s$.

4.7.8 $\text{MgFe}_{1.96}\text{In}_{0.04}\text{O}_4$

The XPS spectra for $\text{MgFe}_{1.96}\text{In}_{0.04}\text{O}_4$ nanoparticles are displayed in Fig.4.47. The full scan plot substantiates the presence of the elements Mg, Fe, In and O. The prominent

indium peak which was absent in the full scan of pristine compound is well resolved in the doped sample confirming its presence. The core spectrum for Fe 2p depicts two distinct peaks at 711.1 eV and 724.7 eV corresponding to Fe 2p_{3/2} and Fe 2p_{1/2} respectively suggesting the valence state of iron to be Fe³⁺ and not Fe²⁺, this is further confirmed by the presence of a satellite peak of Fe 2p_{3/2} at around 718.0 eV, above the

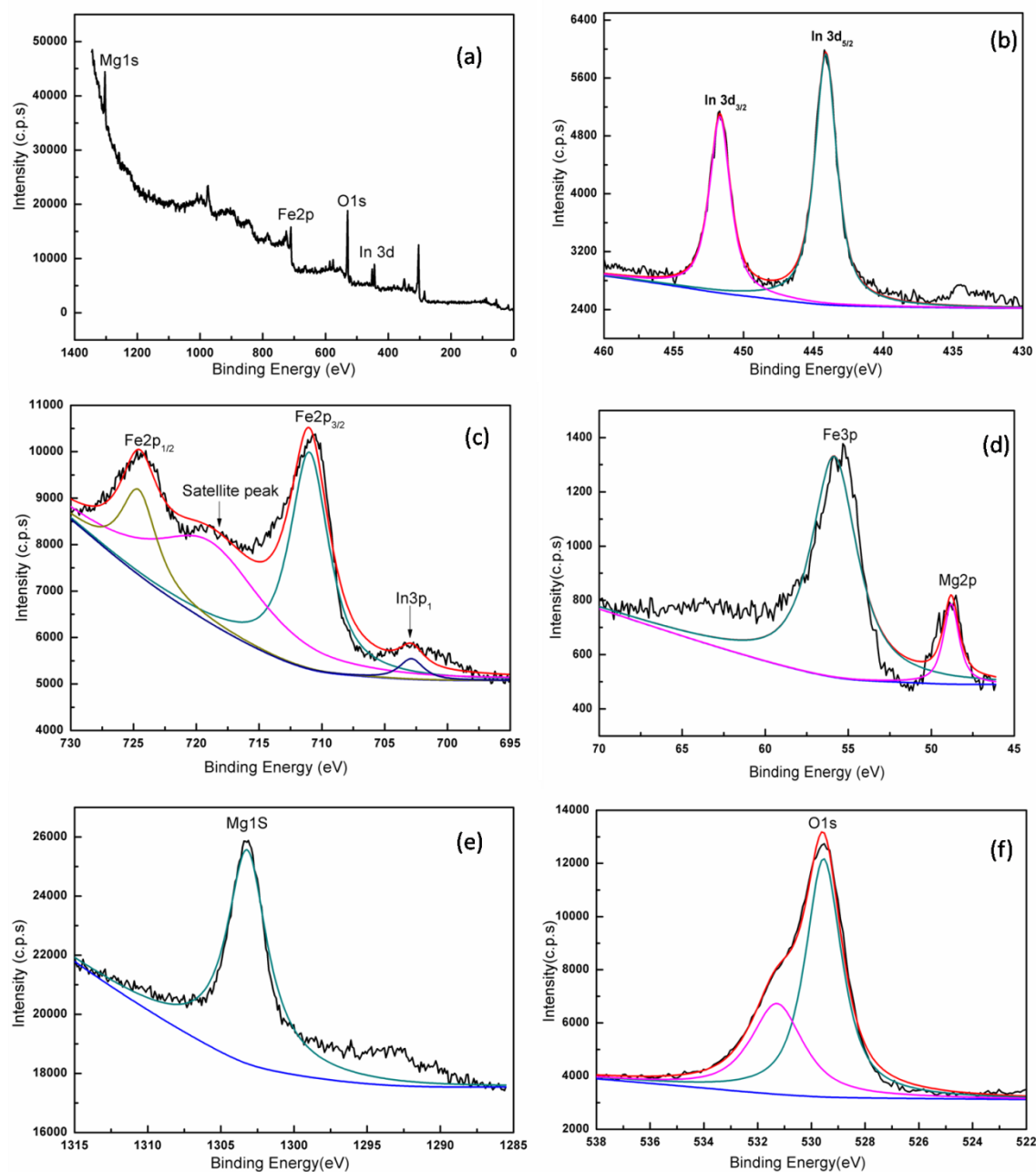


Fig. 4.47 XPS plots of $MgFe_{1.96}In_{0.04}O_4$ (a) Full scan (b) In3d (c) Fe2p (d) Fe3p and Mg 2p (e) Mg1s and (f) O1s.

main peak In 3d spectrum shows two peaks located at 444.1 and 451.6 eV, which are attributed to the characteristic spin-orbit split $3d_{5/2}$ and $3d_{3/2}$ respectively, confirming the valence state of indium to be +3. The Mg 1s peak is observed at 1303.2 eV as expected for $MgFe_2O_4$ where Mg is in +2 oxidation state. These are also substantiated by the presence of Mg 2p and Fe 3p peaks. Here it is much clear that the magnetism arising from these nanoparticles clearly depends on oxidation state of iron and the occupancies of the different cations. The O1s fitting spectra shows the splitting of the 1s peak into two, the peak observed at around 529.5 eV corresponds to the lattice oxygen whereas the one at 531.5 eV is owing to the presence of oxygen defects [341,352-354].

4.8 Mössbauer spectroscopy

4.8.1 $MgFe_{2-x}In_xO_4$

Mössbauer is an important technique that can determine the super-paramagnetic relaxation in magnetic nanoparticles. Fig. 4.48 displays the room temperature Mössbauer spectra for pristine, $MgFe_{1.96}In_{0.04}O_4$ and $MgFe_{1.92}In_{0.08}O_4$ compositions.

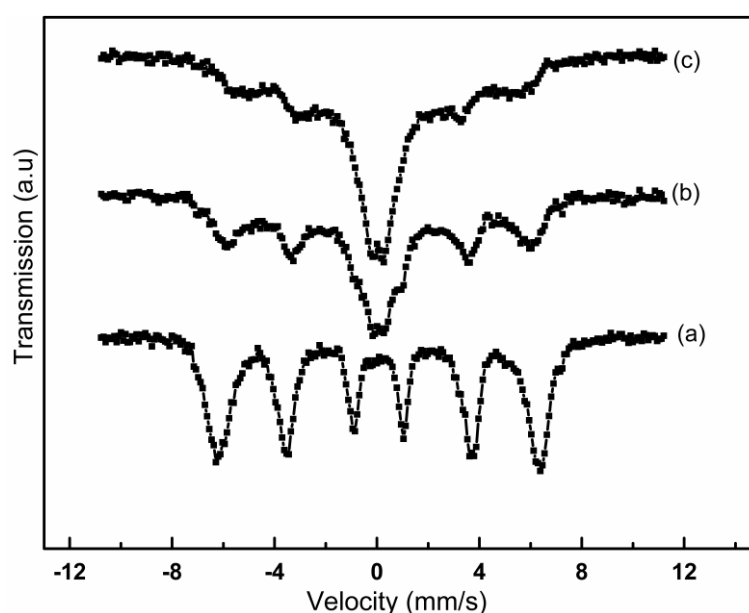


Fig.4.48 Mössbauer spectra for (a) $MgFe_2O_4$ (b) $MgFe_{1.96}In_{0.04}O_4$ (c) $MgFe_{1.92}In_{0.08}O_4$.

The pristine compound shows appearance of a sextet confirming the presence of magnetic iron which on doping, is found to reduce in intensity, thereby making appearance of doublet noticeable as observed for $\text{MgFe}_{1.96}\text{In}_{0.04}\text{O}_4$. Further increase in In content makes the doublet prominent as observed for $\text{MgFe}_{1.92}\text{In}_{0.08}\text{O}_4$ composition. Eventually the relative area of a paramagnetic doublet is found to increase at the expense of magnetic sextets in the doped samples. This clearly suggests the presence of super-paramagnetic relaxation in the doped nanoparticles.

4.9 Electrical Resistivity

4.9.1 $\text{In}_{2-x}\text{Co}_x\text{O}_3$

Stoichiometric In_2O_3 shows high resistivity ($\sim 10^8 \Omega\text{cm}$) behaving as a typical insulator with a low free carrier concentration [355]. However, non-stoichiometric indium oxide nano-particles have high free carrier concentration due to oxygen deficiency; here the electrical conductivity arises from these oxygen vacancies which act as donors of electrons to the conduction band. Fig.4.49 shows the effect of temperature and Co doping

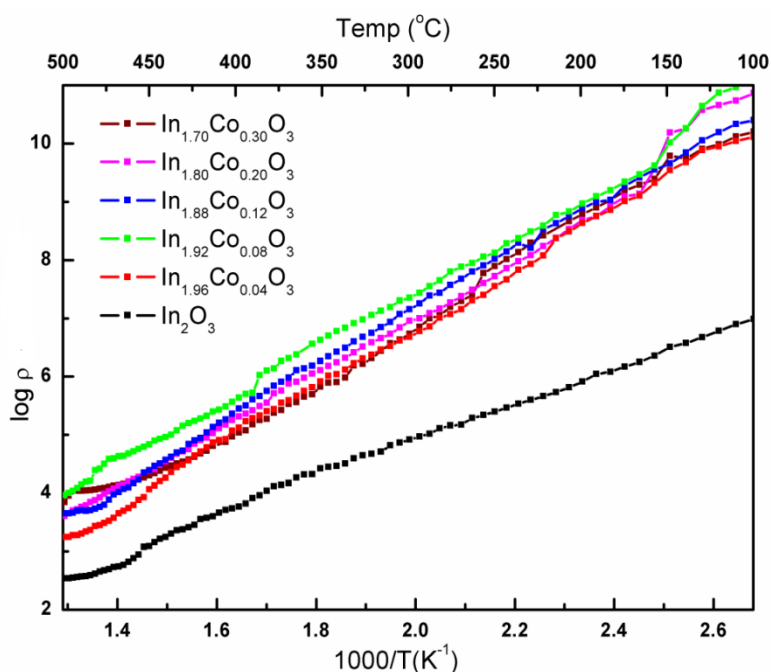


Fig. 4.49 Plots of log resistivity v/s $1000/T$ for $\text{In}_{2-x}\text{Co}_x\text{O}_3$ compounds sintered at $500\text{ }^\circ\text{C}$.

on the electrical resistivity of the In_2O_3 nano-particles. All the samples show a typical semiconducting behaviour as a function of temperature. At the same time, it is astonishing to note that the resistivity increases with Co doping which is due to the formation of p-type defects. The porous nature of the samples as evident from the SEM measurements also contributes to the additional increase in resistivity. In doped In_2O_3 nano-particles, oxygen vacancies and interstitial In^{3+} ions are donors, whereas, interstitial oxygen and indium vacancies along with the doped Co^{2+} ions, acts as acceptors [86]. Thus, the electrons which act as charge carriers in the present case are compensated by the holes generated by acceptors such as Co^{2+} thereby increasing the resistivity.

4.9.2 $\text{In}_{2-x}\text{Cr}_x\text{O}_3$

The plots of log resistivity v/s $1000/T$ for $\text{In}_{2-x}\text{Cr}_x\text{O}_3$ compounds are shown in Fig.4.50. It shows a semiconducting behaviour where a steady decrease in resistivity is

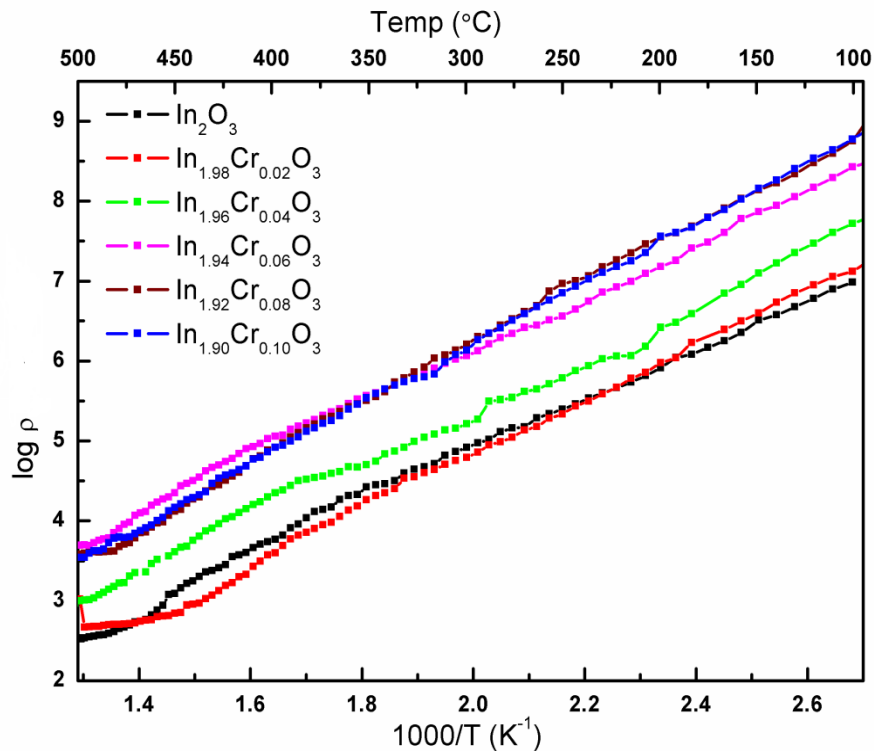


Fig. 4.50 Plots of log resistivity v/s $1000/T$ for $\text{In}_{2-x}\text{Cr}_x\text{O}_3$ compounds sintered at 500 °C.

observed with increase in temperature. Compared to pristine In_2O_3 , doped samples shows more resistance to the flow of electrons. Resistivity is found to increase as the concentration of Cr content increases. This also follows the same trend, where the dopant results in the formation of p-type defects. Thus the compensation of holes and electrons eventually results in increasing resistivity compared to that of pristine.

4.9.3 $\text{In}_{2-x}\text{Ag}_x\text{O}_3$

The resistivity studies for Ag doped In_2O_3 nanoparticles are presented in Fig. 4.51. The resistivity is found to decrease with increase in temperature thus fulfilling the semiconductor behaviour. The incorporation of dopant further decreases the resistivity. As a dopant, Ag^+ ions create a charge imbalance in the system. The mobility of charge carriers is reduced in case of doped samples. The probable reason here could be the electron hole recombination as the band gap is reduced on doping owing to the increase particle size. This ultimately results in increasing the resistivity of the samples.

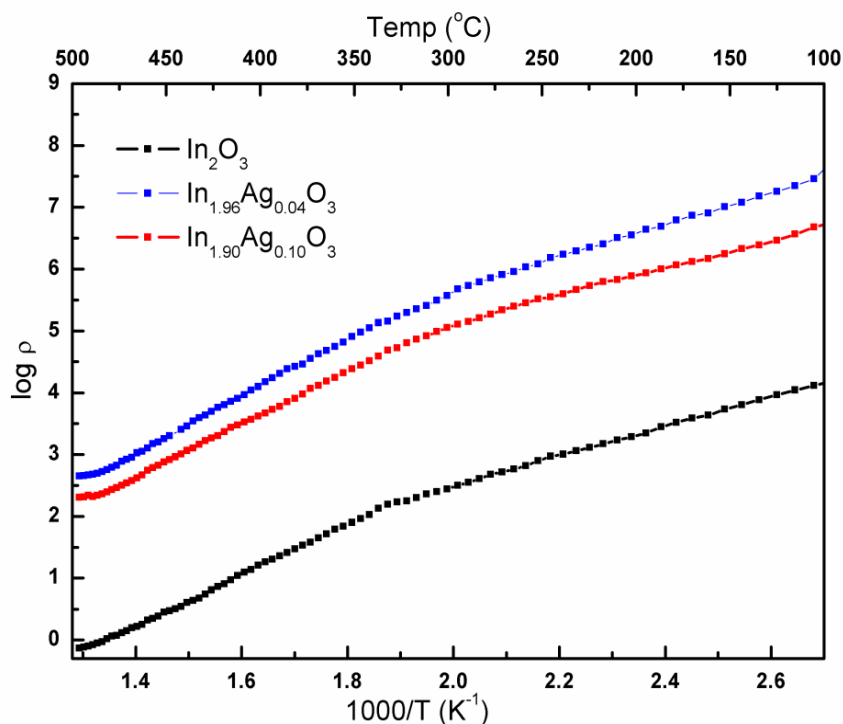


Fig. 4.51 Plots of \log resistivity v/s $1000/T$ for $\text{In}_{2-x}\text{Ag}_x\text{O}_3$ compounds sintered at 600 °C.

4.9.4 $\text{Ce}_{1-x}\text{In}_x\text{O}_2$

Pristine CeO_2 nanoparticles display unique properties owing to its existence as $\text{Ce}^{4+}/\text{Ce}^{3+}$ redox system. The change in oxidation state is compromised by presence of oxygen vacancies. When In^{3+} is incorporated in CeO_2 , the oxygen vacancies are expected to be enhanced thereby influencing its properties. The electrical resistivity measurements of these compounds with respect to temperature are displayed in Fig.4.52. All the compounds are semiconducting in nature. It is interesting to note that the resistivity decreases with increase in In^{3+} content. All the compounds exhibit a common profile, where a slow decrease in resistivity is observed at lower temperature region which decreases abruptly with further increase in temperature. Here the initial decrease represents the extrinsic behaviour whereas latter is due to intrinsic property of a semiconductor.

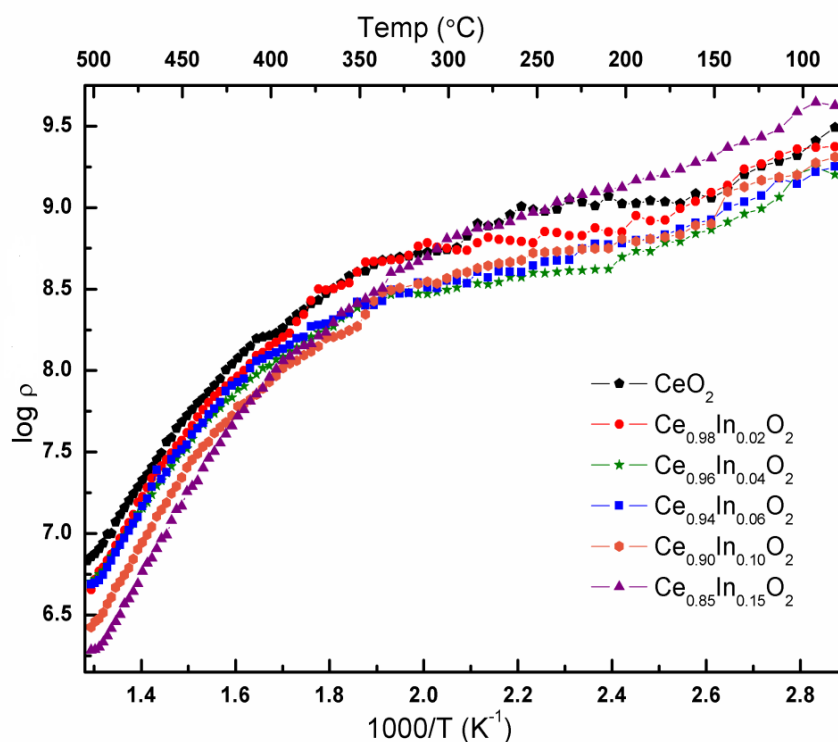


Fig. 4.52 Plots of \log resistivity v/s $1000/T$ for $\text{In}_{2-x}\text{Ag}_x\text{O}_3$ compounds sintered at 600°C .

4.9.5 $\text{MgFe}_{2-x}\text{In}_x\text{O}_4$

The electrical resistivity studies for pristine and In doped MgFe_2O_4 compounds are displayed in Fig. 4.53. All the compounds show a steady decrease in resistivity at the initial stage due to extrinsic contribution, which then displays a steep fall at higher temperature region which is attributed to the intrinsic property of the compounds. These plots display a semiconducting nature of the samples. In case of ferrite material the electrical conductivity is attributed to the hopping of electrons between Fe^{3+} and Fe^{2+} states [356]. Here it is observed that on in the higher temperature region the resistivity of the doped samples is higher than that of pristine ferrite. This could be owing to the replacement of iron which can transit between 3+ and 2+ oxidation states by a stable In^{3+} state. The increase in resistance is also favoured by reduced crystallite size on doping.

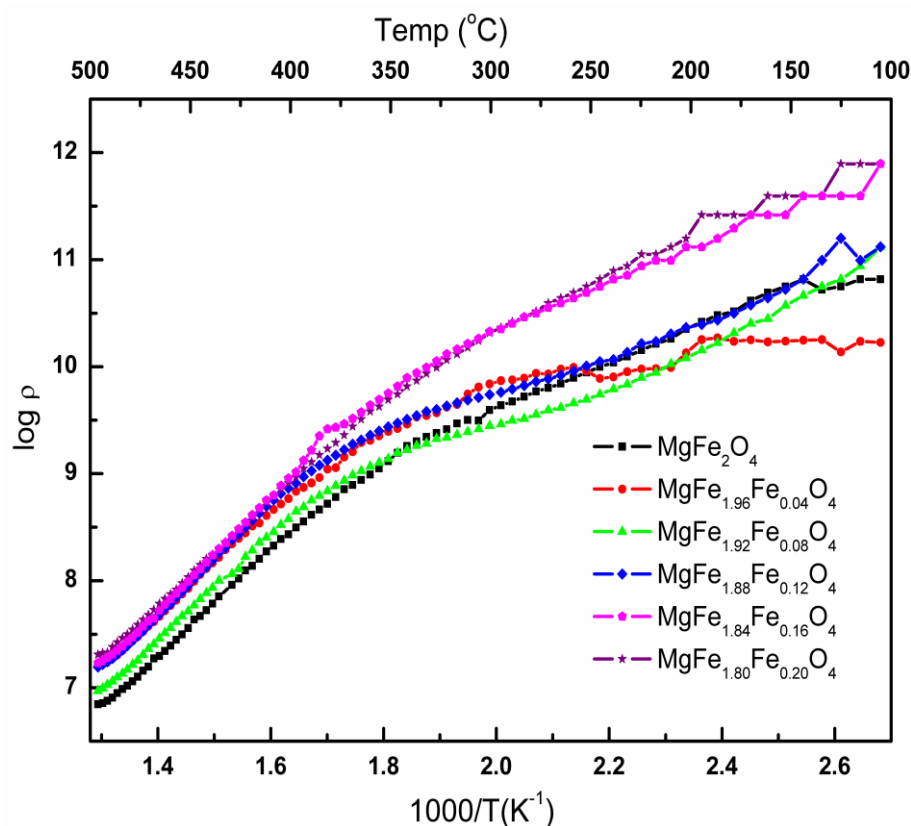


Fig. 4.53 Plots of log resistivity v/s $1000/T$ for $\text{MgFe}_{2-x}\text{In}_x\text{O}_4$ compounds sintered at $600\text{ }^\circ\text{C}$.

4.10 Magnetic Studies

Magnetic studies were carried out using VSM where the magnetization with varying magnetic field of up to 30000 Oe was measured at 300 K and 50 K for all the compounds and magnetisation with varying temperature at a specific fixed magnetic field was also studied in the temperature range of 50 to 400 K.

4.10.1 $\text{In}_{2-x}\text{Co}_x\text{O}_3$

The $M-H$ curves for $\text{In}_{2-x}\text{Co}_x\text{O}_3$ ($x = 0.00, 0.04, 0.08, 0.12, 0.20$ and 0.30) nanoparticles at 300 K are represented in Fig.4.54 (a) and (b) shows the enlarged region. The pristine sample shows very weak ferromagnetism probably owing to the presence of defects as explained by Sundersan et al. [150]. For Co^{2+} doped samples, the compound with lowest dopant concentration ($x = 0.04$) shows a well defined hysteresis prominent at the lower magnetic field region, whereas at higher field distinct paramagnetic nature is visible. This is followed by the compound with $x = (0.08)$ with a small hysteresis loop. Further doping weakens this phenomena and show prominent paramagnetic nature. The origin of hysteresis could be the interaction between the 3d magnetic spins of the Co^{2+} ions and a donor impurity band formed by lattice defects such as oxygen vacancies as

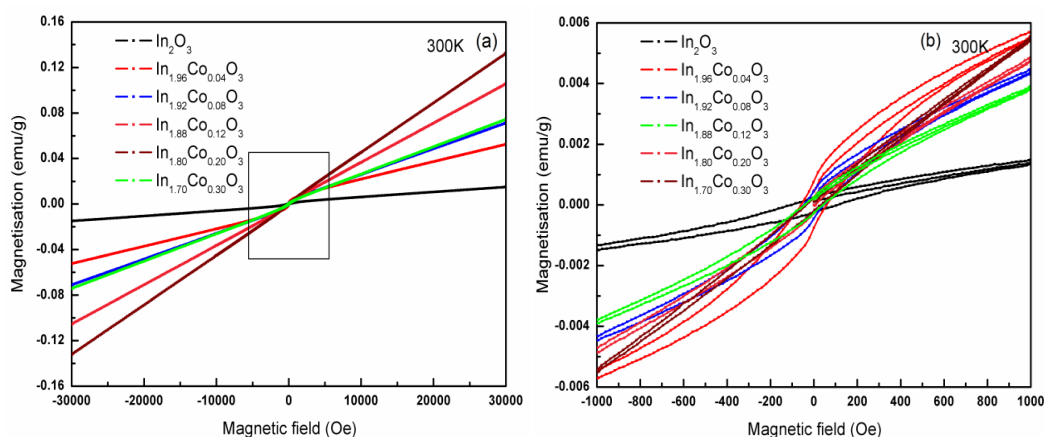


Fig. 4.54 Plots of magnetisation with varying field for (a) $\text{In}_{2-x}\text{Co}_x\text{O}_3$ nanoparticles and (b) magnified view at 300K.

explained in the case of electrical resistivity. The alignment of these magnetic spins results in the observed ferromagnetism [357]. The magnetic ordering arising from secondary magnetic phases is ruled out as in the present study, XRD shows the formation of a pure single phase of In_2O_3 . On further increase in Co^{2+} concentration the paramagnetic contribution is highlighted in the M-H curves. The probable reason for such behaviour could be the presence of $\text{Co}^{2+}-\text{V}_o-\text{Co}^{2+}$ super exchange interaction (where V_o is the oxygen vacancy) which gives rise to anti-ferromagnetic coupling as observed by W. Ye et al. for Co doped CeO_2 nanoparticles [209]. None of the compound shows saturation magnetisation (M_s). The measurable coercivity is obtained only for concentration with $x = 0.04$, which is around 110 Oe and for $x = 0.04$ is around 80 Oe.

The observed room temperature ferromagnetism is razed at 50 K as shown in Fig. 4.55. A linear graph is obtained which suggests that anti-ferromagnetic/paramagnetic alignment of spins is found to be more favourable at lower temperature. The hysteresis observed for $\text{In}_{1.96}\text{Co}_{0.04}\text{O}_3$ composition at 300 K has also weakened at 50 K.

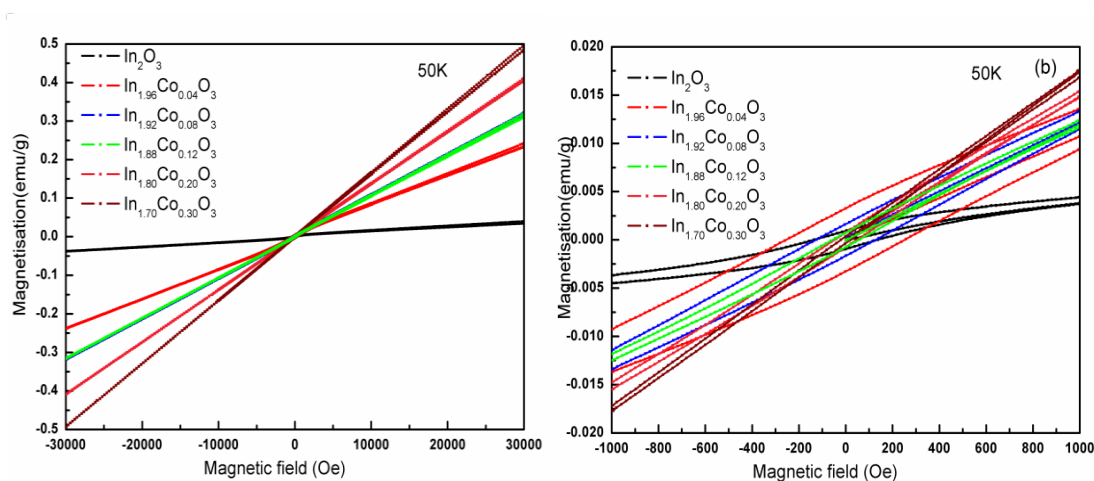


Fig.4.55 Plots of magnetisation with varying field for (a) $\text{In}_{2-x}\text{Co}_x\text{O}_3$ nanoparticles and (b) magnified view at 50 K.

The Magnetisation with varying temperature ($M-T$) plots for $\text{In}_{2-x}\text{Co}_x\text{O}_3$ are displayed in Fig. 4.56 measured at a constant magnetic field of 5000 Oe. For pristine In_2O_3

the zero field cooled (ZFC) curve is independent of temperature till 75 K, further it follows a spin glass behaviour similar to (field cooled) FC curve. The compound (with $x = 0.04$ for Co) shows the maximum separation between FC and ZFC curves compared to rest of the dopants depicting the ferromagnetic behaviour. In this case also the ZFC is found to follow a similar trend as that shown by In_2O_3 . As the concentration of cobalt increases the FC and ZFC do not show much difference, indicating the influence of paramagnetic contribution. The magnetisation value is found to increase below 75 K for all the samples; this is a typical DMS behaviour.

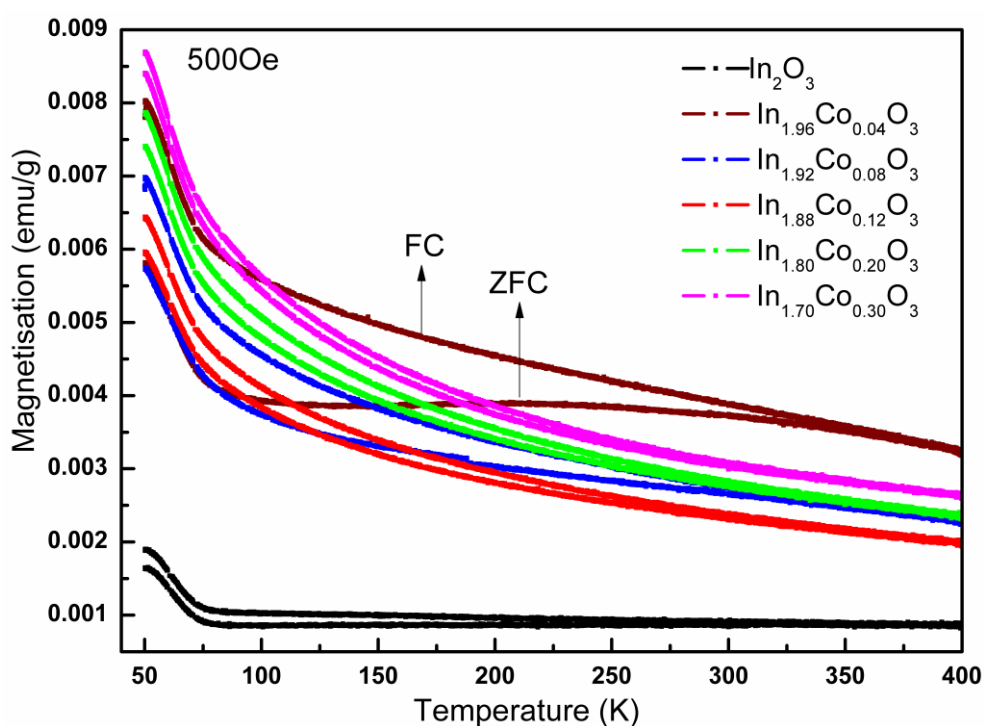


Fig.4.56 Plots of magnetisation with varying temperature for $\text{In}_{2-x}\text{Co}_x\text{O}_3$ nanoparticles at constant field of 500 Oe.

Fig.4.57 shows the $M-T$ curves for $\text{In}_{1.96}\text{Co}_{0.04}\text{O}_3$ compound at different magnetic fields of 250 Oe, 500Oe and 1000Oe. The FC, ZFC separation is found to be more at the lower fields and found to decrease for the field of 1000 Oe. This is in well accordance with the $M-H$ data presented shown earlier where the ferromagnetic ordering is seen in

the lowerfield region whereas at higher fields paramagnetic behaviour is more prominent owing to which no sample shows saturation.

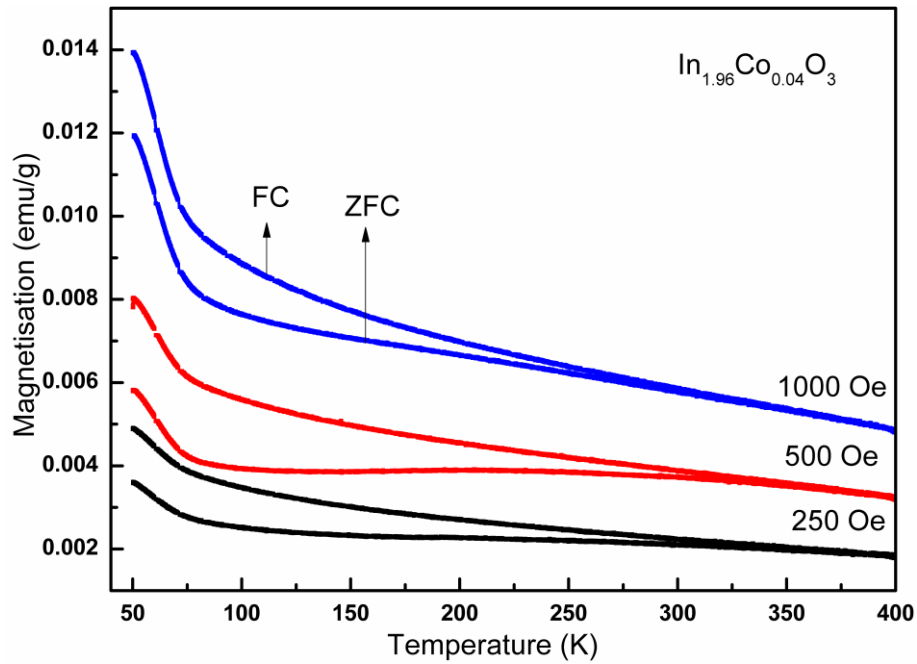


Fig.4.57 Plots of magnetisation with varying temperature for $\text{In}_{1.96}\text{Co}_{0.04}\text{O}_3$ nanoparticles at applied fields of field of 250 Oe, 500 Oe and 1000 Oe.

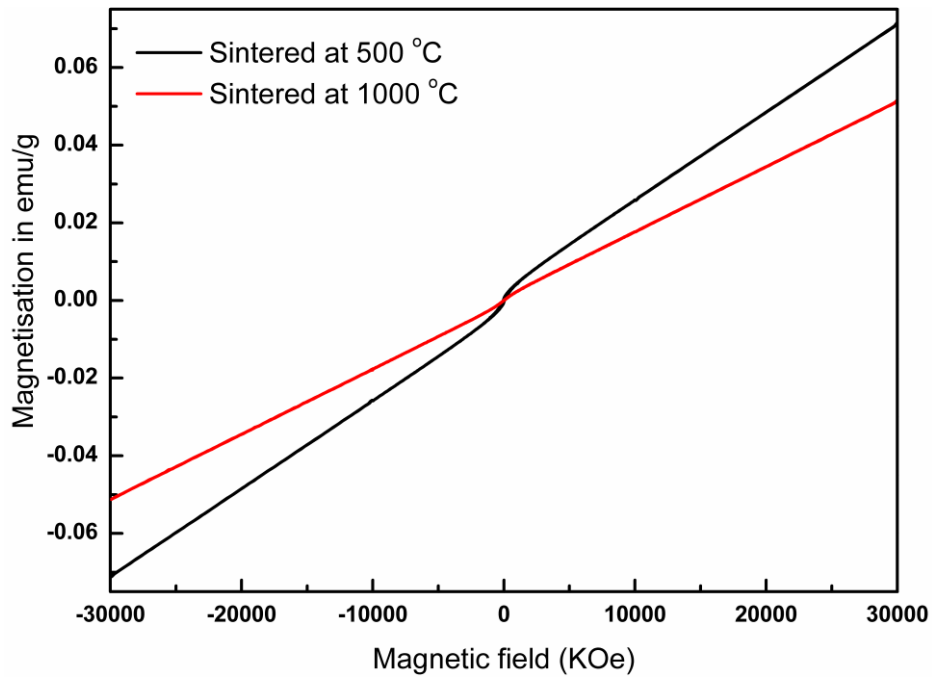


Fig.4.58 Plots of magnetisation with varying field for $\text{In}_{1.92}\text{Co}_{0.08}\text{O}_3$ compound sintered at 500 and 1000 °C.

As discussed earlier in the literature the phenomena of dilute magnetism has been controversial with its existence and origin, we have carried out $M-H$ studies at room temperature on a representative sample with composition $\text{In}_{1.92}\text{Co}_{0.08}\text{O}_3$ which is sintered at $1000\text{ }^\circ\text{C}$ for 10 h and compared it with that of nanosize. The Fig. 4.58 displays these plots where the sample sintered at $1000\text{ }^\circ\text{C}$ shows the deterioration of the weak ferromagnetism obtained for nano sample and depicts a perfect paramagnetic nature. This also suggests that the nano size and the associated defects play a major role in room temperature ferromagnetism observed in DMS.

4.10.2 $\text{In}_{2-x}\text{Cr}_x\text{O}_3$

The $M-H$ curves for $\text{In}_{1-x}\text{Cr}_x\text{O}_3$ ($x = 0.00, 0.02, 0.04, 0.06, 0.08$ and 0.10) compounds measured at room temperature are presented in Fig. 4.59. The pristine compound shows weak ferromagnetism as shown in the earlier analysis of Co doped compounds. Incorporation of Cr into the lattice of In_2O_3 , along with altering the physical properties such as resistivity and band gap also results in enhancing its magnetic properties. Literature suggests the existence and origin of ferromagnetism has been controversial, it could be impurity or defect oriented, some suggests the oxygen vacancies

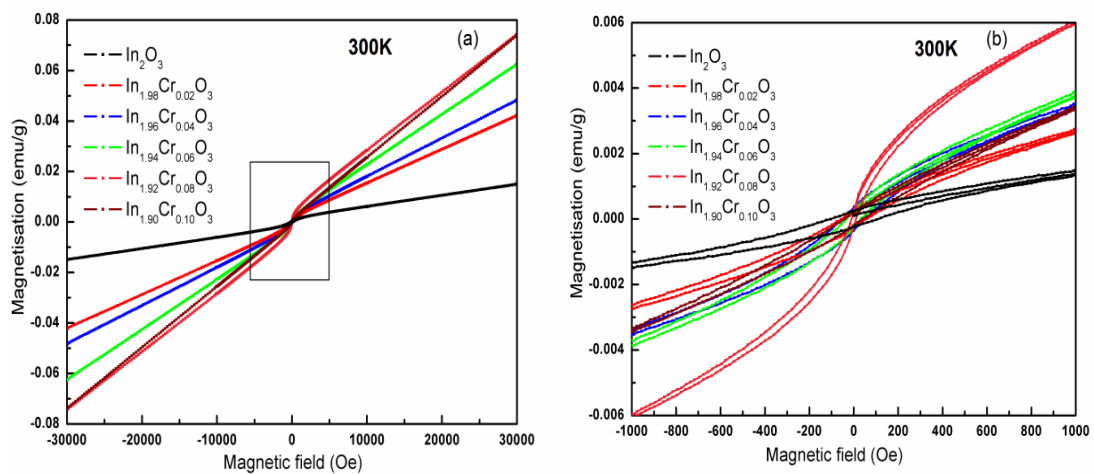


Fig.4.59 Plots of magnetisation with varying field at 300 K for (a) $\text{In}_{1-x}\text{Cr}_x\text{O}_3$ compounds sintered at $500\text{ }^\circ\text{C}$ and (b) magnified view.

(V_o) responsible for it whereas few claim it to be owing to p-type defects such as O interstitial and In vacancies [148]. Coupling of Cr^{3+} 3d electrons and O 2p electrons may also result in the observed ferromagnetic nature which is prominent in the lower field region. We have observed here that as the concentration of Cr exceeds from $x = 0.08$ to $x = 0.10$, the samples show paramagnetic behaviour. No samples show saturation, a linear profile is consistent at higher fields. The $M-H$ plots at 50 K are displayed in Fig. 4.60 showing the similar results as obtained for Co doped In_2O_3 compounds. Anti-ferromagnetic /paramagnetic alignment of spins is found to be more favourable at lower temperatures.

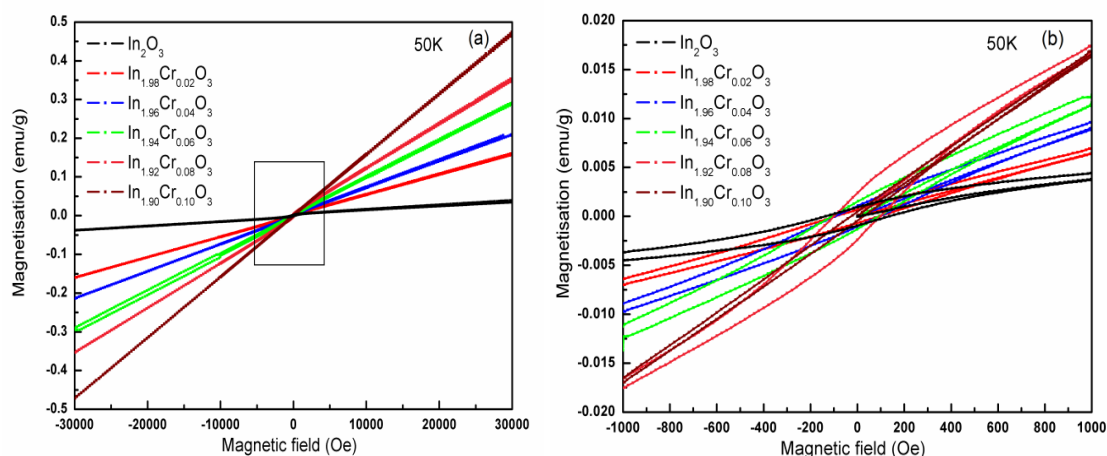


Fig.4.60 Plots of magnetisation with varying field at 50 K for (a) $In_{2-x}Cr_xO_3$ compounds sintered at 500 °C and (b) magnified view.

The $M-T$ graphs for the Cr doped In_2O_3 nanoparticles at a constant applied magnetic field are shown in Fig.4.61. The Pristine shows a very low values of magnetisation where ZFC is independent of temperature till 75 K, below which it follows the DMS behaviour. As the concentration of Cr increases the magnetisation is found to increase, until it exceeds $x = 0.08$, where magnetisation is found to decrease. The FC and ZFC shows a similar pattern where the maximum separation between the two is observed

for Cr concentration $x = 0.08$ whereas compound with Cr Concentration $x = 0.10$ shows a paramagnetic nature where FC and ZFC do not show much variation[138].

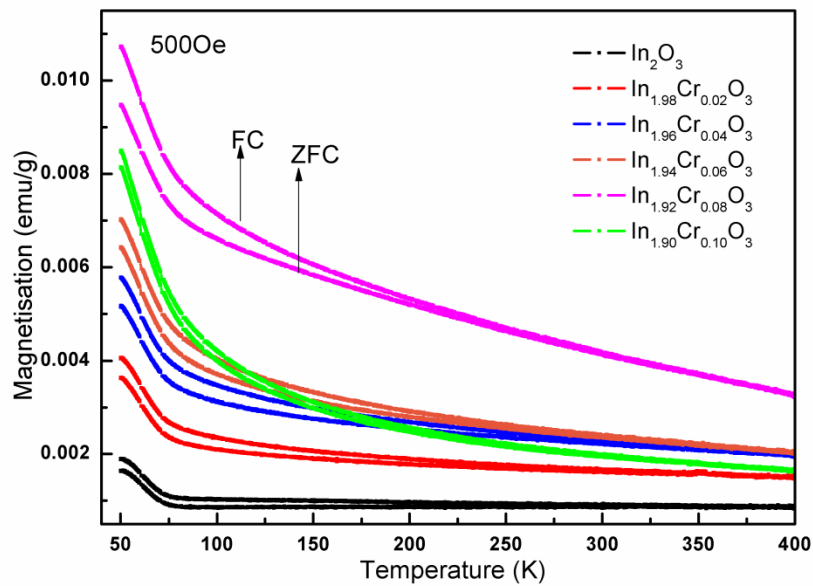


Fig.4.61 Plots of magnetisation with varying temperature for $In_{2-x}Cr_xO_3$ nanoparticles at constant field of 500 Oe.

4.10.3 $In_{2-x}Ag_xO_3$

The magnetisation v/s field data for $In_{2-x}Ag_xO_3$ ($x = 0.00$ and 0.04) nanoparticles has been presented in Fig. 4.62 (a) where the inset shows the enlarged view. The pristine and doped sample shows a very weak ferromagnetism as shown in earlier studies. Here

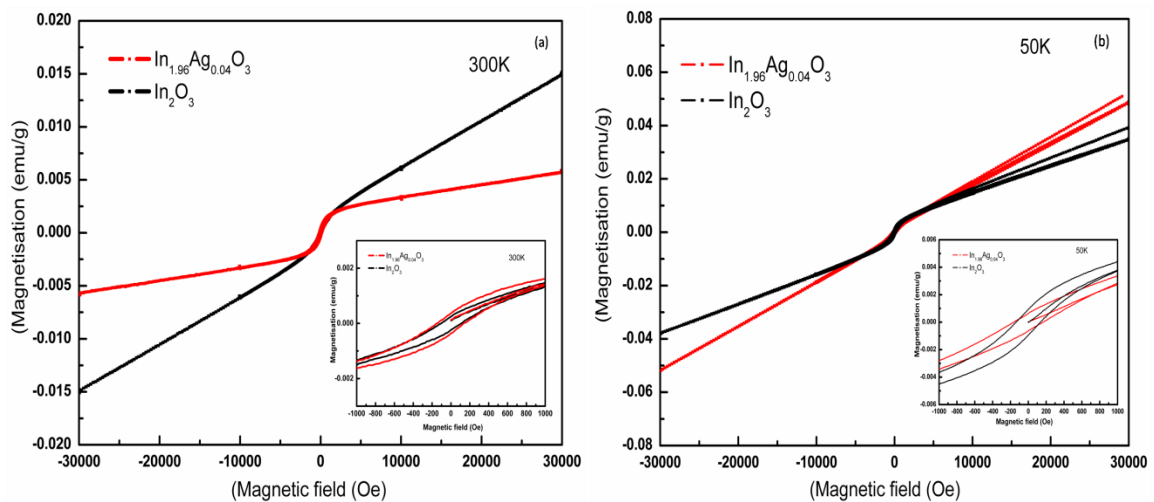


Fig.4.62 Plots of magnetisation with varying field at (a) 300 K and (b) 50 K for $In_{2-x}Ag_xO_3$ compounds sintered at 600 °C, insets shows the magnified region.

the dopant ion is silver which is in +1 oxidation state as understood from the XPS data explained in section 4.7.5. Silver here being a diamagnetic species, the observed effect of its incorporation on magnetic properties would result from the defects it creates. No saturation is observed for both the compounds. At 50 K the ferromagnetic ordering is observed to decrease for doped compound compared to that of pristine as shown in Fig. 4.62(b).

The $M-T$ curves are presented in Fig 4.63 for the $\text{In}_{2-x}\text{Ag}_x\text{O}_3$ ($x = 0.00$ and 0.04). Both the compounds show a similar FC-ZFC pattern and almost same magnetisation below 75 K. Above this temperature for both the compounds magnetisation is independent of temperature.

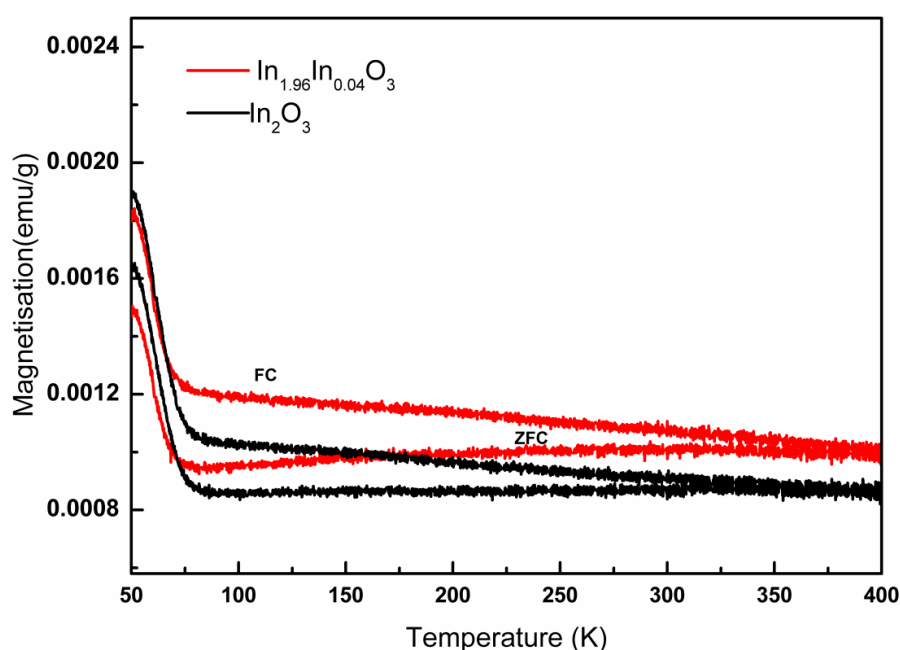


Fig.4.63 Plots of magnetisation with varying temperature for $\text{In}_{2-x}\text{Ag}_x\text{O}_3$ nanoparticles at constant field of 500 Oe.

4.10.4 $\text{Ce}_{1-x}\text{In}_x\text{O}_2$

CeO_2 has also been known as one of the strong DMS candidate. In the present study we have explored the magnetic properties of CeO_2 by introducing In^{3+} a non magnetic ion into it. The $M-H$ plots measured at 300K are displayed in Fig. 4.64 (a), The

pristine sample shows a weak ferromagnetism, as the concentration of dopant increases above $x = 0.04$, the magnetisation is found to increase although no compound shows saturation at room temperature (300K). The compound with $Ce_{0.85}In_{0.15}O_2$ composition shows the highest magnetisation with sigmoidal plot similar to the super-paramagnetic material. The enlarged view in Fig. 4.64 (b) shows that the compound has negligible coercivity almost close to zero.

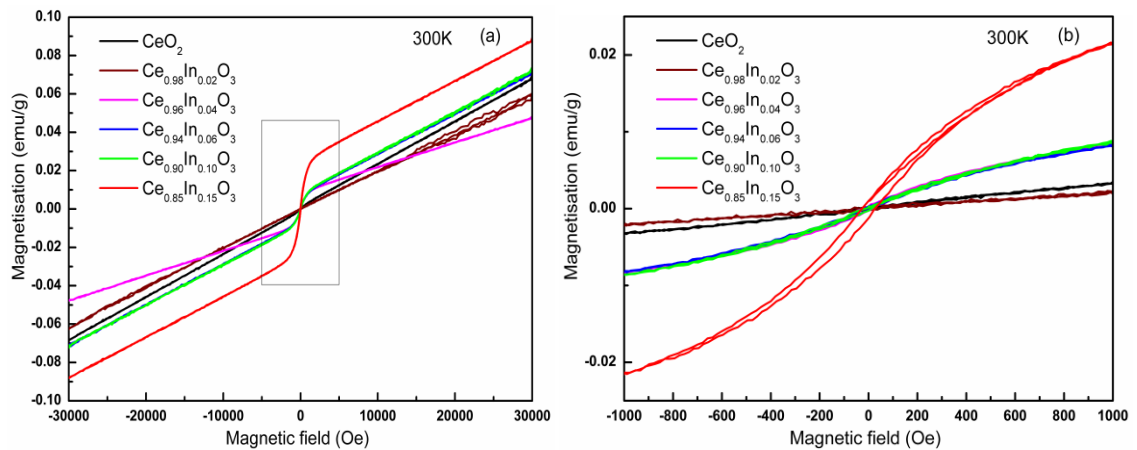


Fig.4.64 Plots of magnetisation with varying field at 300 K for (a) $Ce_{1-x}In_xO_2$ compounds sintered at 600 °C (b) magnified view.

At 50 K as shown in Fig. 4.65 (a) the compounds with compositions above $x = 0.04$ showed magnetisation with saturation. M_s obtained for samples are 0.010, 0.011, 0.013 and 0.034

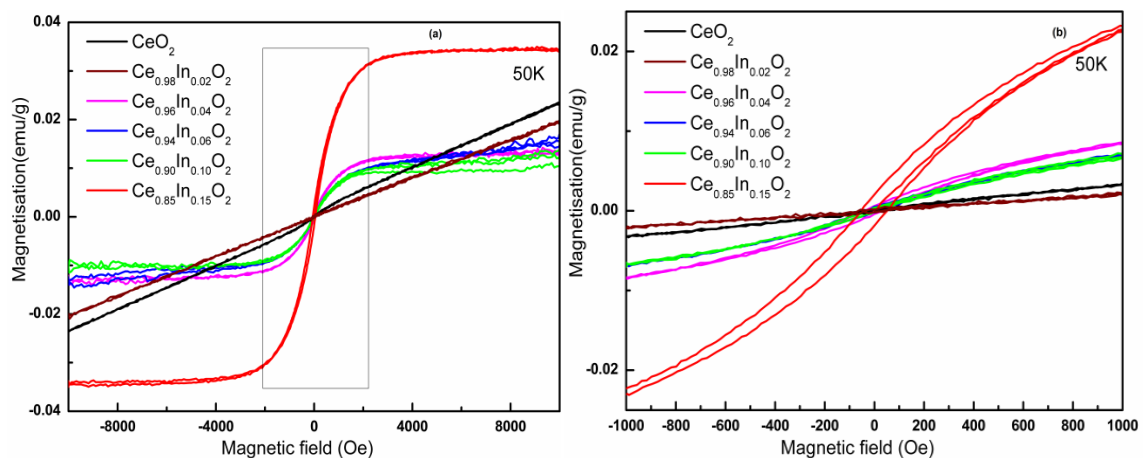


Fig.4.65 Plots of magnetisation with varying field AT 50K for (a) $Ce_{1-x}In_xO_2$ compounds sintered at 600°C (b) magnified view .

Oe for $Ce_{1-x}In_xO_2$ where $x= 0.04, 0.06, 0.10$ and 0.15 respectively. The enlarged view shown in Fig.4.65 (b) also reveals that coercivity increases at 50K which is found to be around 1200Oe for $Ce_{0.85}In_{0.15}O_2$.

Fig 4.66 presents $M-T$ plots where FC and ZFC curves are displayed. As the concentration of In^{3+} increases the separation between FC and ZFC becomes more prominent confirming existence of magnetic ordering in the samples.

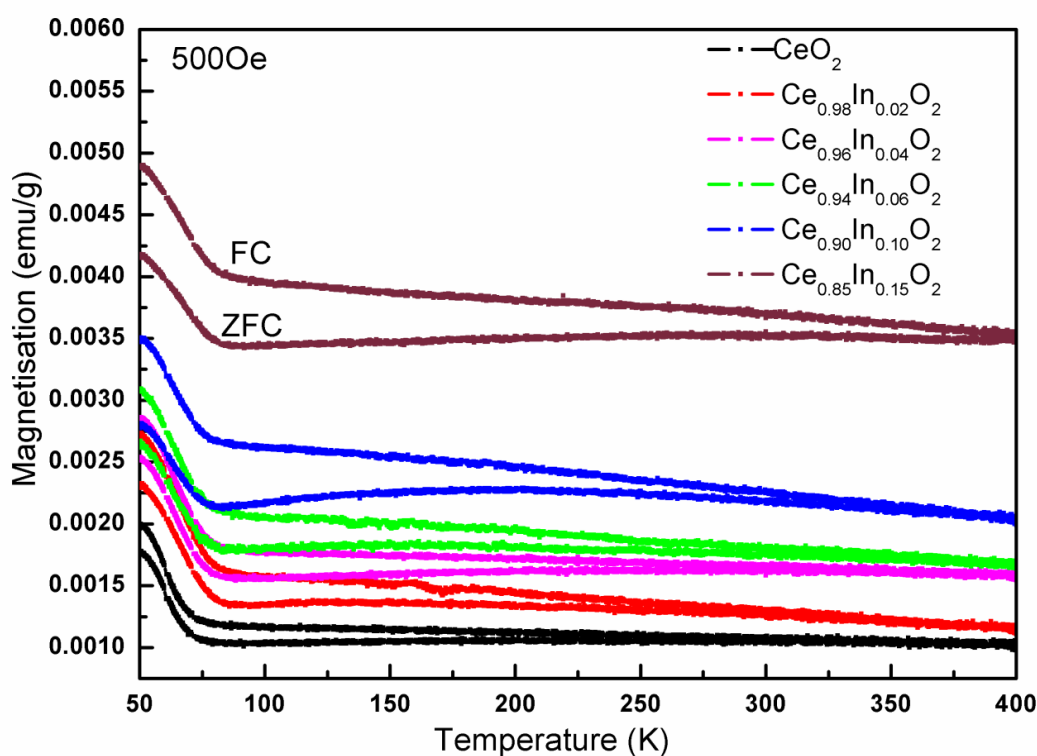


Fig.4.66 Plots of magnetisation with varying temperature for $Ce_{1-x}In_xO_2$ nanoparticles sintered at $600\text{ }^\circ\text{C}$ at constant field of 500 Oe .

To identify the influence of nano size on the magnetic properties the representative compound $Ce_{0.85}In_{0.15}O_2$ was sintered at $1000\text{ }^\circ\text{C}$ for 24 h and the $M-H$ studies were carried out at 300 K and 50 K . The obtained results are compared with the nano size compounds. From the Fig.4.67 it is very much clear that the magnetisation is found to be reduced with increase in sintering temperature that is due to destruction of nano-size. Thus the nano-size and associated defects play a major role in magnetism

observed in DMS material. Earlier pristine transition, rare earth and non magnetic ions like Ca^{2+} doped cerium oxide has been reported to show magnetism where the defects such as oxygen vacancies are considered to be the main reason for observed RT ferromagnetism. This is the first report on In^{3+} doped CeO_2 nanoparticles, where it is observed that the defects and the nano-size are the two possible reasons associated with the observed ferromagnetism.

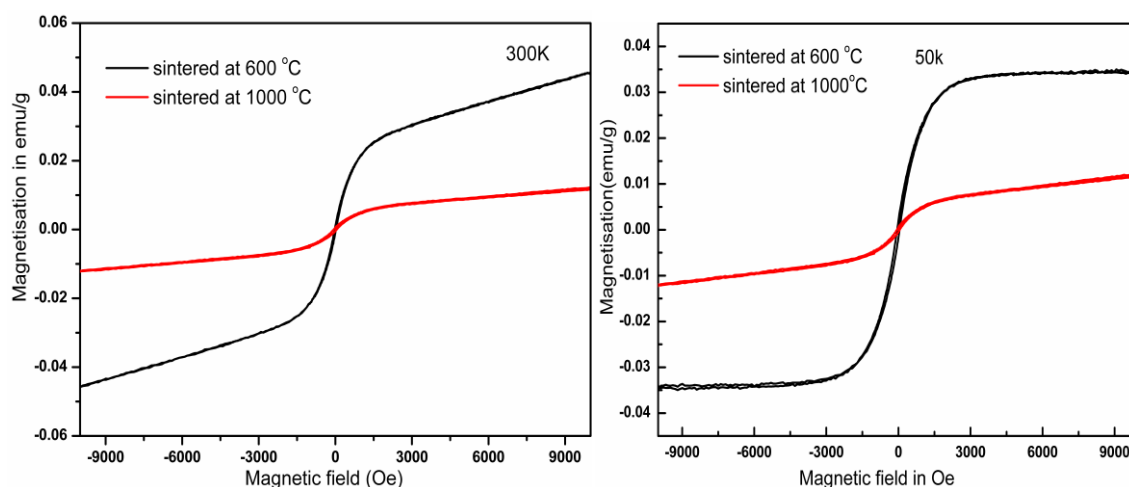


Fig.4.67 Plots of magnetisation with varying field at 300 K and 50 K for $\text{Ce}_{0.85}\text{In}_{0.15}\text{O}_2$ sintered at $1000\text{ }^\circ\text{C}$ for 24 h.

4.10.5 $\text{MgFe}_{2-x}\text{In}_x\text{O}_4$

Fig.4.68 displays the M - H curves for the samples at room temperature (300 K) and Fig. 4.69 represents the M - H curves for the samples at 50 K. At 300 K it was observed that all the samples exhibit a low saturation magnetisation (M_s) and a very low coercivity (H_c) which is a characteristic of a very soft magnetic material. Upon doping the M_s and H_c values of the samples decreased considerably compared to pristine MgFe_2O_4 , this is owing to the replacement of Fe^{3+} ions by diamagnetic In^{3+} ions. Here the interesting fact is that, as the dopant concentration increased, the H_c values decreased and becomes almost zero for the concentration where $x = 0.12$ thereby making it a perfect superparamagnetic material [358]. Further increase in indium content increased the H_c and M_s .

but not exceeding pristine. Considering the three kinds of exchange interactions between the magnetic ions, lying on two different sub-lattices of ferrites are AA interaction, BB interaction and AB interactions. The AB interaction strongly predominates over AA and BB interactions. The net magnetic moment is given by $M = M_B - M_A$ i.e. difference in moments of B and A sub-lattices. Tetrahedral sites are bigger in size compared to octahedral and In^{3+} ions having larger radii are expected to enter the tetrahedral sites. Literature also reports the A site preference of In^{3+} at lower concentration [360, 361]. In such case In^{3+} replaces Fe^{3+} at A site, which decreases the magnetic moment at A site resulting in enhancement of overall magnetic moment. Whereas if In^{3+} occupies octahedral B sites by replacing Fe^{3+} ions, the magnetisation of B lattice will decrease keeping the magnetisation of A lattice constant, thereby decreasing the resultant magnetisation [362]. The observed decrease in M_s on doping in the present study suggests that In^{3+} ions occupy the octahedral sites. Decrease in particle size also adds on to the reduction in magnetisation. The magnetic parameters are presented in the Table 4.6. The compound with Indium concentration $x = 0.16$ shows a higher M_s values compared to $x = 0.20$, it is owing to the presence of Fe_2O_3 impurity phase, also detected in the XRD pattern as discussed in section.4.2.5.

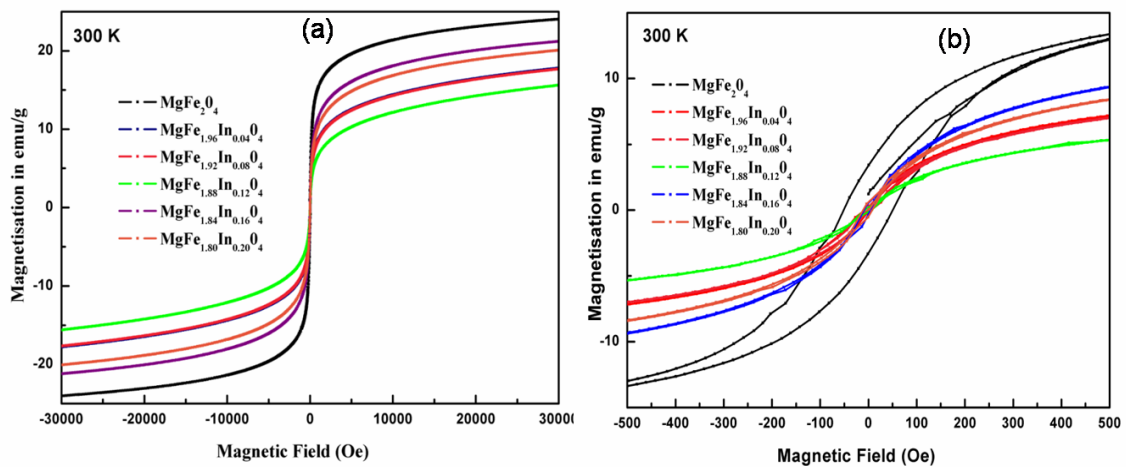


Fig.4.68 Plots of magnetisation with varying field at 300 K for (a) $\text{MgFe}_{2-x}\text{In}_x\text{O}_4$ sintered at 600 °C, (b) enlarged view.

At 50 K measurements, the similar trend was observed for M_s and M_r , whereas H_c was found to increase with In^{3+} doping. Another highlighting observation was that the distinct super-paramagnetism at 300 K is razed at 50 K as shown in Fig.4.69(a) the magnified portion is also displayed in Fig.4.69 (b). This was well supported by the magnetisation v/s temperature ($M-T$) data.

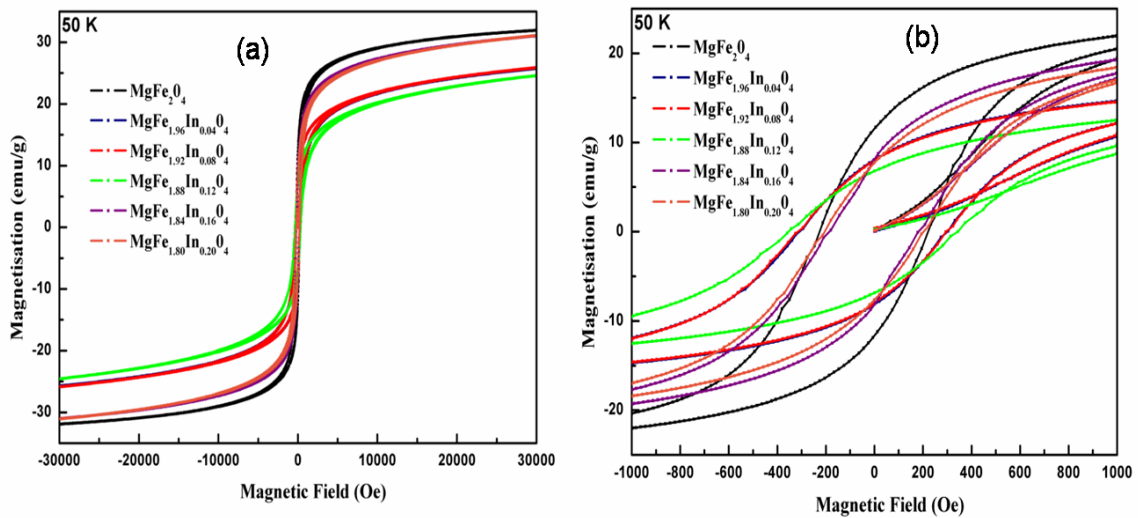


Fig.4.69 Plots of magnetisation with varying field at 50K for (a) $\text{MgFe}_{2-x}\text{In}_x\text{O}_4$ sintered at $600\text{ }^\circ\text{C}$, (b) enlarged view.

Table 4.6 Magnetic parameters, saturation magnetisation (M_s) coercivity (H_c) and retentivity (M_r) obtained for the nanoparticles at 300 K and 50 K

Compositions	300K			50K		
	(M_s) emu/g	(M_r) emu/g	(H_c)	(M_s) emu/g	(M_r) emu/g	(H_c)
MgFe_2O_4	23.90	3.47	106	31.82	10.93	419
$\text{MgFe}_{1.96}\text{In}_{0.04}\text{O}_4$	17.74	0.304	17	25.73	8.357	554
$\text{MgFe}_{1.92}\text{In}_{0.08}\text{O}_4$	17.58	0.668	37	25.65	8.125	554
$\text{MgFe}_{1.88}\text{In}_{0.12}\text{O}_4$	15.49	0	0	24.48	6.964	686
$\text{MgFe}_{1.84}\text{In}_{0.16}\text{O}_4$	21.15	0	0	30.92	7.686	400
$\text{MgFe}_{1.80}\text{In}_{0.20}\text{O}_4$	19.82	0	0	30.62	8.453	466

The MT studies are shown in Fig.4.70 where the temperature dependent field cooled (FC) and the zero field cooled (ZFC) magnetisation were measured for the samples at a specific constant magnetic field. The bifurcated temperature of FC and ZFC is defined as the blocking temperature (T_b) [297]. The blocking temperature is found to be inversely proportional to the applied magnetic field. Fig. 4.71 shows decrease in the blocking temperature value of pristine MgFe_2O_4 nanoparticles as the applied magnetic field is increased. Further, keeping the magnetic field constant FC and ZFC plots for all the sample compositions were studied to monitor the doping effect of In^{3+} on the blocking temperature. The observation reveals that, below blocking temperature the nanoparticles that show hysteresis loop follows the Curie-Weiss law in higher temperature region. The obtained (T_b) for MgFe_2O_4 was 370 K, In^{3+} doping reduced the blocking temperature reaching almost close to the room temperature as shown in Fig.4.70 at a constant magnetic field of 250 Oe.

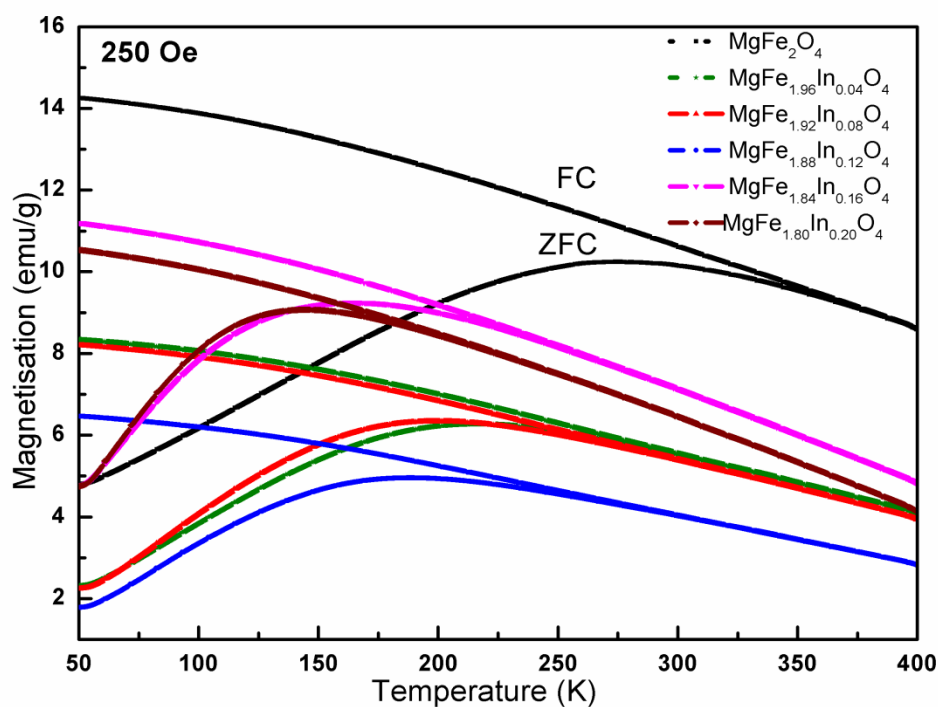


Fig. 4.70 Plots of magnetisation with varying temperature for $\text{MgFe}_{2-x}\text{In}_x\text{O}_4$ compounds sintered at 600 °C at applied field of 250 Oe.

As mentioned in literature the usual multi domain structure of a bulk magnetic material, below a critical size of ~ 50 nm forms a single domain and exhibit an interesting property such as super-paramagnetism where the blocking temperature and the coercivity can be controlled by the size of the nanoparticles [265, 363]. This is in accordance with our observed results where on doping with In^{3+} there was a reduction in crystallite size of the samples and they exhibit super-paramagnetism above blocking temperature. Here the significant achievement was that on In^{3+} doping it was able to attain the blocking temperature of the MgFe_2O_4 at room temperature at an applied magnetic field of 250 Oe, also $M-H$ data at RT despite showing low emu/g for doped samples that is. low M_s fulfils the criteria of achieving the zero H_c , enhancing the super-paramagnetic nature.

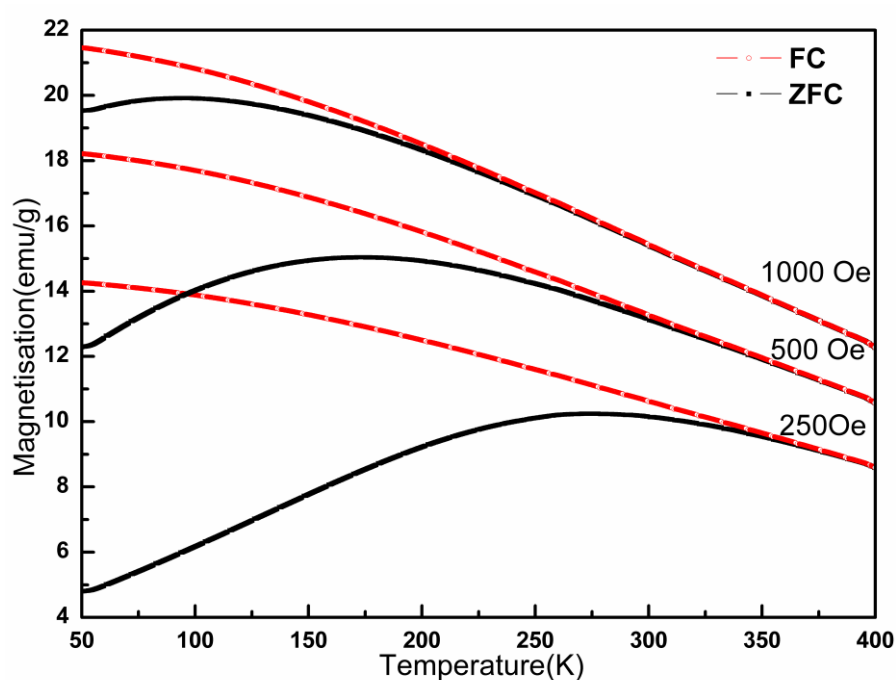


Fig. 4.71 Plots of magnetisation with varying temperature for MgFe_2O_4 at different applied magnetic field.

4.10.6 AC Susceptibility Measurements.

The temperature dependence of the relative magnetic moment obtained from AC susceptibility studies for the monophasic samples is displayed in Fig.4.72. It was

observed that the relative magnetic moment for the pristine MgFe_2O_4 nano-particles slowly increases up to a certain temperature and then suddenly drops to zero at Curie temperature (T_c) which is 630 K for pristine sample. Initial increase in relative magnetic moment and then a sudden drop is a characteristic of a single domain state [364]. On doping the T_c was found to decrease as the concentration of In^{3+} increased. The highlighting part in this analysis was the graph profile for doped samples where relative magnetic moment decreases as the temperature increases in a manner typical of super-paramagnetic particles. This transition from a single domain to perfect super-paramagnetism triggered by the incorporation of In^{3+} is also explained earlier in the magnetic properties carried out on VSM.

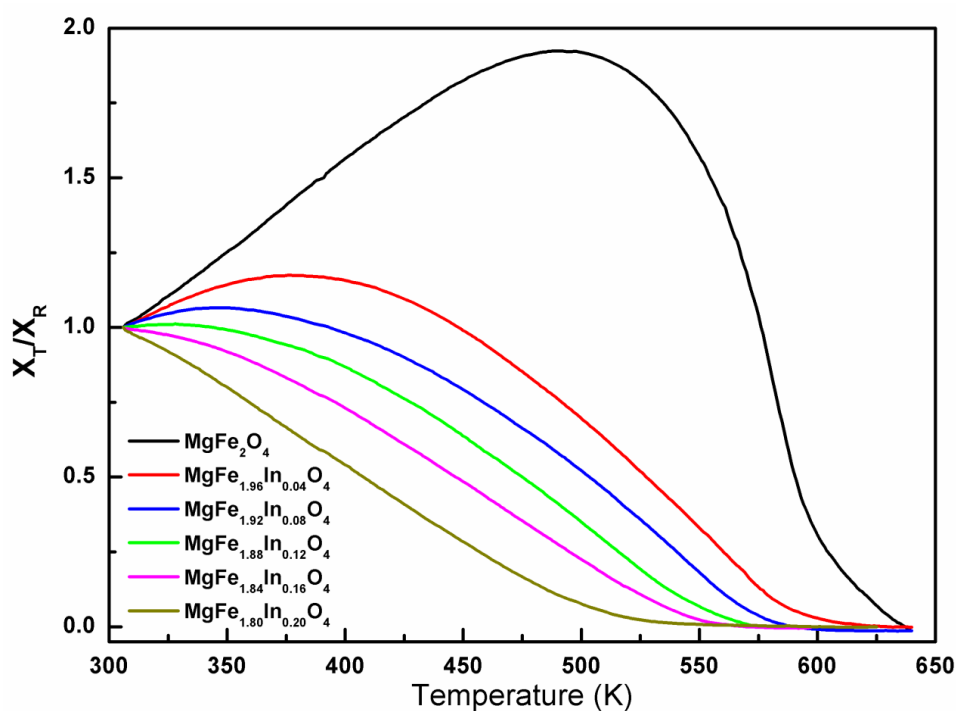


Fig. 4.72 Plots of relative magnetic moment with varying temperature for $\text{MgFe}_{2-x}\text{In}_x\text{O}_4$ compounds

CATALYTIC AND BIOMEDICAL APPLICATIONS

The surface area plays a major role in catalytic applications of nanoparticles. The surface area and porosity of the Co doped In_2O_3 nanoparticles have been found using BET surface area analyser and the results are discussed below. The nanoparticles were then tested for their catalytic applications.

5.1 BET Surface Area

The BET surface area estimated by N_2 adsorption measurements of pristine In_2O_3 nano-particles is $20.14 \text{ m}^2/\text{g}$. The surface area was found to increase with cobalt doping. The observed surface areas for the samples are 38.09, 73.54 and 180.46, 103.35 and $123.22 \text{ m}^2/\text{g}$ for $\text{In}_{2-x}\text{Co}_x\text{O}_3$ (where $x = 0.04, 0.08, 0.12, 0.20, 0.30$) respectively. The pore volume is also found to increase in similar manner, where the observed values are 0.027, 0.050, 0.119, 0.582, 0.311 and 0.312 cc/g with increasing Co concentration ($x = 0.00, 0.04, 0.08, 0.12, 0.20$ and 0.30 respectively). This implies that Co substitution increases the porosity of samples as evident from the SEM images, leading to subsequent increase in surface area. The $\text{In}_{1.88}\text{Co}_{0.12}\text{O}_6$ compound shows the highest surface area and the pore

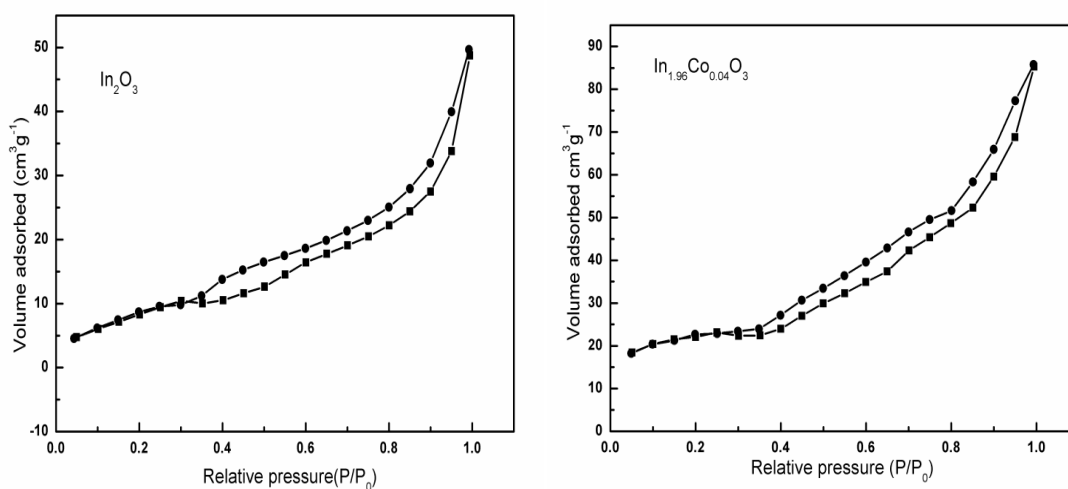


Fig.5. N_2 adsorption and desorption isotherms for In_2O_3 and $\text{In}_{1.96}\text{Co}_{0.04}\text{O}_3$ compounds.

volume which is in accordance with the crystallite size values where $\text{In}_{1.88}\text{Co}_{0.12}\text{O}_6$ shows smallest crystallite size hence the larger surface area. This increase in surface area and porosity is well exploited for the CO oxidation reaction over these nano-particles. The observed isotherms for the pristine and $\text{In}_{1.96}\text{Co}_{0.04}\text{O}_3$ are shown in Fig. 5.1.

5.2 CO oxidation

The prepared nanoparticles were used as a catalyst of CO oxidation and few organic transformations. The obtained results are discussed in this section of the chapter. Catalytic reactions for CO oxidation were carried out in a continuous flow fixed bed glass reactor. Catalyst (1.0 g) was sandwiched between the two layers of the glass wool. The catalyst was activated with oxygen (250 mL/h) in nitrogen at 150 °C for half an hour prior to the reaction. The feed gas composition of 5% CO, 5% O₂ in nitrogen was used to determine the catalytic activity. The gas flow rates were controlled using flow meters and precision needle valves. The feed gases and products were analysed by an online Gas Chromatograph where separation was done by a packed column molecular sieve 13X and analysed by thermal conductivity detector (TCD) using H₂ as a gas carrier. Standard procedure was employed to prepare CO and was purified by passing through appropriate traps [365]. Pure nitrogen, oxygen and hydrogen gases were used from commercial cylinders. The prepared nanoparticles have been exploited for its catalytic activity in CO oxidation.

5.2.1 $\text{In}_{1-x}\text{Co}_x\text{O}_3$

The catalytic behaviour for CO oxidation to CO₂ as a function of temperature for pristine and Co doped In_2O_3 nano-particles is shown in Fig. 5.2. None of the catalysts show activity at room temperature. For pristine In_2O_3 , conversion is observed at a very

slow rate above 80 °C which increases significantly above 240 °C and a complete CO conversion is achieved at 290 °C. In case of Co doped samples, the CO conversion is instigated at 40 °C for all the dopant concentrations. Catalyst with composition $\text{In}_{1.96}\text{Co}_{0.04}\text{O}_3$ shows conversion profile similar to the pristine with 100% CO conversion at 218 °C, whereas catalyst with $\text{In}_{1.92}\text{Co}_{0.08}\text{O}_3$ and $\text{In}_{1.88}\text{Co}_{0.12}\text{O}_3$ compositions shows a drastic increase in percentage of CO conversion above 90 °C. The complete CO conversion for $\text{In}_{1.92}\text{Co}_{0.08}\text{O}_3$ and $\text{In}_{1.88}\text{Co}_{0.12}\text{O}_3$ compositions is accomplished at 150 °C and 130 °C respectively which is a much lower temperature compared to that obtained for pristine In_2O_3 , the compositions $\text{In}_{1.80}\text{Co}_{0.20}\text{O}_3$ and $\text{In}_{1.70}\text{Co}_{0.30}\text{O}_3$ shows complete CO oxidation at 165 and 130 °C respectively. This slight increase and again a decrease in temperature could be owing to the variations in the surface areas of the samples. The observed onset and offset temperatures for CO conversion by pristine as well as doped samples are exceptionally lower than those reported earlier for the In_2O_3 nanostructures [160]. It is observed that the incorporation of Co^{2+} into the In_2O_3 lattice increases its catalytic activity.

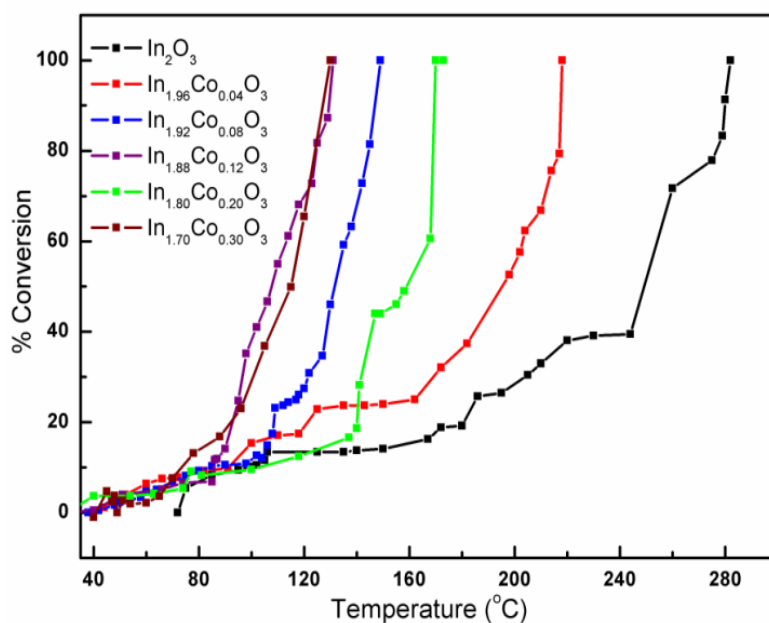


Fig. 5.2 CO oxidation reaction over $\text{In}_{2-x}\text{Co}_x\text{O}_3$ catalysts.

As evident from the BET surface area analysis, Co substitution results in increasing the surface area and porosity of In_2O_3 nano-particles which aids in its catalytic performance by providing a larger surface area for molecular interactions. Cobalt substitution also alters the oxygen mobility of the samples which also plays an important role in CO oxidation.

5.2.2 $\text{In}_{2-x}\text{Cr}_x\text{O}_3$

Fig. 5.3 presents the CO oxidation profile for $\text{In}_{1.90}\text{Cr}_{0.10}\text{O}_3$ nanoparticles compared with data for pristine. The pristine shows 100% conversion at 290°C as discussed in earlier section whereas the Cr incorporation reduces the temperature to 270°C . The reduction is not so significant to consider the compound to be a good catalyst. The decrease in temperature could be related to the reduction in crystallite size which ultimately increases the surface area for the catalytic reaction.

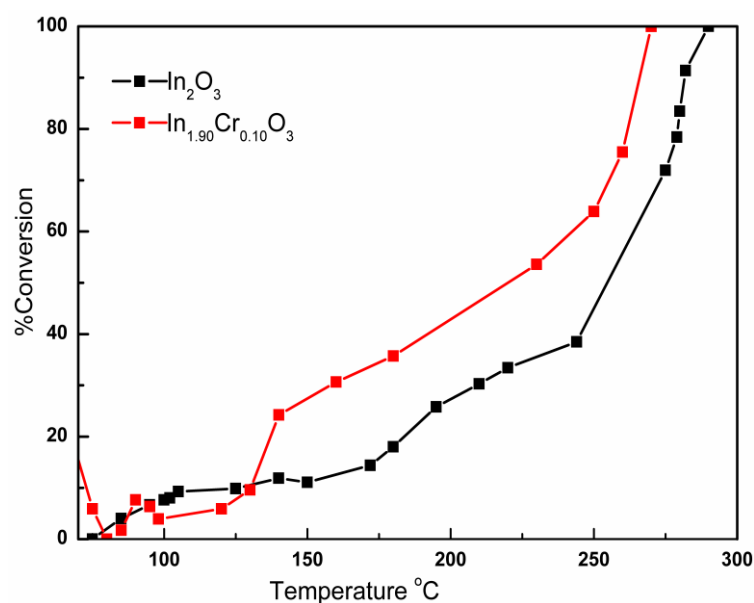


Fig.5.3 CO oxidation reaction over $\text{In}_{2-x}\text{Cr}_x\text{O}_3$ catalyst.

5.2.3 $\text{Ce}_{1-x}\text{In}_x\text{O}_2$

CeO_2 is a well known catalyst used for oxidation reactions and has been reported for CO oxidation, also acts as a good support material for other catalyst. Fig. 5.4 presents

the CO oxidation carried out on CeO₂ and Indium doped CeO₂ nanoparticles. For the pristine sample, initially there is no conversion until a temperature of 250 °C was attained. The oxidation proceeds slowly and a complete conversion was achieved at 345°C. For the doped sample with composition Ce_{0.9}In_{0.1}O₂, the oxidation is initiated at 170 °C and a complete conversion takes place at 270 °C. The In³⁺ doping in CeO₂ leads to the formation of oxygen deficient compound owing to its lower oxidation state compared to that of Ce⁴⁺. This increases the presence of cerium in Ce³⁺/Ce⁴⁺ dual oxidation states. These alterations in the structure increases its ability to play with oxygen mobility ,which could be the reason for obtaining complete conversion at lower temperature compared to that of pristine sample.

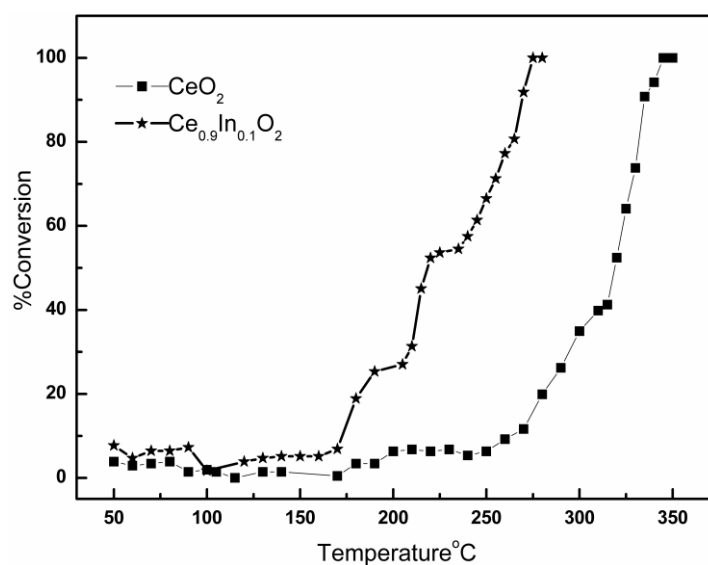


Fig.5.4 CO oxidation reaction over Ce_{1-x}In_xO₂ catalysts.

5.2.4 MgFe_{2-x}In_xO₄

Pristine and In³⁺ doped MgFe₂O₄ nanoparticles were screened for its catalytic activity for CO oxidation and the results are displayed in Fig. 5.5. For the pristine sample the conversion is initiated at 270°C, and a complete CO oxidation is attained at 380°C whereas in case of In³⁺ doped ferrite sample the CO oxidation is initiated at 188 °C, the

reaction proceeds at steady rate with 100% conversion achieved at 340°C. Reduction in the temperature for complete oxidation is obtained on doping.

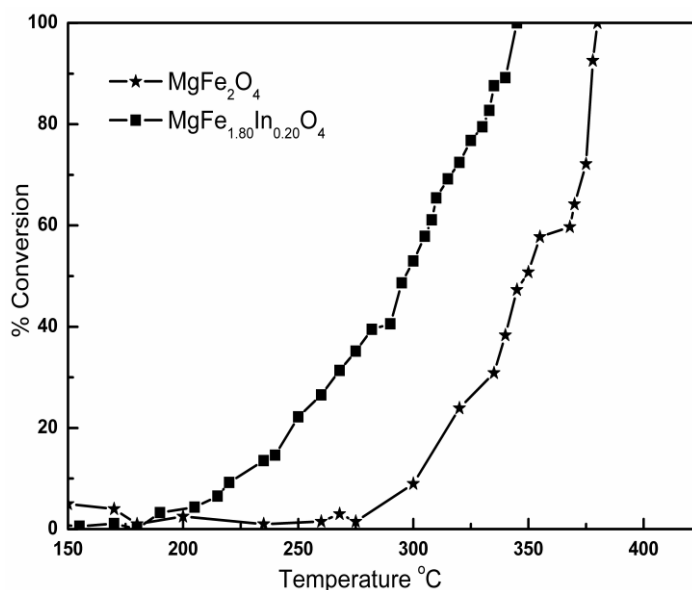


Fig.5.5 CO oxidation reaction over $MgFe_{2-x}In_xO_4$ catalysts.

5.3 Organic Transformations

Metal oxides have proved to be efficient heterogeneous catalysts for several organic transformations. Lewis acidity is one of the highlighting properties of these systems which are highly exploited in such reactions. In the present work we have investigated the catalytic activity of our prepared nanoparticles towards the following organic transformations.

5.3.1 Henry reaction

Henry reaction also known as the nitro aldol reaction is one of the important C-C bond formation reactions discovered by the chemist Louis Henry in 1895. It is a reaction between the nitroalkanes and the aldehyde or ketone to give β -nitro alcohol, the nitroaldol product. The nitroaldol products are of great importance as they can be further converted

to different important intermediates which find several applications including pharmaceuticals [366-370]. The development of heterogeneous solid catalysts for such reactions is one of the exciting tasks and the work is progressing in this field. With our prepared nanoparticles as catalysts we carried out the Henry reaction as follows:

5.3.1.1 Experimental

In a typical synthesis the aldehyde (1 mmol) and the nitro alkane (5 mL) which also acts as a solvent, were added to the round bottom flask containing the weighed amount of catalyst. The reaction mixture was kept for stirring for 24 h. The progress of the reaction was monitored with the help of thin layer chromatography (TLC) using (ethyl acetate /pet ether as the mobile phase). After 24 h the catalyst was separated with the help of the magnet/filtration. The reaction mixture was then extracted using ether and the product was purified by silica gel column chromatography. The compound was then dried and characterised by its melting point, IR and ^1H NMR and ^{13}C NMR wherever possible.

5.3.1.2 Results and discussions.

The initial optimisation was carried out using p-NO₂-C₆H₅-CHO and NO₂Me as the standard reaction. The different catalysts were tried initially, the one showing the best result was then used for optimisation of the amount of catalyst to be used. The observations are tabulated below in table 5.1.

Table 5.1 Screening of different catalysts for Henry reaction.

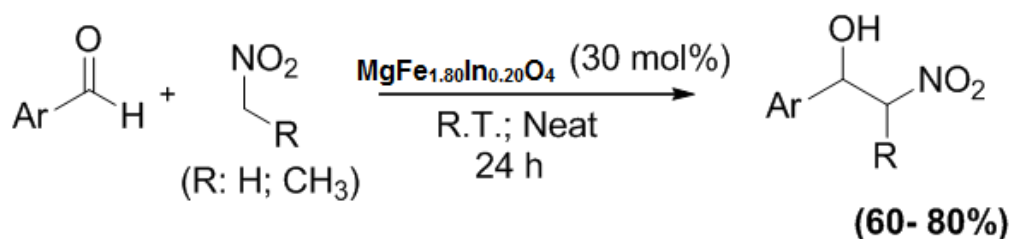
Sr. No.	Catalyst	Yield (%)
1	Blank reaction	No product
2	In ₂ O ₃	57
3	CeO ₂	50
4	MgFe ₂ O ₄	70
5	MgFe _{1.80} In _{0.20} O ₄	75

As seen from the above Table 5.1 the best yield was obtained with $\text{MgFe}_{1.80}\text{In}_{0.20}\text{O}_4$ catalyst. Further work was carried out to optimise the amount of catalyst to be used

Table 5.2 Optimisation of the amount of catalyst

Sr. No.	Amount of catalyst in mol%	Yield (%)
1	10	57
2	20	69
3	30	75
4	40	73

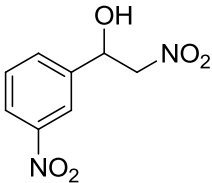
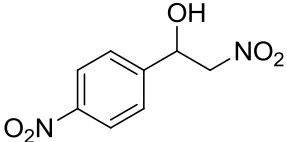
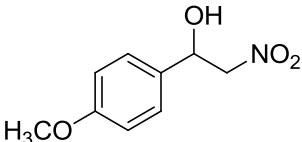
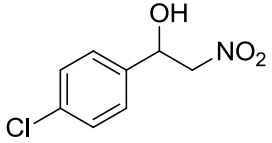
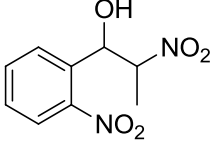
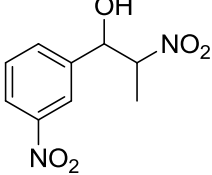
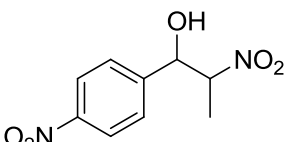
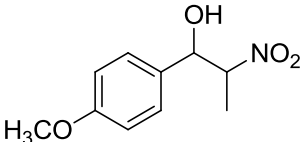
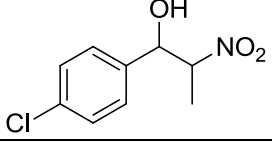
Several derivatives were prepared using 30 mol% of the catalyst using the following conditions given in the scheme 5.1. The results are tabulated in the table given below:



Scheme 5.1 Henry reaction on various substituted aromatic aldehydes with nitro methane and nitro ethane.

Table 5.3: Henry reactions of various substituted aromatic aldehydes with nitromethane and nitroethane using $\text{MgFe}_{1.80}\text{In}_{0.20}\text{O}_4$ catalyst.

Sr. No.	Aldehyde (Ar-CHO)	R	Product	Yield* (%)			IR (KBr) (cm ⁻¹)
					Reported	observed	
1	<i>o</i> -nitro benzaldehyde	H		72	63	61	3534, 1335, 1526

2	<i>m</i> - nitro benzaldehyde	H		70	63	63	3506, 1356, 1526
3	<i>p</i> - nitro benzaldehyde	H		75	85- 86	86	3528, 1342, 1530
4	<i>p</i> -anisaldehyde	H		60	40- 41	42	3512, 1354, 1556
5	<i>p</i> - chlorobenzaldehyde	H		62	35- 37	34	3510, 1353, 1549
6	<i>o</i> -nitro benzaldehyde	CH ₃		77	92	93	3545, 1345, 1550
7	<i>m</i> -nitro benzaldehyde	CH ₃		78	71	72	3541, 1342, 1539
8	<i>p</i> - nitro benzaldehyde	CH ₃		80	83	82	3513, 1335, 1553
9	<i>p</i> -anisaldehyde	CH ₃		61	*	*	3492, 1363, 1553
10	<i>p</i> - chlorobenzaldehyde	CH ₃		64	*	*	3500, 1350, 1540

*Thick yellow oil

The catalyst worked efficiently at room temperature giving products in fairly good yield. IR values corresponding to hydroxyl and nitro group are mentioned. NMR of some of the compounds are discussed below:

Table 5.3 Entry 1: ^1H NMR (Fig.5.6 (a)) (400 MHz, CDCl_3): δ 7.9-8.0 (m, 2H), 7.5-7.74 (m, 2H), 5.97 (brs, 1H), 4.3-4.8 (m, 2H), 4.02 (brs, 1H); ^{13}C MR (Fig. 5.6 (b)) (100 MHz, CDCl_3): δ 146.96 (Cq), 134.53 (CH), 134.39 (Cq), 129.67 (CH), 128.70 (CH), 124.93 (CH), 80.18($\text{CH}_2\text{-NO}_2$), 66.81(CH-OH).

Entry 2: ^1H NMR(Fig. 5.7 (a)) (400MHz, CDCl_3): δ 8.15-8.18 (m, 2H), 7.62-7.64 (dd, 2H, $J=8\text{Hz}$), 5.628/5.63 (t, 1H), 4.65 (d, 2H), 4.24-4.26 (brs, 1H); ^{13}C MR (Fig. 5.7 (b)) (100 MHz, CDCl_3): δ 147.74 (Cq), 145.84 (CH), 145.8 (CH), 127 (CH), 124 (CH), 80.74 (CH-OH), 69.98 ($\text{CH}_2\text{-NO}_2$).

Entry 3: ^1H NMR (Fig. 5.8) (400MHz, CDCl_3): δ 8.18-8.35 (m, 2H), 7.7-7.8 (m, 1H), 7.6-7.65 (m, 1H), 5.61-5.65 (m, 1H), 4.59-4.65 (m, 2H), 4.68 (m, 1H).

Entry 6: Compound had (1:1) ratio of mixtures of diastereomers. ^1H NMR(Fig. 5.9) (400 MHz, CDCl_3): δ 8.035-8.038 (dd, 1H), 8.017(dd, 1H), 7.93 (dd, 1H), 7.62-7.68 (m, 3H), 7.45-7.49 (m, 2H), 6.02 (d, 1H), 5.65 (d, 1H), 4.89-4.95 (m, 2H), 2.8 (brs, 2H), 1.45-1.48 (m, 6H).

Entry 7: Compound had (1:1) ratio of mixtures of diastereomers. ^1H NMR(Fig. 5.10) (400 MHz, CDCl_3): δ 8.127-8.24 (m, 4H), 7.2-7.68 (m, 4H), 5.47-5.48 (m, 1H), 5.11-5.13 (dd, 1H), 4.5-4.76(m, 2H), 3.3-3.4 (brs, 2H), 1.43-1.45 (dd, 3H), 1.32-1.34 (dd, 3H).

Entry 8: Compound had (1:1) ratio of mixtures of diastereomers. ^1H NMR(Fig. 5.11) (400 MHz, CDCl_3): δ 8.26-8.29 (m, 4H), 7.59-7.63 (m, 4H), 5.57-5.58 (m, 1H), 5.2-5.22 (d, 1H), 4.47-4.8 (m, 2H), 2.47 (brs, 2H), 1.5-1.52 (dd, 3H), 1.4-1.42(dd, 3H).

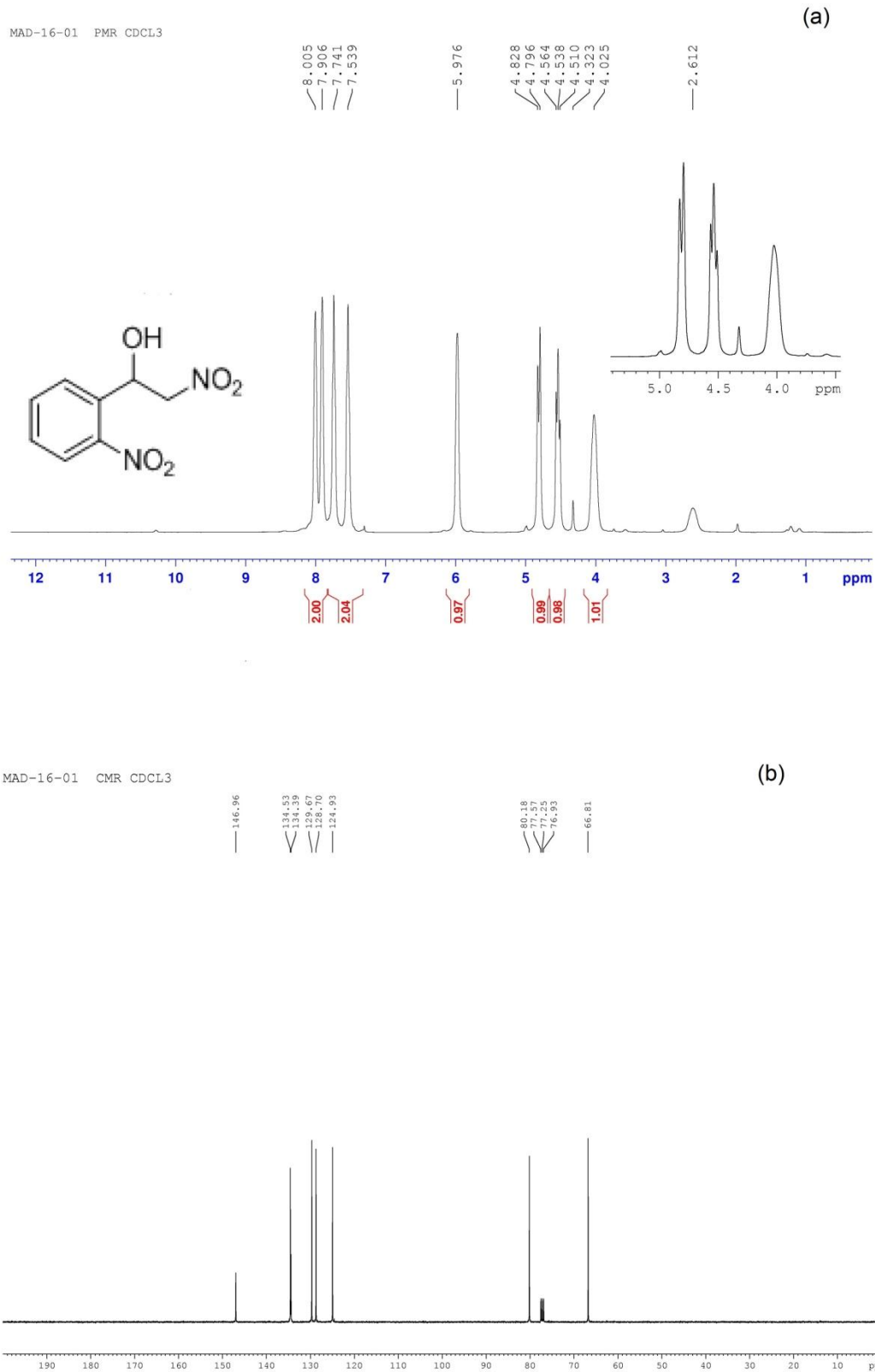


Fig.5.6 (a) ¹H and (b) ¹³C NMR spectra for compound 1 (Table 5.3).

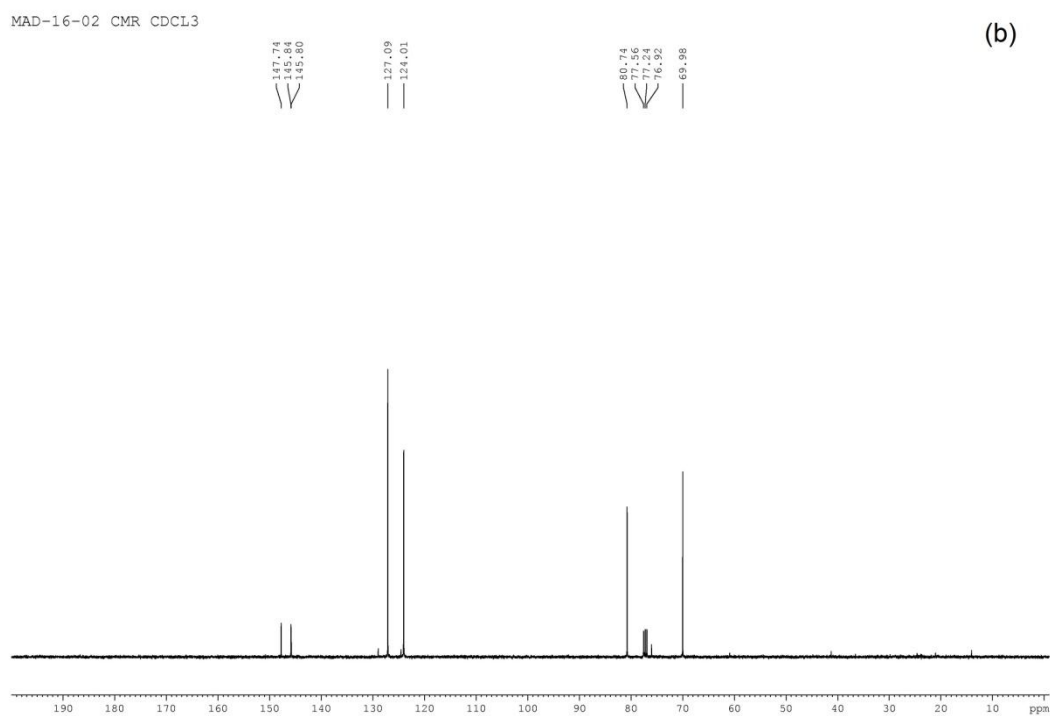
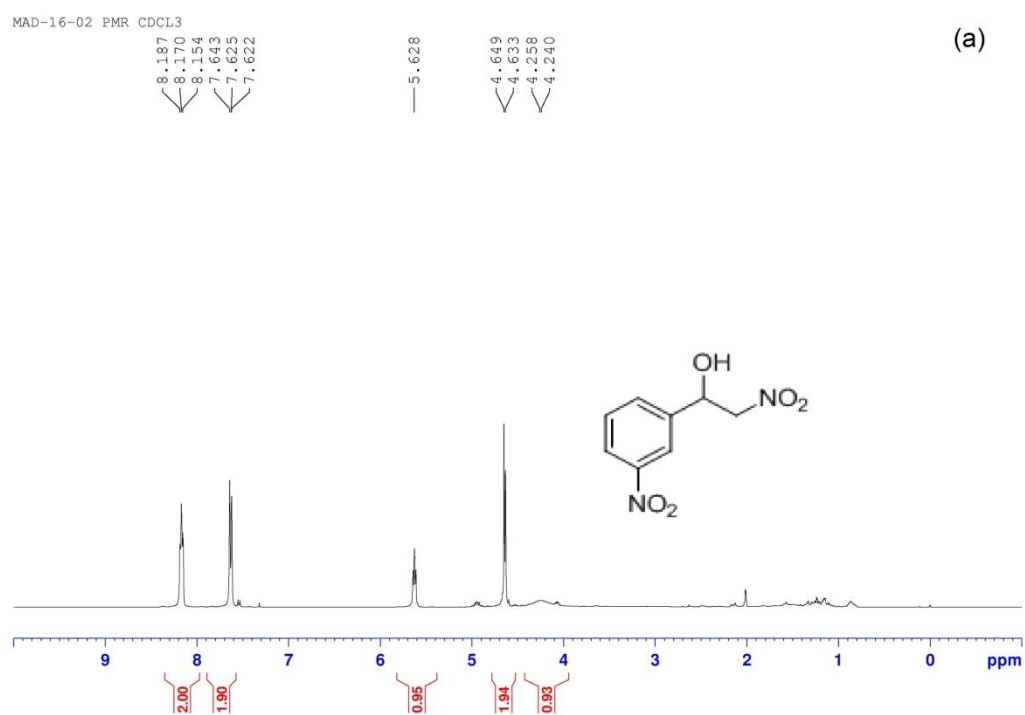


Fig.5.7(a) ¹H and (b) ¹³C NMR spectra for compound2 (Table 5.3).

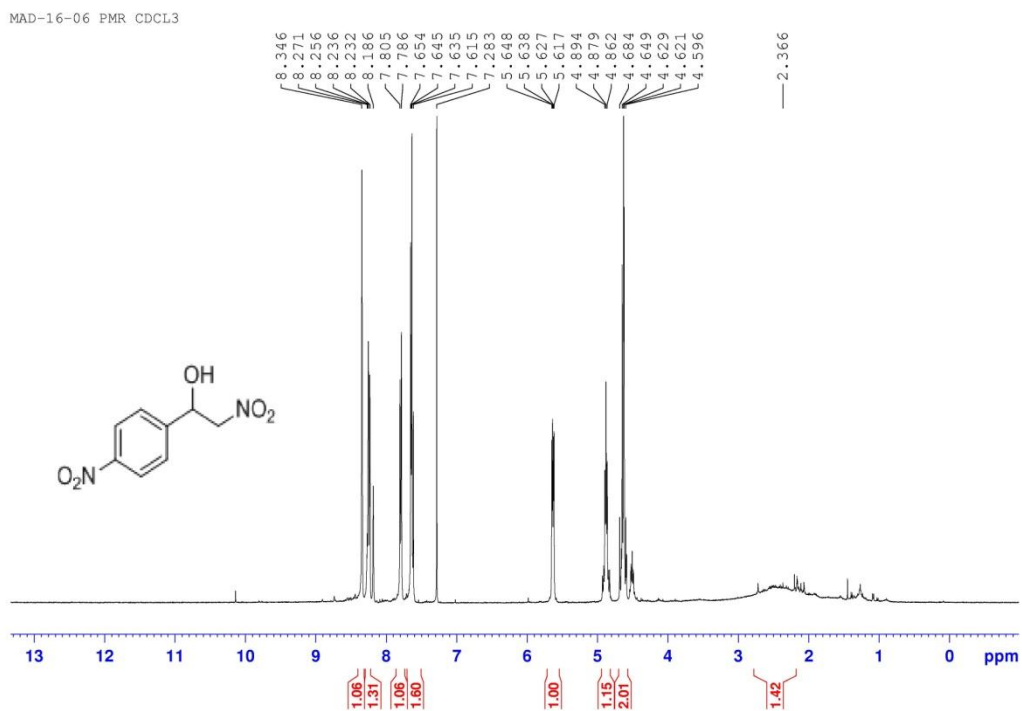


Fig.5.8¹H NMR spectra for compound3 (Table 5.3).

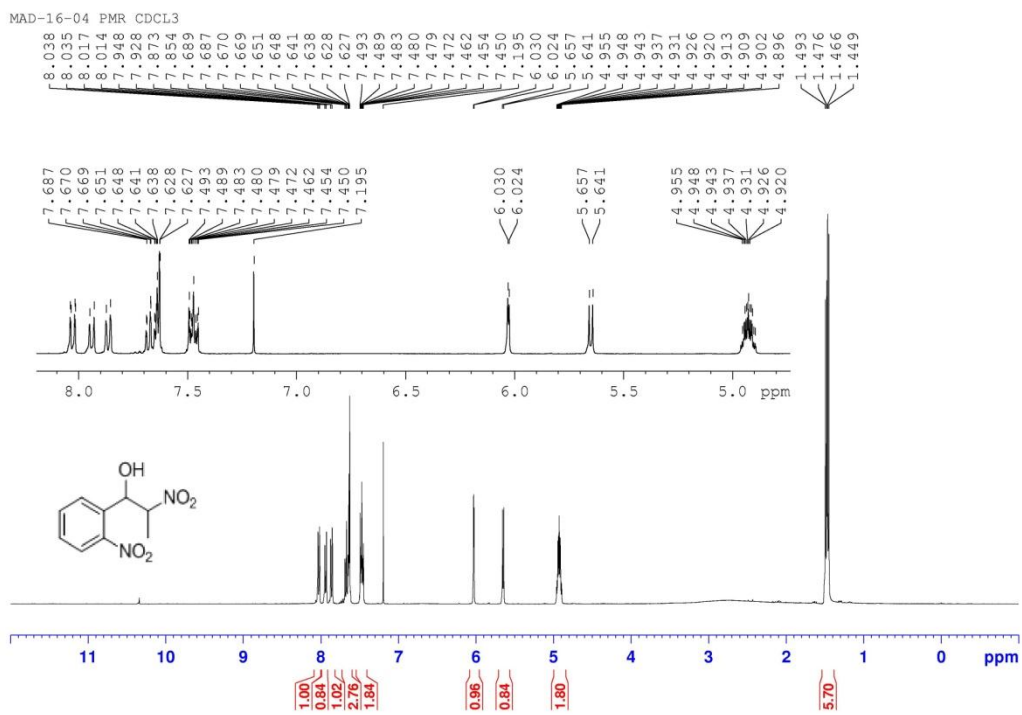


Fig.5.9¹H NMR spectra for compound6 (Table 5.3).

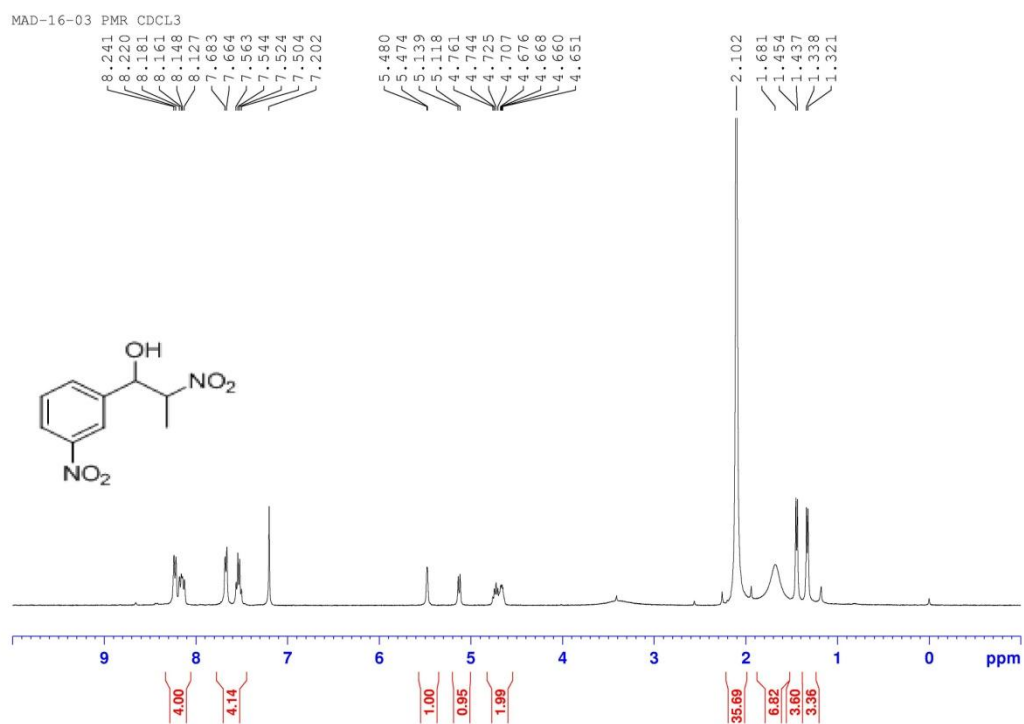


Fig.5.10 ¹H NMR spectra for compound7 (Table 5.3).

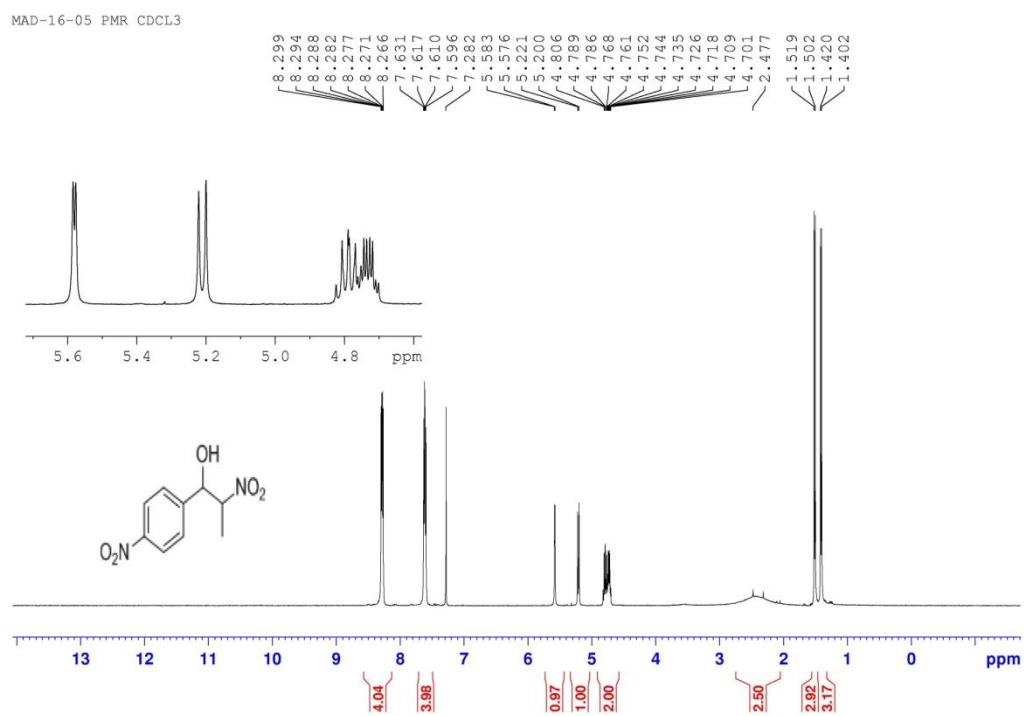


Fig.5.11 ¹H NMR spectra for compound8 (Table 5.3).

5.3.2 Quinazolinones Synthesis.

Quinazolinones are the group of heterocyclic compounds that are part of different natural and synthetic products. Their scaffolds form the important constituents of several pharmaceutical drugs which possesses the properties such as antifungal, anticonvulsant, antibacterial, anti-HIV, anticancerous, anti-inflammatory [371]. Numerous methods have been reported for the synthesis of different functionalised quinazolinones including reaction of Isotactic anhydride with aldehyde and NH_4OAc [372-375]. We carried out the synthesis of this molecule using our catalysts under microwave irradiation. The observed results are given below:

5.3.2.1 Experimental:

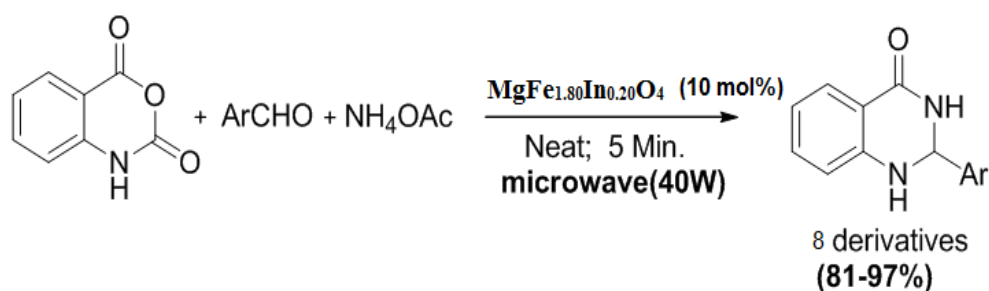
In a typical synthesis isotactic anhydride, aldehyde and ammonium acetate were taken in 1:1:1 ratio. These were added to the flask containing weighed amount of the catalyst. The reaction mixture was subjected to microwave radiation and the progress was monitored using TLC. The workup was carried out using ethanol and the obtained products were characterised by melting point, IR and NMR in few cases.

5.3.2.2 Results and discussion

The optimisation reaction was carried out using *p*-Cl –benzaldehyde, isotactic anhydride and NH_4OAc . MgFe_2O_4 and $\text{MgFe}_{1.80}\text{In}_{0.20}\text{O}_4$ were the only two catalysts screened for this reaction under microwave where former gave the yield of 90% whereas latter gave 94% yield. So $\text{MgFe}_{1.80}\text{In}_{0.20}\text{O}_4$ was chosen as the catalyst. Further the amount of catalyst to be used was optimised. As seen from Table 5.4, no great difference in % yield was obtained for 10 and 20 mol % of the catalyst so further reactions were carried out in 10 mol % of the catalyst as per the following scheme 5. 2.

Table 5.4 Optimisation of the amount of catalyst.

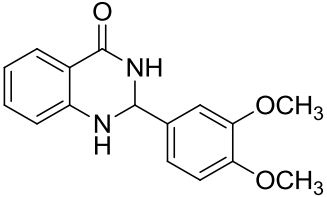
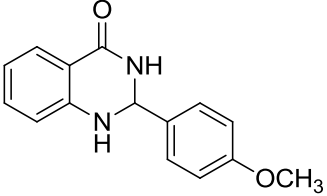
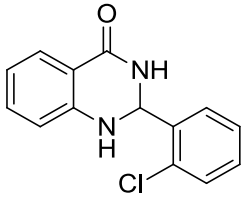
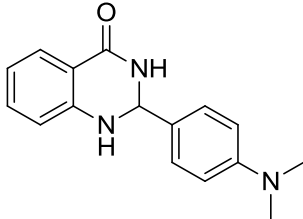
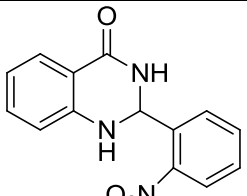
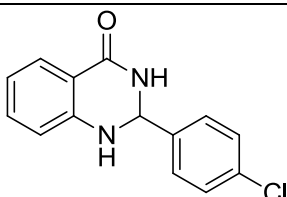
Sr. No.	Amount of catalyst (mol %)	% Yield
1	5	86
2	10	94
3	20	95



Scheme 5.2 Synthesis of 2,3 dihydroquinazolinones-4(1H)-one

Table 5.5 Synthesis of derivatives of Quinazolinones

Sr. No	Aldehyde (Ar-CHO)	Product	Recrystallized yield (%)	Melting point		IR (KBr, cm^{-1})
				Observed	Reported	
1	Benzaldehyde		93	219	219-228	3304, 1666
2	Salicylaldehyde		93	220	218-219	3340, 3205, 1666
3	<i>m</i> -hydroxybenzaldehyde		87	207	209	3242, 3223, 1643

4	Veratraldehyde		96	206	208- 213	3354, 1666, 1016
5	<i>p</i> -anisaldehyde		86	174	177- 179	3300, 1658, 1033
6	<i>o</i> -chlorobenzaldehyde		92	202	202- 204	3361, 1643
7	<i>p</i> -(<i>N,N</i> -dimethylamino) benzaldehyde		80	205	205- 207	3296, 1666
8	<i>o</i> -nitrobenzaldehyde		95	180	190- 192	3423, 3340, 1658, 1514, 1342
9	<i>p</i> -Chloro benzaldehyde		94	200	198- 200	3307, 1651

The compounds were recrystallised using ethanol. The Infra red values corresponding to carbonyl, amine and nitro are obtained and are specified in the table.

NMR: Table 5.5 Entry 6: ¹H NMR (Fig. 5.12) (400MHz, DMSO-d₆): δ 6.13(s, 1H,), 6.71(t, 1H, J=8.0Hz), 6.76(d 1H, J=8.0Hz,), 7.03 (s, 1H, NH), 7.26 (dt, J=7.6, 1.6 Hz, Ar-H), 7.38-7.42(m, 2H,), 7.48 -7.52 (m, 1H,), 7.64-7.67(m, 1H,), 8.2(s, 1H, NH).

Table 5.5 Entry 9: $^1\text{H-NMR}$ (Fig.5.13) (400 MHz, DMSO-d_6): $\delta = 5.77$ (s, 1H), 6.7-6.76 (m, 2H), 7.17 (s, 1H, NH), 7.27-7.62 (m, 6H), 8.37 (s, 1H, NH)

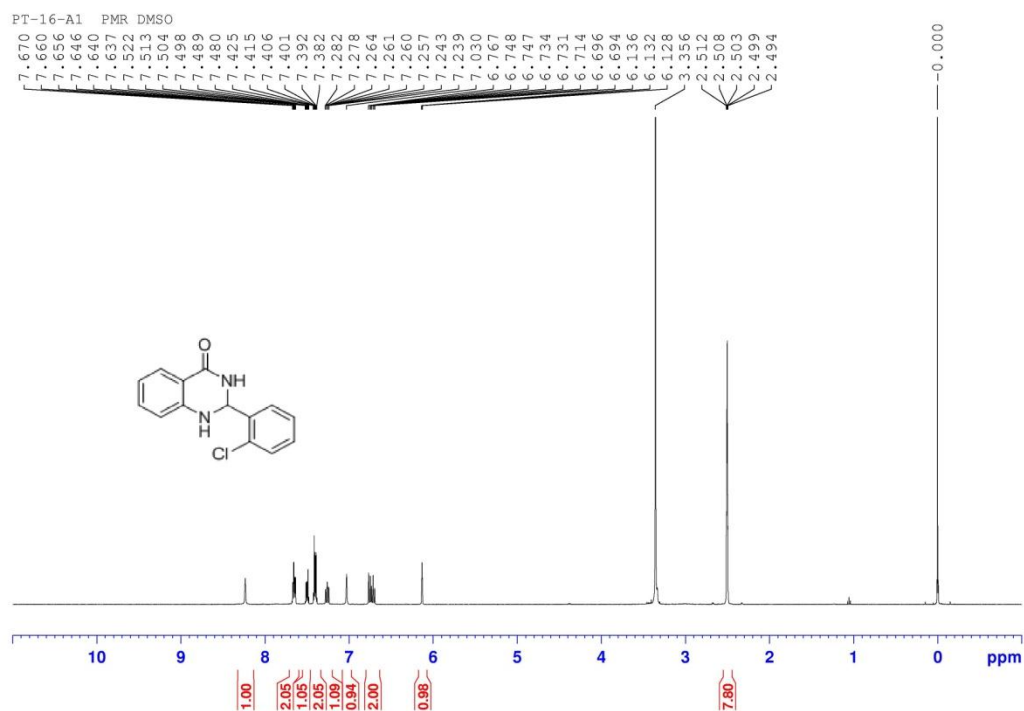


Fig.5.12 $^1\text{H NMR}$ spectra for compound 6 (Table 5.5).

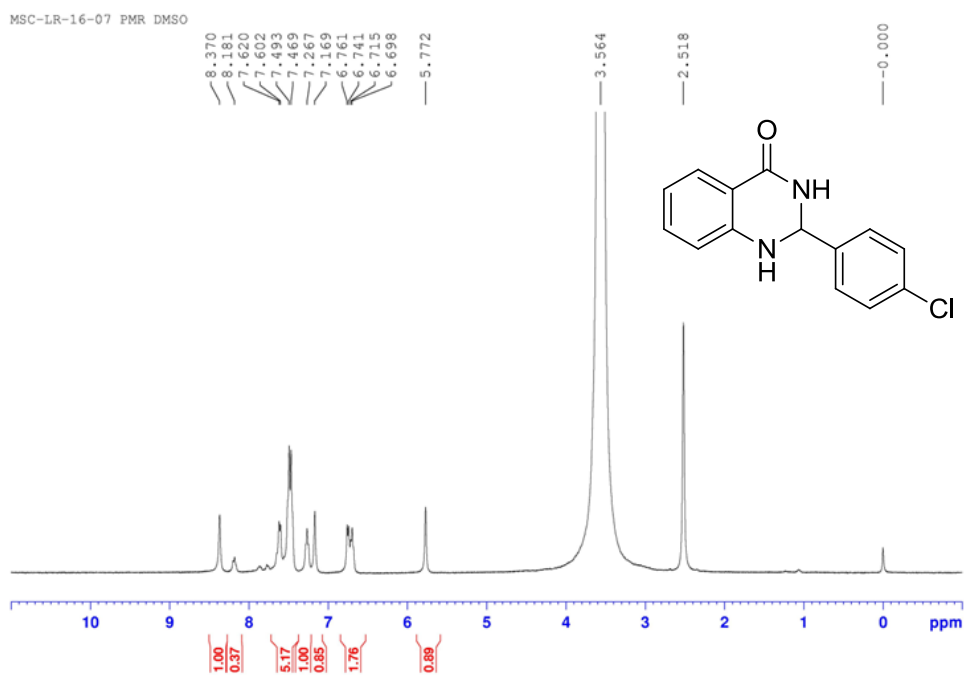


Fig.5.13 $^1\text{H NMR}$ spectra for compound 9 (Table 5.5)

5.3.3. Benzimidazole synthesis

Benzimidazole is a heterocyclic compound that forms an important scaffold of biological and pharmacological products. Several compounds containing benzimidazole component display biological properties like antiulcer, anticancer, antimalarial, antihistaminic, anti-oxidant, antiviral, antifungal and many more [376]. Ultimately they have formed the key part of important marketed drugs like *Omeprazole*, *Candesertan*, *Mebendazole*, *Astemizole* [377-379]. The application of benzimidazoles attracts researchers to develop faster and better methods of synthesis and the work has progressed immensely. Several solid state catalysts have been employed to synthesize substituted benzimidazoles from *o*-phenylenediamine and aldehydes including $\text{Fe/CeO}_2\text{-ZrO}_2$, $\text{MoO}_3/\text{CeO}_2\text{-ZrO}_2$, In_2O_3 , MnFe_2O_4 [154, 380-382]. The products obtained were either mono-substituted, di-substituted or mixture of both. We have carried out the synthesis of substituted benzimidazoles using our prepared catalyst.

5.3.3.1 Experimental

In a typical synthetic procedure 1 mmol of the *o*-phenylenediamine (OPD) and 2 mmol of aldehyde are added to the 50 ml round bottom flask containing 10 mol% of the catalyst in 5 mL of ethanol as solvent. The reaction mixture was then stirred continuously on magnetic stirrer and the progress of the reaction was monitored by TLC using 20% ethyl acetate and pet ether mixture as the mobile phase. The catalyst was separated either magnetically or by filtration as per the nature of the catalyst. The reaction mixture was extracted in ether. The product obtained after removing the solvent was purified on silica gel column using ethyl acetate / pet ether mixture. The products were characterised by their melting points and IR.

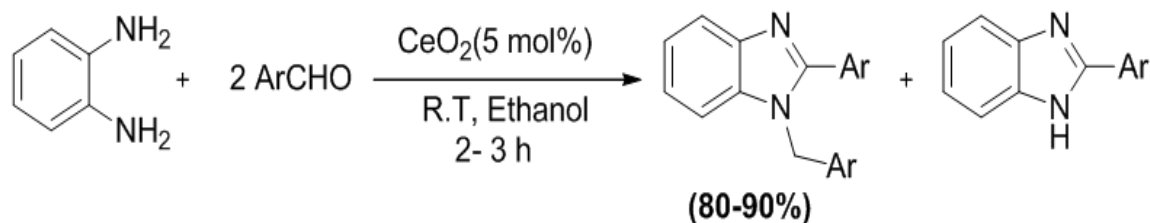
5.3.3.2 Results and discussion

The standard reaction for screening of catalyst was carried out with OPD and benzaldehyde using 5 mol% of the catalyst. Table 5.6 shows the optimisation of the catalysts.

Table 5.6 Screening of the catalyst

Sr. No.	Catalyst	Yield (%)
1	Blank reaction	35
2	In ₂ O ₃	63
3	CeO ₂	90
3	MgFe ₂ O ₄	74

Using CeO₂ as the catalyst which gave the best yield, few derivatives were prepared as per the given Scheme. Disubstituted benzimidazole was the major product obtained in all the reactions.



Scheme 5.3: Synthesis of 2-aryl-1-arylmethyl-1H-benzimidazole from OPD and aryl aldehydes.

Table 5.7 Synthesis of 2-aryl-1-arylmethyl-1H-benzimidazole

Sr. No.	Ar	Yield (%) (disubstituted product)	Melting points °C.	
			Reported	Observed
1	C ₆ H ₅	90	132-134	132
2	p-NO ₂ -C ₆ H ₅	88	306-308	304
3	P-OCH ₃ -C ₆ H ₅	83	128-132	131
4	p-Cl-C ₆ H ₅	82	136	134

The work on benzimidazole synthesis with the CeO₂ catalyst was found to be published in 2013 by R. Shelkaret al .[250].

5.3.4 Friedel Crafts reaction

Friedel crafts reactions are a class of c-c bond formation reactions catalysed by lewis acids. The friedel crafts acylation and alkylation are the two reactions mostly carried out using AlCl₃. The amount of AlCl₃ required is more than the stoichiometric and also its disposal is a tedious work. Other homogenous catalysts include BF₃, H₂SO₄, FeCl₃ and ZnCl₂[383, 384]. Researchers started identifying new catalyst that can be used to carry out these reactions. Several metal triflates [385,386] ionic liquids [387] In₂O₃, Ga₂O₃, and ZnO supported on high silica mesoporous MCM-41 and Fe₂O₃, FeCl₃ on mesoporous silica by V.R Chaudhary [388-389] zeolites [390].

We have carried out the Friedle Crafts acylation reactions with our prepared catalyst and the results are shown below:

5.3.4.1 Experimental:

The standard reaction was carried out using anisaldehyde and benzyl chloride. The reactants were taken in 1:1 ratio and were added to the 10 mol% of the catalyst and were kept for stirring. The reaction was monitored using TLC (using 10% mixture of ethyl acetate and pet ether) followed by a work up. The compound was purified on silica gel column and the product was identified by comparing with the authentic sample.

Table 5.8 Screening of catalyst

Sr.No.	Catalyst	% yield
1	In ₂ O ₃	74
2	CeO ₂	No product
3	MgFe ₂ O ₄	No product
4	neat	No product

The product was formed in good yields using In_2O_3 as a catalyst but unfortunately the catalyst could not be recovered so we did not go further with these reactions.

5.4 Biomedical application: Enzyme inhibition

Pristine and Ag doped In_2O_3 nanoparticles were screened for its *In vitro* enzyme inhibition activity against α -amylase and α -glucosidase. The inhibition assays were carried out as follows

5.4.1 Experimental:

In vitro α -amylase and α -glucosidase inhibition assays

The α -amylase inhibition activity of synthesized nanoparticles was determined by following 3, 5-dinitrosalicylic acid (DNSA) colorimetric method [391]. Pristine In_2O_3 and silver doped In_2O_3 nanoparticles were dispersed in sodium phosphate buffer (pH 6.9). The stock solution of α -amylase also prepared in sodium phosphate buffer (pH 6.9) was mixed with the different concentrations (25 μg to 300 $\mu\text{g}/\text{mL}$) of pristine In_2O_3 or 2% silver doped In_2O_3 and incubated at 37 °C for 30 min. To this 1% starch (Merk Pvt. Ltd.) was added, and continued for incubation for 30 more min. DNSA was added to the above reaction mixture followed by boiling in water bath for 10 min. The tubes were cooled and spectrophotometer (Shimadzu analytical India Pvt. Ltd.) readings were taken at 540 nm in triplicates.

The α -glucosidase inhibition assay was carried out following Nitrophenol- α -D-Glucopyranoside (pNPG) colorimetric method [392]. The α -glucosidase solution prepared in sodium phosphate buffer (pH 6.9) was mixed with different concentrations of In_2O_3 or silver doped In_2O_3 nanoparticles (0.015 μg to 300 $\mu\text{g}/\text{mL}$). After incubation of above

mixture at 37 °C for 15 min, PNPG (Himedia Pvt. Ltd.) was added to it. The reaction mixture was incubated for 10 min at 37 °C. To stop the reaction, Na₂CO₃ (0.1 M) was added and spectrophotometer readings were taken at 405 nm in triplicates. Standard anti-diabetic drug Acarbose (PHR1253, Fluka) was used as a positive control for both α -amylase and α -glucosidase inhibition assay. Controls for both assays contain only starch and α -amylase/ α -glucosidase without nanoparticles or Acarbose. The percent inhibition of enzyme activity was determined as: % inhibition = (Test control - test sample / Test control) \times 100.

Statistical analyses of the assays were carried out by using Microsoft Excel. All samples were evaluated in triplicates and standard deviation was calculated. Sample data were analysed with student's t-test and One-way Analysis of variance (ANOVA) with Tukey's test. Within the single experiment, the significance of the data for each dose against that of the respective control was evaluated by the Student's t-test. Dose dependent response of In₂O₃ and silver doped In₂O₃ nanoparticles on both α -amylase and α -glucosidase were evaluated by one-way ANOVA Tukey's test. A level of probability of P < 0.05 was considered as statistically significant data.

5.4.2 Results and discussion

The dose-dependent inhibition of α -amylase by pristine In₂O₃ nanoparticles was observed, with a minimum inhibition (5.55 \pm 0.91%) at 25 μ g/mL and the maximum inhibition (26.39 \pm 6.36%) at the 300 μ g/mL. Dose dependent α -amylase inhibition shown by pristine In₂O₃ nanoparticles observed at various concentrations of In₂O₃ was significant in comparison to their respective controls as per the t-test (Fig. 5.14 (a)). One way ANOVA of the percentage inhibition of α -amylase observed in the control and different concentrations of In₂O₃ showed significance at P < 0.0001 (F = 20.18).

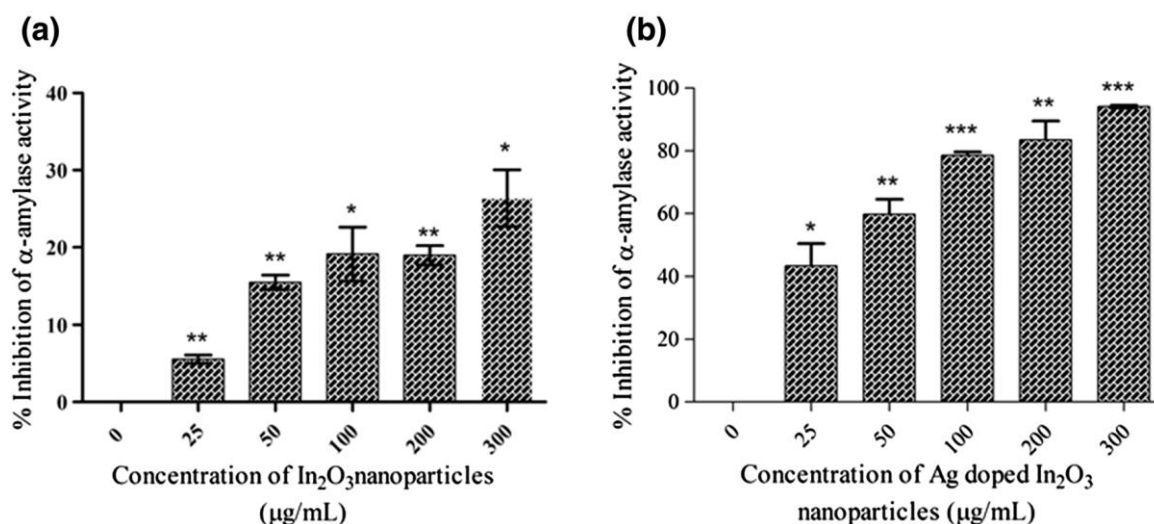


Fig.5.14 Percentage inhibition of α -amylase by various doses of In_2O_3 (a) and Ag-doped In_2O_3 (b). Data are mean \pm SD (* P <0.05; ** P <0.01; *** P <0.001 denote statistically significant difference from the test control, Student's t test significance)

Similarly, dose dependent inhibition by silver doped In_2O_3 nanoparticles indicated significant inhibition of α -amylase at all doses of silver doped In_2O_3 nanoparticles studied as per the t -test (Fig. 5.14 (b)). It ranged from $43.31 \pm 7.15\%$ at $25 \mu\text{g/mL}$ to the $94.08 \pm 0.4895\%$ at $300 \mu\text{g/mL}$. One way ANOVA of the percentage inhibition of α -amylase observed in the control and at various concentrations of silver doped In_2O_3 exhibited significance at $P < 0.0001$ ($F = 64.33$).

Significant α -glucosidase inhibition was depicted by all the concentrations of pristine In_2O_3 and silver doped In_2O_3 nanoparticles, in comparison to their respective controls (t -test) (Fig. 5.15 (a) and 5.15 (b)). Dose dependent inhibition of α -glucosidase by pristine In_2O_3 ranged from $13.29 \pm 0.96\%$ at the lowest concentration ($25 \mu\text{g/mL}$) to $65.25 \pm 2.28\%$ at $300 \mu\text{g/mL}$. One way ANOVA of the percentage inhibition of α -glucosidase observed in the control and different doses of pristine In_2O_3 showed significance at $P < 0.0001$ ($F = 117.6$). Whereas, inhibition depicted by silver doped In_2O_3 ranged from $6.397 \pm 0.45\%$ at $0.015 \mu\text{g/mL}$ to $99.62 \pm 0.16\%$ at $0.18 \mu\text{g/mL}$. One

way ANOVA of the percentage inhibition of α -glucosidase observed in the control and different doses of silver doped In_2O_3 also depicted significance at $P < 0.0001$ ($F = 538.7$).

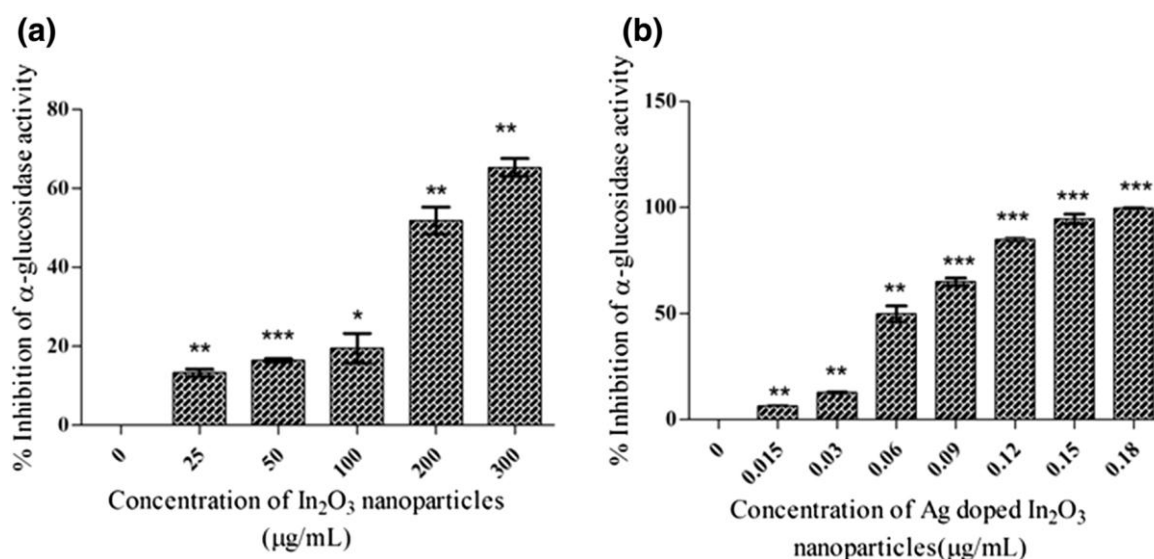


Fig. 5.15 Percentage inhibition of α -glucosidase by various doses of In_2O_3 (a) and Ag-doped In_2O_3 (b). Data are mean \pm SD (* $P < 0.05$; ** $P < 0.01$; *** $P < 0.001$ denote statistically significant difference from the test control, Student's t test significance)

The dose-dependent inhibition of α -amylase and α -glucosidase by standard anti-diabetic drug Acarbose is as shown in Fig. 5.16 (a) and (b). The α -amylase and α -glucosidase inhibition at various doses of pristine In_2O_3 , silver doped In_2O_3 nanoparticles

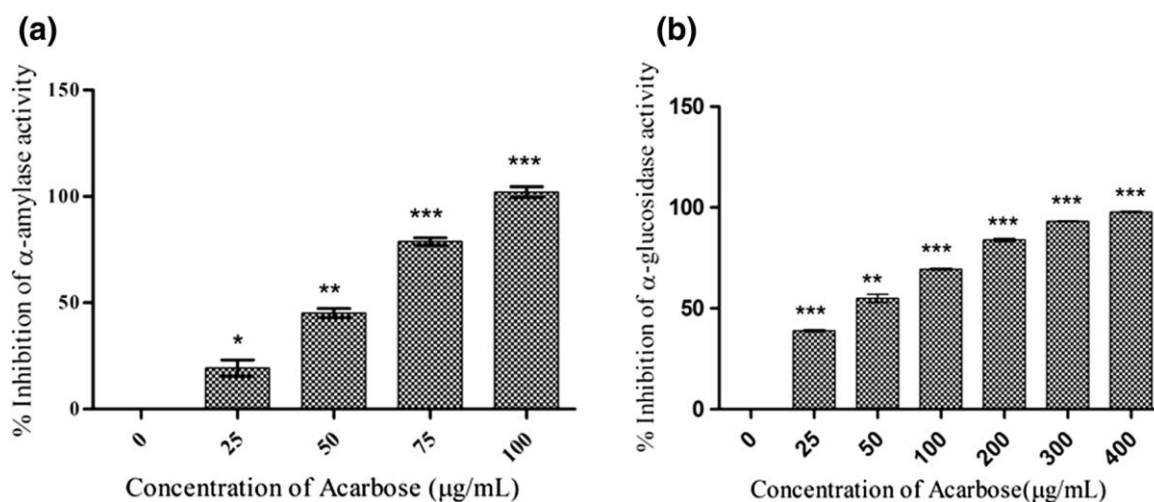


Fig. 5.16 Percentage inhibition of α -amylase (a) and α -glucosidase (b) by various doses of acarbose. Data are mean \pm SD (* $P < 0.05$; ** $P < 0.01$; *** $P < 0.001$ denote statistically significant difference from the test control, Student's t test significance)

and Acarbose were compared with each other and represented graphically in Fig. 5.17 (a) and 5.17(b) respectively. A linear increase in % inhibition of α -amylase was observed with the increasing doses of pristine In_2O_3 , silver doped In_2O_3 nanoparticles and Acarbose respectively (Fig. 5.17 (a)). The silver doped In_2O_3 nanoparticles demonstrated, 3.5 fold higher inhibition of α -amylase compared to pristine In_2O_3 nanoparticles. Similarly, a linear increase in α -glucosidase inhibition was observed with increasing doses of pristine In_2O_3 and silver doped In_2O_3 nanoparticles. The inhibition of α -glucosidase by silver doped In_2O_3 was approximately 2.5×10^3 fold higher than pristine In_2O_3 nanoparticles and 2.2×10^3 fold more than Acarbose at all the concentrations.

At concentration of 100 $\mu\text{g}/\text{mL}$ silver doped In_2O_3 demonstrated 80% inhibition of α -amylase in comparison to 100% inhibition by Acarbose. However silver doped In_2O_3 nanoparticles depicted exceptional inhibition of α -glucosidase activity (100% inhibition at 0.18 $\mu\text{g}/\text{mL}$) in contrast to Acarbose (97.72% inhibition at 400 $\mu\text{g}/\text{mL}$) under standard conditions (Fig. 5.17 (a, b)).

The inhibition of α -amylase and α -glucosidase activity by pristine In_2O_3 and silver doped In_2O_3 is remarkably distinct as presented in Fig. 5.17. It is noteworthy that silver

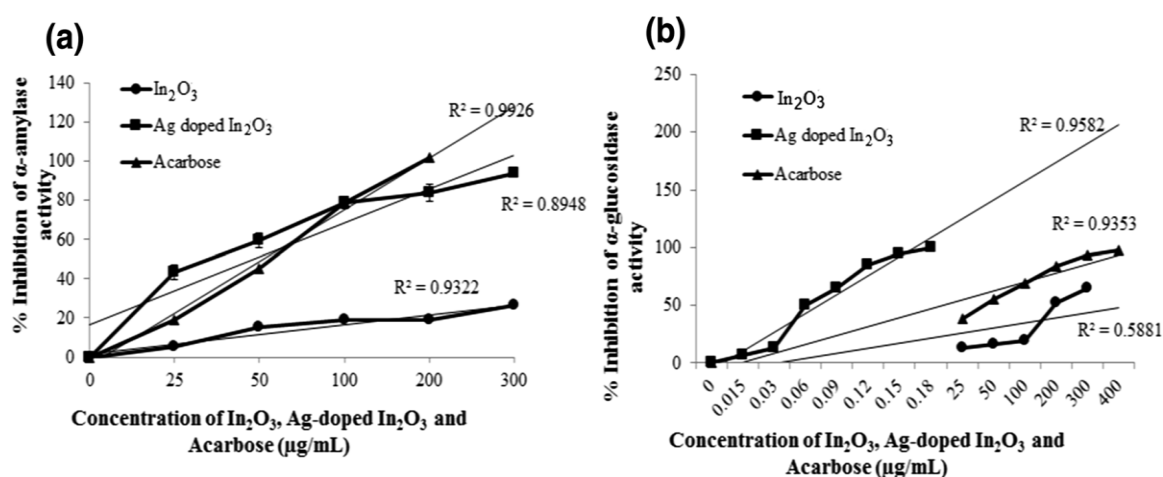


Fig. 5.17 Comparison of the percentage inhibition of α -amylase and α -glucosidase induced by various doses of In_2O_3 , Ag-doped In_2O_3 and acarbose. Each point indicates the mean \pm SD

doping of In₂O₃ improves its potential to substantially inhibit the activities of two model enzymes (α -amylase and α -glucosidase) in comparison to pristine In₂O₃. Thus, silver doped In₂O₃ nanoparticles were found to be potential enzyme inhibitors at very low concentrations especially for α -glucosidase, and are thus can be a good candidate drug as starch blocker. The free silver is reported to be toxic and doping of silver in metal oxide reduces the toxicity of free silver to human cells. An effective strategy for type-2 diabetes management, is the strong inhibition of intestinal α -glucosidase and mild inhibition of pancreatic α -amylase, because high α -amylase inhibition could be related to intestinal discomfort [393, 394]. Our results are in agreement with these findings.

5.5 Toxicity Studies

One of the challenges in the field of nanotechnology is environmental health and safety, which is focusing on the consideration of the properties of nanoparticles that could pose hazards to the environment and human beings [395]. It is conceivable that aquatic environments may be polluted with nanoparticles resulting from consumer products as well as from accidental releases during nanoparticle production, transportation and disposal operations. Thus, these nanoparticles pose risk of causing damage to aquatic organisms and eventually becoming a new class of hazardous material to humans through food web. Both *in vivo* and *in vitro* study was carried out. For *in vivo* study zebrafish as taken as model organism and for *in vitro* study was carried in up human peripheral blood lymphocytes culture. Zebrafish (*Danio rerio*) have been used extensively as a vertebrate model for nanotoxicology studies because of their short breeding cycle, fast rate of development, lower husbandry cost, small size, and completely sequenced genome [396-399].

Comet assay is a gel electrophoresis based method that can be used to measure DNA damage in individual eukaryotic cells. It is versatile, relatively simple to perform and sensitive assay developed by Singh et al.[400].

Pristine and Ag and Co doped In_2O_3 nanoparticles In_2O_3 showed descent biomedical and catalytic activities respectively. Among the prepared nanoparticles pristine In_2O_3 , $\text{In}_{1.96}\text{Ag}_{0.04}\text{O}_3$ and $\text{In}_{1.88}\text{Co}_{0.12}\text{O}_3$ were studied for their toxicity effects on zebrafish embryos and isolated human lymphocytes. The results obtained are discussed in this section.

5.5.1 Results and discussion

5.5.1.1 Effect on Zebrafish embriyo

The damage of zebrafish embriyo is shown by the tailing of the embriyo as shown in Fig. 5.18.

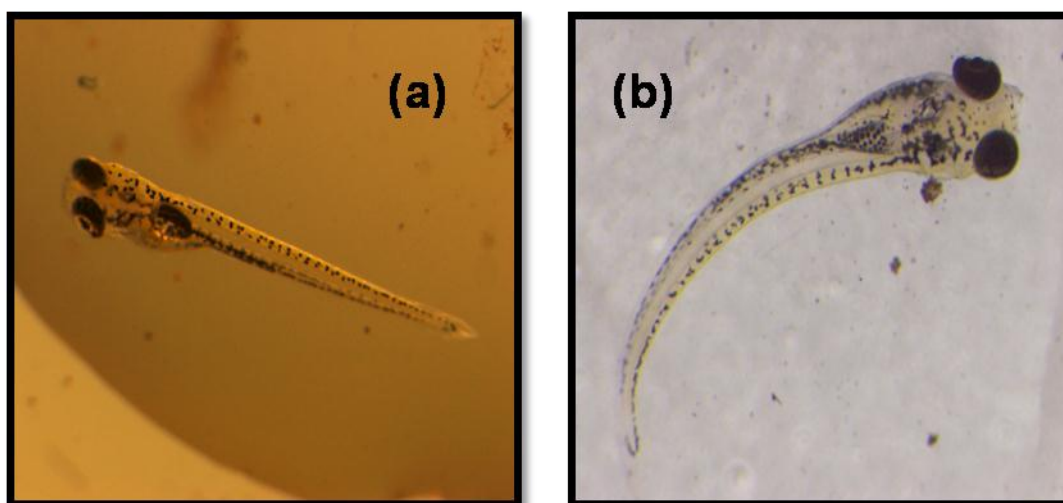


Fig 5.18 (a) Normal embriyo (b) Damaged embriyo

a) In_2O_3 Nanoparticles

Percentage of DNA damage observed during exposure of Zebrafish embryos to Indium oxide nanoparticle at 120 hpf is graphically represented in Fig. 5.19. A dose dependent increase in the single stranded breaks in the form of comet(% tail DNA) was observed. However none of the doses induced statistically significant DNA damage.

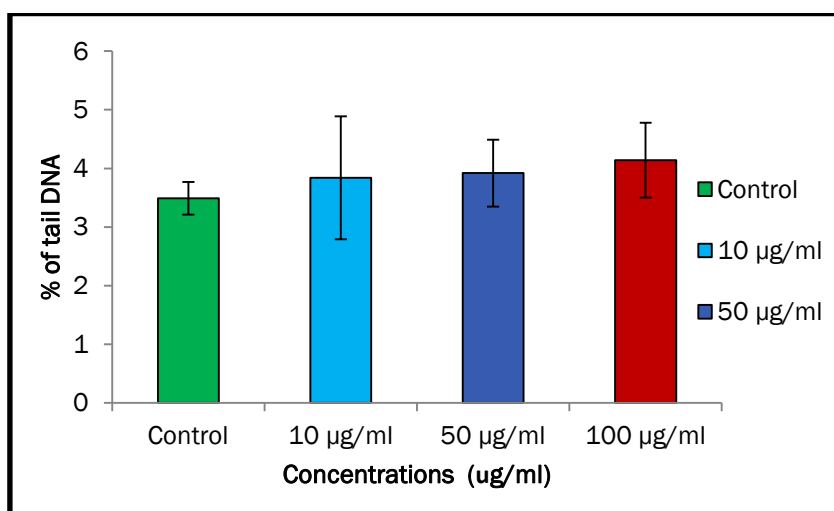


Fig. 5.19: % tail DNA in zebrafish larvae exposed to indium oxide nanoparticle solution at 120hpf

b) $\text{In}_{1.88}\text{Co}_{0.12}\text{O}_3$ nanoparticles

Percentage of DNA damage observed due to exposure of Zebrafish embryos to cobalt doped Indium oxide nanoparticle at 120 hpf is graphically represented in Fig.

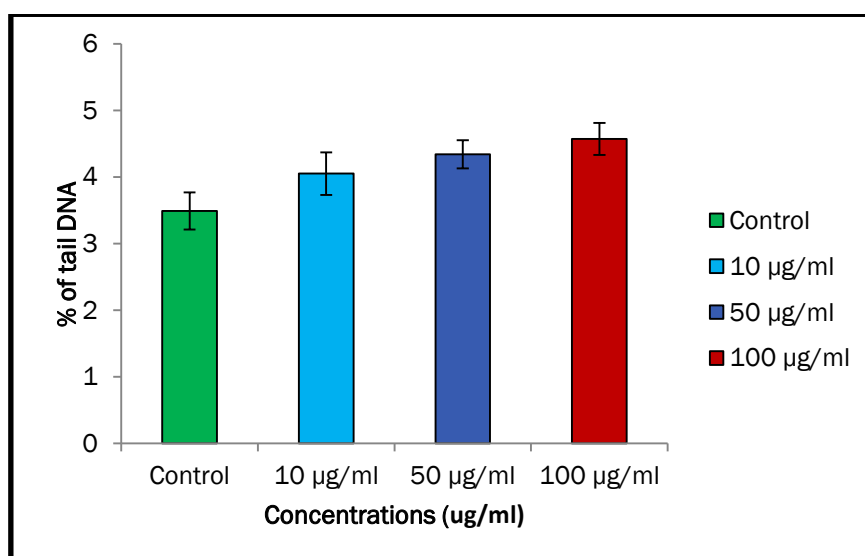


Fig. 5.20: % tail DNA in zebrafish larvae exposed to cobalt doped indium oxide nanoparticle solution at 120 hpf

5.20. The single stranded DNA damage was found to elevate with the increase in the dose level of the test solution. However it did not show a statistically significant increase as compared to the control.

c) $\text{In}_{1.96}\text{Ag}_{0.04}\text{O}_3$ nanoparticles

Percentage of DNA damage observed due to exposure of Zebrafish embryos to 2% silver doped Indium oxide nanoparticle solution at 120 hpf is graphically represented in Fig. 5.21A statistically significant increase in the DNA damage was observed at a higher dose (100 $\mu\text{g}/\text{ml}$) showing ($p < 0.05$) level.

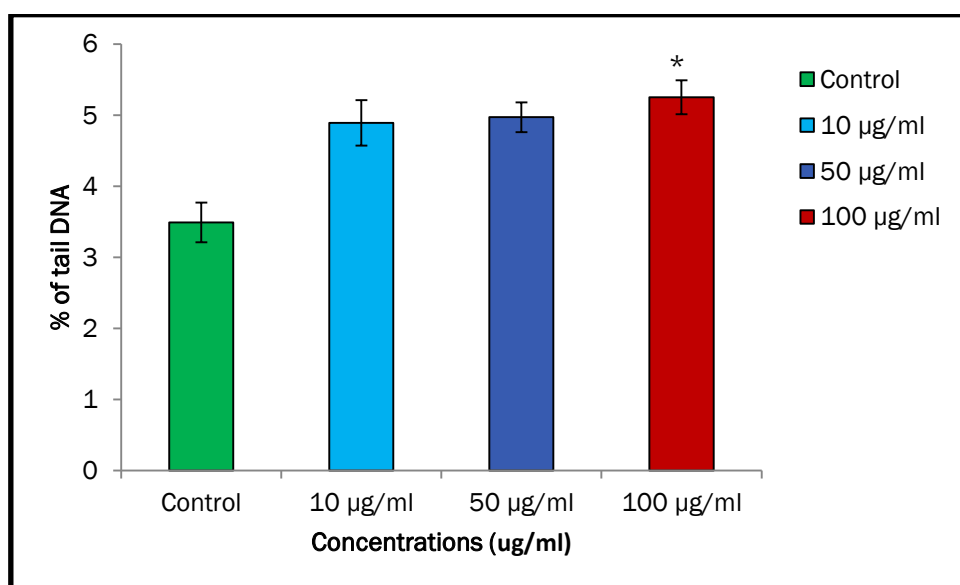


Fig.5.21 % tail DNA in zebrafish larvae exposed to 2%Ag doped indium oxide nanoparticle solution at 120 hpf

5.5.1.2 Effect on human lymphocytes.

The damaged cells can be distinguished on the basis of the comet assay where the tailing of DNA in damaged cells shows dragging like appearance as shown in Fig.

5.22

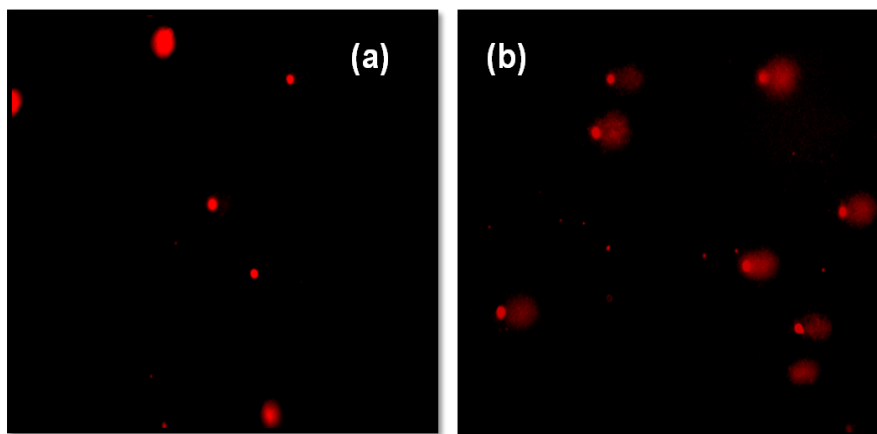
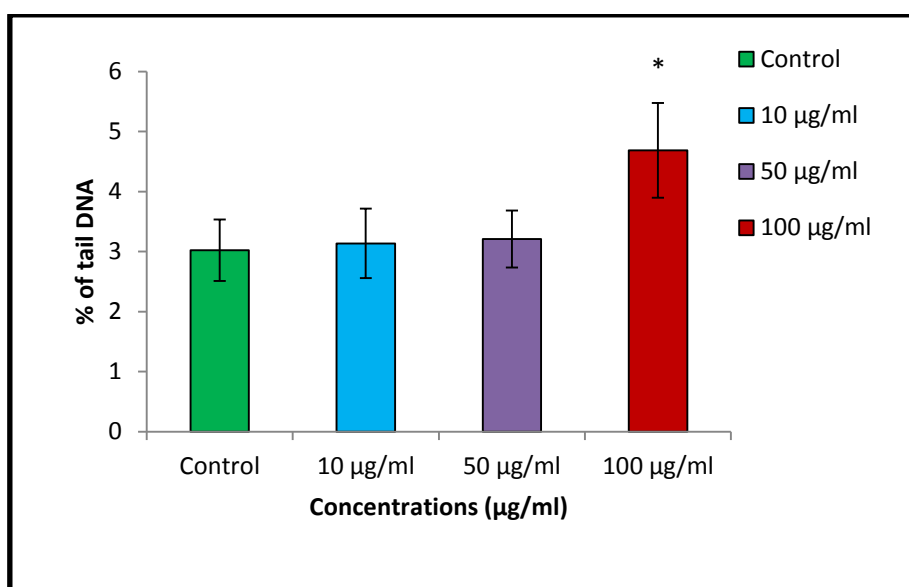


Fig.5.22 (a) normal cells and (b) damaged cells

a) In_2O_3 Nanoparticles

The % tail DNA in the cells of the whole blood culture exposed to various concentrations viz 10, 50, 100 $\mu\text{g}/\text{ml}$ of Indium oxide nanoparticles which are graphically presented in Fig 5.23. DNA damage was observed to increase in a dose dependent manner while statistically significant values were found only at the higher concentrations (100 $\mu\text{g}/\text{ml}$) of the NP at ($p < 0.05$) level.

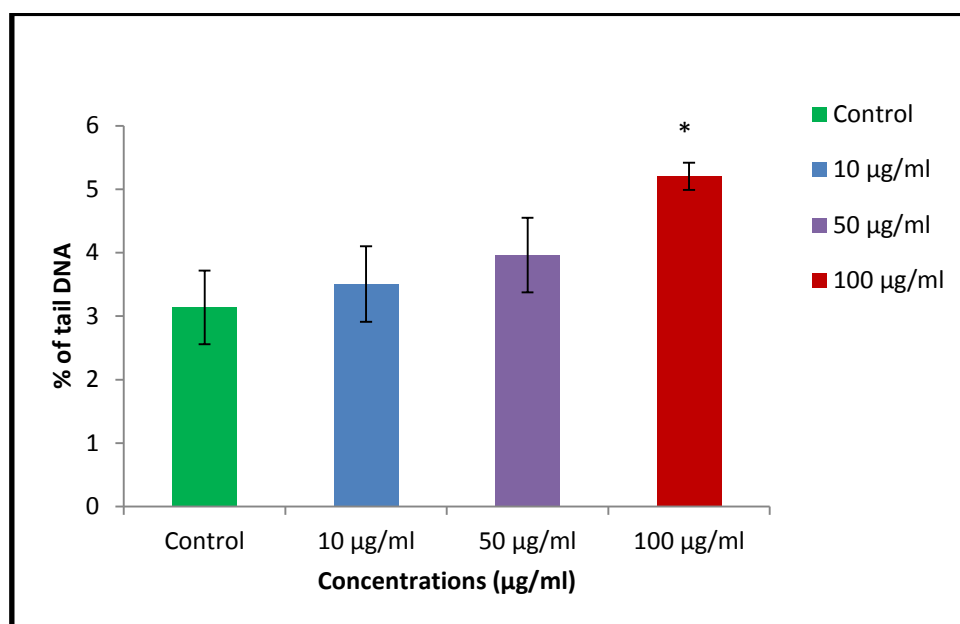


* $p < 0.05$

Fig. 5.23: Mean DNA damage in human blood exposed to Indium oxide nanoparticle at 72h

b) $\text{In}_{1.88}\text{Co}_{0.12}\text{O}_3$ nanoparticles

The extent of DNA damage observed in the whole blood culture exposed to various doses viz 10, 50, 100 $\mu\text{g}/\text{ml}$ in the form of % tail DNA is presented in Fig 5.24. Here, the amount of single stranded breaks were found to increase in a dose dependent manner with 100 $\mu\text{g}/\text{ml}$ showing the highest damage at ($p < 0.05$) level.

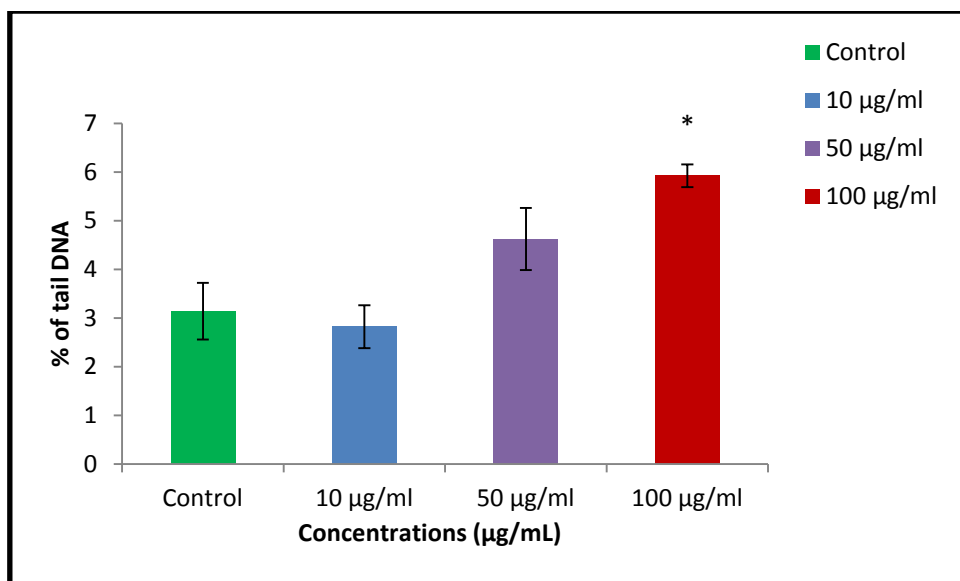


* $p < 0.05$

Fig. 5.24: Mean DNA damage in human blood exposed to cobalt doped Indium oxide nanoparticle at 72h

c) $\text{In}_{1.96}\text{Ag}_{0.04}\text{O}_3$ nanoparticles

The DNA damage induced by various doses of silver doped indium oxide viz 10, 50, 100 $\mu\text{g}/\text{ml}$ NP in whole blood culture is graphically presented in Fig. 5.25. Although the damage increased in a dose dependent manner only the highest dose showed a statistically significant value i.e. ($p < 0.05$).



* $p < 0.05$

Fig. 5.25: Mean DNA damage in human blood exposed to 2% silver Indium oxide nanoparticle at 72h

As seen from the above data of toxicity studies on zebrafishembriyo and human blood sample for DNA damage, significant value is obtained only for higher dosage of 100µg/mL. This suggests that in lower concentrations the nano particles are found to be non- toxic.

SUMMARY AND CONCLUSION

6.1 Summary

The contents of the thesis are divided into six chapters. Each chapter can be summarised as follows:

Chapter 1

Chapter 1 gives the basic introduction on the material science field and its development over the period. The advent of nanotechnology, its impact on the research field and eventually on the modern technological devices has also been discussed. The nanomaterials can be synthesised in the various forms such as nanoparticles, nanorods, nanowires, nanocubes and nanospheres. Properties vary with respect to the size and shape the nano-material is prepared with. Metal oxides form the major component of material research field. Over the years ZnO, TiO₂, Cr₂O₃, Mn₂O₃, Co₃O₄, NiO, CuO, SnO₂, In₂O₃, Fe₂O₃, Y₂O₃, Bi₂O₃, spinels and perovskites are some of the metal oxides that have been extensively studied. Doping these metal oxides with different metal ions also results in altering the properties of material which can add on to their applications in various fields. Different methods are available for synthesizing metal oxides in nanoform majorly forming two categories viz top down and bottom up approach. Few of the bottom up methods have been mentioned in this chapter. Dilute magnetic semiconductor (DMS) is an important field recently associated with metal oxides has been introduced. It has been shown that metal oxides when prepared in nanoform finds several applications in fields like catalysis, photocatalysis, biomedical appliances as well as in drug delivery agents. Further in this chapter the highlights of the thesis and organisation of the chapters is presented.

Chapter 2

Chapter 2 presents the literature survey on the metal oxides that are studied in this thesis and their related properties. First the introduction about the DMS material is presented. The DMS originated from the discovery of magnetism in transition metal doped II-VI semiconductors like CdTe, CdSe, ZnSe and CdS. A series of theoretical and experimental studies followed where transition metal doped metal oxides have come forward as the strong candidates in the DMS field. The highlighting report in this field was the observation of unusual ferromagnetism in the undoped diamagnetic oxides. Number of models and theories put forward to explain the observed ferromagnetism have been discussed in this chapter. Most of the theories relate the origin ferromagnetism to the lattice defects such as cation/anion vacancies or cation anion interstitials. Till today the topic has been controversial and findings are in progress to understand and substantiate the origin and existence of the ferromagnetism in such compounds.

Further this chapter deals with understanding the structure and properties of indium oxide and doped indium oxide material, where it is shown that the In_2O_3 crystallise in a cubic bixbyte structure. Different methods have been discussed for the synthesis of pristine and doped In_2O_3 nanoparticles and thin films including sol gel, combustion co-precipitation, hydrothermal/solvothermal, RF/magnetron sputtering, PLD and CVD.

The electrical properties studied for these materials have been discussed which displays the increase in electrical resistance on doping with transition metal. The magnetic properties observed are conflict-ridden where some report RT ferromagnetism in TM doped In_2O_3 nanoparticles whereas others observed paramagnetic behaviour. Various explanations are given to substantiate the observed results, where ferromagnetism is explained to be originating from the oxygen vacancies and in few cases from cation interstitials.

Indium oxide (In_2O_3) nanoparticles have been gaining importance in the catalytic field recently and several organic transformations that are carried out using this catalyst have also been discussed. This proves that In_2O_3 is highly applicative material and has a lot of potential in material chemistry and catalysis.

The literature on cerium oxide (CeO_2) describes that it crystallises in a face centered cubic fluorite structure with space group Fm_3m . The lattice when exist with oxygen vacancies, there is a presence of $\text{Ce}^{3+}/\text{Ce}^{4+}$ redox states. This property makes it an interesting material and can be exploited for several applications including catalysis. There are different methods reported in the literature for synthesizing CeO_2 in nano-size. The widely used methods are discussed in this chapter such as sol-gel, combustion, microwave assisted hydrothermal and co precipitation.

The literature also demonstrates the presence RT ferromagnetism in CeO_2 . Transition and non-transition metal doped CeO_2 nanoparticles have been reported to display the dilute magnetism thus making it a strong candidate in DMS field. Presence of weak ferromagnetism in pristine compound has also been shown. It is well known that CeO_2 is used in different catalytic reactions. The organic reactions catalysed by CeO_2 are discussed here. It is widely used as the support material for CO oxidation reaction owing to the mobility of the oxygen species into the lattice.

Ferrites are cubic spinels with formula AB_2O_4 . They crystallize in a face centered cubic structure with Fd_3m space group. The MgFe_2O_4 is one of the widely studied ferrite, when synthesized in a nanosize shows a super paramagnetic nature which finds application in magnetic resonance imaging, ferro-fluids, magneto-caloric refrigeration, drug delivery etc. It is a soft ferrite and there are several methods reported in the literature

for its synthesis in nano-range including combustion, sol gel, combination of both known as sol- gel combustion and co-precipitation.

Pristine and doped ferrite materials are a very important class of materials where the properties depend on the occupancy of cations in octahedral and tetrahedral sites. Many transition and rare earth doped MgFe_2O_4 compounds have been reported in the literature and their magnetic properties have been discussed. Ferrites have also entered the field of heterogeneous catalysis and the available reports are presented in this chapter.

Chapter 3

Chapter 3 describes experimental work including the methods of preparation of nanoparticles presented in this thesis and the instrumental techniques used to characterise them. Pristine and Co, Cr and Ag doped In_2O_3 nanoparticles have been synthesized by combustion method using glycine as a fuel. The voluminous compound was obtained on combustion for all dopants and their respective concentrations. It was then calcined and sintered at desired temperatures. Pristine and In doped CeO_2 and MgFe_2O_4 have synthesized by sol-gel method using citric acid. The mixture of metal nitrates and citric acid forms a gel on heating which further undergoes decomposition forming the compound. The obtained compound was then ground, calcined and sintered at desired temperatures.

The precursor gels obtained during the preparation were characterised by thermo gravimetric analysis where the decomposition process was monitored. The final compounds were then subjected to several characterisation techniques such as XRD, IR, UV-DRS, SEM, TEM, XPS and Mössbauer in case of ferrite compound. Two probe DC electrical resistivity and VSM were used for electrical and magnetic studies. The NMR

spectroscopy was used to characterise the reaction products catalysed by the nanoparticles. All the instrumentation techniques have been described in this chapter.

Chapter 4

All the spectroscopic and solid state analysis, their observations and results are discussed in this chapter.

The thermo-gravimetric (TG) analysis accompanied by DTA/DSC for $\text{In}_{1.88}\text{Co}_{0.12}\text{O}_3$, $\text{In}_{1.90}\text{Cr}_{0.10}\text{O}_3$ and $\text{In}_{1.96}\text{Ag}_{0.04}\text{O}_3$ gel shows the initial weight loss owing to the loss of water molecule accompanied by endothermic peak followed by the major weight loss resulting from the combustion reaction which is accompanied by a sharp exothermic peak at 200°C . No major weight loss is observed beyond 230°C . On decomposition the metal oxides are formed and the organic impurity gets converted to oxides of carbon and nitrogen. $\text{Ce}_{0.90}\text{In}_{0.10}\text{O}_2$ gel shows that initial weight loss is followed by decomposition that proceeds in two steps with distinct exothermic peaks at 207 and 294°C . Compound is highly stable beyond 310°C . For $\text{MgFe}_{1.96}\text{In}_{0.04}\text{O}_4$ gel initially weight loss is due to loss of water followed by decomposition reaction which accompanied by two exotherms at 206°C and 322°C . The compound is found to be stable beyond 400°C .

The X-ray powder pattern for pristine and Co, Cr and Ag doped In_2O_3 compounds show that they crystallize in a cubic bixbyte structure. No impurity phase is observed except for $\text{In}_{1.90}\text{Ag}_{0.10}\text{O}_3$ composition which shows a secondary phase of silver oxide. All the peaks were matched with the JCPDS data and indexed with their corresponding *hkl* values. The lattice parameters and crystallite size calculated by Sherrer's formula depict the nano-crystalline nature of the compounds. The XRD powder pattern for pristine and In doped CeO_2 compounds shows that it crystallizes in a fluorite structure. The peaks are

matched with the JCPDS data and the corresponding hkl values are indexed. The crystallite size reveals the nano-crystalline nature of all compounds. X-ray powder pattern for pristine and In doped MgFe_2O_4 depicts the cubic spinel structure. All the compositions form single phase except for $\text{MgFe}_{1.84}\text{In}_{0.16}\text{O}_4$, which shows an impurity peak corresponding to $\alpha\text{-Fe}_2\text{O}_3$. The crystallite size is obtained in nano range and lattice parameters have also been calculated.

The infrared spectra for gel as prepared and sintered sample are presented for all the compounds. The gel shows the presence of organic moiety and their corresponding vibrations coming from glycine in case of pristine and doped In_2O_3 and citric acid in case of pristine and CeO_2 and MgFe_2O_4 compounds. In the as prepared samples some of these peaks start disappearing and the peaks corresponding to metal oxides become visible. In the sintered samples no organic impurity is observed and the metal oxide peaks corresponding to In-O vibrations are observed at 601, 567 and 538 cm^{-1} and for MgFe_2O_4 at 578 and 408 cm^{-1} corresponding to tetrahedral and octahedral M-O stretching respectively.

The UV DRS studies showed the presence of charge transfer band for all the samples and the band gaps have been calculated from Taucs plot. All the samples show a band gap in the semiconductor range.

The microscopic analyses were carried out on scanning and transmission electron microscope. All the compounds show spherical morphology with few aggregates in case of ferrite samples owing to their magnetic nature. The $\text{Ce}_{1-x}\text{In}_x\text{O}_2$ compounds showed flakes like appearance in SEM. The TEM displayed the exact particle size of compounds which is in the nano-meter range for all the compounds. The doping reduced the particle size compared to pristine in all the compounds except for Ag doped samples which was

found to increase. The ED patterns displayed the concentric rings corresponding to diffraction pattern and are indexed with their *hkl* values.

X-ray photoelectron spectroscopy was employed to identify the valence states of the metal ions. In Co, Cr and Ag doped In_2O_3 compounds the observed oxidation states of the elements are Co^{2+} , Cr^{3+} , Ag^{1+} and In^{3+} . In case of indium doped CeO_2 , In^{3+} was identified whereas for cerium a mixed valence states of Ce^{3+} and Ce^{4+} . Oxidation states of the elements in In doped MgFe_2O_4 were Mg^{2+} , Fe^{3+} , and In^{3+} . In all the compounds deconvoluted spectra of oxygen showed two peaks corresponding to lattice oxygen and oxygen defects.

Mossbauer spectra showed the appearance of sextet for pristine compound and as the dopant concentration increased the intensity of sextet was reduced while the paramagnetic doublet became more prominent, this is owing to the super paramagnetic nature of the compounds.

Electrical resistivity studies carried on two probe resistivity setup revealed the semiconductor behaviour of all the samples the resistivity was found to decrease with increase in temperature.

Magnetic studies for the samples were carried out on VSM. The magnetisation v/s field (M-H) and magnetisation v/s temperature (M-T) were the measurements carried out. The Co, Cr, Ag doped compounds showed weak ferromagnetism at room temperature with lower dopant concentrations whereas the paramagnetic ordering was found to be prominent at 50 K. The pristine In_2O_3 displayed a weak ferromagnetism at both the temperatures. Similarly pristine CeO_2 also showed weak ferromagnetism which was found to enhance on doping with indium. When compared with the bulk sample, observed ferromagnetism was found to be razed. This suggests that the dilute magnetic behaviour

originates from the defects in the crystal formed during the preparation which are prominent in the nanoscale. The FC and ZFC curves also depict the DMS behaviour. Whereas in case of In doped ferrite sample the saturation magnetisation decreases but the super-paramagnetic behaviour is enhanced on doping where compounds show negligible coercivity at room temperature. At 50 K the magnetisation as well as coercivity was found to increase. The blocking temperature was found to be reduced to RT for the doped compound at the applied field of 250 Oe. The AC susceptibility studies also substantiate for the super paramagnetic nature of the compounds.

Chapter 5

The CO oxidation reaction was carried out on the prepared nanoparticles, where Co doped In_2O_3 showed the best catalytic activity; the 100% CO conversion was achieved at 130 °C for $\text{In}_{1.88}\text{Co}_{0.12}\text{O}_3$ composition. The surface area and the porosity measurements of the catalyst $\text{In}_{1-x}\text{Co}_x\text{O}_3$ reveals the increase in surface area doping which influence the catalytic property. Few organic transformation reactions were also carried out using these catalysts, $\text{MgFe}_{1.80}\text{In}_{0.20}\text{O}_4$ was found to be active for Henry reaction giving nitro-aldol product and for Quinazolinone synthesis. The experimental procedure and the schemes are presented in this chapter. The IR and NMR of the products obtained have also been discussed.

Pristine In_2O_3 and $\text{In}_{1.96}\text{Ag}_{0.04}\text{O}_3$ nanoparticles were tested for the *Invitro* α -amylase and α -glucosidase inhibition activity, which is an effective strategy for type-2 diabetes management. The $\text{In}_{1.96}\text{Ag}_{0.04}\text{O}_3$ nanoparticles showed the best activity for inhibition of both the enzymes at a very low concentration when compared with pristine compound as well as with the standard drugs.

The pristine In_2O_3 , $\text{In}_{1.96}\text{Ag}_{0.04}\text{O}_3$ and $\text{In}_{1.88}\text{Co}_{0.12}\text{O}_3$ were further tested for their toxicity effects on zebra fish and human blood samples. The results obtained are discussed in this chapter. No measurable toxicity was observed for all the compounds.

6.2 Conclusions

In conclusion, Pristine and Co, Cr and Ag doped In_2O_3 nanoparticles have been successfully synthesized by combustion method using glycine as a fuel. Pristine and In doped CeO_2 and MgFe_2O_4 nanoparticles were prepared using sol-gel method using citric acid. The gel precursors were characterised by TG-DTA/DSC analysis and the stability of the compound with respect to temperature was found out. The X-ray diffraction analysis confirmed the phase formation of the compounds by matching with the JCPDS data. Pristine and doped In_2O_3 compound crystallises in a cubic bixbyte structure whereas pristine and doped CeO_2 compounds crystallizes in a fluorite structure. The cubic spinel structure of ferrite was also confirmed. The infrared analysis showed that the final compounds do not contain any organic impurity at the same time the respective M-O vibrations were also found to be present. The UV DRS data showed the absorption bands of all compounds and the band gaps were calculated using Taucs plot which lie in the semiconductor range. The spherical morphology and nanosize is confirmed from SEM and TEM analysis. The XPS validates the elemental oxidation states which are as follows Co^{2+} , Cr^{3+} , Ag^{1+} and In^{3+} for $\text{In}_{1-x}\text{M}_x\text{O}_3$ (M=Co, Cr and Ag) compounds. Cerium showed a mixture of Ce^{3+} and Ce^{4+} along with In^{3+} for $\text{Ce}_{1-x}\text{In}_x\text{O}_2$ compounds. The oxidation states of elements observed for $\text{MgFe}_{2-x}\text{In}_x\text{O}_4$ compounds are Mg^{2+} , In^{3+} and Fe^{3+} . The oxygen showed two peaks corresponding to lattice oxygen and oxygen vacancies for all the compounds. The mössbauer data revealed the existence of super paramagnetic relaxation in the In doped MgFe_2O_4 compounds. The magnetic studies carried on pristine In_2O_3 and CeO_2 showed weak ferromagnetism at RT and 50 K. Co, Cr and Ag doped samples also

revealed weak ferromagnetism at RT, which is found to be raised as the concentration of dopant increased and also when measured at 50 K. The paramagnetic /anti-ferromagnetic ordering is found to be more favourable. The In doped samples showed enhancement in the magnetic property as the concentration of dopant increased at temperatures, 300 and 50 K. The super paramagnetic behaviour was observed at RT. When compared with bulk sample both $\text{In}_{1-x}\text{Co}_x\text{O}_3$ and $\text{Ce}_{1-x}\text{In}_x\text{O}_2$ showed decreased or absence of the magnetic behaviour observed in nanoscale. Thus we conclude that the Dilute magnetism observed in these compounds originate from the lattice defects such as oxygen vacancies or cation/anion interstitials, and are more prominent at nanoscale. Magnetic studies on indium doped MgFe_2O_4 nanoparticles revealed the super paramagnetic nature, where doping reduces the coercivity to almost zero and T_c is lowered to room temperature T applied field of 250 Oe. The AC susceptibility study and mössbauer data also substantiates the super-paramagnetic nature of the nanoparticles. The CO oxidation studies showed the best CO conversion activity of Co doped In_2O_3 sample where 100% conversion was obtained at 130 °C for $\text{In}_{1.88}\text{Co}_{0.12}\text{O}_3$, which can be attributed to the smaller particle, size high surface area and porosity as well as the to the oxygen mobility of the compound. The $\text{MgFe}_{1.80}\text{In}_{0.20}\text{O}_4$ was found to be the best catalyst for organic transformations such as Henry reaction and quinazolinones synthesis at room temperatures. $\text{In}_{1.96}\text{Ag}_{0.04}\text{O}_3$ nanoparticles showed the enzyme inhibition activity towards α -amylase and α -glucosidase at a very low concentration of 100 $\mu\text{g/mL}$ and 0.18 $\mu\text{g/mL}$ respectively and hence displays its property as a starch blocker. The toxicity studies of pristine In_2O_3 , $\text{In}_{1.96}\text{Ag}_{0.04}\text{O}_3$ and $\text{In}_{1.88}\text{Co}_{0.12}\text{O}_3$ on zebra fish embryos and human blood cells do not show distinct / measurable toxicity thus proving their application to be safe.

REFERENCES:

- [1] R. P. Feynman, In: Engineering and Science, Caltech, Pasadena, 23(1960) 22.
- [2] K.E. Drexler, Nanosystems: Molecular Machinery, Manufacturing and Computation; Wiley (1992).
- [3] K. E. Drexler, Engines of Creation: The Coming Era of Nanotechnology; Doubleday (1986).
- [5] G. Wang, J. Park, D. Wexler, M. S. Park and J. H. Ahn, Inorganic Chemistry, 46 (2007) 12.
- [6] X. Jiang, Y. Wang, and T. Herricks, J. Mater. Chem. 14 (2004) 695.
- [7] Q. Sun, Y.P Zeng and D. Jiang, Sol. State Comm. 151 (2011) 1220.
- [8] G. Cheng, E. Stern, S. Guthrie, M.A. Reed, R. Klie and Y. Hao, Appl. Phys. A, 85 (2006) 233.
- [9] N. H. Hong, J. Sakai and N. T. Huong, J. Mag. Mat.302(2006)228.
- [10] J. Wu, J. Cao, W.Q. Han, A. Janotti and H.C. Kim Functional Metal Oxide Nanostructures, Springer publications, Volume 149 (2012)
- [11] S. A. Wolf, D. D. Awschalom, R. A. Buhrman, J.M. Daughton, S. V.Molnar, M. L. Roukes, A. Y. Chtchelkanova and D. M. Treger ,Science 294 (2001)1488.
- [12] H. Munekata, H. Ohno, S. V. Molnar, A. Segmüller, L. L. Chang and L. L. Esaki, Phys. Rev. Lett. 63(1989)1849.
- [13] H. Ohno, H. Munekata, T. Penney, S. V. Molnar and L.L. Chang, Phys. Rev. Lett. 68 (1992) 2664.
- [14] H. Ohno, A. Shen, F. Matsukura, A. Oiwa, A. Endo, S. Katsumoto and Y. Iye, Appl. Phys. Lett. 69 (1996) 363.
- [15] W. Prellier, A. Fouchet and B. Mercey, J. Phys.: Condens. Matter 15 (2003) R1583.

- [16] G. Peleckis, Thesis: Studies on diluted oxide magnetic semiconductors for spin electronic applications, Institute of Superconducting and electronic materials and faculty of engineering, University of Wollongong, 2006.
- [17] R. Kofenstein, T. Walther, D. Hesse and S. G. Ebbinghaus, *J. Mater. Sci.* 48 (2013) 6509.
- [18] S. Thankachan, B. P. Jacob, S. Xavier and E. M. Mohammed, *J. Magn. Mater.* 348 (2013) 140.
- [19] W. Tang, Y. Su, Q. Li, S. Gao and J. K. Shang, *Water Res.* 47 (2013) 3624.
- [20] S. Maensiri, M. Sangmanee and A. Wiengmoon, *Nanoscale Res. Lett.* 4 (2009) 221.
- [21] J. L. Dormann and D. Fiorani (Eds.), *Magnetic Properties of Fine Particles*, North-Holland, Amsterdam (1992) 115.
- [22] J. Popplewell and L. Sakhnini, *J. Magn. Mater.* 149 (1995) 72.
- [23] K. Raj, B. Moskowitz and R. Casciari, *J. Magn. Mater.* 149 (1995) 174-180.
- [24] U. Hafeli, W. Schutt, J. Teller and M. Zborowski (Eds.), *Scientific and Clinical Applications of Magnetic Carriers*, Plenum Press, New York, (1997).
- [25] Q. Chen, A. J. Rondinone, B. C. Chakoumakos and Z. J. Zhang, *J. Magn. Mater.* 194 (1999) 1.
- [26] K. Hemalatha, G. Madhumitha, A. Kajbafvala, N. Anupama, R. Sompalle, and S.M. Roopan, *J. Nanomater.* 2013(2013) Article ID 341015, 23 pages.
- [27] S. Royer and D. Duprez, *chem. cat. chem.* 3(2011) 24.
- [28] S. Hong, S. Chan, T. Y. Wu, J. C. Juan and C. Y. Teh, *J. Chem. Technol. Biotechnol.* 86 (2011) 1.
- [29] R. Subbiah, M. Veerapandian and K.S. Yun, *Curr. Med. Chem.* 17(2010)4559.
- [30] H. Wang, X. Xu, J. Zhang, and C. Li, *J. Mater. Sci. Technol.* 26 (2010) 1037.
- [31] S. S. Farvid, L. Ju, M. Worden, and P.V. Radovanovic, *J. Phys. Chem. C*, 112 (2008) 46

- [32] M. I. Ivanovskaya, E. A. Ovodok, and D. A. Kotsikau, *Glass Phys. Chem.* 37(2011)5.
- [33] J. Xu, X. Wang and J. Shen, *Sens. Actuators B*, 115(2006) 642.
- [34] M. Raukas, A. Konrad, K.C. Mishra and J. Lumin. 122(2007) 773.
- [35] V. Uskokovick, M. Drogenik, *Surf. Rev. Letter*, 12(2005)239.
- [36] S.T. Aruna and A.S. Mukasyan, *Curr. Opin. Sol. State Mat. Sci.* 12(2008) 44.
- [37] J. Yu, L.B. Duan, Y.C. Wang and G.H. Rao, *J. Sol. State Chem.*, 182(2009)1563.
- [38] J.K. Furdyna, *J. Appl. Phys.* 64 (1988) R29.
- [39] T. Fukumura, Z. Jin, A. Ohtomo, H. Koinuma and M. Kawasaki, *Appl. Phys. Lett.* 75 (1999) 3366.
- [40] K. Sato and H. K. Yoshida *Japan. J. Appl. Phys.* 39 (2000) L555.
- [41] T. Dietl, H. Ohno, F. Matsukura, J. Cibert and D. Ferrand, *Science* 287 (2000) 1019.
- [42] S. Kolesnik, B. Dabrowski and J. Mais, *J. Appl. Phys.* 95 (2004) 2582.
- [43] G.T. Thaler, et al., *Appl. Phys. Lett.* 80 (2002) 3964.
- [44] K. Sato and H. K. Yoshida, *Japan. J. Appl. Phys.* 40 (2001) L334.
- [45] Y. Matsumoto, M. Murakami, T. Shono, T. Hasegawa, T. Fukumara, M. Kawasaki, P. Ahmet, T. Chikyow, S. Y. Koshihara and H. Koinuma, *Science* 291(2001) 854.
- [46] Y.M. Cho, W.K. Choo, H. Kim, D. Kim and Y. Ihm, *Appl. Phys. Lett.* 80 (2002) 3358.
- [47] S.W. Yoon, S.B. Cho, S. C. We, S. Yoon, B. J. Suh, H.K. Song and Y.J. Shin, *J. Appl. Phys.* 93 (2003) 7879.
- [48] P. Sharma, A. Gupta, K.V. Rao, F.J. Owens, R. Sharma, R. Ahuja, J.M.O. Guillen, B. Johansson and G.A. Gehring, *Nat. Mater.* 2 (2003) 673.
- [49] J.M.D. Coey, M. Venkatesan and C.B. Fitzgerald, *Nat. Mater.* 4 (2005) 173

- [50] J.Y. Kim, et al., Phys. Rev. Lett. 90 (2003) 017401.
- [51] K.A. Griffin, M. Varela, S.J. Pennycook, A.B. Pakhomov and K.M. Krishnan, J. Appl. Phys. 99 (2006) 08M114.
- [52] T.C. Kaspar, et al., Phys. Rev. B, 73 (2006) 155327.
- [53] Y.J. Kim, S. Thevuthasan, T. Droubay, A.S. Lea, C.M. Wang, V. Shutthanandan, S.A. Chambers, R.P. Sears, B. Taylor and B. Sinkovic, Appl. Phys. Lett. 84 (2004) 3531.
- [54] C. B. Fitzgerald , M. Venkatesan , A. P. Douvalis , S. Huber , J. M. D. Coey and T. Bakas , J. Appl. Phys.95 (2004)7390 .
- [55] K.A. Griffin, A.B. Pakhomov, C.M. Wang, S.M. Healdv and K.M. Krishnan, Phys. Rev. Lett. 94 (2005)157204.
- [56] N. H. Hong , J. Sakai , N. T. Huong and V. Brizé , Appl. Phys. Lett.87 (2005) 102505.
- [57] P. I. Archer, P. V. Radovanovic , S. M. Heald and D. R. Gamelin , J. Am. Chem. Soc.127 (2005)14479.
- [58] J. Philip, A. Punnoose, B. I. Kim, K. M. Reddy, S. Layne, J .O. Holmes, B. Satpati, P. R. Leclair, T. S. Santos and J. S Moodera, Nat. Mater. 5(2006)298.
- [59] J. Philip, N. Theodoropoulou, G. Berera, J.S. Moodera and B. Satpati, Appl. Phys. Lett. 85(2004)777.
- [60] G. Peleckis, X. Wang and S. X. Dou, Appl. Phys. Lett. 89 (2006)022501.
- [61] Z. G. Yu, J. He, S. Xu, Q. Xue, O. M. J. van't Erve, B. T. Jonker, M. A. Marcus, Y. K. Yoo, S. Cheng and X. Xiang, Phys. Rev. B,74(2006)165321.
- [62] G. Z. Xing, J. B. Yi, D. D. Wang, L. Liao , T. Yu, Z. X. Shen , C. H. A. Huan, T. C. Sum, J. Ding and T. Wu, Phys. Rev. B , 79(2009)174406.
- [63] X. Meng, L. Tang, and J. Li, J. Phys. Chem. C, 114 (2010)17569.
- [64] C. Xia, C. Hu, P. Chen, B. Wan, X. He and Y. Tian, Mater. Res. Bull.45(2010)794.

- [65] P.C.A. Brito, D. A. A. Santos, J.G.S. Duque and M.A. Macêdo, *Phys. B Condens. Matter*, 405 (2010)1821.
- [66] V. Ferrari, A.M. Llois and V. Vildosola, *J. Phys. Condens. Matter* 22 (2010) doi:10.1088/0953-8984/22/27/276002.
- [67] A. Thurber, K. M. Reddy, *J. Appl. Phys.* 101 (2007) 09N506.
- [68] N.H. Hong, J. Sakai, N. Poirot and V. Brize, *Phys. Rev. B* 73 (2006) 132404.
- [69] A. Sundaresan, R. Bhargavi, N. Rangarajan, U. Siddesh and C.N.R. Rao, *Phys. Rev. B* 74 (2006)161306.
- [70] C. Sudakar, A. Dixit, S. Kumar, M.B. Sahana, G. Lawes, R. Naik and V.M. Naik, *Scr. Mater.* 62 (2010) 63.
- [71] N.H. Hong, N. Poirot and J. Sakai, *Phys. Rev. B* 77 (2008) 033205
- [72] C. Zener, *Phys. Rev.* 81(1951) 440.
- [73] C. Zener , *Phys. Rev.* 83(1951) 299.
- [74] P. W. Anderson *Phys. Rev.* 79(1950)350.
- [75] T. Dietl, A. Haury, A. Merle and Y. eacute, *Phys. Rev. B* 55 (1997) R3347.
- [76] M. A. Ruderman, C. Kittel, *Phys. Rev.* 96 (1954) 99.
- [77] K. Yosida, *Theory of Magnetism*. Springer, Berlin, 1996.
- [78] N. Akdoğan, *Origin of Ferromagnetism in Oxide-Based Diluted Magnetic Semiconductors*, Thesis: Submitted to The Faculty of Physics and Astronomy, Ruhr-Universität at Bochum Bochum, Germany February 2008.
- [79] G. Lixiu , *First-principles study of the magnetism in indium oxide-based dilute magnetic semiconductors* ,school of physical and mathematical sciences 2011.
- [80] C. Zener, *Phys. Rev.* 82(1951)403.
- [81] J. N. Lalena and D. A. Cleary "Principles of Inorganic Materials Design," 2nd ed., John Wiley & Sons, New York, (2010) 345.

- [82] S. D. Sarma, E.H. Hwang, A. Kaminski, Phys. Rev. B 67 (2003) 155201.
- [83] L. R. Shah, B. Ali, H. Zhu, W. G. Wang, Y. Q. Song, H. W. Zhang, S. I. Shah and J. Q. Xiao, J. Phys. Cond. Matt. 21 (2009) 486004.
- [84] T. Dhannia, Thesis: Investigations on the structural, optical and magnetic properties of nanostructured cerium oxide in pure and doped forms and its polymer nanocomposites, Department of physics, Cochin University of science and technology Cochin, January 2012.
- [85] S. Maensiri, P. Laokul, J. Klinkaewnarong, S. Phokha, V.Promarak, S. Seraphin and J. Optoelec.Advance. Mat. 10 (2008)161.
- [86] K. Palandage and G.W. Fernando, Phy. Lett.A , 374 (2010)2879.
- [87] H. A. Rahnamaye Aliabad , Y. Asadi and I. Ahmad , Optical Materials, 34(2012) 1406.
- [88] A. J. C. Wilson, The International Union of Crystallography, International Tables for Crystallography, Kluwer Academic Publishers, Dordrecht, the Netherlands, 1992.
- [89] M. F. Garcia, J. A. Rodriguez, “Nanomaterials: Inorganic and Bioinorganic Perspectives”, 2007.
- [90] S.G. Chen, C.H. Li, W.H. Xiong, L.M. Liu and H. Wang, Mater. Lett. 58 (2004) 294
- [91] K.Y. Kim and S.B. Park, Mater. Chem. Phys. 86 (2004) 210.
- [92] S.J. Limmer, K. Takahashi and G. Cao, Proc. SPIE 5224 (2003) 25.
- [93] S. Li, X. Qiao, J. Chen, H. Wang, F. Jia and X. Qiu, J. Cryst. Growth 289 (2006) 151.
- [94] M. Farahmandjou ,Int. J. Bio-Inorg. Hybd.Nanomat., 2 (2013)373.
- [95] J. Chandradass , D.S. Bae and K. H. Kim , Adv. Powder Technol.22 (2011) 370.
- [96] J. M. Kim, J. K. Park, K. N. Kim ,C.H. Kim and H.G. Jang ,Curr. Appl. Phys. 6S1 (2006) e198..

- [97] R. Prakash , S. Kumar , F. Ahmed , C. G. Lee and J. I. Song , *Thin Solid Films* 519 (2011) 8243.
- [98] S. Dussan, M. K. Singh, A. Kumar and R. S. Katiyar, *Integr. Ferroelectr.*125(2011)155.
- [99] J. Chandradass, D. S. Bae, M. Balasubramanian and K. H. Kim, *Mater. Manuf. Process.* 26 (2011) 325–329,
- [100] S. Yan, W. Qiao, W. Zhong, C.T. Au and Y. Dou, *Appl. Phys. Lett.* 104, (2014) 062404.
- [101] A. Gurlo, M. Ivanovskaya, N. Barsan, M. S. Berberich, U. Weimar, W. Gopel and A. Dieguez, *Sens. Actuat. B.* 44, (1997) 327.
- [102] M. Ivanovskaya, A. Gurlo and P. Bogdanov , *Sens. Actuat. B.* 77 (2001) 264.
- [103] M. Epifani and P. Siciliano, *J. Am. Chem. Soc.* 126 (2004) 4078.
- [104] R. Sarhaddi , N. Shahtahmasebi, M. R. R. Abadi and M.M.Bagheri-Mohagheghi, *Physica E* 43 (2010) 452.
- [105] O. D. Jayakumar, I. K. Gopalakrishnan, S. K. Kulshreshtha, Amita Gupta, K. V. Rao, D. V. Louzguine-Luzgin, A. Inoue, P.A. Glans,J.-H. Guo, K. Samanta, M. K. Singh and R. S. Katiyar, *Appl. Phys. Lett.* 91(2007) 052504.
- [106]Q. Sun, Y. Zeng, D. Jiang , *J. Nanopart. Res.*14 (2012) 655.
- [107] D. Yu, D. Wang, W. Yu and Y. Qian, *Mater.Lett.*58 (2003) 84.
- [108] J. E. Song, Y.S. Kang, *Proc. Mater. Res. Soc. Symp.* 818 (2004)1.
- [109] C.Chen, D. Chen, X. Jiao, S. Chen, *J. Phys. Chem. C*, 111(2007)18039.
- [110] H.W. Kim, N.H. Kim, C. Lee, *Appl. Phys.* A81(2005)1135.
- [111] J.Q. Xu, X.H. Wang and J.N. Shen, *Sens. Actuators B* 115 (2006) 642.
- [112] J. Yang, C. Li, Z. Quan, D. Kong, X. Zhang, P. Yang andJ. Lin, *Cryst. Growth & Des*, 8(2008) 695.

- [113] S. Elouali, L. G. Bloor, R. Binions, I. P. Parkin, C. J. Carmalt and J. A. Darr, *Langmuir* 28 (2012) 1879.
- [114] Q. Xiao, Y. Liu, L. Liu, R. Li, W. Luo and X. Chen, *J. Phys.Chem.C*,114 (2010) 9314.
- [115] M. Raukasa, A. Konrad and K.C. Mishra, *J. Lumin.* 122 (2007) 773.
- [116] C. Liang, G. Meng, Y. Lei, F. Phillipp and L. Zhang, *Adv. Mater.*13(2001)1330.
- [117] J.S. Jeong, J.Y. Lee, C.J. Lee, S.J.An, and G.C. Yi, *Chem. Phys. Lett.*384(2004) 246.
- [118] Y. Hao, G. Meng, C. Ye and L. Zhang, *Cryst.Growth Des.* 5 (2005)1617.
- [119] J. Lao, J. Huang, D. Wang and Z. Ren, *Adv. Mater.*16 2004)65.
- [120] F.X. Jiang, X. H. Xu, J. Zhang, X. C. Fan, H. S. Wu and G. A. Gehring, *Appl. Phys. Lett.* 96 (2010) 052503.
- [121] F. X. Jiang, X. H. Xu, J. Zhang, X. C. Fan, H. S. Wu, M. Alshammari, Q. Feng, H. J. Blythe, D. S. Score, K. Addison, M. A. Qahtani and G. A. Gehring *J. Appl. Phys.* 109(2011) 053907.
- [122] R. K. Gupta , K. Ghosh , S.R. Mishra amd P.K. Kahol , *Thin Solid Films* ,516 (2008) 3204.
- [123] H. K. Kim, C. C. Li, G. Nykolak and P.C. Becker *J. Appl. Phys.* 76, (1994) 8209.
- [124] F. Ye, X. M. Cai , X. Zhong, X.Q. Tian, S. Y. Jing , L.B. Huang ,V.A.L. Royc, D.P. Zhang , P. Fana, J.T. Luo, Z.H. Zheng and G.-X.Liang , *Thin Solid Films* 556 (2014) 44.
- [125] L.C. Chen, C. H. Tien and W. C. Liao, *J. Phys. D: Appl. Phys.* 44 (2011) 165101.
- [126] S. Shanmugan and D. Mutharasu, *Metall.Mater. Trans. A*, 43(2012) 6.
- [127] M. Sucheá ,N. Katsarakis, S. Christoulakis , S. Nikolopoulou and G. Kiriakidis, *Sens. Actuators B* 118 (2006) 135.
- [128] J. J. Prince, S. Ramamurthy and B. Subramanian, *J. Cryst.Growth.*240 (2002)142.

- [129] D. P. Dutta, V. Sudarsan, P. Srinivasu, A. Vinu and A. K. Tyagi *J. Phys. Chem. C*, 112 (2008) 6781.
- [130] A. Murali, A. Barve, V. J. Leppert and S.H. Risbud *Nano Lett.* 1(2001)287.
- [131] W. S. Seo, H. H. Jo, K. Lee and J. T. Park, *Adv. Mater.* 15 (2003) 795.
- [132] G. Jo, W. K. Hong, J. Maeng, T. W. Kim, G. Wang, A. Yoon, S. S. Kwon, S. Song and T. Lee, *Colloids Surf. A: Physicochem. Eng. Aspects*, 313 (2008) 308.
- [133] S. J. Wen, G. Couturier, J.P. Chaminade, E. Marquestaut, J. Claverie and P. Hagenmuller, *J. Solid State Chem.* 101 (1992) 203.
- [134] A. H. Hafeezullah, Z. H. Yamani, J. Iqbal, A. Qurashi, A. Hakeem, *J. Alloy. Compd.* 616 (2014) 76.
- [135] E.A. Forsh, A.V. Marikutsa, M.N. Martyshov, P.A. Forsh, M.N. Rumyantseva, A.M. Gaskov and P.K. Kashkarov, *Thin Solid Films*, 558(2014) 320.
- [136] X. Pengfei, C. Yanxue and S. Shaohua *J. Semicond.*, 34 (2013)023002.
- [137] S. Noguchi and H. Sakata *J. Phys. D: Appl. Phys.* 14 (1981) 1523.
- [138] D. B'erardan, E. Guilmeau and D. Pelloquin, *J. Magn. Magn. Mater.* 320 (2008) 983.
- [139] L.M. Huang, C. Århammar, C.M. Araújo, F. Silvearv and R. Ahuja, *Europhysics Lett.* 89 (2010) 47005.
- [140] Y. An, D. Yang, G. Ma, Y. Zhu, S. Wang, Z. Wu and J. Liu, *J. Phys. Chem. C*, 118(2014)10448.
- [141] S. Khatoun, K. Coolahan, S. E. Lofland and T. Ahmad, *J. Am. Ceram.Soc.* 96(2013)2544.
- [142] N. Deng, J.Li, B. Hong, D. Jin, X. Peng, X. Wang, H. Ge and H. Jin, *J. Nanopart.Res* 17(2015) 191.

- [143] A.P. S. Gaur, S. Sahoo, R. K. Katiyar, C. Rinaldi, J. F. Scott and R. S. Katiyar, *J. Phys. D: Appl. Phys.* 44 (2011) 495002.
- [144] H. Raebiger, S. Lany and A. Zunger, *Phys. Rev. Lett.* 101(2008) 027203.
- [145] C Y Hsu, *J. Phys. D: Appl. Phys.* 44 (2011) 415303.
- [146] P. Kharel, C. Sudakar, M. B. Sahana, G. Lawes, R. Suryanarayanan, R. Naik and V. M. Naik, *J. Appl. Phys.* 101 (2007) 09H117.
- [147] A. Gupta, H. Cao, K. Parekh, K. V. Rao, A. R. Raju and U. V. Waghmare, *J. Appl. Phys.* 101(2007) 09N513.
- [148] L. M. Huang, F. Silvearv, C. Moysés Araújo, and R. Ahuja, *Solid State Commun.* 150 (2010) 663.
- [149] D. J. Payne and E. A. Marquis, *Chem. Mater.* 23 (2011) 1085.
- [150] A. Sundaresan, R. Bhargavi, N. Rangarajan, U. Siddesh and C.N. Rao, *Phys Rev B*, 74 (2006) 161306(R).
- [151] M. Naeem, S. Qaseem, I. Ahmad, M. Maqbool, *J. Nanopart. Res.* 14(2012) 808.
- [152] M. Rahman, A.K. Bagdi, A. Majee and A. Hajra, *Tetrahedron Lett.* 52 (2011) 4437.
- [153] V.P. Reddy, A. V. Kumar, K. Swapna and K. R. Rao, *Org. Lett.* 11(2009) 1697.
- [154] R. Takahashi, I. Yamada, A. Iwata, N. Kurahashi, S. Yoshida and S. Sato, *Appl. Catal A: General* 383 (2010) 134.
- [155] S. Santra, A. Majee and A. Hajra, *Tetrahedron Lett.* 53 (2012) 1974.
- [156] Mitra S, Bagdi AK, Majee A and Hajra A, *Tetrahedron Lett.* 54 (2013) 4982.
- [157] V. R. Chaudhary, S. K. Jana and B.P. Kiran, *Journal of Catalysis* 192 (2000) 257.
- [158] V. Rodríguez-González, R. Zanella, L.A. Calzada and R. Gómez, *J Phys Chem C* 113(2009) 8911.

- [159] Y. Lou, J. Ma, X.M. Cao, L. Wang, Q. Dai, Z. Zhao, Y. Cai, W. Zhan, Y. Guo, P. Hu, G. Lu and Y. Guo ,ACS Catal. 4 (2014) 4143.
- [160] W.J. Kim, D. Pradhan, Y. Sohn . J. Mater. Chem.A 1(2013) 10193.
- [161] P. A. Johnson, H.J. Park and A.J. Driscoll, Methods Mol. Biol. 679(2011)183.
- [162] S. Wang, P. Su, J. Huang, J.Wu ,Y. Yang ,J. Mater. Chem .B.1(2013) 1749.
- [163] B. Zhang, Y. Xing, Z. Li, H. Zhou, Q. Mu and B.Yan Nano Lett. 9 (2009) 2280.
- [164] M .De, S. S.Chou and V.P.Draavid ,J Am Chem Soc. 133(2011) 17524.
- [165] Y. J. Liao, Y.C.Shiang, C.C.Huang and H.T. Chang, Langmuir. 28 (2012) 8944.
- [166] S. Dhobale, T. Thite, S. L. Laware, C.V. Rode, S.J. Koppikar, R. K. Ghanekar and S.N. Kale ,J. Appl. Phys. 104(2008) 094907.
- [167] M.K. Rai, S.D. Deshmukh, A.P. Ingle and A.K.Gade ,J. Appl. Microbiol.112(2012) 841.
- [168] S. A. Di, C. J. Mordas, J. Nikolovski and B.C. Wiegand, Metal coated nanoparticles for use in the treatment of enzymatic dermatitis ,Publication Number :EP2083796 B1, Filing Date: Oct 26 2007,Publication Date :March 16,2011(Patent).
- [169] M. Vishnu Kiran, S. Murugesan, J. Chem. Pharm. Res., 5(2013)1001.
- [170] A. Trovarelli, Catal.Rev. 38 (1996) 439.
- [171] C. Ratnasamy ,J. P. Wagner, Catal. Rev. 51(2009) 325.
- [172] J. Beckers , G Rothenberg. Green Chem. 12 (2010) 939.
- [173] L. Vivier, D. Duprez, Chem. Sus.Chem, 3 (2010)654.
- [174] M. Mogensen, N. M. Sammes, , G. A. Tompsett , Solid State Ionics, 129 (2000)63.
- [175] S. Park, J. M. Vohs, R. J. Gorte, Nature, 404(2000)265.
- [176] A. Atkinson, S. Barnett, R. J. Gorte, J. T. S. Irvine, A. J. McEvoy, M. Mogensen, S. C. Singhal, and J. Vohs, Nat. Mater. 3 (2004)17.

- [177] S. Gangopadhyay D.D. Frolov , A.E. Masunov ,S.Seal ,J. Alloys Compd, 584 (2014) 199.
- [178] K.A. Gschneidner and L. Eyring, Handbook on the Physics and Chemistry of Rare earths, North-Holland Pub. 1999.
- [179] T. D. Golden, Y. Shang, Q. Wang and T.Zhou, Advanced Ceramic Processing. chapt 4, Electrochemical Synthesis of Rare Earth Ceramic Oxide Coatings, Intech Publishers (2015)
- [180] H. Chen and .Chang , Ceram. Int. 31 (2005)795.
- [181] M.J. Godinho, R.F. Goncalves, L.P.S. Santos, J.A. Varela, E. Longo and E.R. Leite Mater. Lett.61(2007)1904.
- [182] Y. Liu, Z.Lockman, A. Azizand J.M. M. Driscoll, J. Phys. Condens.Matter 20 (2008) 165201.
- [183] S.Y.Chen, K.W. Fong, T.T. Peng, C.L. Dong, A. Gloter, D.C. Yan, C.L. Chen, H. J. Lin, and C. Te Chen, J. Phys. Chem. C 116 (2012) 26570.
- [184] L. L. Shaw, C. Shen and E.L. J. Sol-Gel Sci. Tech. 53 (2010)1.
- [185] A. Hartridge and A. K. Bhattacharya, J. Phys.Chem.Solids, 63 (2002)441.
- [186] A. Thurber, K.M. Reddy, V. Shutthanandan, M.H. Engelhard, C. Wang, J. Hays, and A. Punnoose, Phys. Rev. B 76 (2007) 165206.
- [187] N. Ozer, Sol. Energy Mater.Sol. Cells 68, (2001)391.
- [188] L. G. Teoh and G. W. Chiang, J.Sol-Gel Sci. Technol. 64(2012) 530.
- [189] X. Chen.G.Li, Y. Su, X. Qiu, L. Liand Z. Zou Nanotechnology 20(2009) 115606.
- [190] R. A. Kumar, K. S. Babu, A. Dasgupta and R. Ramaseshan, RSC Adv.5(2015) 103465.
- [191] A.I.Y. Tok, F.Y.C. Boey, Z. Dong and X.L. Sun , J. Mater. Processing Tech. 190 (2007) 217.

- [192] P. Shuk and M. Greenblatt, *Solid State Ionics*, 116 (1999)217.
- [193] S. Dikmen, P. Shuk, M. Greenblatt and H. Gocmez, *Solid State Sci.* 4(2002)585.
- [194] F. Gao, Q. Lu and S. Komarneni, *J Nanosci Nanotechnol* 6(2006)3812.
- [195] A. B. Corradi, F.B. Bondioli, A.M. Ferrari, T. Manfredini, *Mater. Res. Bull.* 41(2006)38.
- [196] M. Zawadzki, *J. Alloys. Compd.* 454(2008)347.
- [197] M. L. Dos Santos, R. C. Lima, C. S. Riccardi, R.L. Tranquilin, P. R. Bueno, J. A. Varela and E. Longo, *Mater. Lett.* 62 (2008) 4509.
- [198] J. Guo, X. Xin, X. Zhang, S. Zhang, *J. Nanoparticle Res.* 11 (2009) 737.
- [199] R. J. Qi, Y. J. Zhu and Y. H. Huang, *Nanotechnology* 16(2005)2502.
- [200] M. Kamruddin, P.K. Ajikumar, R. Nithya, A.K. Tyagi and B. Raj, *Scripta Materialia*, 50 (2004) 417.
- [201] Y. Wang, T. Mori, J. Li and T. Ikegami, *J. Am. Ceram. Soc.* 85(2002)3105
- [202] J. C. Bear, P.D. Mc Naughter, P. Southern, P. O'Brien and C.W. Dunnill, *Crystals*, 5(2015)312.
- [203] X. D. Feng et al. *Science* 312 (2006)1504.
- [204] E. L. Navarrete, A. Caballero, A. R. G. Elipe and M. Ocana, *J. Mater. Res.* 17 (2002) 797.
- [205] M. Hirano, Y. Fukuda, H. Iwata, Y. Hotta and M. Inagaki, *J. Am. Ceram. Soc.* 83(2000)1287.
- [206] C. W. Sun, H. Li, H. R. Zhang, Z. X Wang and L. Q. Chen, *Nanotechnology* 16 (2005)1454.
- [207] A. Bumajdad, M. I. Zaki, J. Eastoe and L. Pasupulety, *Langmuir*, 20 (2004)11223.
- [208] T. Tsuzuki, J. S. Robinson and P. G. J. McCormick, *J. Aust. Ceram. Soc.* 38 (2002) 15.

- [209] Q. Y. Wen, H. W. Zhang, Y. Q. Song, Q. H. Yang, H. Zhu, and J. Q. Xiao, *J. Phys.: Condens. Matter.*19 (2007) 246205.
- [210] M. Y. Ge, H. Wang, E. J. Liu, J. F. Liu, J. Z. Jiang, Y. K. Li, A. Z. Xu, and H. Y. Li, *Appl. Phys. Lett.* 93 (2008) 062505.
- [211] A. Tiwari, V. M. Bhosle, S. Ramachandran, N. Sudhakar, J. Narayan, S. Budak, and A. Gupta, *Appl. Phys. Lett.* 88(2006) 142511.
- [212] M. Santi, P. Sumalin, L. Paveena, and S. Supapan, *J. Nanosci.Nanotechnol.*9 (2009) 6415.
- [213] Z.D. Dohčević-Mitrović, N. Paunović, M. Radović , Z.V. Popović, B. Matović, B. Cekić, V. Ivanovski, *Appl. Phys. Lett.* 96 (2010)203104.
- [214] P. C. A. Brito, D. A. A. Santos, J, G. S. Duque and M. A. Macêdo, *Physica B*, 405 (2010) 1821.
- [215] F. A. Al-Agela, E. Al-Arfaj, A. A. Al-Ghamdia, B. D. Stein, Y. Losovyj, L. M. Bronsteina, F. S.S hokre and W. E. Mahmouda, *Ceram. Int.*41 (2015) 1115.
- [216] A. Thurber, K. M. Reddy, V. Shutthanandan, M. H. Engelhard, C. Wang, J. Hays and A.Punnoose, *Phys. Rev. B*, 76(2007)165206.
- [217] Q. Y. Wen , H.W. Zhang, Q. H. Yang , Y.Q. Song and J. Q. Xiao , *J. Magn. Magn.Mater.*321 (2009) 3110.
- [218] Y.Q. Song , H.W.Zhang , Y.L.Liu , Y. X. Li , L. R. Shah and J. Q. Xiao , *Physica B* 405 (2010) 2530.
- [219] S.Y. Chen, K.W. Fong, T.T. Peng, C.L.Dong, A. Gloter, D.C. Yan,C.L.Chen, H.J. Lin, and C. T. Chen, *J. Phys. Chem. C*, 116(2012) 26570.
- [220]S. Phokha , D. Prabhakaran , A. Boothroyd , S. Pinitsoontorn and S. Maensiri *Microelectron. Eng.* 126 (2014) 93.

- [221] M. C. Dimri, H. Khanduri, H. Kooskora, J. Subbi, I. Heinmaa, A. Mere, J. Krustok, and R. Stern, *Phys. Status Solidi A*, 209 (2012) 353.
- [222] L. Wang and F. Meng, *Mater. Res. Bull.* 48 (2013) 3492.
- [223] Y. Liu, Z. Lockman, A. Aziz and J. MacManus-Driscoll, *J. Phys.: Condens. Matter* 20 (2008) 165201.
- [224] S. Sonsupap, P. Kidkhunthod, N. Chanlek, S. Pinitsoontorn and S. Maensiria, *Appl. Surf. Sci.* 380(2016)16.
- [225] R. Imbihl and G. Ertl, *Chem. Rev.*95(1995) 697.
- [226] A. S. Ivanova, *Kinet.Catal.*50(2009)797.
- [227] K. Reuter and M. Scheffler, *Phys. Rev. Lett.*90(2003) 046103.
- [228] F. Schth, B. E. Henry and L. D. Schmidt, *Adv Catal*, 39(1993)51.
- [229].A. Trovarelli, *Catalysis by Ceria and Related Materials*. 1st ed.; Imperial College Press: London (2002) 508.
- [230] S. Sato, K. Koizumi and F. Nozaki, *J. Catal.*178 (1998) 264.
- [231] S. Sato, R. Takahashi, T. Sodesawa, K. Matsumoto and Y. Kamimura, *J. Catal.*, 184 (1999)180.
- [232] H. Idriss, C. Diagne, J. P. Hindermann, A. Kiennemann and M. Barteau, *J. Catal.*, 155 (1995)219.
- [233] N. Plint, D. Ghavalas, T. Vally, V. D. Sokolovski and N. J. Coville, *Catal. Today*, 49 (1999)71.
- [234] M. Glinski, J. Kijenski and A. Jakubowski, *Appl. Catal. A*,128 (1995), 209.
- [235] T. S. Hendren and K. M. Dooley, *Catal.Today*, 85(2003) 333.
- [236] Y. Kamimura, S. Sato, R. Takahashi, T. Sodesawa and T. Akashi, *Appl. Catal.A*, 252(2003)399.
- [237] Y. Sakata and V. Ponec, *Appl. Catal. A*, 166 (1998) 173–184.

- [238] T. Akashi, S. Sato, R. Takahashi, T. Sodesawa and K. Inui, *Catal. Commun.* 4 (2003) 411.
- [239] A. Igarashi, N. Ichikawa, S. Sato, R. Takahashi and T. Sodesawa, *Appl. Catal. A* 300(2006)50.
- [240] N. Ichikawa, S. Sato, R. Takahashi, T. Sodesawa, H. Fujita, T. Atoguchi and A. Shiga, *J. Catal.* 239(2006)13.
- [241] S. Sato, R. Takahashi, T. Sodesawa, A. Igarashi and H. Inoue, *Appl. Catal. A*, 328(2007)109.
- [242] M. Kobune, S. Sato and R. Takahashi, *J. Mol. Catal. A: Chem.* 279(2008)10.
- [243] M. Tamura, T. Tonomura, K. Shimizu and A. Satsuma, *Green Chem.* 14(2012)984.
- [244] M. Honda, S. Sonehara, H. Yasuda, Y. Nakagawa and K. Tomishige *Green Chem.* 13(2011) 3406.
- [245] M. Tamura, K. Shimizu and A. Satsuma, *Chem. Lett.* 41(2012)1397.
- [246] R. W. Snell and B. H. Shanks, *ACS Catal.* 3 (2013) 783.
- [247] R. Juarez, A. Corma and H. Garcia, *Green Chem.* 11 (2009) 949.
- [248] S. M. Agawane, J. M. Nagarkar, *Tetrahedron Lett.* 52 (2011)3499.
- [249] D. Terribile, A. Trovarelli, J. Llorca, C. Leitenburg, G. Dolcetti, *J. Catal.* 178 (1998) 299.
- [250] R. Shelkar, S. Sarode, J. Nagarkar, *Tetrahedron Lett.* 54 (2013) 6986.
- [251] H. Miura, K. Wada, S. Hosokawa, M. Inoue, *Chem. Eur. J.* 16(2010)4186.
- [252] S. Imamura, K. Denpo, H. Kanai, H. Yamane, Y. Saito, Y. Matsumura, *J. Jpn. Petrol. Inst.* 44 (2001) 293–302.
- [253] S. Imamura, J. Tadani, Y. Saito, Y. Okamoto, H. Jindai, C. Kaito, *Appl. Catal. A: Gen.* 201 (2000) 121–127.

- [254] P. Bera, A. Gayen, M.S. Hegde, N.P. Lalla, L. Spadaro, F. Frusteri, F. Arena, J. Phys.Chem. B, 107 (2003) 6122.
- [255] S. Sun, D. Mao, J. Yu, Z. Yang, G. Lu and Z. Ma, Catal. Sci. Technol.5(2015), 3166.
- [256] Y. Li, Y. Cai, X. Xing, N. Chen, D. Deng and Y. Wang, Anal. Methods.7(2015) 3238.
- [257] E. M. Slavinskaya, T. Yu. Kardash, O. A. Stonkus, R. V. Gulyaev, I. N. Lapin, V. A. Svetlichnyi and A. I. Boronin, Catal. Sci. Technol.6(2016)6650.
- [258] H.Y. Kim, H. M. Lee and G. Henkelman, J. Am. Chem. Soc. 134 (2012) 1560.
- [259] T. Alammari, H. Noei, Y. Wang, W. Grü nert and A. V. Mudring, ACS Sustainable Chem. Eng. 3(2015) 42.
- [260] D. N. Durgasri , T. Vinodkumar , P. Sudarsanam and B. M. Reddy, Catal. Lett.144 (2014) 971.
- [261] B. M. Reddy , G. Thrimurthulu and L. Katta, Catal. Lett.141(2011) 572.
- [262] J. Zhang, H. Yang, S.Wang, W. Liu, X. Liu, J. Guo and Y. Yang Cryst. Eng. Comm. 16(2014)8777.
- [263] A.S. Edelstein, R.C. Cammarata, Nanomaterials: Synthesis, Properties and Applications, Institute of Physics Publishing, Bristol, UK, 1996.
- [264] P. Tartaj, M.P. Morales, S.V. Verdaguier, T.G. Carreno and C.J. Serna, J. Phys. D: Appl. Phys. 36 (2003) R182.
- [265] M. Raghasudha, D. Ravinder and P. Veerasomaiah, J. Magn.Magn.Mater. 355 (2014) 210.
- [266] J. L. Dormann, D. Fiorani (Eds.), Magnetic Properties of Fine Particles, North-Holland, Amsterdam, 1992.

- [267] M. Gaudon, N. Pailhe , A. Wattiaux and A. Demourgues, Mater. Res. Bull. 44 (2009) 479.
- [268] B. Issa , I. M. Obaidat , B. A. Albiss and Y. Haik, Int. J. Mol. Sci. 14(2013) 21266.
- [269] Y. Shimizu, H. Arai and T. Seiyama, Sens. Actuators 7 (1985) 11.
- [270] Y. L. Liu, Z. M. Liu, Y. Yang, H. F. Yang, G. L. Shen, and R. Q. Yu, Sens. Actuators B, 107 (2005) 600–60
- [271] G. Busca, E. Finocchio, V. Lorenzelli, M. Trombetta, and S.A. Rossini, J. Chem. Soc., Faraday Trans. 92 (1996) 4687.
- [272] A. Goldman, Modern Ferrite Technology, Van Nostrand, New York, 1990.
- [273] R.A. McCurrie, Ferromagnetic Materials: Structure and Properties, Academic Press, London, 1994, 180 & 234.
- [274] W. Schutt, C. Gruttner, J. Teller, F. Westphal, U. Hafeli, B. Paulke, P. Goetz, W. Finck, Artif. Organs.23(1999)98.
- [275] Y. W. Jun, Y.M.Huh, J. S. Choi, J. H. Lee, H. T. Song, S. Kim, S. Yoon, K. S. Kim, J.S. Suh and J.Cheon,J.Am.Chem.Soc.127(2005)5732.
- [276] A.Ito, Y. Kuga, H. Honda, H. Kikkawa, A. Horiuchi, Y. Watanabe and T. Kobayash, Cancer Lett.212(2004).
- [277] R. Ivkov, S.J.Denardo, W.Daum, A. R. Foreman, R. C. Goldstein, V. S. Nemkov and G. L. Denardo, Clin. Cancer Res. 11(2005)7093S.
- [278] A.Jordan, R. Scholz, P. Wust, H. Fahling and R. Felix J. Magn.Magn.Mater.201 (1999)413.
- [279] V. P. Torchilin, Eur. J. Pharma.Sci.11(2000)S81.
- [280]C. Alexiou,W. Arnold, R. J. Klein, F. G. Parak, P. Hulin, C. Bergemann, W. Erhardt, S. Wagenpfeil and A. S. Lubbe, Cancer Res.60(2000)6641.

- [281] S. D. Dalt, A. S. Takimi, T. M. Volkmer, V. C. Sousa and C. P. Bergmann, *Powd. Technol.* 210 (2011)103.
- [282] Y. Shena, Q. Zhao, X. Li, Y. Houa and G. Chen, *Colloids Surf. A: Physicochemical and Engineering Aspects* 403(2012)35.
- [283] Y.J.Huang, J.Wang and Q.W.Chen, *Chin. J. Inorg. Chem.* 21(2005)697.
- [284] M.G. FerreiradaSilva, M. A. Valente, *Mater. Chem. Phys.* 132(2012)264.
- [285] Y. L. Liu, Z. M. Liu, Y. Yang, H. F. Yang, G. L. Shen, R. Q. Yu, *Sens. Actuators B*107 (2005)600.
- [286] S.K. Pradhan, S. Bid , M. Gateshki and V. Petkov *Mater. Chem. Phys.* 93(2005)224.
- [287] V. Sepelak, A. Feldhoff, P. Heitjans, F. Krumeich, D. Menzel and F. J. Litterst, *Chem. Mater.*18 (2006) 3057.
- [288] P. Holec, J. Plocek, D. Nižňansky, J. PoltieroVa Vejpravov, *J.Sol–Gel Sci. Technol.* 51(2009)301.
- [289] R. Dom, R. Subasri, K. Radha, P. H. Borse, *Solid State Commun.*151(2011) 470.
- [290] S. D. Dalt , A. S. Takimi , V. C. Sousa and C. P. Bergmann.*Part.Sci. Technol.* 27 (2009)519.
- [291]M. Azam, S. Riaz, A. Akbar and S. Naseem, *J Sol-Gel Sci. Technol.* 74(2015)340.
- [292]S.I. Hussein, A.S. Elkady, M.M. Rashad, A.G. Mostafa and R.M. Megahid, *J. Magn. Magn.Mater.*379 (2015) 9.
- [293]A. S. Elkady, S. I. Hussein and M. M. Rashad, *J. Magn. Magn.Mater.*385(2015)70.
- [294] Y. Yin, B. Zhang, X. Zhang , J. Xu , S. Yang, *J Sol-Gel Sci. Technol.* 66(2013) 540.
- [295]V. Naidu, S. Chandra, K. S, P. Durairaj, J. Kalyana Sundar4 and M.Sivabharathy, *Int.J. Chem Tech Res.* 6(2014) 5595.

- [296] M.I. M. Omer, A. A. Elbadawi and O. A. Yassin, *Journal of Applied and Industrial Sciences*, 1(2013) 20.
- [298] M. G. Naseri , M. H. M. Ara, E. B. Saion and A. H. Shaari ,*J. Magn, Magn. Mater.*350 (2014)141.
- [299] R. Tadi, Y. -Il Kim , A. K. Sarella, C. G. Kim and K. S. Ryu , *J. Magn. Magn.Mater.*322 (2010) 3372.
- [300] P. P. Hankare, V. T. Vader, N. M. Patil, S. D. Jadhav, U. B. Sankpal, M.R. Kadam, B. K. Chougule, N.S. Gajbhiye, *Mater. Chem. Phys.* 113 (2009) 233.
- [301] K.K. Bamzai, G. Kour , B. Kaur and S. D. Kulkarni, *J. Magn. Magn.Mater.*327 (2013) 159.
- [302] S. Thankachan, B. P. Jacob, S. Xavier and E. M. Mohammed, *J. Magn.Magn.Mater.*348 (2013) 140.
- [303] A.C. Druc, A.I. Borhan, A. Diaconu, A.R. Iordan, G.G. Nedelcu, L. Leontie and M. N. Palamaru, *Ceram. Intl.* 40 (2014) 13573.
- [304] R. Ali, A. Mahmood, M.A. Khan, A.H. Chughtai, M. Shahid, I. Shakir and M.F. Warsi, *J. Alloy. Compd.* 584 (2014) 363.
- [305] A.C. Druc, A.I. Borhan, G.G. Nedelcu, L. Leontie, A.R. Iordan and M.N. Palamaru, *Mater. Res. Bull.* 48 (2013) 4647.
- [306] M.J. Iqbal, Z. Ahmad, T. Meydan and Y. Melikhov, *J. Magn.Magn.Mater.*324 (2012) 3986.
- [307] M. Kaur, S. Rana and P.S. Tarsikka, *Ceram. Intl.* 38 (2012) 4319.
- [308] J. Shah, M. Arora, L.P. Purohit and R.K. Kotnala, *Sens. Actuators A* 167 (2011) 332.
- [309] M.A. Khan, M.U. Islam, M. Ishaque and I.Z. Rahman, *Ceram.Intl.* 37 (2011) 2519.

- [310] R.K. Kotnala, J. Shah, B. Singh, H. kishan, S. Singh, S.K. Dhawan and A. Sengupta, *Sens. Actuators, B: Chem.* 129 (2008) 909.
- [311] B. S. Chauhan, R. Kumar, K. M. Jadhav and M. Singh, *J. Magn. Mater.* 283(2004)71.
- [312] M. Singh, *J. Magn. Mater.* 299(2006)397.
- [313] H.H. Joshi and R.G. Kulkarni, *J. Mater. Sci.* 21(1986)2138.
- [314] K.B. Modi, H.H. Joshi, R.G. Kulkarni and *J. Mater. Sci.* 31(1996)1311.
- [315] K.K. Bamzai, G. Kour, B. Kaur and S.D. Kulkarni, *J. Mater.* 2014 (2014) 8.
- [316] S.I. Hussein, A.S. Elkady, M.M. Rashad, A.G. Mostafa and R.M. Megahid, *J. Magn. Mater.* 379 (2015) 9.
- [317] M. Raghasudha, D. Ravinder, and P. V. Somaiah, *Journal of Chemistry*, 2013(2013)Article ID 804042, 6 pages.
- [318] B. I. Kharisov, H.V. Rasika Dias and O. V. Kharissova, *Arabian Journal of Chemistry* (2014) doi:10.1016/j.arabjc.2014.10.049
- [319] M. A. Gibson and J. W. Hightower, *J. Cat.* 41(1976) 431.
- [320] J. Lu, X. Wei, Y. Chang, S. Tian and Ya Xiong *J. Chem. Technol. Biotechnol.* 91(2016) 985.
- [321] M. Sheykhan, H. Mohammadnejad, J. Akbari and A. Heydari, *Tetrahedron Lett.* 53 (2012) 2959.
- [322] C. A. Ladole, N. G. Salunkhe, R. S. Bhaskar and A. S. Aswar, *European Journal of Chemistry* 5 (2014) 122.
- [323] Y. H. Lee, G.D. Lee, S. S. Park and S.S. Hong, *React. Kinet. Catal. Lett.* 84 (2005)311.
- [324] C.J. Jia, Y. Liu, M. Schwickardi, C. Weidenthaler B. Spliethoff, *Appl. Catal. A: General* 386(2010)94.

- [325] A. R. West. Solid state chemistry and its applications, John Wiley and Sons, publications, Singapore, Student edition.(2003) 102.
- [326] A. Patterson, Phys. Rev. 56 (1939)978.
- [327] S. Charurvedi and P. N. Dave, Current Microscopy Contributions to Advances in Science and Technology, Microscopy in Nanotechnology, A. Méndez-Vilas, Ed. 946.
- [328] H. Lee and N. T. Flynn X-ray photoelectron spectroscopy, chapt 11, Handbook of Applied Solid State Spectroscopy, Springer publication (2006)485.
- [329] V. Luca, S. Djajanti and R. F. Howe, J. Phys. Chem .B, 102 (998)10650.
- [330] A. Younis, D. Chu and S. Li, RSC Adv. 3(2013)13422.
- [331] S. Verma, J. Chand and M. Singh, J. Magn. Mater. 324 (2012) 3252.
- [332] S.R. Naik and A. V. Salker, J. Mater. Chem. 22 (2012) 2740.
- [333] M. Pashchanka, R. C. Hoffmann, A. Gurlo and J. J. Schneider, J. Mater. Chem., 20(2010)8311.
- [334] E. Hammarberg, A. Prodi-Schwab and C. Feldmann , Thin Solid Films 516 (2008) 7437.
- [335] I. A. Farbun, I. V. Romanova, T. E. Terikovskaya, D. I. Dzanashvili and S. A. Kirillov, Russ.J. Appl. Chem. (80)2007) 17981803.
- [336] R. Prakash, J. IL Song, S. Kumar and C.G. lee, Int. J. Nanosci. 10 (2011) 961.
- [337] D. Liu, W.W. Lei, B. Zou, S.D. Yu, J. Hao, K. Wang, B.B. Liu, Q.L. Cui and G.T. Zou, J. Appl. Phys. 104 (2008)083506.
- [338] H.A.R. Aliabad, M. Bazrafshan, H. Vaezi, M. Yousaf, J. Munir and M.A. Saeed, Chinese . Phys. Lett. 30 (2013)127101.
- [339] M. Sasaki, K. Yasui, S. Kohiki, H. Deguchi, S. Matsushima, M. Oku and T. Shishido, J. Alloys Compd. 334 (2002)205.

- [340] H.G. Kim, P.H. Borse, J.S. Jang, E.D. Jeong, O.S. Jung, Y.J. Suh and J.S. Lee, Chem. Commun 39(2009) 5889.
- [341] J.Gan, X. Lu, J. Wu, S. Xie, T. Zhai, M. Yu, Z. Zhang, Y. Mao, S. Chi, I. Wang, Y. Shen and Y. Tong, Sci. Rep.3(2013)1021.
- [342] L. L. Kazmerski, O. Jamjoum, P. J. Ireland, S. K. Deb, R. A. Mickelsen and W. Chen, J. Vac. Sci. Technol. 19(1981) 467.
- [343] B. Li, Y. Xie, M. Jing, G. Rong, Y.Tang and G. Zhang, Langmuir, 22 (2006) 9380.
- [344] G. Subi'as, J. Stankiewicz, F. Villuendas, M. P. Lozano and J. Garcí'a, Rev. B , 79(2009) 094118.
- [345] T. L. Daulton and B.J. Little, Ultramicroscopy 106 (2006) 561.
- [346] K. M. Reddy, R. Benson, J. Hays, A. Thurber, M. H. Engelhard, V. Shutthanandan, R. Hanson, W. B. Knowlton and A. Punnoose, Sol. Energy Mater. Sol. Cells, 91 (2007)1496–1502
- [347] Y. Zheng, C. Chen, Y. Zhan, X. Lin, Q. Zheng, K. Wei and J. Zhu, J. Phys. Chem. C 112 (2008) 10773.
- [348] M. Habibi and R. Sheibani, J. Sol-Gel Sci. Technol. 54 (2010) 195.
- [349] E. Bêche, P. Charvin, D. Perarnau, S. Abanades and G. Flamant, Surf. Interface Anal. 40 (2008) 264.
- [350] F. Zhang, P. Wang, J. Koberstein, S. Khalid, S. W. Chan, Surf. Sci. 563 (2004) 74.
- [351] J. C. Clinton, Thesis : Colloidal Cerium Oxide Nanoparticles: Synthesis and Characterization Techniques, submitted to Virginia Polytechnic Institute and State University Master of Science Electrical Science and Engineering (2008) Blacksburg, Virginia.

- [352] V. K. Mittal, P. Chandramohan, S. Bera, M. P. Srinivasan, S. Velmurgan and S.V. Narsimhan, *Solid State Commun.* 137 (2006) 6.
- [353] T. Yamashita, P. Hayes, *Appl. Surf. Sci.* 254 (2008) 2441.
- [354] S.R. Naik and A.V. Salker, S.M. Yusuf and S.S. Meena, *J. Alloys Compd.* 566(2013) 54.
- [355] B. Mohagheghi, M. S. Saremi, *Semicond.Sci. Technol.* 18 (2003) 97.
- [356] B. P. Ladgaonkar, P. N. Vasambekar, A. S. Vaingankar, *J. Mater. Sci. Lett.* 19(2000)1375.
- [357] A. Singhal, S.N. Achary, J. Manjanna, O.D. Jayakumar, R.M. Kadam, A.K. Tyagi, *J. Phys. Chem. C.* 113 (2009) 3600.
- [358] M. C. Dimri, A. Verma, S. C. Kashyap, D. C. Dube, O. P. Thakur, and C. Prakash, *Mater.Sci.Eng. B* 133 (2006) 42.
- [359] J. Smith and H. P. J. Wijn, *Ferrites*, Philips Technical Library, London, 1959.
- [360] A. Lakshman, K. H. Rao, R. G. Mendiratta, *J. Magn. Magn.Mater.* 250 (2002).
- [361] S. E. Shirsath, B. G. Toksha and K. M. Jadhav, *Mater. Chem. Phys.* 117 (2009) 163.
- [362] S. Verma, J. Chand and M. Singh, *J. Magn. Magn.Mater.* 324 (2012) 3252.
- [363] A. Verma, T.C. Goel and R.G. Mendiratta, *Mater. Sci. Technol.* 16 (2000) 712.
- [364] B.P. Ladgaonkar, P.N. Vasambekar and A.S. Vaingankar, *J. Magn. Magn. Mater.* 210(2000) 289.
- [365] A.V. Salker and S. M. Gurav, *J. Mater.Sci.* 35(2000)4713.
- [366] Y. Sohtome, N. Takemura, T. Iguchi, Y. Hashimoto, K. Nagasawa, *Synlett* (2006)144.
- [367] G. Klein, S. Pandiaraj and O. Reiser, *Tetrahedron Lett.* 43(2002) 7503.
- [368] D. Ma, Q. Pan and F Han, *Tetrahedron Lett.* 43(2002) 9401.
- [369] Y. Misumi and K. Matsumoto, *Angew. Chem., Int. Ed.*, 41(2002)1031.

- [370] C. Palomo, M. Oiarbide and A. Laso, *Angew. Chem., Int. Ed.* 44 (2005)3881.
- [371]E. Jafari, M. R. Khajouei,F. Hassanzadeh,G. H. Hakimelahiand G. A. Khodarahmi, *Res. Pharm. Sci*, 11 (2016) 1.
- [372] S. Rostamizadeh, A. M. Amani, R. Aryan, H. R. Ghaieni and N. Shadjou, *Synth, Commun.*38 (2008)3567.
- [373]S. Khaskar, M. Gholami, *Res.Chem.Intermed.*,41(2015)3709.
- [374] A. Mayar and Z. Hell, *Catal Lett* (2016)10.
- [375] S. Rostamizadeh, M. Nojavan, R. Aryan, E. Isapoor, M. Azad, *J. Mole.Catal. A: Chem.* 374(2013) 102.
- [376] M. J. Tebbe, W. A. Spitzer, F. Victor, S. C. Miller, C. C. Lee, T. R. Sattelberg Sr., E. Mckinney and J. C. Tang, *J. Med. Chem.*40(1997)3937.
- [377] S. J. Konturek, M. Cieszkowski, N. Kwiecien´, J. Konturek, J. Tasler and J. Bilski, *Gastroenterology*, 86(1984)71.
- [378]M. Pfeffer, K. Swedberg, C. Granger, P. Held, J. McMurray, E. Michelson, B. Olofsson, J. Ostergren, S. Yusuf and S. Pocock, *Lancet*, 362 (2003) 9386.
- [379] P. J. Luder, B. Siffert, F. Witassek, F. Meister and J. Bircher, *Eur. J. Clin.Pharmacol.*31(1986) 443.
- [380] G.Brahmachari, S. Laskar and P.Barik, *RSC Adv.* 3(2013)14245.
- [381] F. K. Behbahani , P. Ziaei , Z. Fakhroueian and N. Doragi, *Monatsh Chem.* 142(2011)901.
- [382] S. B. Rathod, M. K. Lande, and B. R. Arbad, *Bull.Korean Chem. Soc.* 31(2010)2835.
- [383] G.A. Olah, *Friedel-Crafts Chemistry*, Wiley, New York (1973).
- [384] G.A. Olah, G.K.S. Prakash, J. Sommer, *Superacids*, Wiley- Interscience, New York (1985).

- [385] S. Prajapati, A. P. Mishra and A. Srivastava, *Int. J. Pharm. Chem. Biol. Sci.* 2(2012)52.
- [386] M. Soueidan, J. Collin and R. Gil, *Tetrahedron Lett.* 47(2006)5467.
- [387] C. Hardacre, P. Nancarrow, D.W. Rooney, and J. M. Thompson, *Organic Process Research & Development* 12(2008)1156.
- [388] V. R. Choudhary, S. K. Jana, *J. Mol. Catal. A: Chem.* 184(2002) 247.
- [389] V. R. Choudhary, S.K. Jana, A. S. Mamman, *Microporous and Mesoporous Mater.* 56 (2002) 65.
- [390] Y. Sun and R. Prins *Appl. Catal. A: General* 336 (2008) 11.
- [391] G. L. Miller, *Anal Chem* 31 (1959)426.
- [392] J. S Kim, J. Yang, M.J. Kim *J Med Plant Res* 5(2011) 778.
- [393] A. J. Krentz, C. J. Bailey. *Drugs* 65(2005) 385.
- [394] M. L. Cho, J .H. Han, S. G. You, *LWT - Food Sci Technol* 44(2011) 1164.
- [395] C.R Thomas, S. George, A.M. Horst, Z. Ji, R. J. Miller , *ACS Nano* 5(2011)13.
- [396] V.E. Fako, D.Y. Furgeson ,*Adv Drug Deliv Rev* 61(2009) 478.
- [397] S. Lin, Y. Zhao, A. E. Nel, S. Lin, *Small* 9(2013)1608.
- [398] A. Hallare, K. Nagel, H. R. Kohler and R. Triebskorn, *Ecotoxicol. Environ. Saf.* 63(2006)378.
- [399] J.C. Samson and J. Shenker , *Aquat Toxicol* 48(2000) 343.
- [400] N. Singh, M. Coy, R. Tice, E. Schneider, *Exp. Cell.Res.* 175(1988) 184.

APPENDIX I

Publications:

- **M. Z. Naik**, S. N. Meena, S. C. Ghadi, M. M. Naik, A. V. Salker “Evaluation of silver-doped Indium oxide nanoparticles as *in vitro* alpha – amylase and alpha – glucosidase inhibitor”. **Med. Chem. Res.** 25:3(2016) 381-389.
- **M. Z. Naik** and A.V.Salker, “Tailoring the superparamagnetic nature of MgFe₂O₄ nanoparticles by In³⁺ incorporation”. **Mater. Sci. Eng. B**, 211 (2016) 37–44.
- **M. Z. Naik** and A.V. Salker, “A systematic study of cobalt doped In₂O₃ nanoparticles and their applications”**Mater. Res. Innov.** DOI: 10.1080/14328917-2016.1207044

Conference / Symposium Presentations:

- “Magnetic Electrical and catalytic properties of Co doped In₂O₃” at Interdisciplinary symposium for Material Chemistry -2012, held at BARC – Mumbai from 11-15 December 2012.
- “Preparation and solid state studies on Cr³⁺ doped Indium Oxide Nanoparticles” at Nano India 2013, held at NIIST, Trivandrum from 18-19 February 2013.
- “Thermal and Electrical studies of doped Indium Oxide nanoparticles” at the “THERMANS -2013” symposium organised by ITAS at BARC, Trombay.

